UNIVERSITÀ DEGLI STUDI
DI GENOVA

ISTITUTO ITALIANO
DI TECNOLOGIA

Halide perovskite nanocrystal-based light emitting diodes

Fang Chen

PhD Thesis in Sciences and Technologies of
Chemistry and Materials
March 2021

Tutors:
Dr. Mirko Prato (Istituto Italiano di Tecnologia)
Prof. Davide Comoretto (Università degli Studi di Genova)

Advisor:
Dr. Marco Salerno (Istituto Italiano di Tecnologia)

Declaration

I hereby declare that this thesis represents my own work which has been done after registration for the degree of PhD at Università degli Studi di Genova, and has not been previously included in a thesis or dissertation submitted to this or any other institution for a degree, diploma or other qualifications.

陈芳

Contents

Abstract

Lead halide perovskite (LHP)-based optoelectronic device has been a hot research topic in the last years, owing to the versatile optoelectronic properties of this class of materials, such as large light absorption coefficient, long-range charge carrier mobility, high defect tolerance, direct bandgap, and to the facile synthesis process. Since their synthesis by Kovalenko group in 2015, LHP nanocrystals (NCs) gained increasing attention also for application in light-emitting diodes (LEDs), owing to the possibility to easily tune their emission wavelength across the whole range of visible light and their high color purity. A detailed introduction on the chemistry and physics of LHP NCs, some basic knowledge about LEDs and the development of LEDs based on the LHP NCs are provided in Chapter 1.

In Chapter 2, the chemicals, the basic experiments and the characterization techniques adopted in the thesis are introduced.

In Chapter 3, I identified four issues that need to be solved before the colloidal LHP NCs could be efficiently applied into the fabrication of high efficient and stable LEDs. Given that long-chain and insulating ligands are used during the NC synthesis to ensure their good solubility and stability in solution, conductivity of LHP NCs films is too low to transport carriers efficiently. Secondly, post-treatments on the LHP NCs, often aimed at improving the aforementioned transport properties, are easy to introduce new defects and compromise the optical properties of the LHP NCs. Thirdly, since LHP NCs are ionic crystals and sensitive to humid air as well as to post-treatments, their long-term stability is still a big issue. Finally, it is difficult to obtain smooth and compact LHP NCs films, which are necessary for low current leakage and high-efficient devices. I addressed the above four issues step-by-step and obtained highly stable LHP NCs films. A combination of benzoyl bromide, ammonium thiocyanate and ethyl acetate was used to treat the pristine LHP NC solution. The method demonstrated to be able to improve the conductivity of the LHP NCs films and well retain the optical properties and morphology even after ten months.

Based on the proposed treatment method in Chapter 3, I employed the obtained NCs as emissive layer in green LEDs in Chapter 4. The champion device showed high efficiency of 1.2% at 518 nm with a maximum brightness near 3000 cd/m^2 and high stability during operation with a half-lifetime of 27 min at a constant bias of 5 V as well as during storage (23 days in air). Furthermore, I conducted a mechanism study on the efficiency roll-off of the NCs-based LEDs

using conductive atomic force microscopy (c-AFM). Morphology and current distribution of the NCs films under increasing bias were collected and a new insight about the efficiency roll-off was proposed.

In Chapter 5, I further focused on the improvement of the efficiency of blue LEDs based on LHP NCs, which is still lower than that of green and red ones. In this context, I studied the effect of addition of various metal halides during the synthesis of LHP NCs on their optical properties. I found that the post-synthesis addition of $CuCl_2$ leads to the formation of NCs with sky-blue emission and high stability in air. I applied the obtained NCs in the fabrication of sky-blue LEDs. The champion device, based on NCs with further optimized ligands, produces the up-to-date highest external quantum efficiency (EQE) of 5.02% and the highest luminance of 130 cd/m^2 at the maximum EQE.

In summary, this thesis firstly provides a promising route and proposes a possible mechanism to achieve high stable LHP NCs film. Secondly, efficient green LHP LEDs were obtained. Thirdly, a possible mechanism of the efficiency roll-off in LHP NC LED was proposed and may give guidance for the design of NC LEDs with suppressed efficiency roll-off in the future. Last but not least, high efficient and stable sky-blue LED was fabricated based on $CuCl_2$-treated LHP NCs, paving a promising way towards the fabrication of highly efficient LHP NC-based blue LEDs.

Chapter 1: Introduction

Research on halide perovskites has been a hot topic in recent few years owing to the all-round performance of this class of materials. Its excellent physical and chemical properties make it promising to be widely applied in optoelectronic devices [1]. The high absorption coefficient of visible light and the high carrier mobility entail halide perovskite competitive candidates for solar cell. Several reports have shown power conversion efficiency (PCE) above 20% with increasingly high stability for commercial application, which is on par with the current silicon-based solar cells but with a much lower cost [2-6]. The high carrier mobility and facile fabrication of the materials make it potential as photodetectors and field effect transistors [7, 8]. The wide color gamut and high color purity propel widespread studies of the halide perovskite materials in application of displays [9]. The low threshold for amplified spontaneous emission (ASE) boosts research of halide perovskite as lasers [1, 10]. The benign defect tolerance property and the high color purity make it potential to fabricate light emitting diodes (LEDs), among which in-situ prepared thin film perovskite LEDs with green or near-infrared emission have achieved EQE higher than 20% [11, 12]. Comparing with thin film perovskite, perovskite nanocrystals (NCs) have higher color purity, which is favorable for obtaining LEDs with narrow emission wavelength [13]. Application of perovskite NCs in LEDs has also made continuous progress in recent years [10, 14].

In this chapter, the chemical and physical background of perovskite NCs are introduced. A short review of the application of perovskite NCs in LEDs is presented. Eventually, the aim of the work of the project is introduced.

1.1 Chemistry of lead halide perovskites

1.1.1 Composition

A large family of compounds could be identified with the term “perovskite”, spanning from oxides, to fluorides, chlorides, hydroxides, arsenides, and intermetallic compounds [15]. Synthetic perovskites span across the whole periodic table in terms of elemental composition, and they can exist in many complex formulas[15]. Halide perovskites share a formula ABX_3 in a strict sense [15, 16]. Here, A represents a monovalent cation, including methylammonium ion (MA^+), formamidinium ion (FA^+), Cs^+, or any of their combinations. B usually represents a bivalent cation, including Pb^{2+}, Sn^{2+}. X represents a halide ion, including Cl^-, Br^-, I^-, or any of their combinations. In this thesis, I will focus on the lead halide perovskite NCs (abbreviated as LHP NCs).

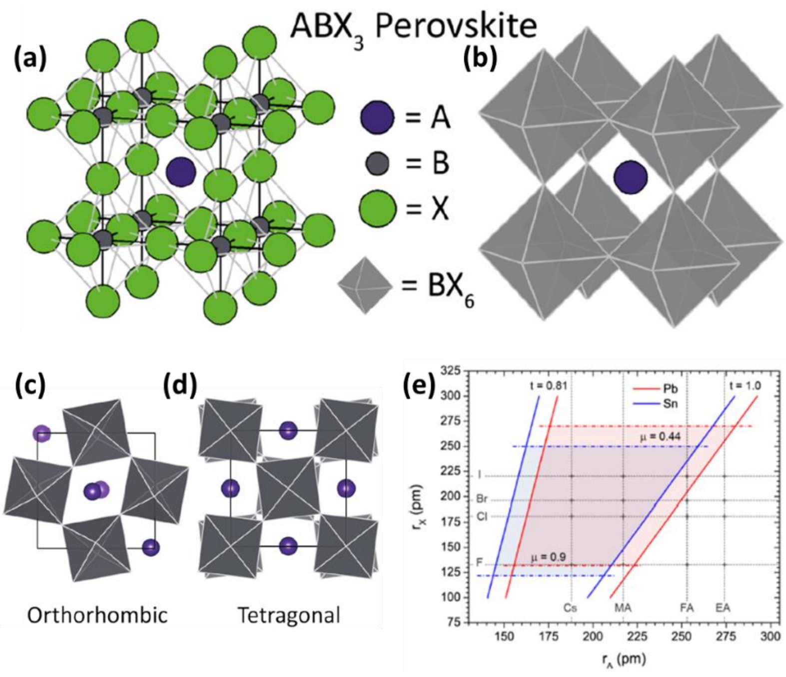

Figure 1.1. Chemical and structural compositions of LHP NCs. (a) Standard depiction of the aristotype cubic perovskite. Shown in display styles evidencing either all the atoms (left) or only the BX_6 octahedral network and A atoms (right); (c) Common orthorhombic and (c) tetragonal disordered perovskites, arising from the tilting of the octahedral; Reprinted with permission from [15]. Copyright (2020) American Chemical Society. (e) Formability of 3D lead (red) and tin (blue) halide perovskites as a function of A-site cation and halide anion radii. Solid and dashed lines mark the bounds of the tolerance and octahedral factors, respectively. The ionic radii of six-coordinate Pb(II) and Sn(II) are taken as 119 and 110 pm, respectively [16]. Reprinted with permission from American Chemical Society.

From the crystallographic point of view, LHPs are networks of corner-sharing octahedra, in which Pb is coordinated to six halides to form $[PbX_6]^{4-}$ units (Figure 1.1a). Monovalent cations fill the dodecahedral space among the $[PbX_6]^{4-}$ octahedral arrays [16]. The crystal phase of the LHP includes cubic, tetragonal and orthorhombic phases, as displayed in Figure 1.1b-d.The orthorhombic and the tetragonal phases originate from the tilted octahedron in the cubic structure, and are more common than cubic phase for LHP due to the size difference between A, B and X [15].

LHPs with proper chemical compositions and stable crystal structures satisfy the so-called Goldschmidt tolerance factor, t, and octahedral factor, μ [17, 18]:

$$t = \frac{R_A + R_X}{\sqrt{2}(R_B + R_X)} \tag{1}$$

$$\mu = \frac{R_B}{R_X} \tag{2}$$

Here, R_A, R_B, and R_X are the ionic radii of A, B, and X components, respectively. For a typical stable LHP, t ranges from 0.81 to 1.0, and μ ranges from 0.44 to 0.90 (Figure 1.1e).

1.1.2 Synthesis of lead halide perovskite nanocrystals

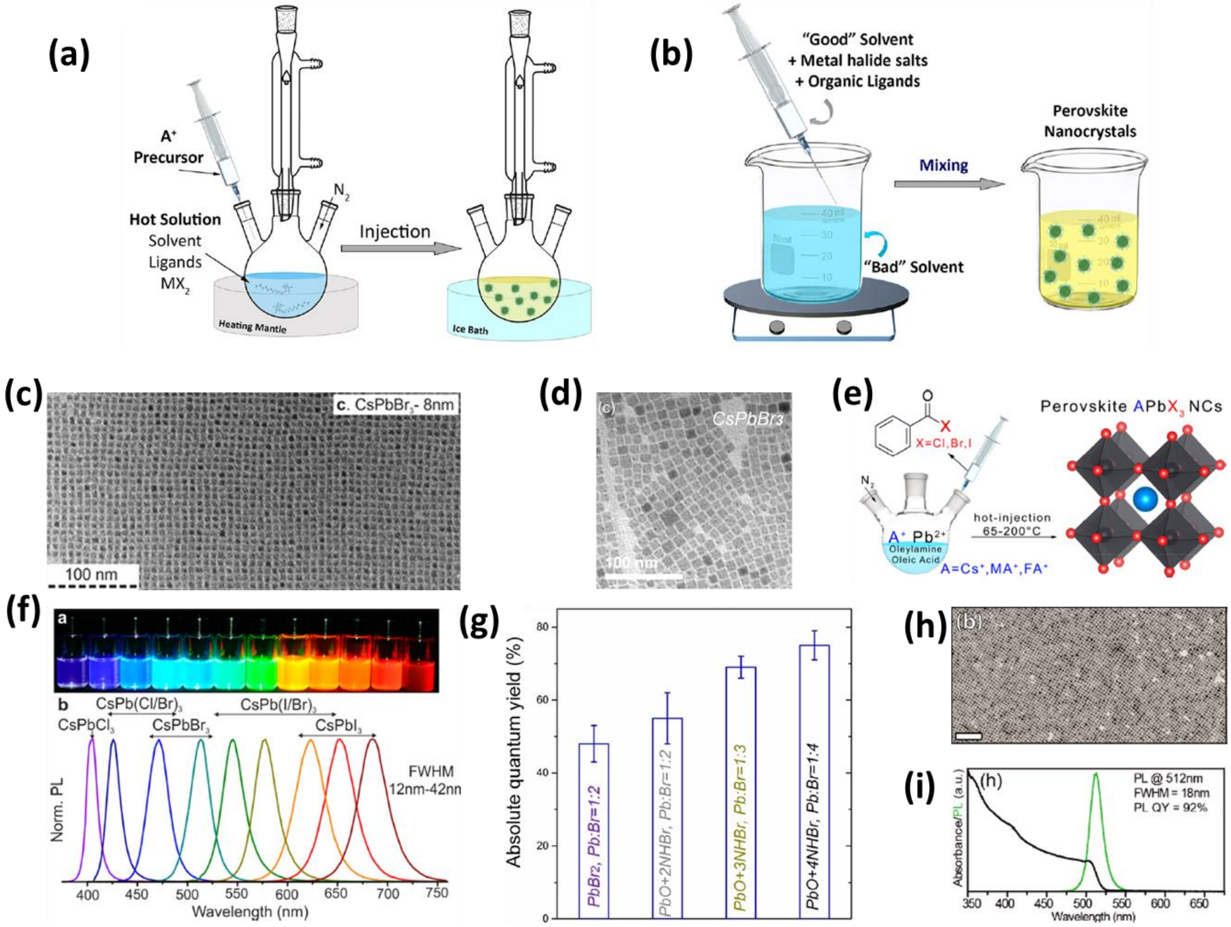

Figure 1.2. Synthesis of $CsPbX_3$ NC solutions. Schematic diagrams of (a) hot injection (HI) and (b) ligand-assisted re-precipitation (LARP) methods [13]. https://pubs.acs.org/doi/10.1021/acs.chemrev.8b00644 Reprinted with permission from American Chemical Society. (c) TEM image and (f) photos as well as PL spectra of $CsPbX_3$ NC solutions synthesized with $PbBr_2$ [19]. https://pubs.acs.org/doi/10.1021/nl5048779 Reprinted with permission from American Chemical Society. (d) TEM image and (g) statistics of PL QY of $CsPbBr_3$ NC solutions synthesized with PbO and NH_4Br. Reprinted with permission from [20]. Copyright (2016) American Chemical Society. (e) Schematic synthesis diagram, (h) TEM image and (i) optical characterization results of $CsPbBr_3$ NC solutions synthesized with benzoyl bromide (BBr) [21]. https://pubs.acs.org/doi/10.1021/nl5048779 Reprinted with permission from American Chemical Society.

Several methods have been developed to synthesize LHP NCs. These include wet-chemical routes such as hot-injection (HI) and ligand-assisted re-precipitation (LARP), and wet ball-milling route [13]. The difficulty lies in the solubility of the different element sources in the reaction solvent.

The HI method is usually performed at high temperature and in vacuum (Figure 1.2a). The precursors for the different components are usually separated at the beginning. When the precursors for lead and cesium, originally in solid state, are fully dissolved in non-polar solvents, such as octadecene (ODE) and trioctylphosphine oxide (TOPO), with assistance of ligands such as oleic acid (OA) and oleylamine (OLAM), and when the chosen reaction temperature is reached, the halide precursor is swiftly injected into the reactive solution. After a short time, *e.g.*, less than 1 minute, the reaction system is quickly cooled down with ice bath to obtain monodisperse LHP NCs. In the following, the synthesis of $CsPbBr_3$ is taken as reference, and the different HI approaches are discussed.

Protesescu *et al.* [19] synthesized for the first time $CsPbBr_3$ NCs via the HI route. They used lead bromide as source of lead and bromine, cesium carbonate as source of cesium and OA as well as OLAM as ligands dissolved in ODE solvent. Monodisperse colloidal nano-cubes of ~ 8 nm in size (Figure 1.2c) were obtained at a reaction temperature of 120 °C. They were able to obtain $CsPbCl_3$ and $CsPbI_3$ NCs as well, by replacing lead bromide with lead chloride or lead iodide, respectively (Figure 1.2f); also, by tuning the reaction temperature, they were able to control the size of $CsPbBr_3$ NCs through quantum confinement. One of the features of this procedure is that the ratio of lead and bromine in the precursors is fixed because of the choice of the precursors themselves and cannot be adjusted.

The possibility of playing with the ratio between the different components may exert a significant effect on the final obtained NCs. Thus, alternative sources for bromine and lead were explored by researchers. Liu *et al.* [20] replaced lead halide with lead oxide and ammonium halide (Figure 1.2g) and realized controllable adjustment of the ratio between lead and halide. Through controlling the amount of ammonium bromide relative to the lead oxide, they were able to obtain either bromide-poor or bromide-rich $CsPbBr_3$ NCs via a three-precursor HI approach at 180 °C (Figure 1.2d). Later, Imran *et al.* [21] further updated the source of bromine. They used lead acetate trihydrate as source of lead and cesium carbonate as source of cesium, and injected benzoyl bromide (BBr) into the reaction system at 180 °C, obtaining $CsPbBr_3$ NCs with near-unity PL QY (Figures 1.2e, h, i).

The LARP method is usually performed at room temperature (RT) with a simple apparatus (Figure 1.2b). First, metal halide salts, such as cesium bromide and lead bromide, are fully dissolved in a “good” solvent which has high polarity and could dissolve the salts, such as dimethylformamide (DMF) and dimethylsulfoxide (DMSO) [22, 23]. Subsequently, the dissolved solution is poured into a “bad” solvent which has low polarity and low solubility for salts, such as toluene and hexane, in the presence of a proper amount of ligands [13, 24]. Based on the difference in solubility of the LHP NCs in the good and in the bad solvent, LHP NCs are formed in the bad solvent [25, 26]. Since it is reported that much more ligands are needed in the LARP case than in the HI case, the work done in the present project was not focused on LHP NCs prepared by the LARP method, because too much ligand in NC solution is unfavorable for optoelectronic devices.

High-energy ball milling also received attention in synthesis of LHP NCs in recent two years. Mechanical energy is provided to the system to realize mechanical friction between the grinding medium, such as grinding balls with the same or various sizes, and the source materials. This method includes dry milling [27, 28] and wet milling[29]. For example, Kovalenko and co-workers report successful synthesis of $FAPbBr_3$ and $CsPbBr_3$ NCs by wet ball milling. The as-synthesized NCs show as good optical performance as that of NCs synthesized by the HI method [29]. Palazon *et al* synthesized phase-pure $CsPbBr_3$ via a fast dry ball milling.

1.1.3 Surface capping ligands

Surfactants or surface capping ligands play a significant role in the synthesis as well as in the application of LHP NCs [30]. Ligands are usually divided, according to covalent bond classification (Figure 1.3c), into L-type, X-type and Z-type ligands, depending on the number of electrons shared with the NC by the ligand, if 0, 1 or 2 electrons, respectively [31]. In this thesis, I divide the ligands for the LHP NCs into organic ligands and inorganic ligands.

The class of the “organic ligands” include both small molecules (with various carbon chain lengths and functional groups) and polymers, characterized by different steric effects. So far, small molecules having been explored as ligands of LHP NCs include OA [32], OLAM [19], secondary aliphatic amines (*e.g.*, didodecylamine [33]), ammonium bromides (*e.g.*, didodecyl ammonium bromide (DDAB) and tetraoctylammonium bromide (TOAB) [34]), conjugated alkyl-amine (*e.g.*, 3-phenyl-2-propen-1-amine (PPA) [35]), zwitterionic molecules (*e.g.*, 3-(N,N-dimethyloctadecylammonio)-propanesulfonate [36]), bidentate ligands (*e.g.*, 2,2’-iminodibenzoic acid (IDA) [37]), octylphosphonic acid (OPA) [38], TOPO [24], crown ethers (*e.g.*, dibenzo-21-crown-7 [22]), ammonium thiocyanate [39, 40], organoammonium iodides (*e.g.*, 4-fluorophenylmethylamine iodide), or combinations of the above. Polymers include *e.g*. poly(propylene carbonate) (PPC, $[C_4H_6O_3]_n$) [41], poly(2-hydroxyethyl methacrylate) (poly-HEMA) [42].

Inorganic ligands include halide ions (e.g., Br^- [43] [44], Cl^- [45]) and metal ions (*e.g.*, Ag^+ [46], Zn^{2+} [47]).

Ligands can be used for LHP NCs either during synthesis or during post-synthesis processing. During the synthesis, ligands are used to control the nucleation and growth of LHP NCs, and thus their resulting size and morphology. Length, quantity and/or functional groups of the ligands may all play a significant effect. For example, long-chain ligands at a relatively high amount are expected to facilitate the formation of the so-called 2D halide perovskites [48, 49]. The presence of specific functional groups in the ligands may induce bonding with certain reactive components and influence the reaction rate as well as the morphology of the final products[22].

Ligands are added to ensure solubility and stability of the colloidal LHP NCs in solvents (Figure 1.3a) [50]. For example, OA and/or OLAM are usually used in NC synthesis to obtain stable LHP NC solutions [19]. Moreover, ligands are expected to bridge the LHP NCs and the external environment. For example, optoelectronic devices based on LHP NCs require ligands with proper spatial effect to avoid aggregation as well as avoid resonance energy transfer, and provide assistance in the conductivity to facilitate carrier transfer among NCs [51].

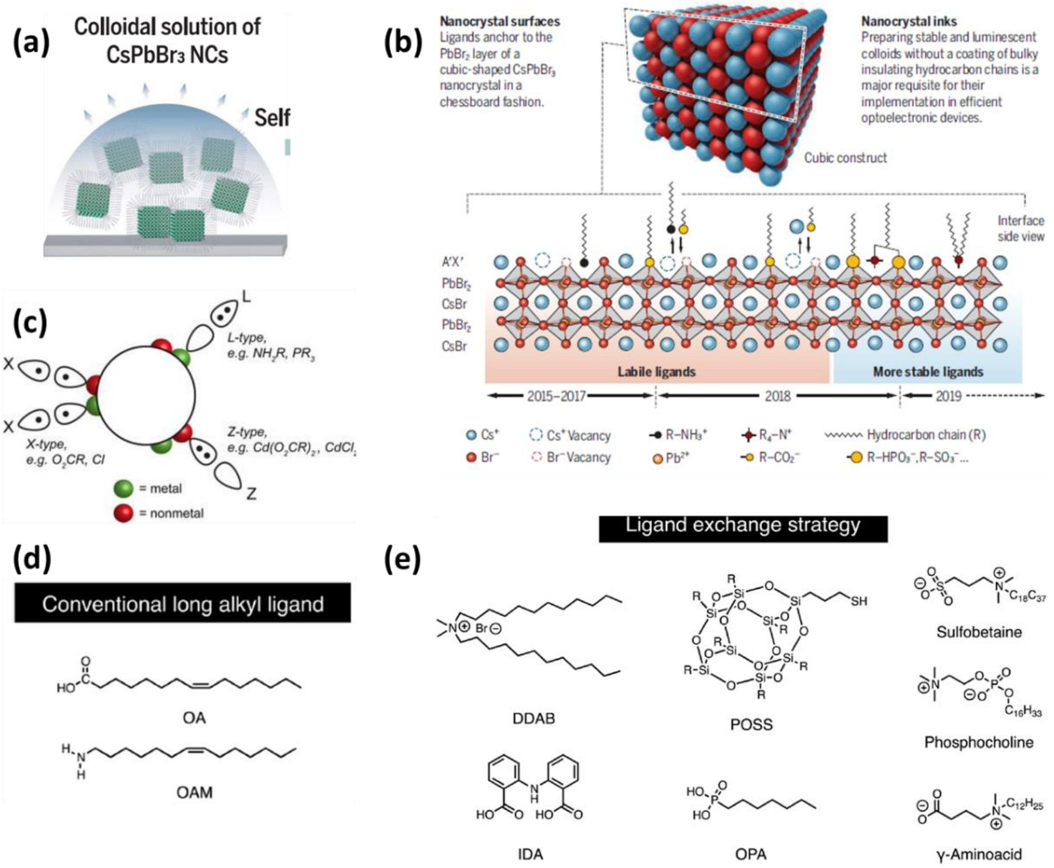

Figure 1.3. Role of ligands in LHP NCs. (a) Colloidal LHP NCs with ligands around to be soluble and stable in solution[50, 52]; (b) interaction between ligands and surface of LHP NCs [53]; (c) motifs of binding between nanocrystal and ligand according to the covalent bond classification method [31]; typical molecular structures of (d) conventional long-chain and labile ligands; and (e) ligands with shorter chains and higher bonding with LHP NCs. Reproduced from the respective references, on permission by the Publishers.

In addition, ligands are necessary for the passivation of surface defects on LHP NCs (Figure 1.3b) [53], which are detrimental for their optical and electrical properties. Possible surface defects on the LHP NCs may include halide vacancies, under-coordinated lead ions, or free lead atoms [54]. Proper ligands are able to passivate the defects [55]. Firstly, organic ligands, which are able to form strong bonding with the surface of LHP NCs, are widely proved to be good passivating agents (Figure 1.3e). Quaternary ammonium bromides (R_4NBr) are widely used to improve photoluminescence (PL) quantum yield (QY) of the LHP NCs. For example, Chen *et al.* [56] found that the PL QY increased from 78% to 85% in NC solution and from 8.2% to 23.6% in NC film after treating $CsPbBr_3$ NCs with DDAB, suggesting strong bonding between NC surfaces and DDAB molecules. Also, Imran *et al.* [34] achieved near-unity PL QY using didodecyl dimethylammonium bromide (DDDMAB, C12), indicating excellent passivation effect of R_4NBr (Figure 1.4a).

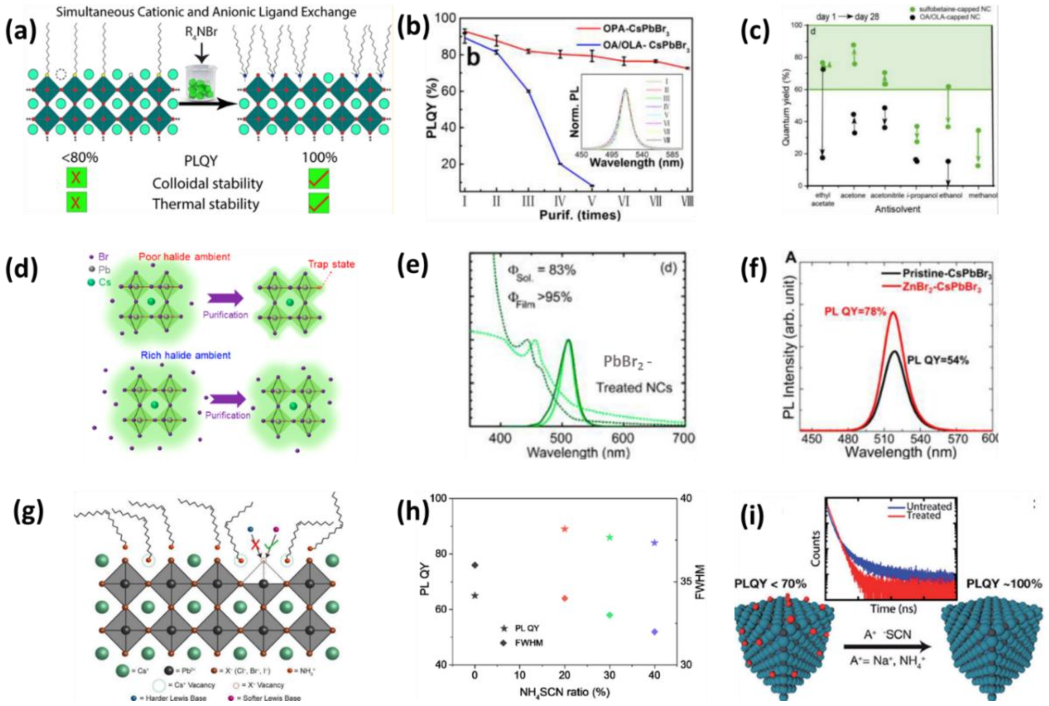

Figure 1.4. Passivation effect on LHP NCs. Passivation of LHP NC surface with organic ligands (a) R$_4$NBr; Reprinted with permission from [34]. Copyright (2019) American Chemical Society. (b) OPA; Reprinted with permission from [38]. Copyright (2018) American Chemical Society. and (c) sulfobetaine [36]. https://pubs.acs.org/doi/10.1021/jacs.7b13477 Reprinted with permission from American Chemical Society. (d) Schematic mechanism of passivation of LHP NC surface with bromide ions[20]; passivation effect on LHP NCs with (e) PbBr$_2$; Reprinted with permission from [43]. Copyright (2017) American Chemical Society. and (f) ZnBr$_2$; Reprinted with permission from [57]. Copyright (2017) American Chemical Society. (g) Schematic mechanism of passivation of LHP NC surface with soft Lewis base Reprinted with permission from [31]. Copyright (2018) American Chemical Society. (e) passivation effect on LHP NCs with NH$_4$SCN [39], and (f) schematic passivation effect on LHP NCs with SCN; Reprinted with permission from $^-$ [58, 59]. Copyright (2017) American Chemical Society.

Other organic molecules have been also used to passivate the LHP NCs. For example, Tan *et al.* [38] achieved a high PL QY of ~90% using OPA to cap the CsPbBr$_3$ NCs (Figure 1.4b). Pan *et al.* [37] increased the PL QY of CsPbI$_3$ NCs from 80% to 95% after treating the NCs with bidentate IDA. Thanks to its two carboxylic functional groups, IDA has a binding energy of 1.4 eV with the NC surface, which is higher than 1.14 eV for OA-treated NCs, thus improving the stability of the NCs. Krieg *et al.* [36] obtained highly passivated CsPbBr$_3$ NCs with zwitterionic ligands as capping agent, achieving PL QY as high as 90%; the treatment proved to effectively retain up to 60% of the initial PL QY in films stored for more than 10 months under ambient conditions. Moreover, the PL QY of the NCs could be well preserved even after purification by various polar solvents (Figure 1.4c). Hassan *et al.* [26] improved the PL QY of MAPbI$_2$Br NC solutions from 20-25% to 60-85% by treating the NCs with 1-adamantanecarboxylic acid (ADAC) and 3-aminopropylphosphonic acid.

Metal bromides as inorganic ligands also show to be effective in improving optical performance of halide perovskites (Figure 1.4d). For example, Di Stasio *et al.* [43] treated $CsPbBr_3$ NC solution with $PbBr_2$ and obtained a PL QY higher than 95% on the corresponding film (Figure 1.4e). Woo *et al.* [57] treated $CsPbBr_3$ NC film with $ZnBr_2$ and enhanced the PL QY from 54% to 78% (Figure 1.4f). Similarly, Zeng *et al.* [47] increased PL QY of $CsPbBr_3$ NC film from 58% to 79% by treating the NC solution with $ZnBr_2$. Van der Stam *et al.* [60] also treated $CsPbBr_3$ NC solutions with metal-bromide salts, such as $ZnBr_2$, $CdBr_2$ and $SnBr_2$, in the post-synthesis and were able to preserve more than 60% of the initial PL QY in all cases, although the PL spectra blue-shifted. Li *et al.* [46] used a AgBr-TOP complex to do *in-situ* treatment on $CsPbBr_3$ film and observed noticeable enhancement in the PL intensity.

X-type soft Lewis bases, including R_4NBr, thiophene, pyridine, alkylphosphonates and thio-ion (S^{2-}), have been demonstrated by Nenon *et al.* to be promising candidates to passivate halide vacancies or under-coordinated lead ions on the surface of $CsPbBr_3$ NCs, helping to achieve near-unity PL QY (Figure 1.4g) [31]. Thiocyanate, as a kind of soft Lewis Acid [31, 46], has been previously reported to be a good surface passivator in chalcogenide QDs [61] and LHP NCs. Koscher *et al.* [59] reported that thiocyanate salts could passivate $CsPbBr_3$ NCs in post-synthetic treatment. They showed near-unity PL QY together with single-exponential PL lifetime decay in the case of fresh as well as aged thiocyanate-treated $CsPbBr_3$ NCs (Figure 1.4i). Liu *et al.* [62] proposed that thiocyanate salts are helpful in stabilizing LHP NCs during purification with polar solvents. In their work, they demonstrated in fact that, with thiocyanate ammonium anchoring onto LHP NCs in advance, and then purifying the LHP NCs in ethyl acetate saturated with $Pb(OAc)_2$, the prepared solar cell reached an efficiency of 14.4%. Lu *et al.* [39] added ammonium thiocyanate (NH_4SCN) during the synthesis of $CsPbI_3$ and obtained NCs with PL QY increasing from 65% to 84% with increasing amount of NH_4SCN, suggesting suppressed non-radiative recombination in the passivated NCs (Figure 1.4h).

1.1.4 Post-synthesis treatments

LHP NCs synthesized via the above routes are usually characterized by the presence of labile ligands and/or by an excess of ligands. While the ligands could ensure colloidal as well as optical stability, as discussed in the previous section, they can become obstacles for carrier transport [51, 63, 64] in LHP NC-based optoelectronic devices [65-67]. Currently, two methods, namely ligand purification and post-synthesis ligand exchange, are mainly implemented to alleviate the negative effect of organic ligands on the transport property of LHP NC-based films. Ligand purification of LHP NCs using solvents of different polarity [68] is widely adopted to reduce the amount of original long-chain organic ligands on the surface of LHP NCs[69, 70]. Post-synthesis ligand exchange [26, 34, 71-73] is used to replace the original long-chain and labile organic ligands, like OA and OLA, with short-chain organic ligands or conjugated ligands [35, 74]. These treatments could favor higher carrier mobility in LHP NC-based films, but are often accompanied by compromised structural and optical stability of LHP NCs. For example, LHP NCs may be decomposed, and/or PLQY of the LHP NCs may seriously decrease due to the introduction of a large amount of surface defects as non-radiative pathways[65]. Thus, post-synthesis treatments on the LHP NCs should be optimized to balance improved conductivity and high PLQY. In the following, the methods reported in literature are shortly summarized.

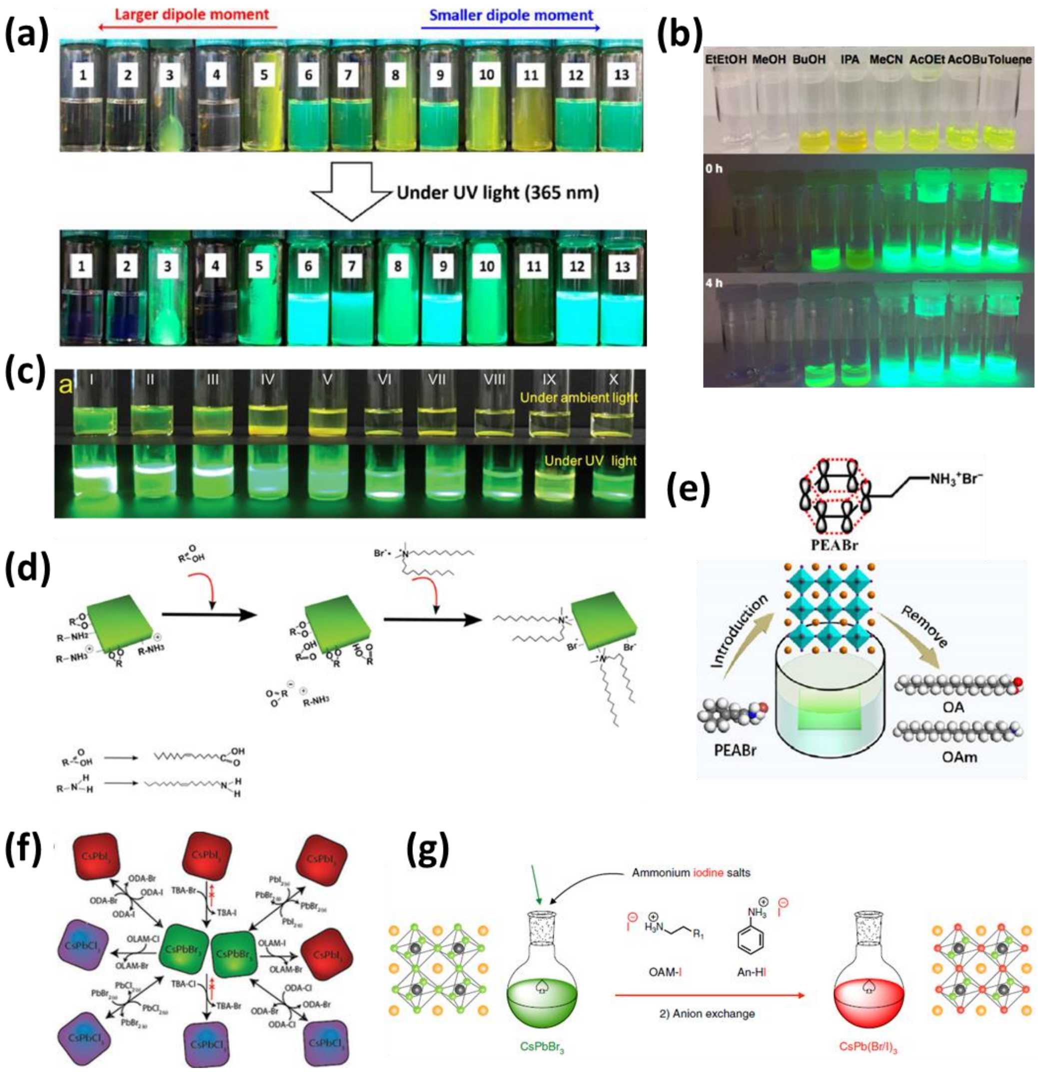

Figure 1.5. Post-synthesis of CsPbBr₃ NC solutions. (a) Effect of polar solvents on crude solutions of as-synthesized CsPbBr₃ NCs. All mixtures of crude solution and polar solvents (with the volume ratio 1:1) in each vial were centrifuged at 8000 rpm for 30 min. The solvents appear in order of increasing dipole moment: (1) dimethyl sulfoxide, (2) dimethylformamide, (3) acetonitrile, (4) methanol (MeOH), (5) acetone, (6) ethyl acetate (EA), (7) tert-butanol, (8) 1-butanol, (9) tetrahydrofuran, (10) isopropyl alcohol (IPA), (11) ethanol, (12) chloroform, and (13) dichloromethane; Reprinted with permission from [68]. Copyright (2017) American Chemical Society. (b) CsPbBr₃ NCs in toluene and purified with various polar solvents; 2-ethoxyethanol (EtEtOH), MeOH, butanol (BuOH), IPA, acetonitrile (MeCN), EA, butyl acetate (AcOBu), and toluene; Reprinted with permission from [69]. Copyright (2017) American Chemical Society. (c) CsPbBr₃ QD inks without (upper) and with (below) UV light excitation after one to ten cycles of treatments; Reprinted by permission John Wiley and Sons: [65] COPYRIGHT (2017), doi: 10.1002/adma.201603885. Adv. Mater. Ligand exchange with (d) DDAB; Reprinted by permission John Wiley and Sons: [73] COPYRIGHT (2016), doi: 10.1002/adma.201600784. Adv. Mater.; and (e) conjugated PEABr molecules; Reprinted by permission from Spring Nature:[74] COPYRIGHT (2018), doi: 10.1007/s12274-018-2187-5. Nano Research. (f) diagram of anion exchange in CsPbBr₃ NC solutions [75]; https://pubs.acs.org/doi/10.1021/jacs.5b05602 Reprinted with permission from American Chemical Society. And (g) of anion-exchange of synthesized pristine CsPbBr₃ NCs using long alkyl ammonium and aryl ammonium; Reprinted by permission from Spring Nature: [76] COPYRIGHT (2020), doi: 10.1038/s41566-018-0260-y. Nature Photonics.

Concerning ligand purification, researchers initially used acetone (with high polarity) to purify the NCs [32, 77]. However, Kim *et al.* showed that high polar solvents can easily damage or optically-deactivate the LHP NCs (Figure 1.5a) [68], given that the LHP NCs are ionic crystals and sensitive to polar solvent. Milder polar solvents such as butyl acetate (Figure 1.5b) [69], ethyl acetate (Figure 1.5c) [65], methyl acetate[67, 78] and diglyme [70] were demonstrated to be able to balance ligand purification and structural integrity or optical performance of the LHP NCs.

Ligand exchange is carried out to replace pristine ligands with "ideal" ligands. DDAB has been widely used to replace conventional ligands such as OA and OLAM during post-synthesis, due to its beneficial effect on the passivation of the LHP NC surface and on the enhancement of conductivity in LHP NC films or devices [34, 56, 73, 79]. For example, Pan *et al.* [73] added 50 μL OA and 100 μL DDAB into 1 mL pristine $CsPbBr_3$ NC solution to do partial ligand exchange (Figure 1.5d). Other ligands such as phenylethylammonium bromide (PEABr) (Figure 1.5e) [74] and ADAC [26] were also used to do ligand exchange with or without assistance of OA.

Anion exchange is also a hot topic in the post-processing of LHP NCs. Halides in LHP NCs can experience fast anion exchange owing to their low defect formation energy and fast ion/defect motion (Figure 1.5f) [13]. For example, mixed halide perovskite NCs could be achieved simply by mixing two LHP NC solutions containing different halides[75]. The composition-tailored LHP NCs show photoluminescence tunable over the whole visible spectrum, while the size and shape of the parent LHP NCs are well preserved [13]. However, if the goal is to control the ratio of different halides in the final NCs, it is better to do the anion exchange using a specific halide source, such as trimethylsilyl halides (TMSX) [76], OLAM-X [75] and PbX_2 (X= Cl, Br, I). For example, Creutz *et al.* [80] realized nearly stoichiometric anion exchange with TMSX, and converted polycrystalline $CsPbBr_3$ into $CsPbI_3$ with TMSI. Chiba *et al.* [76] used stoichiometric alkyl-based oleylammonium iodide (OAM-I) and aryl-based aniline hydroiodide (An-HI) to carry out anion exchange on pristine $CsPbBr_3$ NCs, and obtained high-quality red-emitting LHP NCs with PL QY of 80% and 69%, respectively (Figure 1.5g). It is worth to note that the anion exchange in the LHP NCs is completely reversible.

1.2 Physics of lead halide perovskite NCs

1.2.1 Optical properties

The optical properties of LHP NCs depend on the crystal structure and the electronic states of the NCs. The octahedron structure comprised of $[PbX_6]^{4-}$ determines the distribution of the electronic states or the band structure of the LHP NCs. On one side, the *n*p orbitals from the halogens (Cl: *n*=3, Br: *n*=4, I: *n*=5) provide dominating contribution to the valence band maximum

(VBM), while the antibonding orbital σ^* formed between the halogen *n*p and the Pb(6*s*) orbitals only make minor contribution to the VBM (Figure 1.6a) [18, 58]. This leads to high sensitivity of the VBM to the compositions of the halogens. For example, the VBM and the bandgaps of $MAPbX_3$ with different compositions of halogen vary obviously (Figure 1.6b) [81]. On the other side, the empty Pb(6*p*) orbitals determine the conduction band minimum (CBM), with minor contributions from the σ^* orbitals formed by the *n*p orbitals from the halogens and the 6p orbitals from the lead (Figure 1.6a) [82]. In addition, the σ^* that raises the VBM energy, and the relativistic effects of Pb that lowers the CBM energy, make the LHP NCs tolerant to deep-trap defects, which are either shallow energy or resonant within the bands [83]. Apart from direct electron transition between the VBM and the CBM (called B channel), other transition channels are also possible, including trap-mediated (called T channel) recombination, exciton generation and recombination (X channel), and hole-trapping channels [16].

Moreover, the unique electronic structure of the LHP NCs forms direct bandgaps, which are favorable for radiative emission. The band structure affects the optical spectral properties of light absorbance and PL. The absorption and PL spectra of $CsPbX_3$ NC solutions are tunable along the entire visible light region, through varying the halide compositions (Figure 1.6d) [58]. Additionally, the bandgap or the absorption/emission wavelengths can also be tuned by controlling the size of or by applying high pressure onto the NCs [58]. There, decreasing the size of the NCs could enhance the overlapping of the states and widen the bandgap of the NCs (Figure 1.6e). Increasing the pressure on the NCs above a given threshold, could cause gradual distortion of the octahedrons and lead to variation of the electronic states of the components, leading to a shift of the PL spectra (Figure 1.6f).

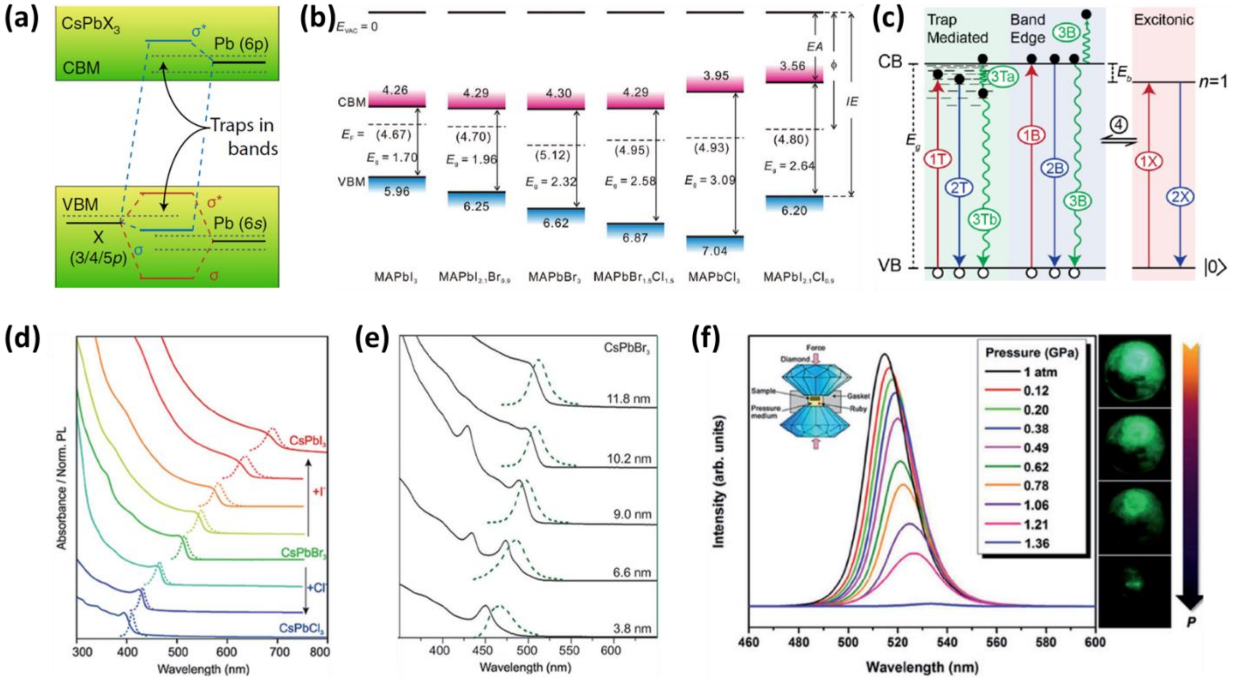

Figure 1.6. Electronic structure and optical property of LHP NCs. (a) Schematic representation of electronic band structure of typical LHPs. Reprinted by permission from Spring Nature: [18] COPYRIGHT (2018), doi: 10.1038/s41563-018-0018-4. Nature Photonics. (b) energy level diagrams of MAPbX$_3$. Reprinted by permission from John Wiley and Sons:[81] *COPYRIGHT (2020), doi: 10.1002/admi.201600694. Adv. Mater. Interfaces. (c) blueprint of the various charge generation and recombination pathways in a bulk semiconductor. The ground state of the crystal is indicated by |0⟩ [16]; Reprinted with permission from American Chemical Society. (d) composition-dependent absorption and emission spectra of CsPbX$_3$ NCs; (e) size-dependent absorption and emission spectra of CsPbBr$_3$ NCs [19]; https://pubs.acs.org/doi/10.1021/nl5048779 and (f) pressure-dependent PL spectra of CsPbBr$_3$ NCs; the inset presents a schematic illustration of the diamond anvil cell in the measurements and the right panel displays micro-images of the sample under pressures of 1 atm, 0.49, 0.78, and 1.21 GPa [58, 84].*

1.2.2 Electrical properties

When the LHP NCs are applied into optoelectronic devices like LEDs, they are required to be able to transfer electrons and holes among them and with the neighboring device layers. However, as discussed in a previous section, films based on the LHP NCs surrounded by conventional ligands exhibit poor conductivity.

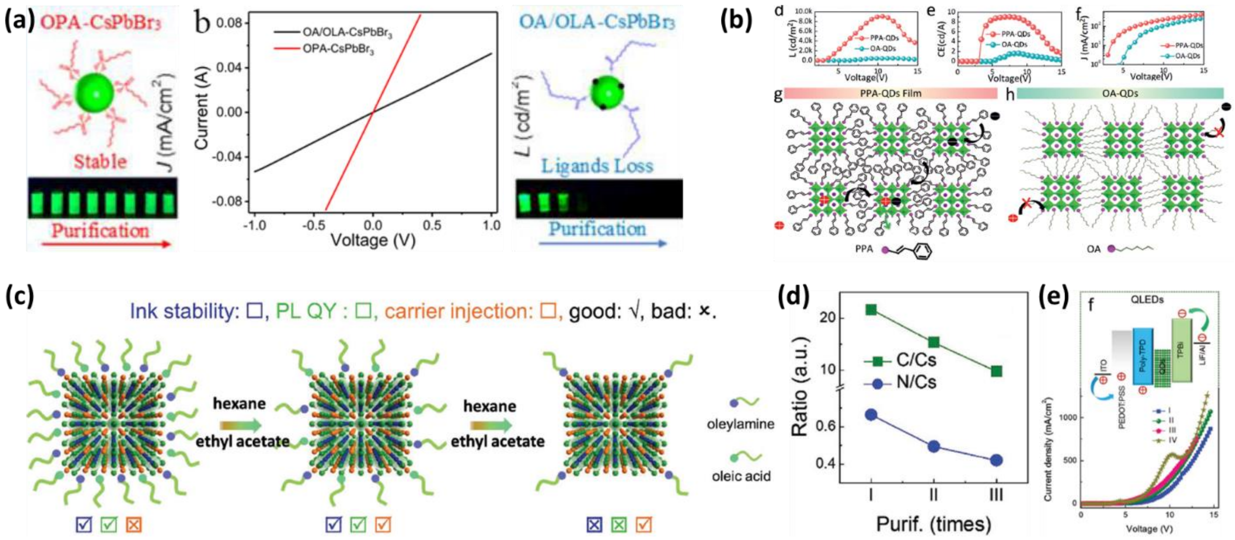

Figure 1.7. Strategies to improve conductivity of LHP NCs. (a) Synthesis of $CsPbBr_3$ NCs with short-chain OPA as ligands to increase conductivity; Reprinted with permission from [38]. Copyright (2018) American Chemical Society.; (b) synthesis of $CsPbBr_3$ NCs with conjugated PPA molecules as ligands to increase NC conductivity and device performance; Reprinted by permission from John Wiley and Sons: [35] COPYRIGHT (2018), doi: 10.1002/anie.201801780. Angew. Chem. Int. Ed..; (c) Schematic illustration of the control of ligand density on $CsPbBr_3$ QD surfaces and the corresponding changes of ink stability, PL QY, and carrier injection; Reprinted by permission John Wiley and Sons: [65] COPYRIGHT (2017), doi: 10.1002/adma.201603885. Adv. Mater. d) relative content of carbon and nitrogen (from ligands) to Cs in $CsPbBr_3$ QDs with different treating cycles plotted from XPS data; and f) energy levels and current density–voltage (J–V) characteristics of QLED devices with different purifying cycles, indicating enhanced conductivity of the NCs after controlling ligand density.

There have been several studies on using unconventional ligands to synthesize the LHP NCs. Akkerman *et al.* [85] used short-chain butylamine and propionic acid as ligands of $CsPbBr_3$ NCs to ensure conductivity of the NCs and applied the as-synthesized NCs into fabrication of solar cell with a high open-circuit voltage. Tan *et al.* [38] used octylphosphonic acid, with a short chain and a strong binding with the LHP NCs, as ligands in the synthesis of $CsPbBr_3$ NCs. A higher conductivity in the OPA-treated $CsPbBr_3$ film was achieved, and the leak current density of the corresponding LED is about one magnitude lower than that of the LED based on NCs with OA/OLAM as ligands (Figure 1.7a). Dai *et al.* [35] applied a conjugated molecule, 3-phenyl-2-propen-1-amine (PPA), as the ligand in the synthesis of $CsPbBr_3$ NCs, and remarkably enhanced the hole mobility of the NC film, which was 20 times more than that of NC film with conventional ligands (Figure 1.7b). Krieg *et al.* [36] synthesized $CsPbBr_3$ NCs with zwitterionic molecule 3-(N,N-dimethyloctadecylammonio)-propanesulfonate, which can bond onto the surface of the NCs strongly. The obtained LED shows a high current density of 21.7 mA/cm^2 at 3.5 V even with a long-chain zwitterionic molecule.

Replacing conventional ligands with ideal ones after synthesis to improve conductivity is more common than engineering better ligands to be used during the synthesis. Li *et al.* [74] performed ligand exchange with PEABr (having a π-conjugation benzene ring) on pristine $CsPbBr_3$ NCs, and remarkably improved the conductivity of the NC layer in green LED. Wheeler *et al.* [72] replaced long-chain OA and OLAM with short-chain acetic acid and formamidinium, and demonstrated high efficiency of the treated LHP NCs in perovskite solar cell.

Comparing with replacing ligands, reducing the amount of pristine ligands in the LHP NC solutions is an alternative way to improve conductivity [65, 67]. For example, Li *et al.* [65] used hexane/acetate mixed solvent to wash OA/OLAM in $CsPbBr_3$ NC solution for a few times to control the surface ligand density and remarkably improved the current density in the green LEDs (Figure 1.7c, d, e).

Alternatively, other groups mixed conductive polymers with LHP NC solutions to enhance the conductivity of the LHP NC film. For example, Shan *et al.* [86] mixed methylammonium lead tribromide with a certain ratio of poly(ethylene oxide) (PEO, average $M_w \approx 5{,}000{,}000$) and poly(vinylpyrrolidone) (PVP, average $M_w \approx 1{,}300{,}000$), and the composite film proved to have better carrier injection properties.

1.3 Applications of lead halide perovskite NCs in optoelectronic devices

1.3.1 Working mechanism of LED

The term LED in this thesis refers to electrically-driven light emitting diodes, which convert electrical energy into light emission. In terms of basic components, a LED device requires only an electron source (negative electrode), a hole source (positive electrode) and an emissive material in which the electrons and holes, injected from the electrodes, recombine radiatively. However, ineffective carrier injections due to improper band alignment between the electrodes and the emissive material strongly limits the efficiency of the electrical energy-to-light conversion process. To overcome these issues, electron transporting materials/layers (ETM/ETL) and hole-transporting materials/layers (HTM/HTL) are introduced into practical LED device.

Without transporting layers, there are large potential differences between the electrodes and the emissive layer, which could lead to a serious loss of carriers at the interfaces. Transporting layers with proper CBs and VBs could make the carrier injection smoother and more efficient. For example, a HTL is expected to have a VB higher than that of the positive electrode and lower than that of the emissive layer to facilitate injection of holes into the ETL, while the CB of the HTL is expected to be higher than that of the emissive layer to block transport of electrons from the emissive layer. Moreover, the electrons and holes are expected to be transported and injected into the emissive layer in a fast and balanced way. Thus, the hole mobility of the HTL and the electron mobility of the ETL are expected to be similar to each other and as high as possible to ensure charge balance in the device [87].

Common ETMs (Figure 1.8a) include small organic molecules, such as 1,3,5-Tris(1-phenyl-1H-benzimidazol-2-yl)benzene (TPBi), 4,7-diphenyl-1, 10-PhenanthrolineSynonym (Bphen), 4,6-Bis(3,5-di(pyridin-3-yl)phenyl)-2-methylpyrimidineSynonym (B3PYMPM), 3,3'-[5'-[3-(3-Pyridinyl)phenyl][1,1':3',1''-terphenyl]-3,3''-diyl]bispyridine (TmPyPB), 4,4'-Bis(9-carbazolyl)-1,1'-biphenyl (CBP) and (6,6)-Phenyl C61 Butyric Acid Methyl Ester (PCBM), and inorganic materials such as ZnO, TiO_2 and MO_3 [88]. Common HTMs (Figure 1.8b) include polymers, such as poly(3,4-ethylenedioxythiophene)-poly(styrenesulfonate) (PEDOT:PSS), poly[N,N'-bis(4-butylphenyl)-N,N'-bis(phenyl)-benzidine] (Poly-TPD), 2,2',7,7'-Tetrakis[N,N-di(4-Methoxyphenyl)aMino]-9,9'-spirobifluorene (Spiro-OMeTAD), poly(N-vinylcarbazole) (PVK), smaller organic molecules such as CBP, and inorganic materials such as NiO [88].

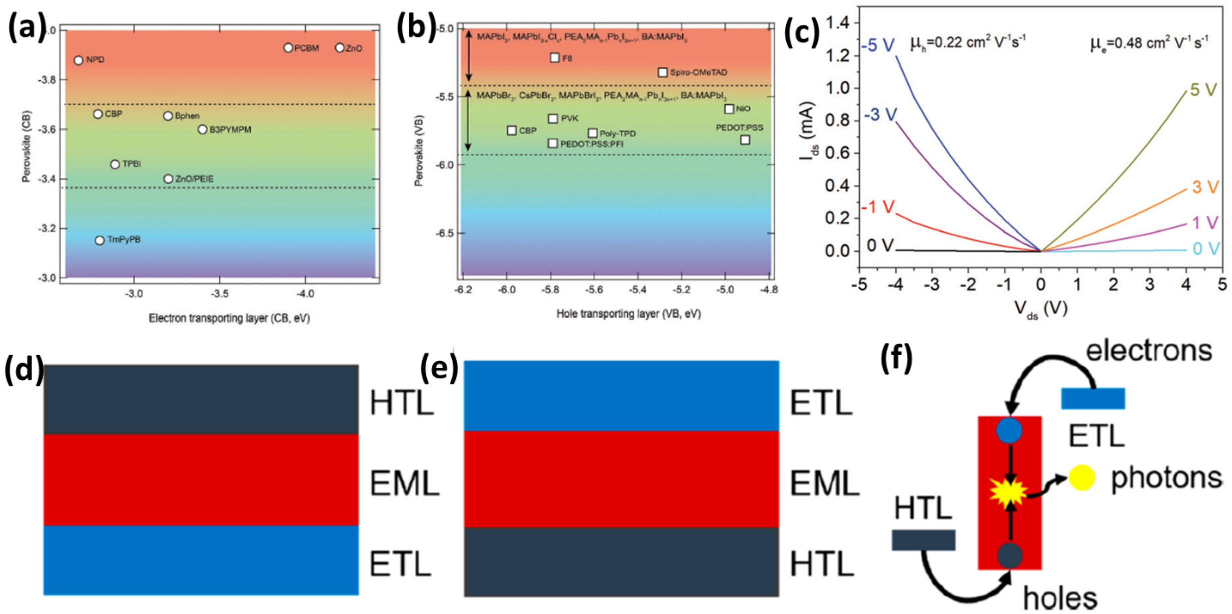

Figure 1.8. LED structure and work mechanism. (a) Selected hole-transporting layers; (b) electron-transporting layers in perovskite LEDs for bandgap-tunable materials; Reprinted by permission from John Wiley and Sons: [88] COPYRIGHT (2018), doi: 10.1002/adma.201801996. Adv. Mater. And (c) mobility levels for the electron and hole derived from a field-effect transistor using $MAPbBr_3$ NCs film as the active layer; Reprinted with permission from [23, 89]. Copyright (2019) American Chemical Society. Cell configuration diagram of (d) the inverted LED structure of ETL/EML/HTL (n-i-p); (e) normal LED structure of HTL/EML/ETL (p-i-n); and (f) operation mechanism diagram of the both structures Reprinted with permission from [87]. Copyright (2019) American Chemical Society.

There are two basic LED structures [87]: one, so-called “normal”, is comprised of HTL/EML/ETL (p-i-n) from the bottom substrate to the top electrode of the device (Figure 1.8d); the other one is “inverted”, comprising ETL/EML/HTL (n-i-p) (Figure 1.8e). The choice of the LED structure depends on the preparation method of the EML [87]. Generally, fabrication of the normal p-i-n LHP NC LED structure consists of the following steps. Firstly, the chosen HTM is spin-coated onto a conductive substrate such as indium tin oxide (ITO) or fluorine doped tin oxide (FTO). Secondly, EML is spin-coated onto the HTL. Then, ETM is deposited on the EML. Finally, the cathode electrode is deposited on the top. Here, since most of the processes involve the deposition of the chosen materials form a liquid phase/solution, particular care should be given to the solubility difference in the used solvents of the materials in neighboring layers ; this is even more true for LHP, since they are extremely sensitive to polar solvents. For example, HTM are usually based on polymers soluble in polar solvents, to avoid being washed away while spin-coating the LHP NCs, that instead are usually dispersed in non-polar solvents. ETM are usually small molecules and are deposited via thermal evaporation. ETM can also be spin-coated on the

EML as long as a proper orthogonal solvent is used to prevent the deposited LHP NCs to be washed away. The fabrication of the inverted LED structure is similar to that of the normal one shown above. Particular care should be given here to the choice of the ETM and its solvent, to avoid its solubilization when depositing the NC layer.

Based on the above LED structures and materials, emission at various wavelengths can be obtained, depending on the bandgaps of the EML. The ETL is designed to inject electrons into the EML, and the HTL is used to inject holes into the EML. Within the EML, the injected electrons and holes are expected to recombine radiatively and release photons (Figure 1.8f). The light emission efficiency of the injected carriers highly depends on the internal optical properties of the LHP NCs, as previously introduced. On the one hand, to achieve effective injection of carriers into the EML, band alignment engineering is necessary [87]. To be specific, the CBM of the EML should be close to the LUMO of the ETL to facilitate injection of electrons from the ETL to the EML, and should be far lower than the LUMO of the HTL to block further transport of the injected electrons from the EML to the HTL. The VBM of the EML should be close to the HOMO of the HTL to facilitate injection of holes from the HTL to the EML, and should be far higher than the HOMO of the ETL to block further transport of the injected holes from the EML to the ETL. Improper band alignment will block effective injection of the carriers into the EML, and cause great loss at the interface. On the other hand, mobility of the ETL and the HTL matters [87]. Given that the hole mobility is usually lower than the electron mobility in the LHP NCs (Figure 8c), it is easy for electrons to accumulate at the interface of ETL/EML [89]. If the hole mobility in the HTL and the electron mobility in the ETL cannot be matched properly, charge imbalance will occur at the interfaces. The accumulated charges at one of the interfaces could change the dielectric field in the device and damage the materials [90-92]. Well-matched hole mobility in the HTL and electron mobility in the ETL are beneficial for charge balance and stable operation of the LED. In addition, the quality of the ETL/EML and EML/HTL interfaces could also make a difference. Formation of defects at interface is unfortunately common. Chemical passivation of the defects can help to suppress the non-radiative recombination and the loss of the injected carriers at the interface [93].

1.3.2 Key parameters for LED

A few key parameters are generally used to measure the LED performance, including EQE, brightness, color and its purity, turn-on voltage and operation time.

The **EQE** is the most important index for the performance of a LED. It is proportional to the ratio of the number N_g of photons generated per second and the number N_i of electrons injected per second into the EML [93]. The EQE could also be defined by the ratio of current injection efficiency η_I, which depends on the proportion of effectively injected current and leakage current, and the radiative efficiency η_R, which depends on the ratio of radiative recombination and non-radiative loss in the EML [93]. Since the generated photons need to penetrate a few layers in the device before being accepted by the detector, they can be absorbed and/or reflected by the other layers. Accordingly, an out-coupling efficiency η_o can be defined as the ratio of photons leaving the LED to those generated [94]. All the mentioned quantities enter the expression of EQE in the following formula:

$$EQE = \eta_o \cdot \frac{\eta_R}{\eta_I} = \eta_o \cdot \frac{N_g}{N_i} \qquad (3)$$

The EQE could also be defined as the product of the injection efficiency, the internal quantum efficiency (IQE) and η_o [94]. The injection efficiency is the ratio of electrons being injected into the EML to those provided by the power source. The IQE is the ratio of photons generated to the number of electron–hole recombination.

However, the physical parameters mentioned above cannot be collected directly in practical experiment. Therefore, the following equation [61, 95], based on the parameters of the detection system, is used instead to calculate the EQE:

$$EQE = \frac{\pi \cdot P_{pd} \cdot l^2 \cdot \lambda \cdot e}{S_{pd} \cdot hc \cdot I} \qquad (4)$$

where S_{pd} is the area of photodetector; P_{pd} is the optical power collected with the photodetector; l is the distance between the photodetector and the device; I is the current flowing through the device, measured between the two electrodes ; λ is the wavelength of the emission; and e is the elementary charge.

Clearly, the EQE is proportional to the number of photons collected by the photodetector and is inversely proportional to the current flowing across the LED. Therefore, the EQE also relates to the current efficiency of the device, expressed in units of cd/A. On one side, the output emission relates to the optical properties of the EML. Therefore, in the case of NCs-based EMLs, improvement of PL QY of the NCs is beneficial for achieving high EQE [96]. On the other side, the current relates to the electrical properties of the device, which depend on several factors [14]

(Figure 1.9a). Firstly, the film quality of the EML matters: if there are pinholes in the LHP NC film, a serious leakage will occur and greatly increase the current, leading to poor emission efficiency [40, 97]. Secondly, the conductivity of the LHP NCs matters: on one hand, NCs with long-chain and labile organic ligands are unable to transport carriers, leading to ineffective injection of electrons and holes [65]; on the other hand, NCs with conductive ligands are favorable for increasing film conductivity but unfavorable for the confinement of the injected electrons and holes and the formation of excitons, leading to low emission efficiency [35]. A balance in conductivity of the NCs is thus important. Thirdly, the band alignment at the interfaces matters: improper band alignment can block the injection of electrons or holes into the EML, leading to low current, which in turn leads to insufficient injection of carriers into the EML and poor emission intensity [98]. Finally, the mobility of holes and electrons in HTL and ETL matters [99] by exerting an effect on the charge balance at the interfaces [100]. The electron mobility in ETL is usually higher than hole mobility in HTL, leading to accumulated electrons at the interface between the ETL and the EML [100]. Overall, a high EQE requires high-quality EML, proper conductivity of the NCs, rationally designed band alignment and well-matched carrier mobility in a running device.

The **brightness** or the luminance of a LED depends on the emission intensity as well as on the emission wavelengths. For a single color, the higher the intensity of the electroluminescence (EL), the higher the brightness of the LED [101, 102]. In this sense, the brightness is associated with the emission efficiency or the EQE. For different colors, human eyes have different sensitivities, which is defined as luminous efficacy [103] and is represented by Figure 1.9 from http://hyperphysics.phy-astr.gsu.edu/hbase/vision/bright.html. The intensity of the lumens in the y axis represents the intensity sensed by human eyes of a light with certain wavelength radiated by one Watt. For example, the highest sensitivity occurs for green light, ~ 507 nm, while sensitivity is far lower for deep blue light as well as near-infrared emission

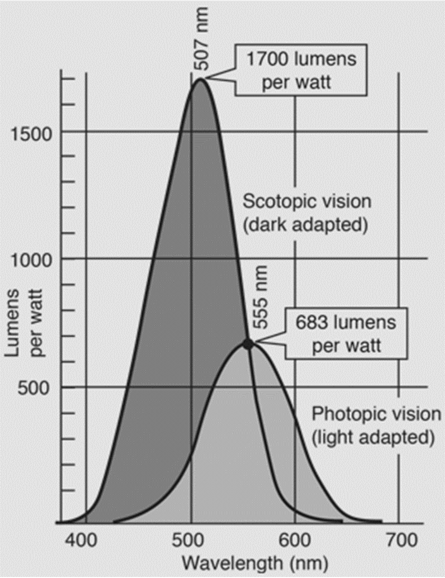

Figure 1.9. Representative diagram of Scotopic Efficacy curve and the Photonic curve.

The **color** of a LED device is defined by a set of space coordinates according to the Commission Internationale de l'Eclairage (CIE), which has standardized the measurement of color by means of color-matching functions and the chromaticity diagram (CIE, 1931) (Figure 1.10 [104]).

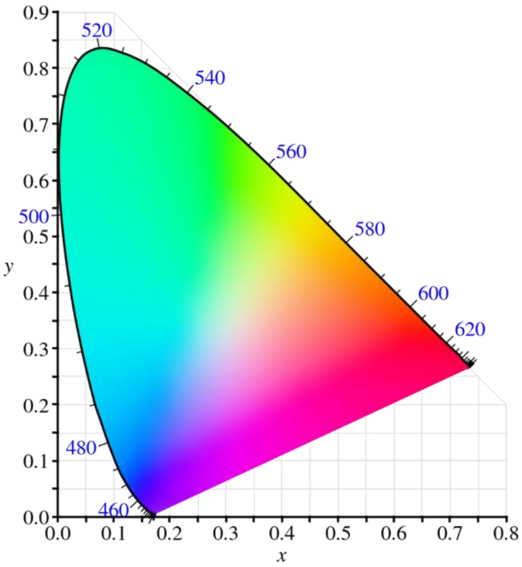

Figure 1.10. CIE 1931 color space chromaticity diagram.

The color **purity** is measured instead by the full width at half maximum (FWHM) of the EL peak. The lower the FWHM, the higher the color purity. The LHP NCs are known for their low FWHM, and outperform their contemporaries such as bulk perovskite and chalcogenide semiconductor NCs in color purity [89, 90]. It is important to obtain emission with high color purity for displays, which require a high color resolution [1]. Additionally, narrow emission wavelength is required in laser fabrication [90]. Therefore, the LHP NCs appear to be promising candidates for the application in optoelectronic devices.

The FWHM of the EL is affected by the size distribution of the NCs [22, 105]. Moreover, the FWHM may also be increased due to emission from the transporting layers [100], when the running LED suffers damages.

The **turn-on voltage** of a LED is another important performance index. Low turn-on voltage is expected in LEDs, meaning that luminance is able to occur at a low bias and with low power, which turns into energy saving and wide use of LED devices. The turn-on voltage depends on the charge transfer barriers between the interfaces, and thus low turn-on voltage requires a rational band alignment [98, 106].

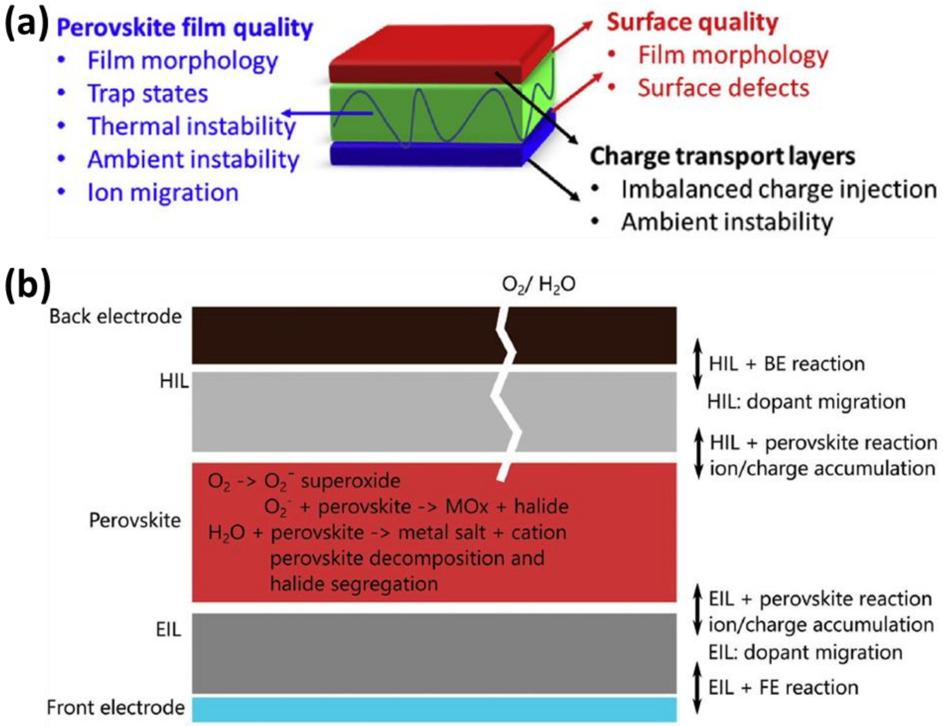

Figure 1.11. Stability of LHP LED. (a) Factors of instability in LHP LED devices; the main ones are: perovskite film quality, surface quality, and device structure; Reprinted by permission from Elsevier: [14] COPYRIGHT (2019), doi: 10.1016/j.mtnano.2019.100028. Mater. Today Nano. (b) Degradation pathways within perovskite LEDs: direct degradation of the active layer takes place via superoxide generation, leading to perovskite decomposition, moisture-induced decomposition, phase segregation and spontaneous decomposition; degradation at device level occurs through EIL/HIL (electron injection layer and hole-injection layer, equal to ETL/HTL) degradation, induced by electrochemical reactions with mobile ions; dopant migration as well as oxygen and moisture penetration into the perovskite active material represent a limiting operational factor for long-term stability, stressing the importance of robust inert encapsulation Reprinted by permission from John Wiley and Sons: [88] COPYRIGHT (2018), doi: 10.1002/adma.201801996. Adv. Mater.

Stability of the LEDs during storage and during operation are both important items for commercial application of the devices. The working time of the LEDs under voltage represents the operation stability. From an operational point of view, the LED is set running at a fixed voltage, and the half-life period is measured, which is the time that the operating LED takes in undergoing a decrease in brightness from the initial one to one half of that. Several factors, among which the EML, the interface, and the transporting layers, may influence the stability of the LEDs (Figure 1.11a) [14]. In terms of the EML, film morphology, trap states, thermal instability, ambient instability and ion migration of the LHP NC film are to be considered. For example, poor film morphology may cause leakage and enhance Joule heating effect with increasing bias [107]. Ion migration may increase halide vacancies and damage the optical properties like spectral stability of the LEDs [101, 108].

In terms of surface quality, defects at the interface play a main role. In terms of the charge transport layers, imbalanced charge injection and ambient instability need to be minimized. In short, competition between the radiative channels and non-radiative channels makes a difference in the stability of the running LED.

On the other hand, the stability during storage depends mainly on the stability of the components of the device itself. Additionally, oxygen together with water or humid atmosphere are known to be the main factors for the instability of the LED in air [88], especially when the device is not well encapsulated (Figure 1.11b).

1.3.3 Green LEDs based on $CsPbBr_3$ NCs

By virtue of their narrow emission bandwidth, spectrally tunable direct bandgap, solution processability as well as quantum confinement effect, LHP NCs have been employed in light emitting devices including LEDs [11, 23, 73, 97, 109-112] and displays [113].

Green LEDs based on bulk perovskite film have achieved EQEs ~ 20% [11, 114]. Green LEDs based on LHP NCs lag far behind. Nevertheless, continuous progresses have been made in applying LHP NCs into fabrication of LEDs with high color purity. In this project, I focused on LEDs based on $CsPbBr_3$ NCs. In this section, I will introduce the evolution of the related studies based on the types of source of materials used in the $CsPbBr_3$ NC synthesis.

Based on the first synthesis route of $CsPbBr_3$ NCs [19], $CsPbBr_3$ NCs synthesized using $PbBr_2$ and Cs_2CO_3 have obtained a fast development in EQE of corresponding LEDs. For example, EQEs of 0.26% [98] and 5.7% [115] have been achieved by optimizing the transporting layers, starting from an initial EQE of 0.026% [98]. Through optimizing ligand washing process, the EQE was increased to 1.7% [107]. Through ligand exchange in the post-synthesis phase, EQE of 3.0% (Figure 1.12b) [73] and 4.33% [74] were realized, respectively, with DDAB and conjugated molecules. Through combination of ligand exchange with DDAB and optimized ligand washing strategy, the EQE was further pushed to more than 8.0% [69, 70]. Application of the $CsPbBr_3$ NCs into LEDs with inverted structure has developed from initial EQE of 0.19% [116] up to 4.63% (Figure 1.12f) [117], by optimizing band alignment of transporting layers and introducing localized surface plasma [117].

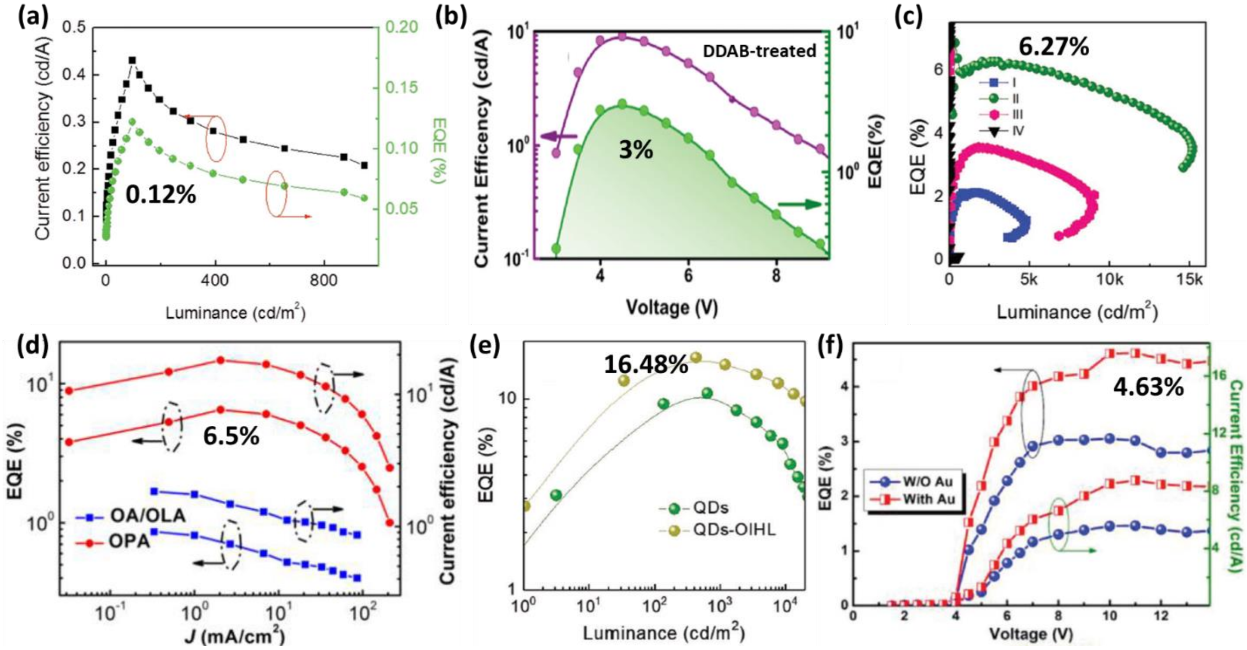

Figure 1.12. Examples of device performance of $CsPbBr_3$ NC-based green LEDs. Performance of LEDs based on NCs (a) with OA/OLAM as ligands; Reprinted by permission from John Wiley and Sons: [77] COPYRIGHT (2015), doi: 10.1002/adma.201502567. Adv. Mater. (b) with DDAB as ligands [73]; (c) with controlled OA/OLAM density; Reprinted by permission John Wiley and Sons: [65] COPYRIGHT (2017), doi: 10.1002/adma.201603885. Adv. Mater. (d) with OPA as ligands; Reprinted with permission from [38]. Copyright (2018) American Chemical Society. (e) with DDAB and OA as ligands and with treatment of $ZnBr_2$; Reprinted by permission from John Wiley and Sons: [47] COPYRIGHT (2018), doi: 10.1002/adma.201805409. Adv. Mater.; and (f) with plasmonic Au as additive in device; Reprinted by permission from John Wiley and Sons: [117] COPYRIGHT (2018), doi: 10.1002/adfm.201707031. Adv. Funct. Mater.

Other groups worked with cesium stearate as the Cs source. Also in these cases, the performance of the corresponding LEDs have seen a steady enhancement with time. Indeed, starting from an initial EQE of 0.12% (Figure 1.12a) [77], further works have increased the EQE to 2.21% by forming composite with $CsPb_2Br_5$ [118], and 6.27% by rational washing procedure of the obtained $CsPbBr_3$ NCs (Figure 1.12c) [65]. In addition, cesium acetate was also applied into synthesis of $CsPbBr_3$ NCs. When used together with octylphosphonic acid as ligand, it allowed achieving an EQE of 6.5% (Figure 1.12d) [38]. Moreover, CsBr was also used to fabricate $CsPbBr_3$ NCs with assistance of crown ethers via LARP, and the corresponding green LED has obtained an EQE of 2.64% [22].

Work has also been carried out to apply new types of halide sources in the synthesis of the $CsPbBr_3$ NCs, *e.g.*, TOABr, NH_4Br, trioctylphosphine-Br_2 and BBr. LEDs based on $CsPbBr_3$ NCs prepared with TOABr as halide source and OA as ligand, obtained a maximum EQE of 0.325% [32]. Through combining mixed cations, ligand exchange, rational washing and surface passivation in the treatment of $CsPbBr_3$ NCs, LEDs based on the $CsPbBr_3$ NCs, synthesized with $PbBr_2$, Cs_2CO_3 and TOABr obtained a maximum EQE of 16.48% (Figure 1.12e) [47]. In other works, LEDs based on $CsPbBr_3$ NCs using NH_4Br [20] and trioctylphosphine-Br_2 [36] in synthesis have also been reported, with maximum EQEs at 1.2% and 2.5%, respectively.

1.3.4 Blue LEDs based on lead halide perovskite NCs

The development of blue LEDs is relatively slower than that of green ones. However, it is recently following up the step of achieving green LEDs at an accelerating speed. There are generally two strategies to obtain LHP with blue emission. One strategy is to increase the bandgap by limiting the size of LHP and realizing quantum confinement effect [19]. Quantum confinement is defined as a reduction in the allowed free space of carriers due to a reduction in the degrees of freedom [119]. When grain size is comparable to the wavelength of the electron, quantum confinement effect could be observed [120]. Usually, the confinement of an electron and hole in NCs significantly depends on the material properties, namely, on the Bohr radius a_B [120]. Protesescu *et al* estimated that the effective a_B of $CsPbBr_3$ to be 7 nm [19]. Quantum well, with quantum confinement effect along one dimension, has been widely used in traditional semiconductor LEDs [121]. 2D LHP, consisting of a few limited layers of lead halide octahedrons sandwiched between organic molecules, were also reported to form quantum wells with wide bandgap [122-125]. However, the FWHM of the corresponding EL spectra are usually wide and only moderate EQE is obtained [122, 126-130]. Quasi-2D or a mixture of 2D and 3D LHP were thus further developed to improve charge transfer efficiency and radiative recombination efficiency of the bulk LHP LEDs. As a result, the EQE of blue LEDs based on the in-situ synthesized quasi-2D LHP has increased from 0.015% up to 11% in only three years (Figure 1.13a-g) [102, 124, 131-135].

The other strategy is to fabricate chloride/bromide mixed-halide-based LHP, which have large bandgap and emit blue light. However, the mixed-halide-based LHP suffers anion migration under electric field, which leads to unstable EL spectra in running LEDs [130, 132, 136].

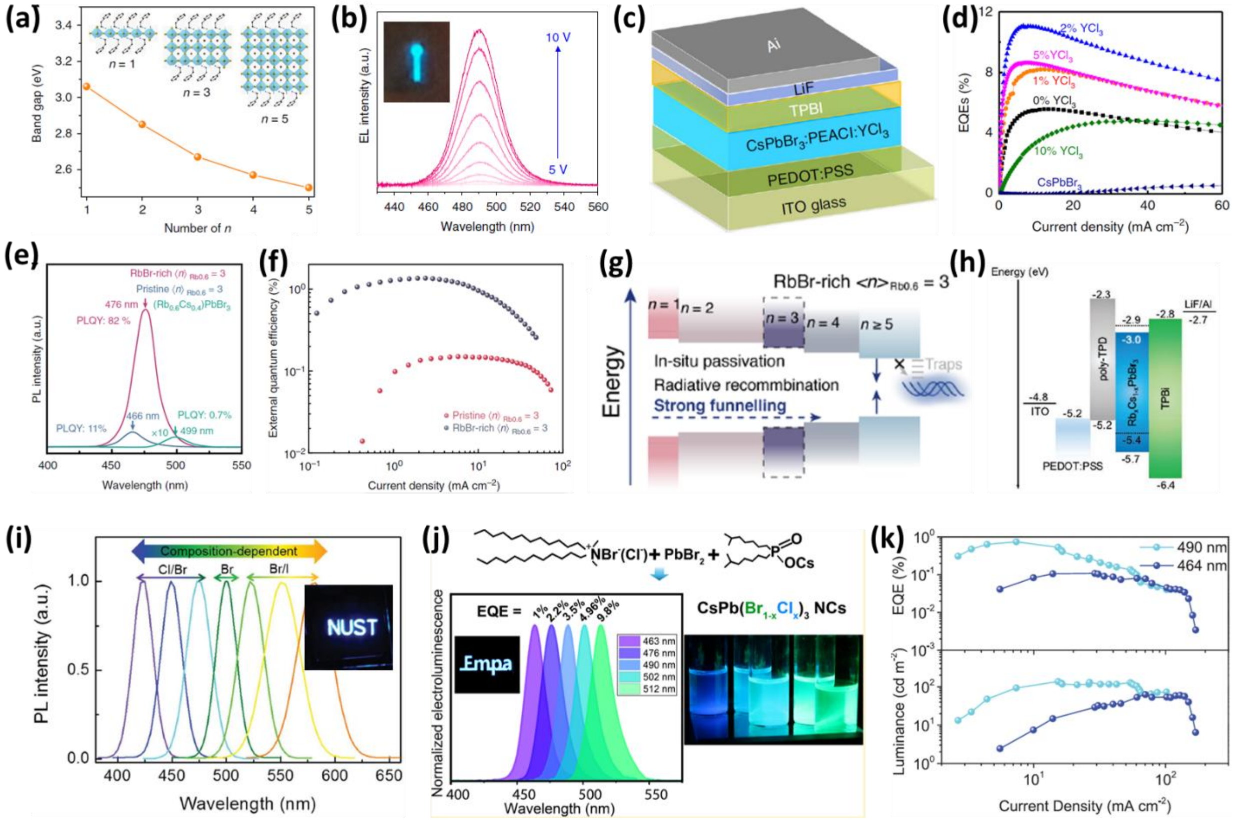

Figure 1.13. Examples of device performance of LHP blue LEDs. Blue LEDs based on quasi-2D LHP: (a) Bandgap of quasi-2D perovskite with n number of layers as determined by transient absorption (TA) measurements. The inset is the atomic model of the quasi-2D perovskite with n =1, 3, and 5; (b) EL spectra of the LED operating under different voltages [122]; (c) Device structure and (d) efficiency of the YCl_3-treated sky-blue quasi-2D LHP LEDs [134]. (e) Steady-state PL spectra and PL QYs of perovskite PEACl:$Rb_{0.6}Cs_{0.4}PbBr_3$, pristine, and RbBr-rich ⟨n⟩$Rb_{0.6}$= 3 films; (f) EQE characteristics of pristine and RbBr-rich <n>$Rb_{0.6}$=3 devices; and (g) diagram of the recombination mechanism of the LHP layer in the quasi-2D LHP LED [124]. Performance of blue LEDs based on LHP NCs: (i) PL spectra and a photo of the running blue LED based on mixed halide LHP NCs[77]; (j) EL spectra of LEDs based on NCs with R_4NBr as ligands, with photo of NC solutions under UV light;. https://pubs.acs.org/doi/abs/10.1021/acsenergylett.9b01915 Reprinted with permission from American Chemical Society. (h) band alignment and (k) performance of LED based on Rb-doped $CsPbBr_3$ NCs. Reprinted by permission from John Wiley and Sons: COPYRIGHT (2019), doi: 10.1002/adom.201901440. Adv. Opt. Mater.

A further strategy to increase the bandgap of LHP NCs in an energy window compatible with blue emission is through doping [137]. This approach has been shown to improve also the emission efficiency [138, 139] and/or the stability of LHP [140-142]. Applications in blue LEDs based on doped LHPs have been advancing steadily. The EQE of blue LEDs based on doped LHP NCs has increased from 0.07% to 3.5% through mixed halide (Figure 1.13i) [77, 136, 143-147] or incorporation of metal elements (Figure 1.13h, k) [148] together with optimization of ligands

(Figure 1.13j) [146, 149]. However, there is obviously still a large room for further improvement of the efficiency of blue LHP LEDs.

1.4 Goals of the thesis project

With respect to the state of the art presented so far in the area of optoelectronic devices based on LHP NCs, the current work of thesis intended to address the points described by the following goals (Figure 1.14):

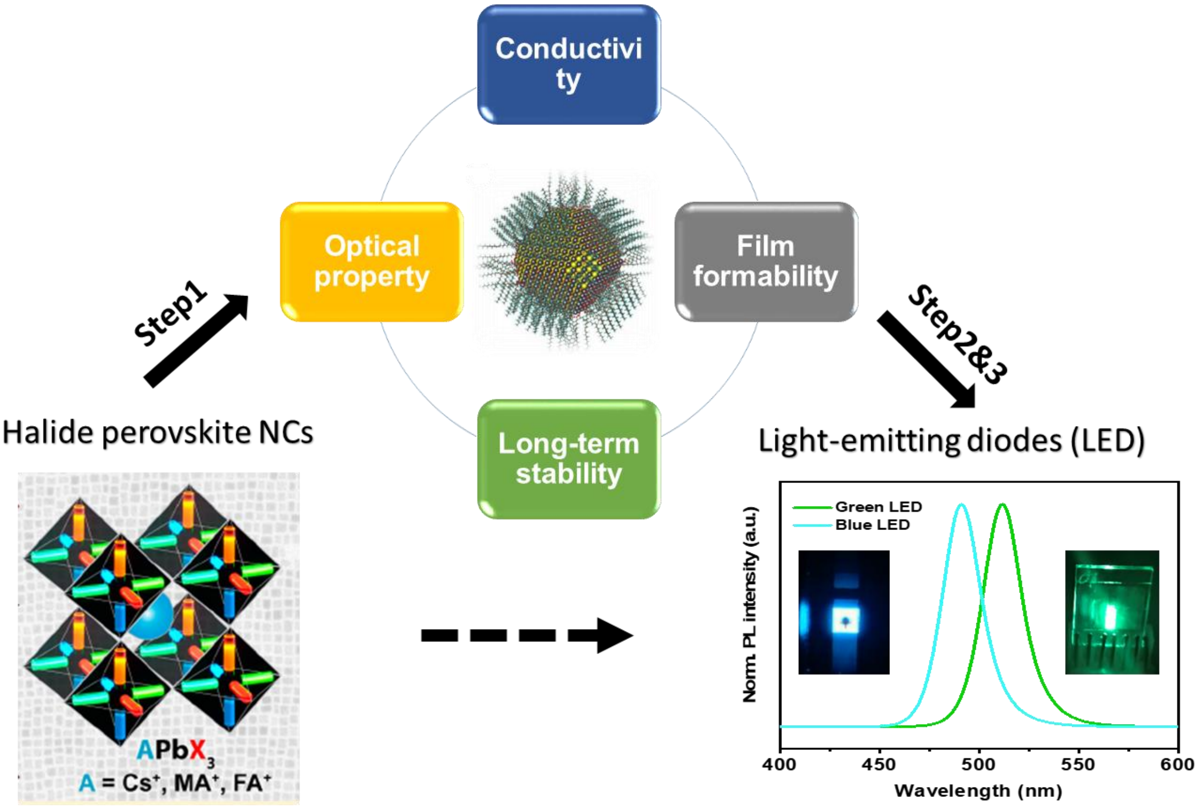

Figure 1.14. A general scheme of the goals of the work.

1) The long-chain insulating organic ligands on the LHP NCs and the requirement of a good carrier injection property in LEDs are conflicting. Chapter 3 aims to address the four issues induced by the ligands originally used in the synthesis, that is, poor conductivity, low optical performance after post-treatment for higher conductivity, poor film coverage and poor stability of the LHP NC films. The aim is to find a treatment method that could balance the conductivity and the optical performance, and improve the film coverage and the stability of the film in the meanwhile.

2) Application of LHP NCs in LEDs are highly expected. Chapter 4 aims to fabricate green LEDs with high efficiency and high stability based on treated NC solutions. It is also desired to reveal a general mechanism to improve the stability of LHP NCs-based films. In addition, the efficiency roll-off common to LEDs is desired to be explored by in-situ characterization method and explained with some new insight.

3) Blue LEDs based on LHP NCs still lag far behind. Chapter 5 aims to fabricate sky-blue and blue LEDs with high efficiency and high stability based on LHP NCs solutions. Metal doping is selected as a promising route. It is desired to elucidate the effect of metal doping in the modification of the LHP NCs

Chapter 2: Experimental techniques

This chapter introduces the used chemicals, synthesis methods and experimental characterization techniques, which are common to the following chapters.

2.1 Materials

Lead acetate trihydrate ($Pb(CH_3COO)_2{\cdot}3H_2O$, 99.99%), cesium carbonate (Cs_2CO_3, reagent Plus, 99%), benzoyl bromide (C_6H_5COBr, 97%, shortly BBr), toluene (anhydrous, 99.5%), octadecene (technical grade, 90%, ODE), oleylamine (70%, OLAM), oleic acid (90%, OA), butylamine (≥ 99%), ethyl acetate (99.8%, EA), ammonium thiocyanate (NH_4SCN, 97.5%), octylphosphonic acid (OPA, 98%), 1-butanol ($CH_3(CH_2)_3OH$, 99.8%), acetone (≥ 99.5%), isopropanol (anhydrous, 99.5%, IPA), diethyl ether (DE) (contains BHT as inhibitor, ≥99.8%), hexane (Hex) (anhydrous, 95%), cyclohexane (anhydrous, 99.5%), octane (anhydrous, ≥99%), 1,2-dichlorobenzene (anhydrous, 99%), chloroform (≥99.5%), dimethyl sulfoxide (DMSO), polyvinyl pyrrolidone (PVP), ZnO NC solution (2% in methanol), and LiF were purchased from Sigma-Aldrich. Poly(3,4-ethylenedioxythiophene)-poly(styrenesulfonate) (PEDOT:PSS), Poly(9-vinylcarbazole) (PVK), 2,2',2"-(1,3,5-Benzinetriyl)-tris(1-phenyl-1-H-benzimidazole) (TPBi) was purchased from Ossila. All chemicals were used without any further purification.

Lead bromide ($PbBr_2$, 99.99%), octanoic acid (OTAc, 99%), formamidine acetate (FA(Ac), 99%), didodecyldimethylammonium bromide (DDAB, 98%), didodecyldimethylammonium chloride (DDAC, 98%), tetra-n-octylammonium bromide (TOAB, 98%) and copper chloride ($CuCl_2$, 99%) were purchased from Macklin Inc. Poly[bis(4-phenyl)(2,4,6-trimethylphenyl)amine (PTAA) and TPBi used in Chapter 5 were purchased from Xi'an Polymer Light Technology Corp. (PLT). Chemical structures of reagents, some of which are used to modify the ligands of the NCs and some of which are used as solvent for NCs dispersion, are shown in Figure 2.1.

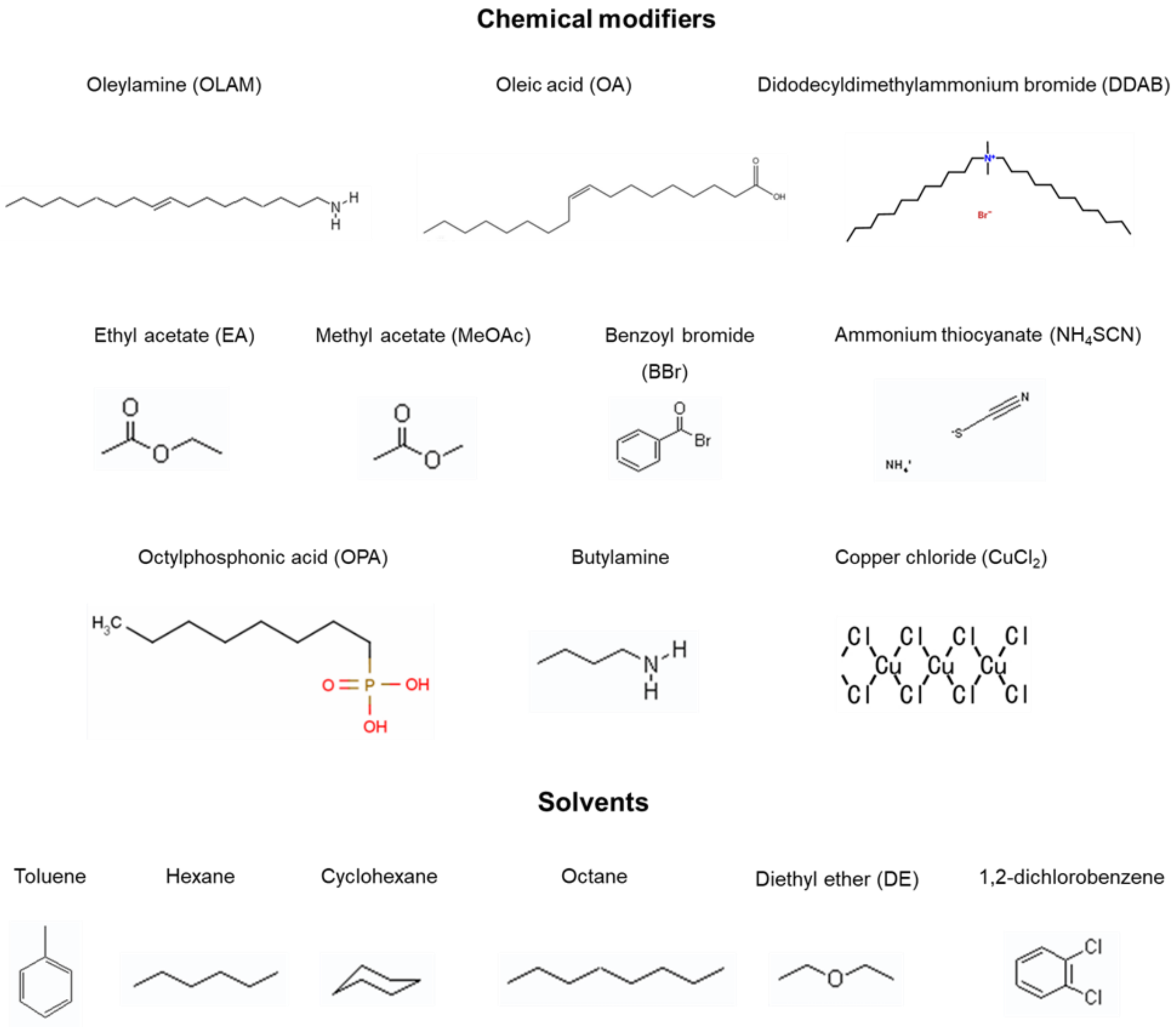

Figure 2.1. Chemical structures of modifiers and solvents used in the thesis.

2.2 Synthesis of perovskite nanocrystals

2.2.1 Hot injection method

The $CsPbBr_3$ NCs used in Chapter 3, Chapter 4 were synthesized according to the HI method, as reported by Imran *et al.* [21], with the only change of 10-times scaling up the amount of used chemicals. In particular, 160 mg of cesium carbonate, 760 mg of lead acetate trihydrate, 3 mL of OA, 10 mL of OLAM and 50 mL of ODE were loaded into a 100 mL 3-neck round bottom flask and dried under vacuum for one hour at 130 °C. Subsequently, the temperature was increased to 170 °C under nitrogen flow, and BBr (700 µL) precursor was swiftly injected into the reaction system. The reaction mixture was immediately cooled down in an ice-water bath. Finally, dry toluene (10 mL) was added to the crude NC solutions, and the resulting mixture was centrifuged for 10 min at 4000 rpm. The supernatant was discarded, and the precipitate was re-dispersed in toluene (10 mL) for further use. The measured concentration [150] of the as-synthesized $CsPbBr_3$ NC is ~ 180 g/L.

2.2.2 Co-precipitation method

The LHP NCs used in Chapter 5 are obtained through a procedure adapted from what is reported by Song *et al* [79]. In detail, cesium and formamidine precursors together with OA dispersed in toluene are injected into lead bromide precursor at RT to obtain $Cs_xFA_{1-x}PbBr_3$ NCs. Here, the lead precursor is prepared by dispersing $PbBr_2$ and TOAB in toluene by sonication. The cesium and formamidinium precursors were prepared by dissolving Cs_2CO_3 or FA(Ac) in OTAc (0.1 mmol/mL), respectively.

The procedure for ligand exchange and modification with $CuCl_2$ on the as-synthesized NCs is shown below. $CuCl_2$/DDAB precursor with different concentrations of $CuCl_2$ is injected into the NC solution. Here, the $CuCl_2$/DDAB precursor was prepared by dissolving different amount of $CuCl_2$, which ranges from 0.1% to 70% molar ratio of $PbBr_2$, in 3 mL DDAB precursor (10 g/L in toluene). After reacting for 2 min under magnetic stir in open air, EA is poured into the solution with a volume ratio of 2:1. After centrifugation at 8000 rpm/s for 1 min, the precipitates were collected and dispersed in toluene. The second purification follows the first one, except that OA and DDAB are supplemented before adding EA. The collected precipitates after the second centrifugation at 4000 rpm/s for 1 min are dispersed in octane or hexane to obtain Cu-treated NCs.

2.3 Preparation of perovskite nanocrystal films

2.3.1 Films based on NCs synthesized by HI method

Clean substrates were prepared by rinsing soda-lime glass slides (Menzel-Gläser superfrost by Thermo Scientific, Braunschweig, Germany) – previously cut into 1.25 cm x 1.25 cm pieces - with acetone, IPA, and Milli-Q water for 10 min in sonication sink in sequence, followed by drying under nitrogen flow. Then, typically 50 µL NC solution was deposited onto the cleaned slides to cover the whole substrate and spin-coated at 2000 rpm for 60 s. Eventually, some prepared films were annealed at 65 °C for 100 min on hotplate to remove the remaining solvent. The others were not annealed. All films were stored on shelf in air.

2.3.2 Films based on NCs synthesized by co-precipitation method

Glass substrates with size of 1.5 cm x 1.5 cm were cleaned with ethyl alcohol firstly. Then, 80-100 μL NC solution was deposited onto the cleaned slides to cover the whole substrate and spin-coated at 2000 rpm for 45 s. All films were stored on shelf in air.

2.4 Fabrication of perovskite-nanocrystal-based LEDs

2.4.1 Fabrication and characterization of green LEDs

Green LEDs were fabricated on patterned ITO glass substrates. The substrates were cleaned in an ultrasonic bath using detergent, deionized (DI) water, IPA and DI water again, sequentially. Prior to depositing hole-transporting layers, the ITO glass substrates were further treated with oxygen plasma for 300 s at 30 W. PEDOT:PSS layer was spin-casted onto the cleaned ITO glass substrates at 4000 rpm and annealed at 150 °C for 30 min in hood. Poly-TPD was spin-coated onto the PEDOT:PSS layer at 5000 rpm and annealed at 120 °C for 20 min in glovebox (GB). Here, the poly-TPD solution was prepared in chlorobenzene (CB) at 8 g/L in GB. As the film cool down, LHP NC solutions were spin-casted at 2000 rpm at a time and annealed at 70 °C for 15 min. Then, electron transporting layer TPBi and electrode LiF and Al were thermal evaporated at rate of 1.5 nm/s, 0.2 nm/s, 2 nm/s, respectively. Finally, the devices were encapsulated with cover glasses and encapsulation oil. The devices were treated by UV light for 15 min to solidify the encapsulation oil in GB.

The current−voltage−luminance measurement was performed using a Keithley 2410 source-measure unit and an Agilent 34410A multi-meter coupled to a calibrated PDA 100A Si switchable gain detector from Thorlabs. The output of the Si detector was converted into power (photon flux) using a 50 Ω load resistance and the responsivity of the detector. The effective area of each device is 4.5 mm^2. The EQE was calculated as the ratio of the photon flux and the driving current of the device. The EL spectra of the devices were collected by an Ocean Optics HR4000+ spectrometer.

2.4.2 Fabrication and characterization of blue LED fabrication

Cleaned ITO-coated glass substrates were treated by O_3 for 15 min. Then, Poly(ethylene dioxythiophene):polystyrene sulphonate (PEDOT:PSS) solutions (Baytron P VPAl 4083, filtered by a 0.45 μm filter) and poly (bis(4-phenyl)(2,4,6-trimethylphenyl) amine) (PTAA) (5 g/L in CB, filtered by 0.22 μm filter) solution were spin-coated on ITO substrates at 3000 rpm for 60 s and annealed, respectively, at 140 °C for 15 min and 120 °C for 25 min. Subsequently, LHP NCs are spin coated at 2000 rpm for 60 s and baked at 60 °C for 10 min. Later, under a vacuum of ~ $2x10^{-4}$ Pa, TOPO (1nm), TPBi (40 nm) and LiF/Al electrodes (1 nm/100 nm) were deposited sequentially in a thermal evaporator with shadow masks. The device active area was 4 mm^2 as defined by the overlapping area of the ITO and Al electrodes.

The I-V-L characteristics, EL spectra and other device performance were collected and calculated using a Keithley 2400 source in combination with a measurement system designed by Everfine corporation.

2.5 Measurement techniques

Light absorption. Absorption spectra were taken on a Varian Cary 5000 UV−vis−NIR spectrophotometer.

Photoluminescence (PL). Steady-state PL, time resolved PL lifetime and PL quantum yield (PL QY) measurements were carried out directly on the films with an Edinburgh fluorescence spectrometer (FLS920). The instrument is equipped with a Xenon lamp and a monochromator for steady-state PL measurement, a calibrated integrating sphere for PL QY measurements, and a time-correlated single-photon counting (TCSPC) unit coupled with a pulsed laser diode (λ = 405 nm, pulse width = 50 ps) for time-resolved PL studies. Both steady-state PL and PL QY were collected with an excitation wavelength of 350 nm. The PL QY measurement on the films were carried out using the procedure developed by J. C. De Mello *et al.* [151].

Confocal PL microscopy. Confocal PL images and spectra were collected using a Nikon A1 microscopy with a laser excitation. The excitation wavelength of the laser was 488 nm or 401 nm.

Scanning electron microscopy (SEM). SEM images were recorded by a field emission SEM (Helios NanoLabTM 650), with an acceleration voltage of 2 kV and a filament current of 0.2 A. The films were directly used for SEM observation after coating the substrates edges with silver paint.

Field-emission gun SEM (FEG-SEM). The films were characterized by HRSEM using a JEOL JSM-7500LA (JEOL, Tokyo, Japan) equipped with a cold field-emission gun (FEG), operating at 20 kV acceleration voltage. No coating was needed. Energy-dispersive spectroscopy (EDS, Oxford instrument, X-Max, 80 mm^2) was used to distinguish the presence and the ratio of Cs, Pb and Br. The Line Type considered for obtaining the most reliable quantification were K

(Br) and L (Pb and Cs). All experiments were done at 8 mm working distance, 20 kV acceleration voltage and 15 sweep count for each sample.

Transmission electron microscopy (TEM). Low-resolution TEM measurements were performed on a JEOL-1100 instrument operating at an acceleration voltage of 100 kV. The NC solutions were drop casted onto carbon-coated copper grids without dilution.

Current-voltage plot (IV). The IV measurement were performed with a combination of a Suess Microtec probe station and a Keithley 2612 source meter in air and in dark. Au electrodes with a gap of 50 μm and thickness of 100 nm were fabricated on top of the LHP NCs film by thermal evaporation of Au and by using a metallic shadow mask.

X-ray diffraction (XRD). XRD analysis was performed on a PANanalytical Empyrean X-ray diffractometer, equipped with a 1.8 kW Cu Kα ceramic X-ray tube and a PIXcel^{3D} 2×2 area detector, operating at 45 kV and 40 mA. Auto-focus alignment was adopted. The diffraction patterns were collected under ambient conditions using parallel beam geometry and symmetric reflection mode. XRD data analysis was conducted using the HighScore 4.1 software from PANanalytical.

X-ray photoelectron spectroscopy (XPS). XPS characterization was performed using a Kratos Axis Ultra DLD spectrometer with a monochromatic Al Kα source (photon energy = 1486.6 eV) operated at 15 kV with an emission current of 20 mA. Wide scans were acquired at an analyzer pass energy of 160 eV and steps of 1 eV. High resolution narrow scans were performed at a pass energy of 10 eV and steps of 0.1 eV. The photoelectrons were detected at a takeoff angle $\Phi = 0°$ with respect to the surface normal. The pressure in the analysis chamber was maintained below 5×10^{-9} Torr for data acquisition. The data were converted to VAMAS format and processed using CasaXPS software. The binding energy scale was referenced to the C 1s peak at 248.8 eV.

Conductive atomic force microscopy (C-AFM). An atomic force microscopy (AFM) system MFP-3D (Asylum Research, CA, US) was used in ORCA mode, with a probe RMN-12PT400B (Bruker, MA, US), consisting of a bent wire of bulk platinum, tapered at the free end. The film substrates were scanned at a set point of 0.5 V static deflection level (in arbitrary units), relative to a reference level for the un-deflected cantilever (off-contact) of 0 V, with an integral gain of 10. The scan was performed within a 1x1 μm^2 area corresponding to 256x256 pixel at a line scan frequency of 0.3 Hz. The contact to the sample was made with a sequence of adhesive copper tape, steel puck substrate mounted on a glass slide with double-sided adhesive amorphous carbon pad, with silver paint surrounding the sample edges. Different voltages of 3 V, 5 V and 7 V were applied on the sample, whereas in this mode the tip is set to virtual ground.

Chapter 3: Perovskite nanocrystal films based on treated NCs

Lead halide perovskite nanocrystals (LHP NCs) are promising in application of optoelectronic devices. However, there are a few issues of LHP NCs to be solved to realize efficient optoelectronic devices. Firstly, conductivity of LHP NCs in film has to be improved since, after synthesis, they are surrounded by insulating and labile organic ligands. Secondly, the stability of LHP NCs in film has to be ensured after post-synthesis treatments which usually introduces defects in the pristine LHP NCs. Thirdly, smooth and compact films from LHP NCs must be obtained, as this is expected to be favorable for high-efficient devices. Last but the least, the exceptional optical properties of LHP NCs in solution has to be well-retained (or possibly improved) in films. In a sentence, it is necessary to improve the above four points as well as to achieve a good balance among the four issues. In this chapter, work on solving each of the four problems as well as achieving a balance are presented in detail.

3.1 Choice of the reagents

Based on the literature reports, a few chemicals have been selected to treat as synthesized LHP NCs and overcome the said issues. In particular, I identified ethyl acetate (EA), methyl acetate (MeOAc), benzoyl bromide (BBr), ammonium thiocyanate (NH_4SCN), and octylphosphonic acid as promising candidates. In fact, pure EA or pure MeOAc were used as purification solutions and were chosen because of their mild polarity, as they were proved to be able to purify perovskite NCs minimizing their damaging and without weakening their PL intensity.[65] Butylamine was chosen as a short-chain and highly volatile ligand.[85] BBr was chosen because of the presence of a benzene ring which may be able to improve conductivity; moreover BBr may supplement Br losses during the treatment and was reported to be beneficial for the PL QY of the NCs. [20] NH_4SCN was chosen because the SCN^- ion may be considered as a quasi-halide and may compensate halide losses during treatment; moreover it could act as short-chain ligand.[152, 153] OPA was chosen for the presence of the PO_3^- group which may be able to bind the NCs strongly.

3.2 Treatment Method

3.2.1 Treatment of perovskite NC films

Nanocrystals' films were prepared according to the procedures reported in Chapter 2. Specifically, 50 μL pristine $CsPbBr_3$ NCs solution was spin coated onto cleaned glass substrate. The proposed treatment methods consist of dropping a volume of the chosen "modification solution" onto the NC film in a N_2-filled glove box (GB), followed by, after 30 s, another spin-coating step, performed at 2000 rpm for 100 s.

The "modification solutions" were prepared as here described:

- The BBr solution was prepared by mixing BBr with hexane at a ratio of 1:80, labeled as BBr:Hex.
- The SCN solution was prepared by mixing 4.5 mL toluene, 3 mL 1-butynol and 0.075 g ammonium thiocyanate, labeled as TOL:BuOH:SCN.
- Two kinds of octylphosphonic acid solutions were prepared. For one, 0.2 g OPA was dissolved in 10 mL IPA, labeled as OPA:IPA. For the other one, 0.2 g OPA was dissolved in a mixture of 5 mL IPA and 5 mL hexane, labeled as OPA:IPA:Hex. For treatment with butylamine, the spin-coated $CsPbBr_3$ NCs film was exposed to a 5 mL vial half-filled with butylamine for 1 min; then the film was annealed on a hot plate at 100 °C for 10 min.

3.2.2 Post-synthesis treatment of perovskite NCs in solution

As an alternative to the treatment of LHP NCs films, treatments in solution were also developed. Pristine $CsPbBr_3$ NCs solution synthesized by HI method was mixed with different "modification solutions", including BBr solution, SCN solution, mixture of BBr and SCN solutions, at a volume ratio of 1:3 to 1:5; after stirring the reaction system for 10 min in GB, the obtained solution was centrifuged at 4000 rpm for 10 min, and the precipitate was re-dissolved in degassed toluene. In this case, the BBr solution was prepared by mixing a certain amount of BBr with EA. The SCN solution was prepared as before. The mixed solution of BBr and SCN was prepared by mixing varying amount of SCN solution and EA with varying amount of BBr. The amount of BBr varied from 2 μL to 36 μL. The amount of SCN solution varies from 10 μL to 200 μL.

In a typical treatment experiment with both BBr and SCN, 300 µL of the as-synthesized $CsPbBr_3$ NC solution was added into a vial. Then, 50 µL of the SCN solution was dropped into the vial containing $CsPbBr_3$ NC solution under stirring in GB. In the following, 9 µL BBr in 1500 µL EA was added into the vial and the mixture was stirred for further 10 min in GB. Then, the so treated $CsPbBr_3$ NCs solution was centrifuged at 4000 rpm for 10 min. Finally, the supernatant was discarded, and the precipitate, labelled as SCNBBr in the following, was re-dispersed in 100 µL degassed toluene for further use. In this chapter, the precipitate was also re-dispersed in diethyl ether (DE), hexane (Hex), cyclohexane, octane and dichlorobenzene/chloroform for comparison in the section about effect on solvent. For comparison, the untreated NC solution underwent a similar stirring process, in which toluene was used as a replacement of EA and no SCN and BBr were added. These untreated sample was labelled as REF in the following.

For NC treatment with PEA, 20 µL PEA was dispersed in 900 µL EA, and the solution is added into 300 µL NCs solution or together with SCN solution and/or BBr.

3.2.3 Annealing of perovskite NC films

In the cases of treatment with SCN and/or BBr, NC films were annealed in an oven at 65 °C for 100 min. In the cases of treatment with PEA, NC films were annealed at 70 °C for 30 min on a hotplate in GB.

3.3 Improving conductivity of perovskite NC films

3.3.1 Conductivity of in-situ treated films

Using the chemicals and protocols described in the previous section, treated $CsPbBr_3$ NCs films were characterized for their transport and optical properties, and the different treatment approaches were compared. The optical performance of the treated films were characterized to ensure that the treatment methods did not weaken the optical properties of the films seriously.

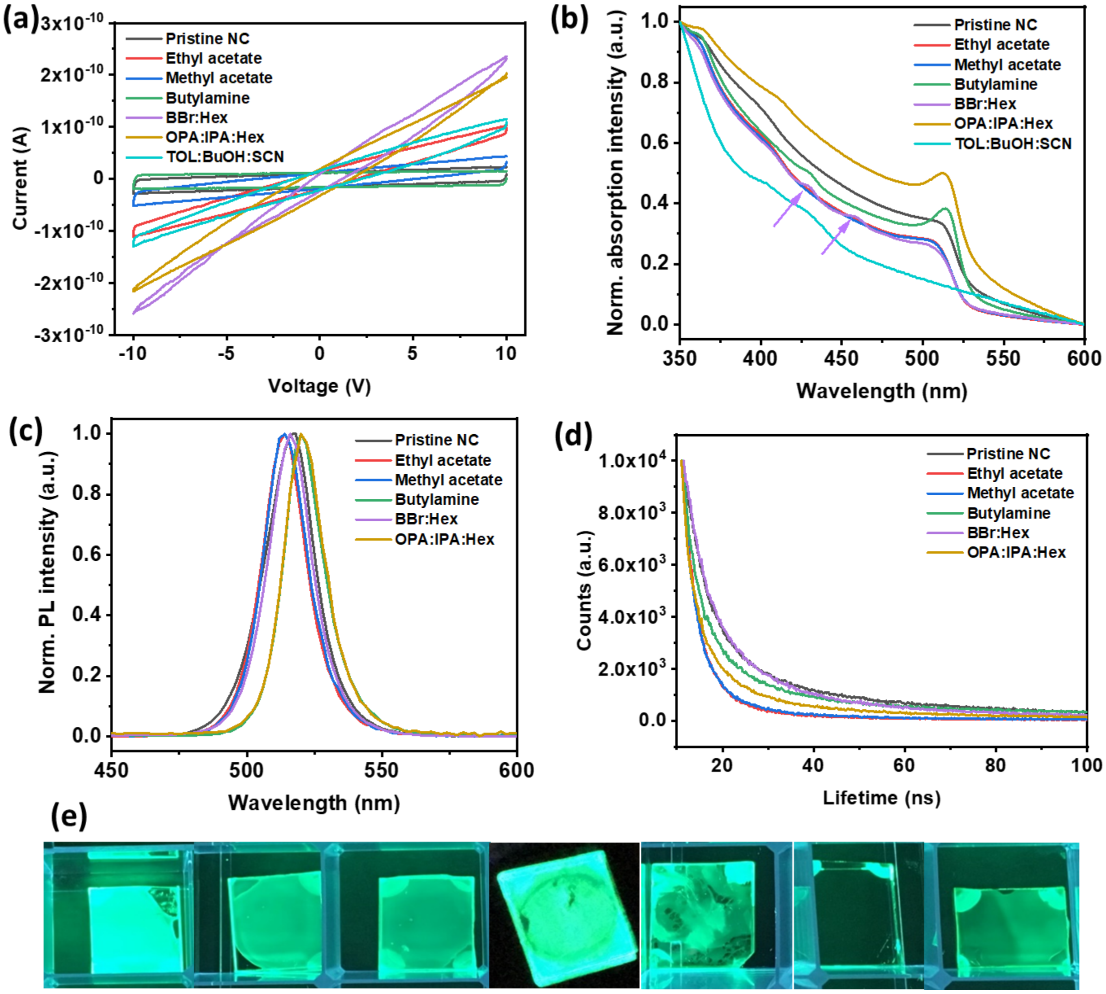

Figure 3.1. Conductivity and optical properties of the in-situ treated films. (a) Conductivity; (b) absorption intensity; (c) photoluminescence intensity; (d) decay lifetime; and (e) photos under UV illumination of the CsPbBr3 NC films (from left to right) untreated and treated by different chemicals such as ethyl acetate, methyl acetate, butylamine, BBr:Hex, TOL:BuOH:SCN, and OPA:IPA:Hex.

From Figure 3.1a, we can see that the film treated with BBr:Hex or OPA:IPA:Hex exhibits the highest conductivity, which was collected on samples with evaporated Au electrodes on the NC films as described in Chapter 2. The film treated with EA has higher conductivity than the film treated with MeOAc. TOL:BuOH:SCN also shows moderate improvement in increasing the conductivity of the pristine film. Butylamine almost has no effect on the improvement of film conductivity.

From Figure 3.1b, it is clear that there are new absorption peaks introduced in the case of BBr:Hex near 430 nm and 460 nm as what the purple arrows indicate. Treatments with butylamine and OPA:IPA:Hex enhanced the excitonic absorption peak, while the absorption plot of the film treated with TOL:BuOH:SCN becomes much weaker and non-featured. The normalized absorption spectra of films treated with EA or MeOAc appear to be the same.

From Figure 3.1c, we can tell that the PL peaks of films treated with EA and MeOAc blue-shift, while there is an obvious red-shift in the PL peaks after treating the pristine NCs film with butylamine or OPA:IPA:Hex. Instead, there is negligible PL shift for the films treated with BBr:Hex. As reported in Table 3.1, the PL QY of the film treated with BBr:Hex is the best. Additionally, the FWHM of PL peaks of all treated NCs films are narrower than that of the pristine NCs film.

According to Table 3.1, the pristine NCs film holds the longest decay lifetime. It is clear from Figure 3.1d that the decay curve in the case of BBr:Hex is similar to that of the pristine NCs film in the fast decay region. Films treated with butylamine have moderately high decay lifetime. The decay lifetimes of films treated with EA and MeOAc are extremely similar, and are significantly lower than that of the pristine NCs film, suggesting that the treatment introduced defects/non-radiative decay channels, in line with the seriously decreased PL QY.

Table 3.1. Statistic results of the optical properties of the treated films.

Treatment method	Pristine NC	Ethyl acetate	Methyl acetate	Butylamine	BBr:Hex	OPA:IPA:Hex
PLQY	25.2%	10.7%	10.6%	7.5%	26.4%	7.80%
Peak(nm)	515.9	514.4	513.9	521.1	516.1	518.7
FWHM(nm)	23.7	21.0	21.0	19.5	21.1	20.4
τ_{ave} (ns)	40.9	7.3	6.5	31.0	30.3	15.4

According to the photos of the films under UV light in Figure 3.1d, we see that all treated films look still bright and smooth except for the film treated with TOL:BuOH:SCN due to introduction of polar solution in a large amount.

With a comprehensive consideration of the above data, we can say that BBr:Hex has the best performance in increasing the conductivity of the pristine NC film as well as in preserving the optical performance of the NCs film, in spite of introducing new optical absorption features into the system according to Figure 3.1b. In addition, although films treated with ethyl acetate and methyl acetate have similar optical performance, films treated with EA have higher conductivity. Therefore, we conclude that EA is a better choice than MeOAc for the current NCs films. Finally, BBr, SCN solution and EA were further selected to treat $CsPbBr_3$ NCs in solution. Incidentally, we could see that OPA:IPA:Hex is also a good choice to treat the pristine film, as demonstrated later by several reports that chemicals containing phosphonic-group could act as good ligands for perovskite NCs [38, 96, 154, 155].

3.3.2 Conductivity of films based on treated perovskite NCs

Considering the results of the different treatments, the combined effect of BBr, SCN and EA was tested on the conductivity of $CsPbBr_3$ NCs films, with varying amounts of BBr and SCN. Although we observed that the SCN solution quenches the PL of the LHP, which may be due to SCN-induced chemical annealing among NCs [156], when it is applied directly onto the NC film (experiments discussed in the previous section), it was also reported to be conducive to suppressing surface defects when it is used in NC solution [59, 62]. So we continued using SCN solution of different concentrations in the treatment of NC solution.

The obtained I-V (current vs. voltage) curves are plotted in figure 3.2.

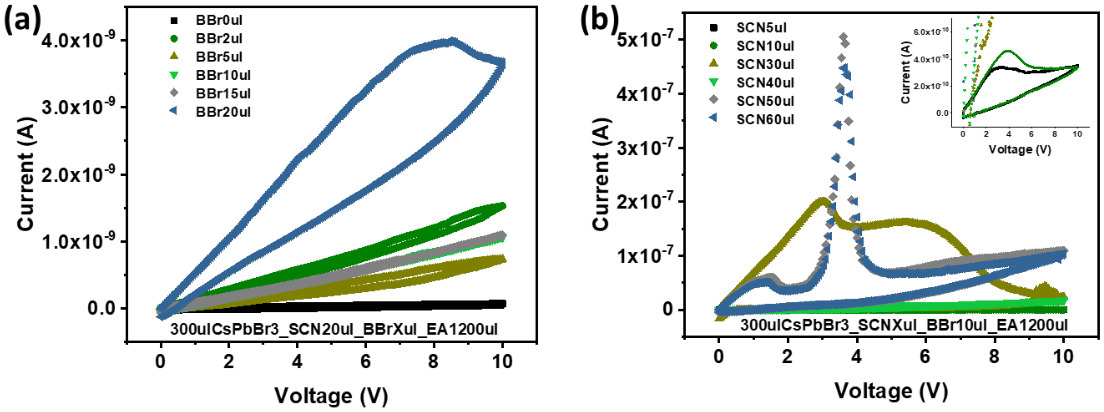

Figure 3.2. Effect of amount of BBr or SCN solution on conductivity of films based on treated NCs. Conductivity of films based on NCs treated with solutions containing various amount of (a) BBr; and (b) SCN solution.

From Figure 3.2a, b, we can see that all the tested combinations of BBr and SCN on the pristine NC solutions are helpful in improving the conductivity of the NC films. In panel a, the I-V curves are acquired on samples obtained with fixed amount of SCN solution (20 µL for 300 µL of $CsPbBr_3$ NCs solution) and at increasing amount of BBr, from 0 to 20 µL; the current shows a steady improvement with the amount of BBr and most of the profiles look linear except for the case of the highest BBr content, where a clear difference between the forward and backward sweeps could be observed. The observed hysteretic behavior might be related to halide ion migration under the applied voltage, as it happens also in LHP-based solar cells [157].

In panel b, instead, the curve are acquired on samples obtained with a fixed amount of BBr (10 μL for 300 μL of $CsPbBr_3$ NCs solution) and at increasing amount of SCN solution, from 5 to 60 μL. The current profiles start to become obviously non-linear when the amount of SCN solution is higher than 30 μL and the current increases sharply around 4 V. The observed behavior has been tentatively assigned to some side-electrochemical reaction, most likely involving the thiocyanate ion; a deeper understanding of the phenomenon was out of the scope of the present thesis, and therefore we did not dig deeper on this point.

According to the above conductivity data, we decided to treat the NCs solution with 2 μL BBr and 20 μL SCN solution in 1200 μL EA in the next step.

3.3.3 Conductivity of annealed films

Considering that the perovskite NCs films are usually annealed in the device fabrication process, we compared the effect of annealing temperature (up to 170 °C) on the conductivity of the films based on pristine NCs and treated NCs. The results are reported in figure 3.3.

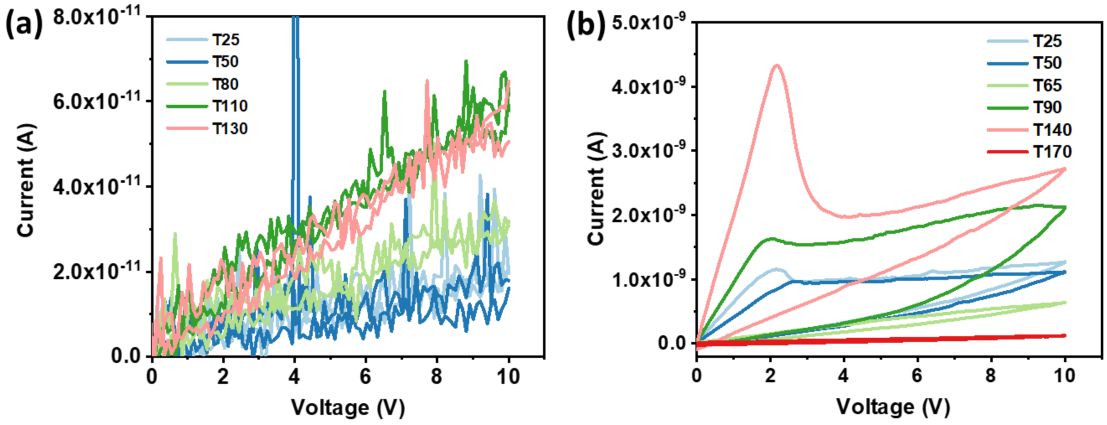

Figure 3.3. Effect of annealing temperature on conductivity of films based on (a) pristine CsPbBr3 NCs; and (b) NCs treated by BBr2µl_SCN20ul_EA1200µl.

From Figure 3.3a, it is clear that the absolute conductivity of the films made of untreated $CsPbBr_3$ NCs increases with increasing annealing temperature, but the net current after annealing is still quite low even under 10 V. In contrast, the I-V profiles of the films based on treated NCs (treatment solution: 2 μL BBr and 20 μL SCN in 1200 μL EA) show significantly higher current values, even if they appear to be non-linear. The current values increase by increasing the annealing temperature. Also in this case, the current profiles show a sharp peak at ~ 2 V, whose origin is not understood yet. Overall, the observed results indicate that annealing helps in improving the conductivity of the NCs films for both the pristine and the treated ones.

3.4 Stability of films based on treated perovskite NCs

The stability of the treated LHP NC solutions has already been studied previously [34, 59]. However, in film form, studies of LHP NCs stability focused so far mainly on $CsPbI_3$ [158] or $MAPbI_3$ NCs [159]. There are only few reports about the stability of films based on $CsPbBr_3$ NCs. For example, Gao and coworkers [160] reported phase transition of $CsPbBr_3$ NC-based films under UV illumination. Kamat and coworkers [161] studied the evolution of $CsPbBr_3$ NCs by annealing the films at different temperatures for a series of time (0-60 min). They reported film degradation with $CsPbBr_3$ evolving from NCs to bulk *via* Ostwald ripening, as the annealing time was increased. However, both aforementioned studies are based on films of $CsPbBr_3$ NCs without purification or treatment. In this section, the optical and morphological stability of films based on treated LHP NCs are characterized in detail and possible mechanism of the high stability was proposed.

Films based on NCs treated with different ratios of BBr and SCN solution were spin-coated on glass substrates. Optical properties and morphology variation of the films before and after aging were studied systematically. In this section, I show the comparison results of the optimal film based on treated NCs (labeled as SCNBBr) and the film based on pristine NCs (labeled as REF).

Figure 3.4 shows representative TEM images of the as-synthesized $CsPbBr_3$ NCs as well as of the fresh and aged REF and SCNBBr NCs, after annealing at 65 °C for 10 min on a copper TEM grid.

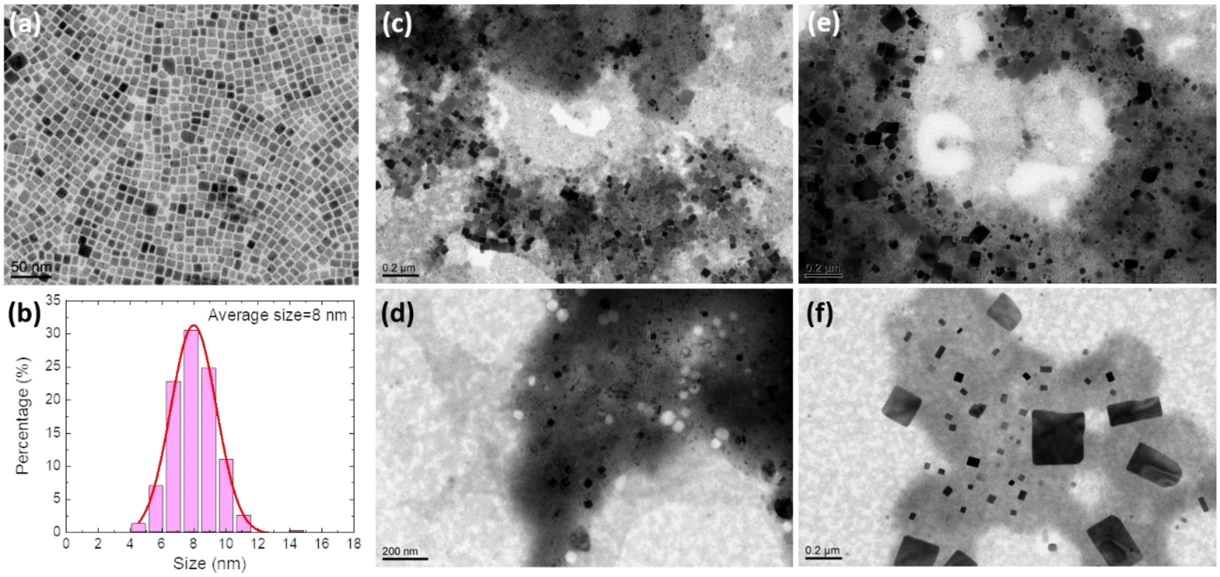

Figure 3.4. (a) Representative TEM image of the as-synthesized CsPbBr$_3$ NCs and (b) statistical analysis of their size, based on measurements over 400 NCs. The average size is (8.0±1.7) nm. (c), (d) TEM images of the fresh REF- and SCNBBr-CsPbBr$_3$ NCs, respectively, after annealing at 65 °C for 10 min; (e), (f) TEM images of the REF and SCNBBr-CsPbBr$_3$ NCs after being stored for ~ 10 months in air [162].

The pristine sample (see Figure 3.4a) was characterized by NCs of almost cubic shape, with average size of 8.0±1.7 nm (see Figure 3.4b for the size distribution histogram). In the present case, the size distribution is slightly broader than what was reported by Imran *et al. [21]*, most likely because the increase in amount of the used chemicals and solvents volumes resulted in a less controlled reaction environment. After annealing on a copper TEM grid, both REF (Figure 3.4c) and SCNBBr (Figure 3.4d) NCs were characterized by two sub-populations of particles with different sizes. Specifically, one family was composed by NCs with size of ~8 nm (Figure 3.5a) as in the pristine sample, while the other was characterized by larger dark objects, labelled as nanoplatelets (NPs) in the following. These NPs appeared to distribute randomly on top of the NCs (see Figure 3.4c-f).

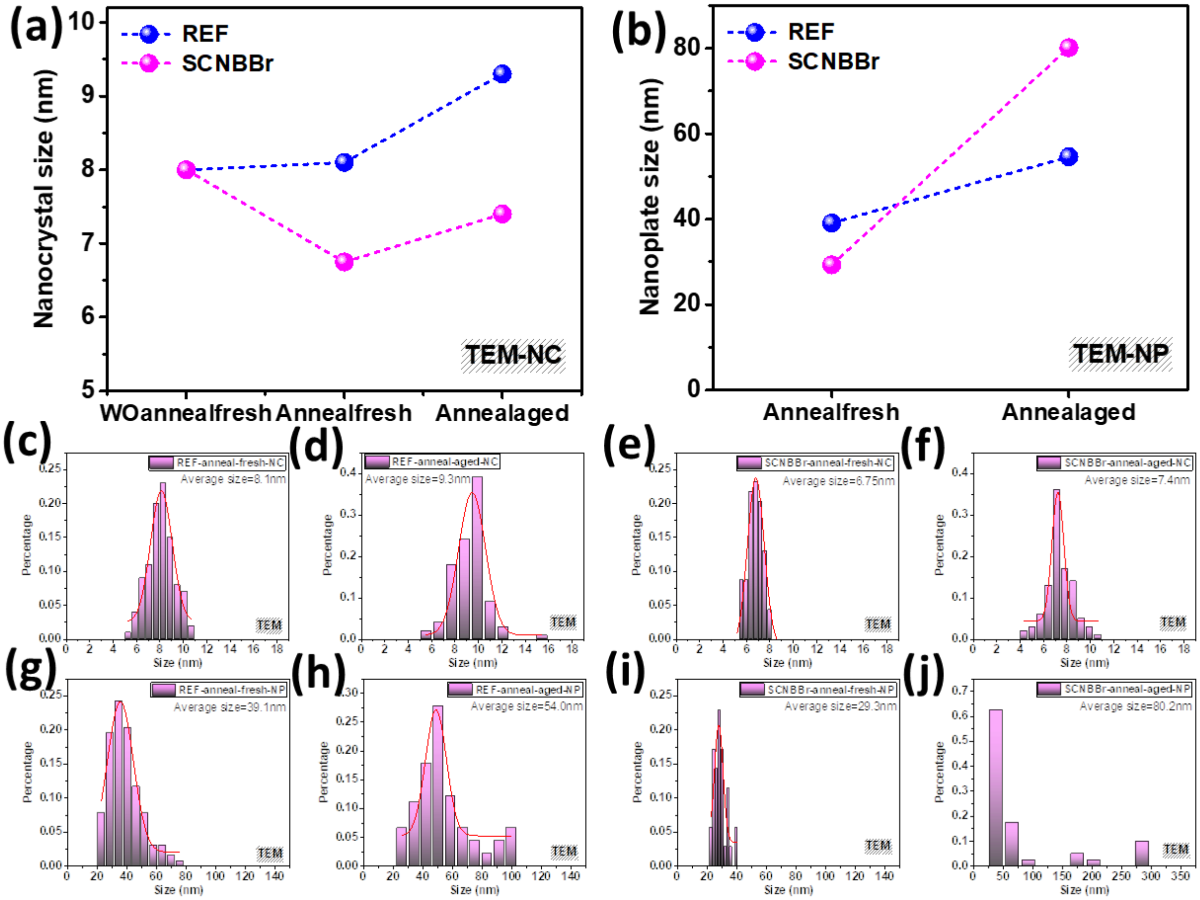

Figure 3.5. Size distributions of (a) nanocrystals (NCs) and (b) nanoplates (NPs) according to TEM images. Statistics of sizes of 100 NCs in (c) fresh and (d) aged REF TEM samples; Statistics of sizes of (e) 70 NCs in fresh and (f) 100 NCs in aged SCNBBr TEM samples; Statistics of sizes of (g) 128 NPs in fresh and (h) 90 NPs in aged REF TEM samples; Statistics of sizes of (i) 35 NPs in fresh and (j) 40 NPs in aged SCNBBr TEM samples.

In the case of REF NCs, the NPs had an average size of ~39 nm (Figure 3.5b); after aging, the average size of the NPs increased further to ~55 nm (Figure 3.4f and Figure 3.5b) and their number increased as well, at the expenses of the NCs population. In the case of fresh SCNBBr (Figure 1d), the NPs had an average size of ~29 nm. After aging, while the average size of the NCs appeared to be stable, with only a minor increase to ~9 nm (Figure 3.4d and Figure 3.5b), the average size of the NPs increases to ~80 nm (Figure 3.4f and Figure 3.5b). Overall, it appears that REF and SCNBBr samples experience different evolution routes during aging.

3.4.1 Stability of optical property of the films

Figure 3.6 displays the results of the optical characterization of REF and SCNBBr films, fresh and aged.

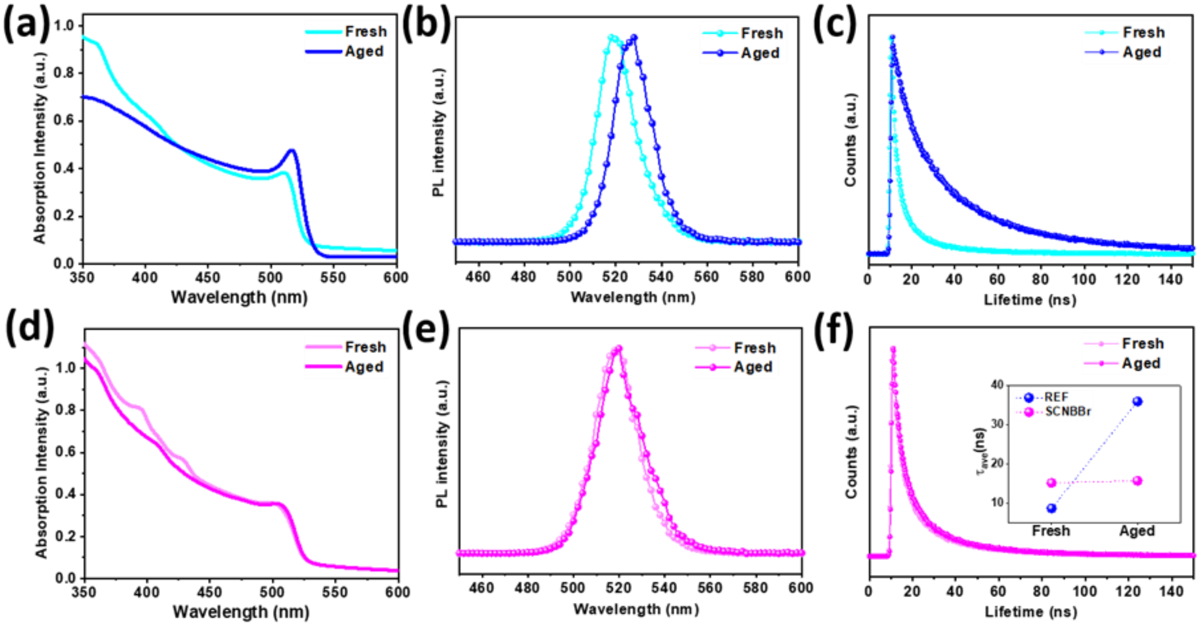

Figure 3.6. Comparison of (a), (b), (c) REF and (d), (e), (f) SCNBBr films, both fresh and aged. (a), (d) absorption, (b), (e) PL and (c), (f) PL decay [162].

For the REF sample (Figure 3.6a-c), there is an obvious change in the absorption profile, PL peak position and PL lifetime between fresh and aged film. In fact, as shown in Figure 3.6a, the aging of the REF film induced a clear strengthening of the excitonic transition, its red-shift from 510 nm to 516 nm, and a sharpening of the absorption edge, together with the disappearance of the weak and broad absorption feature at ~407 nm; these changes may be due to increased NC size [77]. A significant red-shift of the PL peak from 520 nm to 527 nm (Figure 3.6b), in correspondence with the red-shift of the absorption edge, can be observed, further corroborating the increase of the NC size. The FWHM of the PL peak shows a minor decrease from 21.1 nm to 20.3 nm (Table 3.2), which may indicate a slightly narrower distribution of NC sizes [163]. The PL QY of the fresh film with annealing is ~16%, while the PL QY of the REF aged film is merely ~8%. As a reference, the PL QY of a film based on pristine $CsPbBr_3$ NCs is ~25%. The average PL decay lifetime for REF film (Figures 3.6f) shows a noticeable increase on aging, from ~9 ns to ~36 ns. The increased decay lifetime corresponds to the enlarged NC sizes, as seen in the SEM images (Figure 3.6a-b), given that larger size facilitates separation and transport of excitons or carriers and therefore involves a slower recombination [4, 164]. This could also be demonstrated by the increased ratio of τ_2 (Table 3.2), which usually represents slow recombination [165].

On the other side, the SCNBBr treated film does not show drastic changes in absorption profile, PL peak position and average PL lifetime, between the fresh and aged film (Figure 3.6d-f and Table 3.2). Actually, as compared to the REF sample, in addition to the main absorption edge around 504 nm, in Figure 3.6d the fresh SCNBBr film shows two absorption peaks around 430 nm and 396 nm. These new peaks at shorter wavelengths may be attributed to the formation of intermediates, caused by the decomposition of some $CsPbBr_3$ NCs. According to the literature, the peak at 430 nm may tentatively be ascribed to formation of bi-layer 2D structure, and the peak at 396 nm may be due to formation of single-layer 2D structure composed by organic ligand and $[PbBr_4]^{2-}$ layers [166, 167]. In the SCNBBr aged film, the absorption peaks near 430 nm and 396 nm disappear.

Table 3.2. Optical characterization results of fresh and aged REF and SCNBBr films.

Sample	REF-fresh	REF-aged	SCNBBr-fresh	SCNBBr-aged
PL FWHM (nm)	21.1 ± 0.4	20.3 ± 0.2	21.1 ± 0.3	20.8± 0.4
ΔFWHM (nm) (aged – fresh)	-0.9		-0.3	
PL Peak position (nm)	520.2 ± 0.2	527.2 ± 0.1	518.8 ± 0.1	518.8 ± 0.2
ΔPL peak (nm) (aged – fresh)	+7.0		-0.1	
PLQY (%)	~16	7.9	~25	22.1
τ_{ave} (ns)	8.6	35.9	19.5	12.2
$\Delta\tau_{ave}$ (ns) (aged - fresh)	+27.3		-7.3	
τ_1 (ns)	2.1 ± 0.1	11.3 ± 0.1	6.5 ± 0.1	4.3 ± 0.1
τ_1 weight	84.0%	56.3%	74.4%	71.4%
τ_2 (ns)	13.8 ± 0.1	44.0 ± 0.2	28.1 ± 0.2	17.1 ± 0.1
τ_2 weight	16.0%	43.7%	25.6%	28.6%

Regarding the PL profiles, in the SCNBBr samples the PL peaks and the FWHM of the PL peaks remain almost the same (Figure 3.6e and Table 3.2). The PLQY of the aged film is ~22% and that of the fresh one is ~25%, which are not significantly different, as the error associated with these values is ±5%. The PL decay plot in Figure 3.6f shows average lifetimes with a moderate decrease, from 19.5 ns to 12.2 ns, with a stark contrast to that of REF (see inset of Figure 3.6f). Overall, the similar optical characterization results between SCNBBr fresh and aged films indicate that the NCs treated with our optimized combination of SCN and BBr are relatively stable, especially when compared to the untreated REF films. For the latter, the changes in optical performance between fresh and aged films confirms that the untreated NCs are unstable and suffer from fast degradation.

3.4.2 Stability of the morphology of the films

A morphological analysis was carried out by SEM on films prepared from the respective samples. Representative images are shown in Figure 3.7. In Figure 3.8, the quantitative analysis of the NC size is presented, instead.

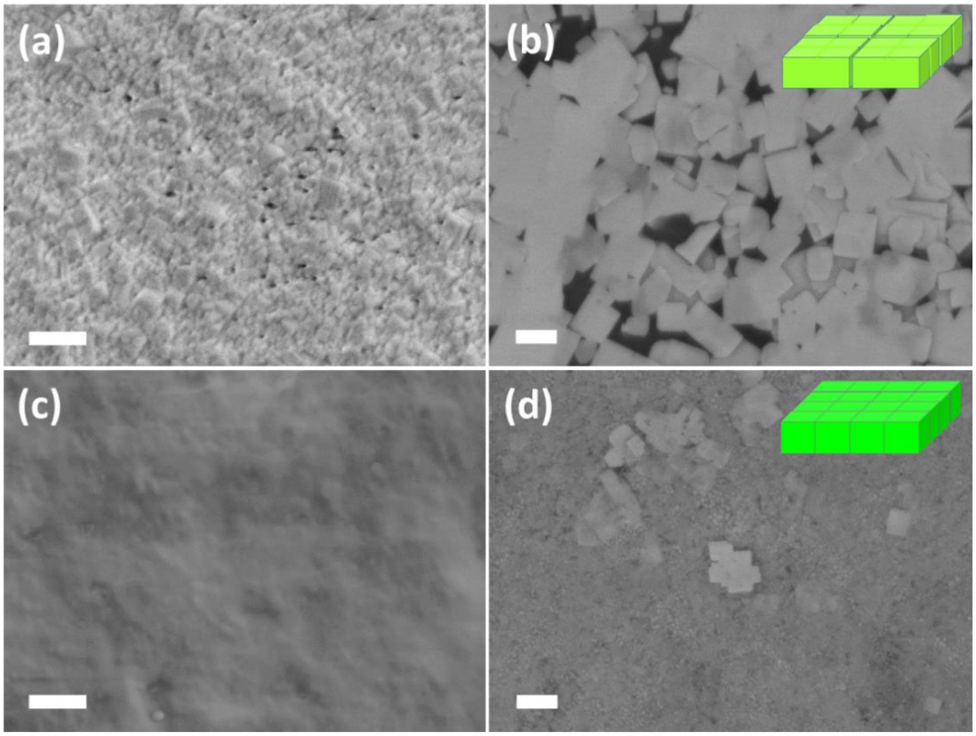

Figure 3.7. SEM images of (a),(b) REF and (c),(d) SCNBBr films, (a),(c) fresh and (b),(d) aged. (The scale bars are 500 nm) [162].

In the fresh REF films (Figure 3.7a), a compact layer of NCs can be seen. However, the effect of the annealing step already induced an increase of their average size from ~9 nm before annealing to ~120 nm after annealing, and then increased up to ~415 nm on aging (Figure 3.7a-b and Figure 3.8).

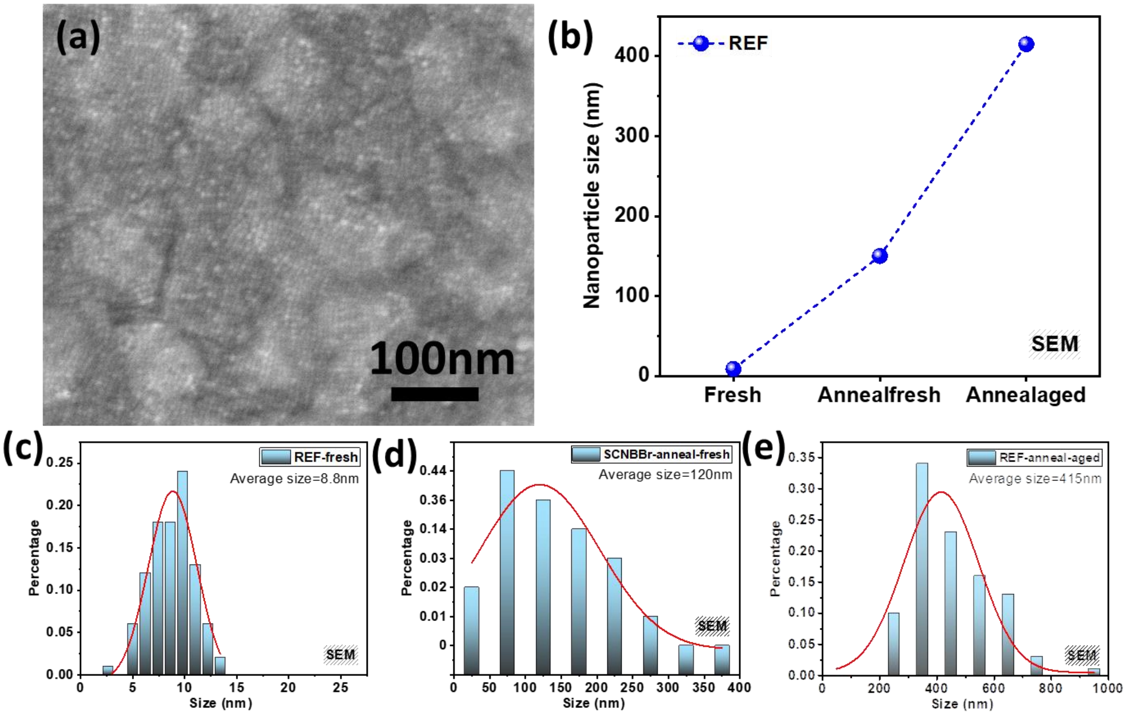

Figure 3.8. (a) SEM image of fresh REF film without annealing; (b) Comparison of average sizes of NCs in REF films. Statistics of sizes of NCs in fresh REF film (c) without annealing and (d) with annealing; and (e) aged REF film with annealing.

In the SCNBBr films, the single NCs could not be resolved both in the fresh (Figure 3.7c) and in the aged (Figure 3.7d) cases, and film coverage appeared to be uniform. After ageing for ten months (see Figure 3.7d and Figure 3.8e), some larger particles appeared, partially embedded in the smooth film.

As observed from TEM images (Figure 3.4), the REF and SCNBBr films show a strikingly different behavior with ageing. The REF film is characterized by an evident growth of the average NCs size, as is not seen in the SCNBBr case, suggesting that the REF film has a poorer stability in the long term [161, 168]. On the other hand, our morphological analysis shows that the SCNBBr treatment has a positive effect in limiting the growth of NCs with time and in retaining film morphology during long-term storage in air, with relative humidity up to 70%.

In order to test the robustness of our approach, we did a systematic study by varying the ratio of SCN and BBr in the treatment of pristine NCs. The optical and morphological characterization results are shown in Figure 3.9. The results demonstrate that our protocol of treating $CsPbBr_3$ NCs with a combination of SCN and BBr is effective for achieving highly stable $CsPbBr_3$ NCs-based film in the long term.

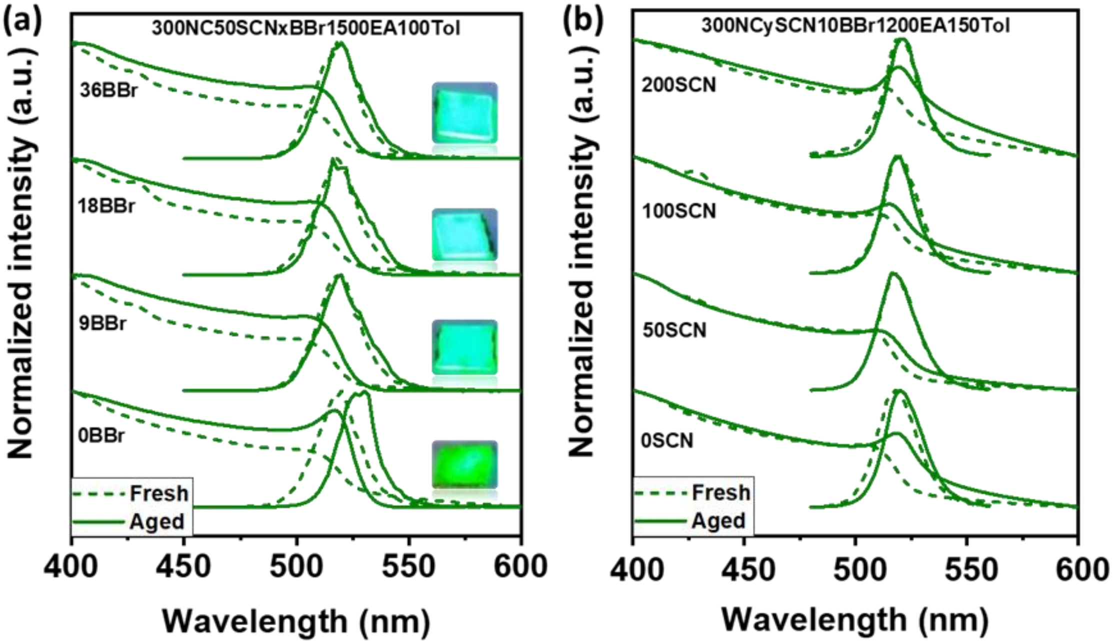

Figure 3.9. Characterization results on fresh and aged films based on CsPbBr3 NCs treated with varying amount of (a) BBr and (b) SCN. UV-Vis absorption profiles and PL spectra with photos of the aged films in the inset.

3.4.3 Discussion on mechanism of high stability

To illustrate the reason of the high stability of the treated film, XRD patterns were collected on the fresh and aged films, as shown in Figure 3.10.

All films display diffraction peaks matching with the orthorhombic $CsPbBr_3$ perovskite structure (ICSD card 00-054-0751, blue vertical lines in all panels).

The effect of the combined NH_4SCN and BBr treatments is already visible on the fresh films; indeed, the XRD pattern collected on the fresh SCNBBr film (Figure 3.10b) shows additional peaks with respect to the one on REF NCs. In particular, the treated sample is characterized by the presence of three sharp and intense diffraction peaks centered at 13.1°, 26.3° and 37.5°. In Figure 3.10b, the experimental pattern is tentatively compared with the reference card for the so-call non-luminescent 0D perovskite Cs_4PbBr_6 structure (ICSD card 98-002-5124, orange vertical lines in Figure 3.10b, d).

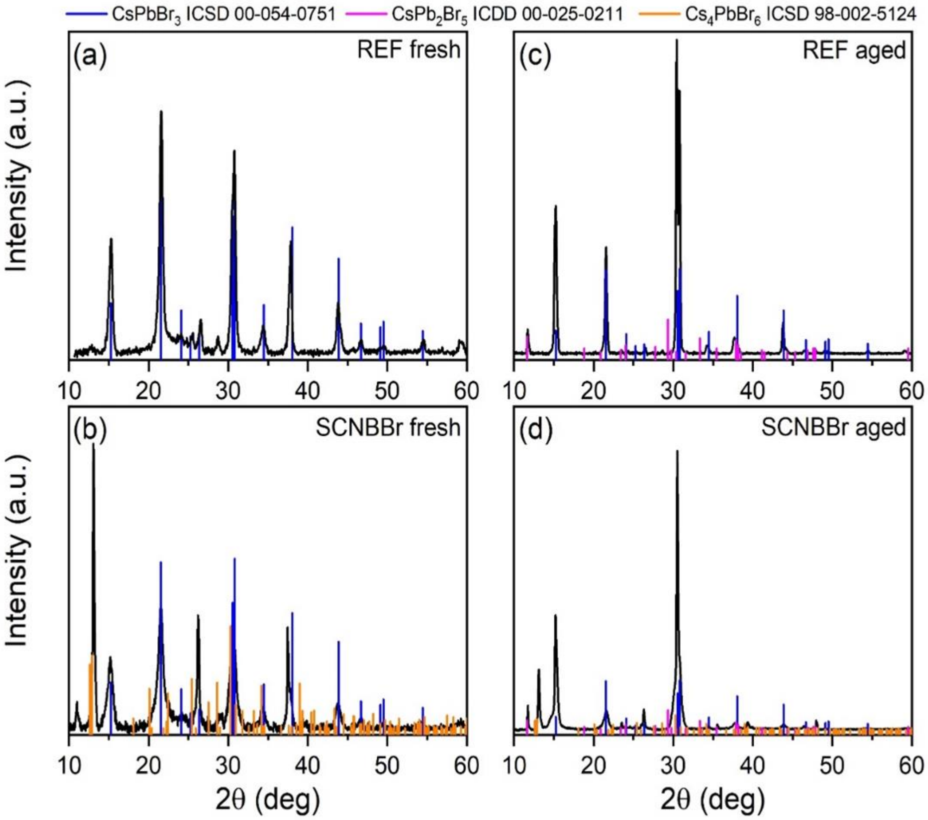

Figure 3.10. XRD patterns of (a) fresh and (c) aged REF film; XRD patterns of (b) fresh and (d) aged SCNBBr film [162].

Although it is evident that the match between experimental and database data is not perfect, we assigned the new peaks to a low dimensionality (either 0D or 2D) phase, which might have arisen from a partial decomposition or restructuring of the NCs during the treatment with SCNBBr in solution.

For both REF and SCNBBr aged films, the XRD patterns are dominated by the peaks at 15.2°, 21.6° and 30.4°, which increased in intensity and became narrower with respect to those of the fresh cases. This indicates that, in both cases, $CsPbBr_3$ crystals have the tendency to grow preferentially along the (020), (002) and (040) directions. In both cases, an additional peak at 11.7° also appeared, which can be assigned to the non-luminescent tetragonal $CsPb_2Br_5$ phase [169, 170] (ICDD card 00-025-0211, magenta vertical lines in Figure 3.10c, d). $CsPb_2Br_5$ is usually plate-like and has an UV-Vis absorbance peak near 400 nm. The presence of this phase is in line with the observed NPs in TEM images (Figure 3.4f) and with the peak ~ 407 nm in the light absorbance plot of SCNBBr aged film (Figure 3.6d). Interestingly, the diffraction peaks at 13.1° and 26.3° in the SCNBBr aged film show absolute diffraction intensities similar to $CsPbBr_3$in the fresh film.

This suggests that those NCs in the SCNBBr fresh film are well retained in the aged film, in spite of the co-existence of $CsPb_2Br_5$ NPs. This observation agrees with the well-retained optical performance (Figure 3.6d-f) of the SCNBBr aged film, as is also observed in the PL mapping results obtained from the confocal microscopy that small amount of non-luminescent particles distributed in the luminescent film (Figure 3.11).

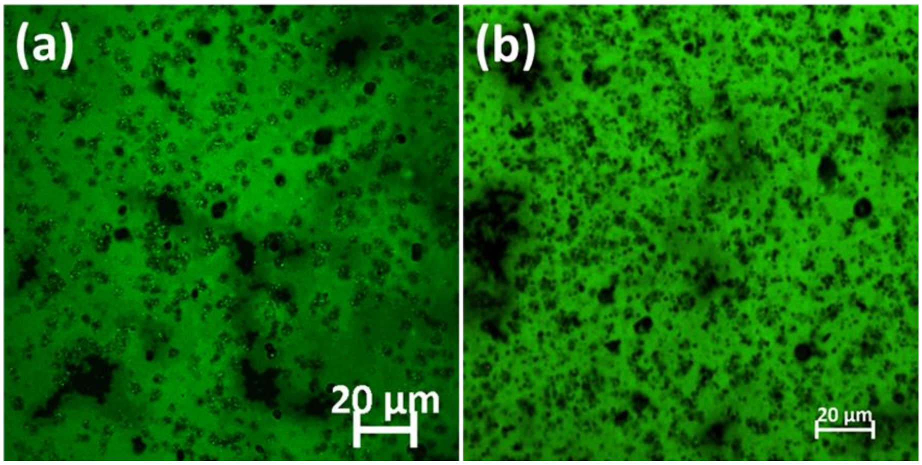

Figure 3.11. PL mapping images by confocal microscopy for (a) fresh and (b) aged SCNBBr film.

The coexistence of different phases could be further confirmed by localized SEM-EDS mapping on the aged films based on the treated NCs (Figure 3.12).

REF aged film clearly shows excess of Cs and Br. SCNBBr aged film also shows excess of Cs and Br, although the ratios of Cs and Br to Pb are lower than those in the REF case. Localized EDS mapping on the sheets in the SCNBBr aged film shows slight Cs-deficiency. Localized EDS mappings on the bars and polyhedra in the SCNBBr aged film further show high excess of Br and Cs (Figure 3.12g-j). These element mapping together with the XRD results (Figure 3.10) confirm co-existence of Cs_2PbBr_5 or Cs_4PbBr_6 in the aged films.

In addition, according to some reports, $CsPbBr_3$ could form composites [118, 171-174] or mixtures of phases [168, 175-177] with Cs_4PbBr_6 or $CsPb_2Br_5$. The composites or mixtures usually show high stability [168, 171, 173, 177, 178], which is in line with what we observed in the current case with a mixture of $CsPbBr_3$, Cs_4PbBr_6 and $CsPb_2Br_5$.

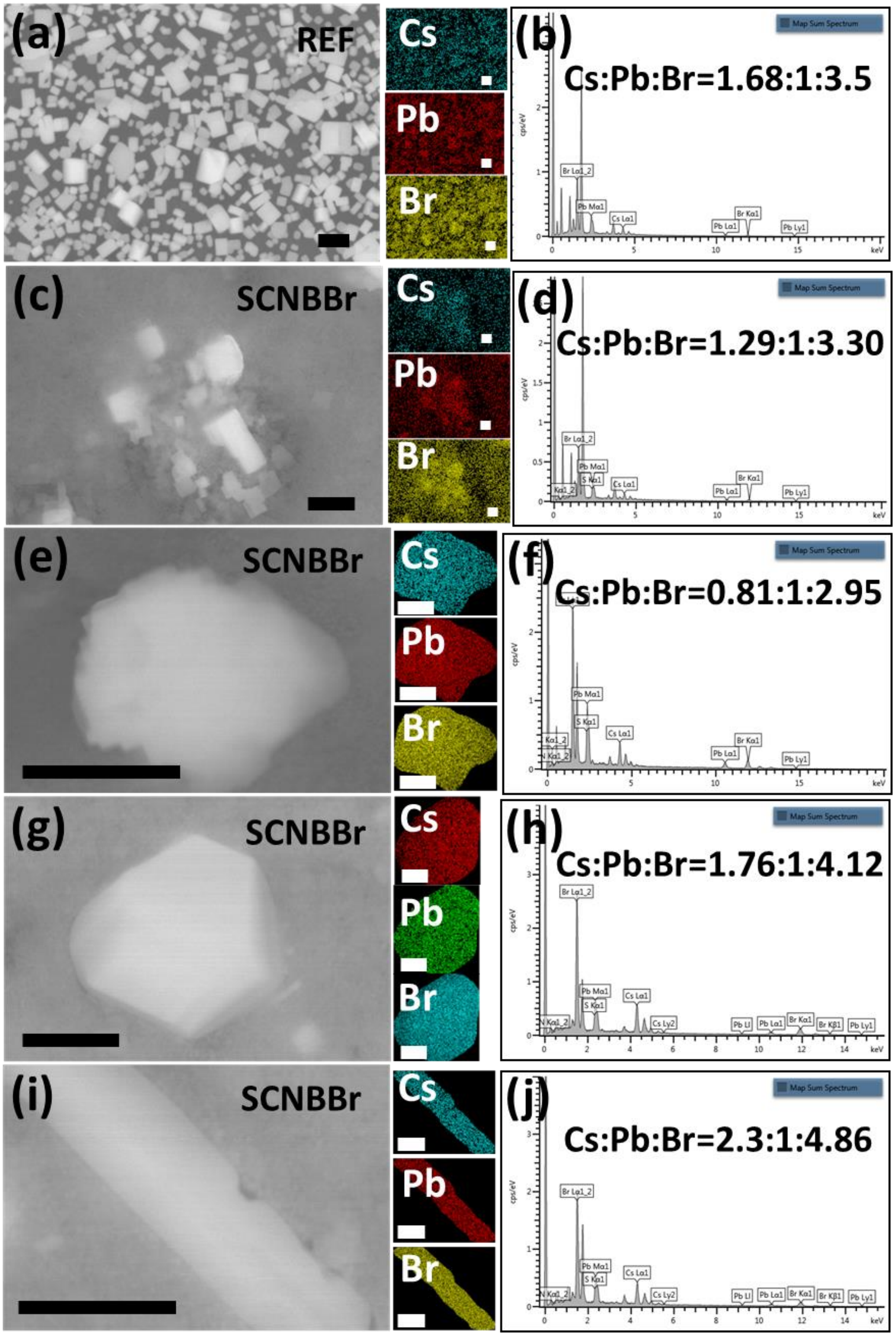

Figure 3.12. (a, c) SEM images and EDS element mapping; and (b, d) EDS spectra of elements including Cs, Pb, as well as Br for REF and SCNBBr aged films, respectively. (e, g, i) SEM images and EDS element mapping; and (f, h, j) EDS spectra of elements including Cs, Pb, as well as Br for localized areas of SCNBBr aged film. Scale bars in all SEM images are 1 μm, while in EDS mapping are 1 μm in (a, c) and 500 nm in (e, g, i).

Several reasons may possibly account for the higher stability of the SCNBBr film in optical performance and NCs behavior, in comparison with the REF film. Firstly, SCN may enhance structural stability of the NCs during treatment in solution, as well as during storage of the film. Since SCN anion is able to replace Br^- [179] and to bind to lead atoms on the surface of the NCs [39], SCN^- may anchor onto some Br-vacancies that are prevalent in $CsPbBr_3$ NCs during treatment in solution, stabilizing the structure and optimizing the optical properties of the NCs [59].

Secondly, BBr may help maintain the PL of the film by providing a Br-rich environment for the NCs [173]. When the highly labile ligands desorb from the NC surface, either during the treatment in solution or the storage in the film form, this usually leads to additional surface defects and structural distortion [62]. Without protection from ligands and with more defects on their surface, the NCs are prone to self-assembly and/or grow larger as in the REF case. The Br-rich environment may relieve the problem and limit the growth of the NCs. However, since SCN^- can play a competitive role to Br^-, it is necessary to control the ratio between SCN and BBr during treatment in solution. On the one hand, according to our observation, addition of BBr is helpful in stabilizing the emission peak (Figure 3.13a), but seems to boost emergence of new phases like Cs_4PbBr_6 (Figure 3.13b). On the other hand, addition of SCN seems to favor formation of NPs, but an excessive amount facilitates chemical sintering among the NCs [156], leading to their fast growth (Figure3.13c-d).

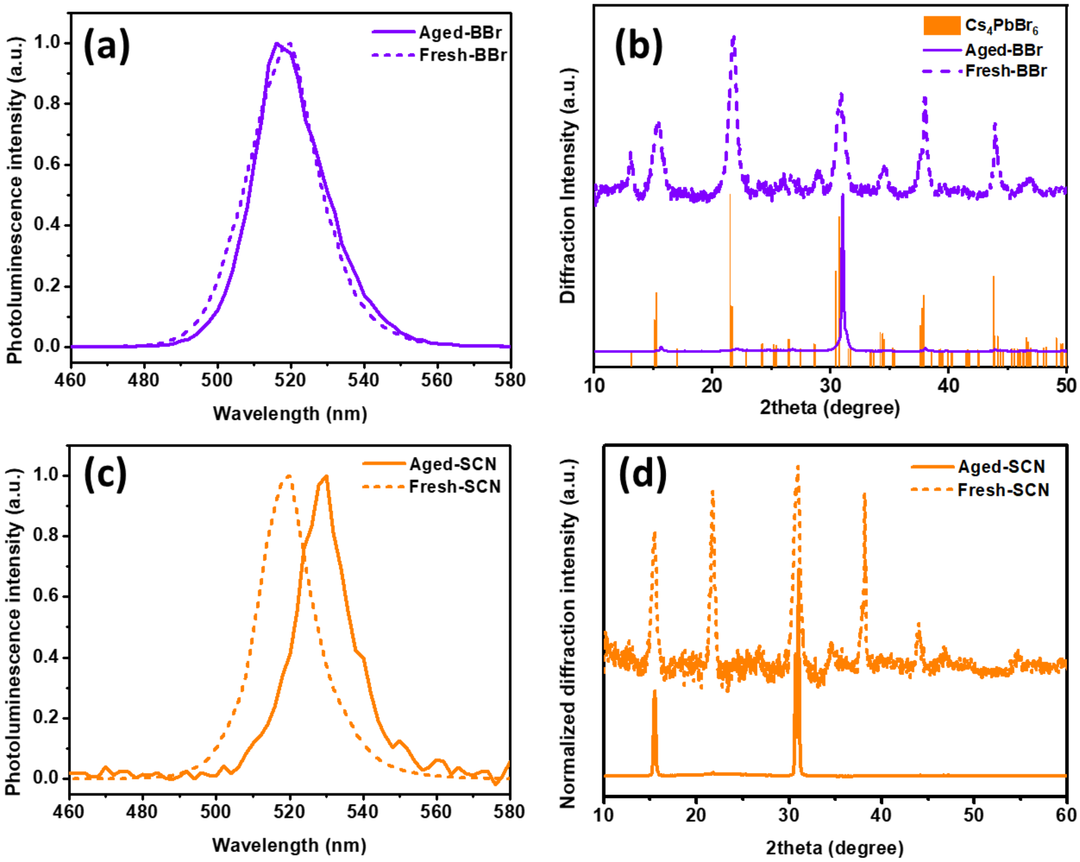

Figure 3.13. (a) PL and (b) XRD patterns of BBr fresh and aged films [180], with Cs_4PbBr_6 (ICSD98-002-5124) as reference; (c) PL and (d) XRD patterns of SCN fresh and aged films.

Thirdly, the coexistence of $CsPbBr_3$, Cs_4PbBr_6 and $CsPb_2Br_5$ phases may enhance the stability of the NCs film [168, 177] due to element balance among the phases [171] and increased entropy of the system [105]. This could be demonstrated by XRD and SEM-EDS characterization results.

3.5 Effect of solvent on film formation

In order to get LHP NC-based optoelectronic devices with excellent performance by spin coating, it is both necessary to optimize NC surface by surface engineering [37, 73, 79] as shown in section 3.3, and to obtain smooth and compact LHP NC films to avoid current leakage [97, 107, 147, 181-183]. In this respect, there are several important conditions [184] to consider, such as wettability of substrates [185], spin-coating speed [186], ambient humidity, NCs concentration, NC size, type and evaporation rates of NCs solvent [187]. Usually, non-polar solvents [77], including toluene [36], hexane [117] and octane [65], are used to dissolve LHP NCs and to maintain their stability [188]. In some cases, the solvent seems to have significant effect on the physical properties of LHP NCs. For example, chloroform was demonstrated to be able to passivate bromide vacancies in perovskite thin films [187]. Although there are studies about the effect of solvents on depositing non-NCs-based halide perovskite thin films [187, 189, 190] and about the effect of polar solvents on LHP NCs during purification [68-70], there has been no report about the effect of solvents used for dispersing LHP NCs on fabricating LHP NC films.

In this section, the effect of a series of solvents on spin-coated LHP NC films was studied. The solvents include DE (S1), hexane (S2), cyclohexane (S3), toluene (S4), octane (S5) and dichlorobenzene/chloroform with a ratio of 2:1 (S6); moving from S1 to S6, the chosen solvents are characterized by increasing boiling points and decreasing vapor pressures, as summarized in Table 3.3. The influence of the evaporation rates and types of solvents on the morphology and on the optical performance of the LHP NC films were characterized in detail.

Table 3.3. Parameters of solvents used in dispersing CBP NCs.

Label	**Solvent**	**Boiling point (◦C)**	**Vapor pressure (mmHg)**	**Relative Polarity**
S1	Diethyl Ether	34.6	440	2.8
S2	Hexane	69	124	0.1
S3	Cyclohexane	80	77	0.2
S4	Toluene	111	21	2.4
S5	Octane	125	10	~0.2
S6	Dichlorobenzene/ Chloroform (2:1)	180/ 60	1.3/ 160	2.7/ 4.1

The NCs used for this study are the ones treated with BBr (10 µL BBr in 900 µL EA). In the final step of purification via centrifugation, the precipitate is dispersed in one of the six solvents, instead of the toluene used in the typical procedure. Figure 3.14 shows TEM images of NCs dissolved in different solvents.

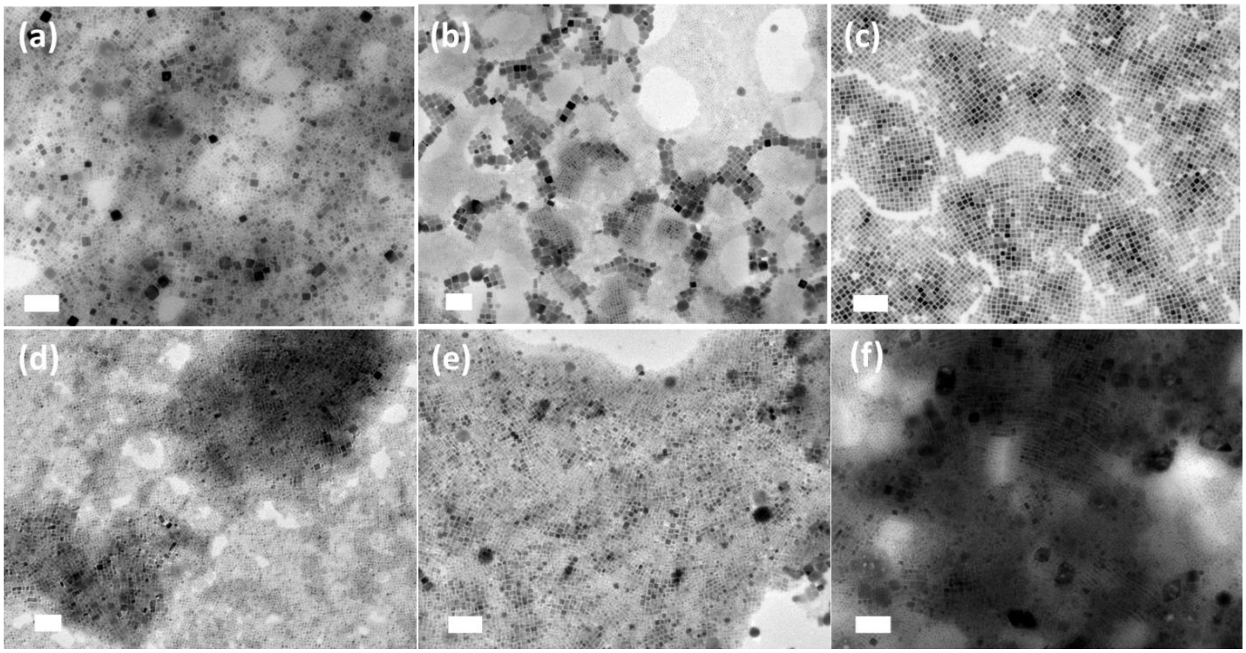

Figure 3.14. TEM images of LHP NCs dispersed in the series of solvents (a) DE (S1), (b) Hex (S2), (c) cyclohexane (S3), (d) toluene (S4), (e) octane (S5) and (f) dichlorobenzene/chloroform (S6).

All the samples seem to be characterized by at least two populations of particles. In DE (S1, Figure 3.14a), NCs appear with an average size of 7 nm as well as larger particles with an average size of 24 nm (Table 3.4). The NCs with different sizes evenly spread across the sample. Some of the large particles seem to sit on top of the other NCs.

Table 3.4. Statistics of average sizes of NCs and large particles in TEM images of NC solutions with different solvents.

TEM	**S1**	**S2**	**S3**	**S4**	**S5**	**S6**
NC (nm)	6.6	7.8	10.3	7.8	9	7.1
Large particle (nm)	23.5	19	17	12	36	33.4

Figure 3.14b (sample in hexane) shows a network of large particles with an average size of 19 nm, and NCs with an average size of 8 nm in the background. In the case of cyclohexane (S3, Figure 3.14c), NCs form several islands separated by cracks. The islands show increasingly darker color from the edge to the center, due to a gradient in NCs size. Apart from the homogeneous distribution of the majority of NCs with an average size of 10 nm in Figure 3.14c, there are also some NCs with larger size ~ 17 nm, as shown in the inset of Figure 3.14c. For NCs dissolved in toluene (S4, Figure 3.14d), a few dark islands appear that are embedded in the orderly distributed

NCs with an average size of 8 nm. In the dark regions there are some large particles with clear edges ~ 12 nm. In the case of NCs in octane (S5, Figure 3.14e), apart from a few round dark points with an average size of 36 nm, the NCs follow a generally homogeneous distribution with an average size of 9 nm. Most NCs show clear edges at current resolution, which is in line with the larger average size, suggesting widespread chemical sintering among the NCs in octane. For NCs dissolved in dichlorobenzene-chloroform (S6, Figure 3.14f), a few squares appear among the NCs with an average size of 7 nm, following the arrangement trend of the surrounding NCs and having an average size of 33 nm. In the darker areas, the population of NCs looks blurred, suggesting a mixture of NCs with different sizes.

In general, in all cases there are some particles with average size larger than that of the pristine NCs. For the large particles stochastically spreading among the NCs or on the top of the NCs, the phenomenon may be attributed to a comprehensive effect of removal of the original labile ligands on the NCs after washing with EA and the respective solvents. It is interesting to observe that samples from S2 (hexane), S3 (cyclohexane) and S5 (octane) show different distribution patterns, suggesting that different solvents can have an impact on the distribution of the LHP NCs on substrates even if they have similar polarities.

Figure 3.15 presents SEM images of NC films on glass substrates spin coated from NCs dissolved in different solvents.

In cases S1 (DE), S3 (cyclohexane) and S6 (dichlorobenzene/chloroform), apart from a few bumps or uneven areas, the film at the current resolution look homogeneous and smooth. In contrast, in cases S2 (hexane), S4 (toluene) and S5 (octane) there are large particles distributing throughout the films, making the surface apparently rougher.

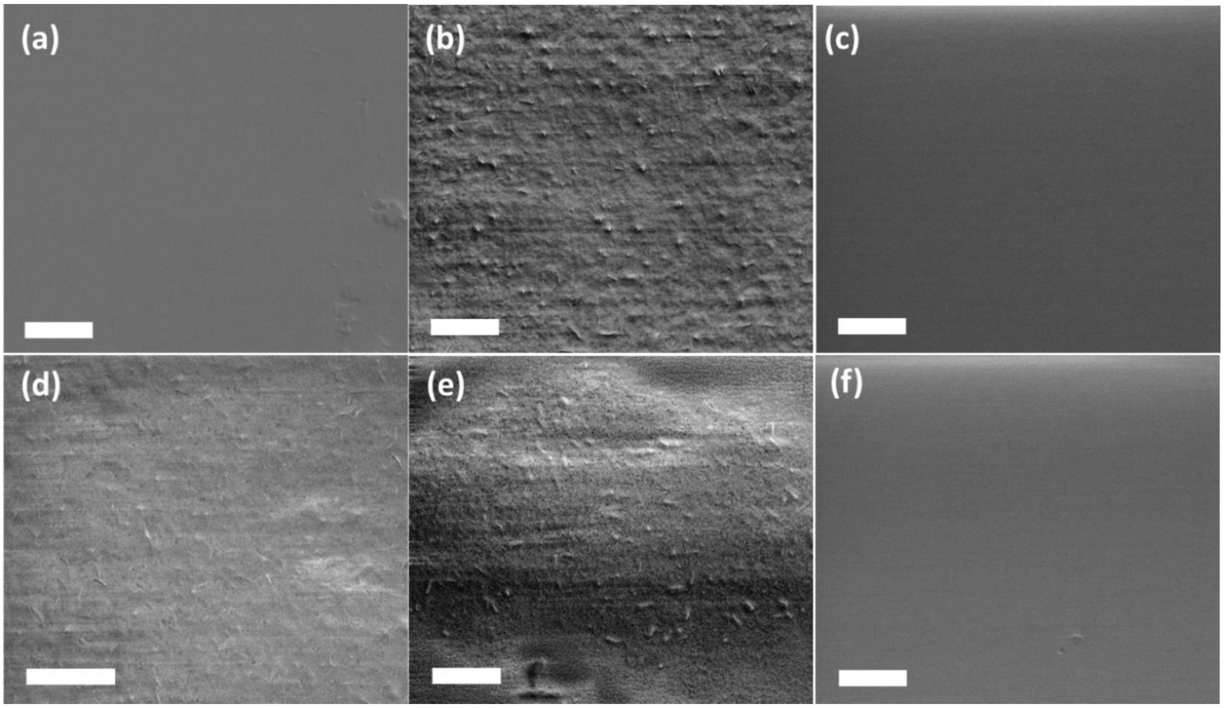

Figure 3.15. SEM images of LHP NC films spin coated from LHP NCs dispersed in the series of solvents (a) DE (S1), (b) Hex (S2), (c) cyclohexane (S3), (d) toluene (S4), (e) octane (S5) and (f) dichlorobenzene/chloroform (S6). The scale bars are 10 μm.

The NC films on glass were further characterized by confocal fluorescence microscopy.

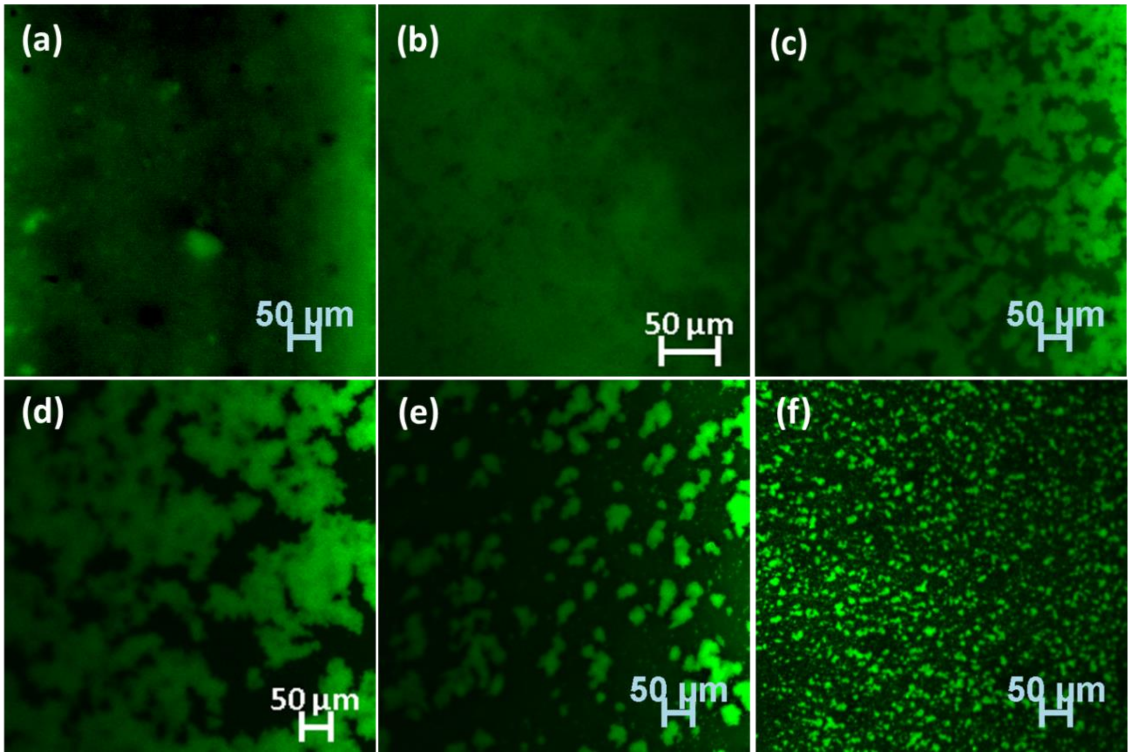

Figure 3.16. Confocal PL mapping images of LHP NC films spin coated from LHP NCs dispersed in the series of solvents (a) DE, (b) hexane, (c) cyclohexane, (d) toluene, (e) octane and (f) dichlorobenzene/chloroform.

From Figure 3.16, it is obvious that NC films deposited from NC solutions in different solvents show different distributions over the glass substrates. When prepared from DE (S1), the NC film appeared relatively compact in spite of some pin-holes. In practice, the film looks like being enwrapped in a thick polymer matrix, which is reflected in the 3D image collected by the confocal fluorescence microscopy (Figure 3.17a). Such an apparently large film thickness was unexpected, when considering that DE has the highest volatility among all solvents, due to the highest vapor pressure at RT. This suggests strong interaction between DE molecules and LHP NCs.

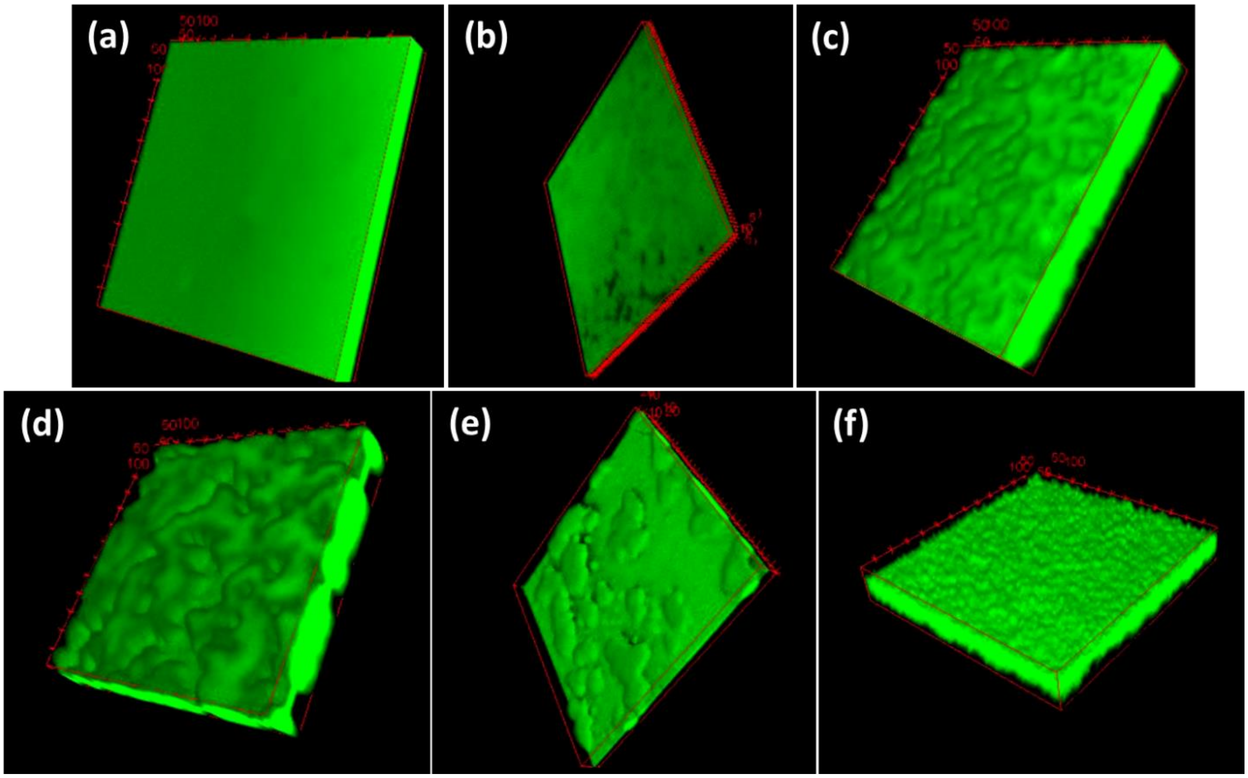

Figure 3.17. Clips of confocal PL 3D scanning images of CPB NC films spin coated from CPB NCs dispersed in the series of solvents (a) diethyl ether, (b) hexane, (c) cyclohexane, (d) toluene, (e) octane and (f) dichlorobenzene/chloroform.

When prepared from hexane (S2), the NCs film looks compact and smooth (Figure 3.16b). When prepared from cyclohexane (S3), the NCs film shows a gully pattern with black areas forming a network among the green areas (Figure 3.16c), suggesting high roughness of the film. The black parts are not necessarily uncovered by NCs. The contrast of black and green areas may be caused by defocus at the black areas due to high roughness of the film, which could be confirmed by the 3D image (Figure 3.17c).

When prepared from toluene (S4), the NCs film also presents a gully pattern, but the distribution of the black and green areas (Figure 3.16d) are more concentrated than those for cyclohexane case (S3). According to the 3D image (Figure 3.17d), the black districts in case of toluene (S4) are seldom covered by NCs and the film has higher roughness than that of the cyclohexane case (S3).

When prepared from octane (S5), a few green islands with an average size of 40 µm distribute sparsely across the darker background (Figure 3.16e). This is in line with the corresponding 3D image (Figure 3.17e), in which the film contains a few bumped islands. It is clear that there are still NCs spreading over the darker area, suggesting that the film is uneven and unsmooth.

Finally, when prepared from dichlorobenzene/chloroform (S6), bright green dots spread homogeneously throughout the NCs film (Figure 3.16f). In general, it seems that the larger are the green islands, the rougher is the film. The green islands may be formed by aggregation of the NCs after evaporation of the solvents. The varying sizes of the green islands may be related to interaction between the NCs and the solvents, e.g., interface energies. Obviously, the solvent of NCs does matter for the NC distribution on glass substrates, and therefore, the formation as well as the morphology of the NC film.

In order to gain better understanding of the effect of the different solvents on the optical properties of the NCs films, light absorption, PL and PL decay lifetime of the NC films were characterized.

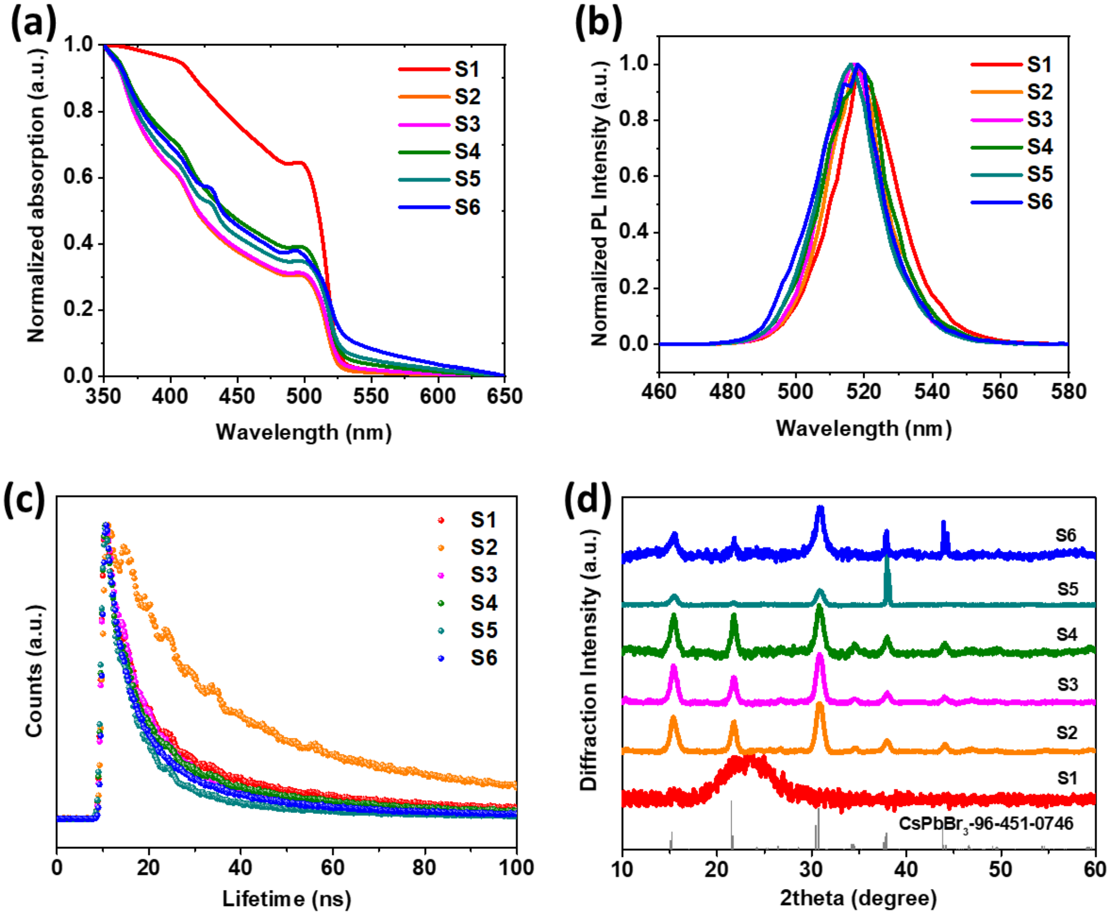

Figure 3.18. (a) Light absorption spectra; (b) PL spectra; (c) Decay lifetime plots; and (d) XRD patterns of LHP NC films spin coated from LHP NCs dispersed in the series of solvents.

Figure 3.18a presents the effect of solvents on light absorption of NC films. It is obvious that light absorption intensities of the NC films present a wide distribution. Interestingly, the light absorption intensities show a sequential decline from S1 (DE) to S6 (dichlorobenzene/chloroform). Since all the other deposition parameters such as NCs concentration and spin-coating procedure were the same, the difference in light absorption intensities may be attributed to the difference in solvent vapor pressure, which may lead to formation of NC films with different thicknesses. In other words, the lower the vapor pressure of the solvent (or the lower its boiling point), the thinner the NCs film. This result gives guidance to determination of the optimal spin-coating parameters. For instance, when the solvent of NCs is changed from hexane (S2) to octane (S5), lower spin-coating rate or higher NC concentration should be used, in order to get NC films with similar thicknesses. In addition, different solvents may also affect the wettability between the NC solutions and the substrates during film formation, contributing to the various thicknesses of the films.

In addition, films from DE (S1) show steeper absorption edge than the others, suggesting a lower level of defects in the film [191], which can be due to its large thickness. In contrast, films from dichlorobenzene/chloroform (S6) display the flattest absorption slope, suggesting a higher level of defects in the film, associated with the thinner film and with the higher polarity of chloroform.

Figure 3.18b shows the PL intensities of the NC films. These follow the same trend as the light absorption intensities, except for DE (S1). The PL of films from DE is lower than expected, which may be attributed to strong self-absorption, consistent with the apparently thick film as seen by the naked eye.

There is also some difference in PL peaks of the NC films. Taking the film from toluene (S4) as a reference sample, the film from DE shows a little red-shifted PL, while those from octane (S5) and dicholorobenzene/chloroform (S6) show a little blue-shifted PL. Here, the red-shift in the case of DE (S1) confirms the effect of self-absorption of the NC film. [192] The blue-shift in case of dicholorobenzene/chloroform (S6) may be due to reaction between the NCs and the solvent, since the chlorine in this solvent may partially replace the original bromine on the surface of the NCs [187].

Table 3.5. Fitting results of decay lifetime plots and PL spectra of films based on NCs dispersed in various solvents.

	Diethyl ether (S1)	**Hexane (S2)**	**Cyclohexane (S3)**	**Toluene (S4)**	**Octane (S5)**	**Dichlorobenzene Chloroform (S6)**
τ_1 (ns)	6.35	17.75	7.33	5.55	5.26	4.87
τ_2 (ns)	44.41	82.78	40.38	36.69	27.58	28.42
τ_{ave} (ns)	29.68	60.50	22.57	23.95	14.61	17.76
τ_1 ratio (ns)	81.5%	70.8%	86.6%	82.1%	87.9%	82.8%
τ_2 ratio (ns)	18.5%	29.2%	13.4%	17.9%	12.1%	17.2%
PL peak (nm)	520.4	517.7	516.3	517.5	515.4	515.6
PL FWHM (nm)	23.5	21.3	20.7	23.4	21.7	24.3

Figure 3.18c displays decay lifetimes of the NC films. The film from hexane (S2) presents the longest average decay lifetime, 61 ns (Table 3.5). This indicates that a compact and smooth film is beneficial for optical performance of the LHP NC film. The decay lifetimes of the other NC films appear to be similar. The average decay lifetime of film from DE (S1) is 30 ns, much lower than that of sample S2. Considering high absorption intensity of S1, the shorter decay lifetime of S1 may suggest that DE introduces more defects than hexane into the NCs. The film from octane (S5) displays the shortest average decay lifetime, 15 ns. In general, the dispersing solvent of the LHP NCs has a significant effect on the optical performance of the NC films.

In order to see whether the solvent has influence on the phase of the NCs and orientation of the NCs films on glass, XRD patterns of the NC films were collected. As shown in Figure 3.18d, all NCs films except that one from DE (S1) show similar XRD peaks, matching well with $CsPbBr_3$ with a code of 96-451-0746. Film S1 shows a wide peak ~ 22°. This may account for the polymer texture of the film. Films S2, S3 and S4 (from hexane, cyclohexane and toluene, respectively) present peaks with almost the same relative intensities. Film S5 (from octane) shows a strong diffraction near 37°, which could be attributed to diffraction from (240), (042), (321) and/or (123) planes. Film S6 (from dichlorobenzene/chloroform) shows relatively higher peaks near 30°, attributed to (040) and (202) planes, and near 44°, attributed to (242), (400) and (004) planes. The diffraction peaks of film S6 are a little broadened relative to the diffraction peaks of the other cases, although there is no peak shift in this case. In general, the solvent does not have obvious effect on the phase of the NCs, but some solvents could lead to preferred orientation with respect to film formation.

The images of the aged NCs solutions and films are displayed in Figure 3.19. Clearly, the aged NC solution of film S4 (from toluene) looks brown, while the other NC solutions still look yellow/green. The aged films show weakening colors from S1 to S6, and the aged film S6 (from dichlorobenzene/chloroform) is non-luminescent.

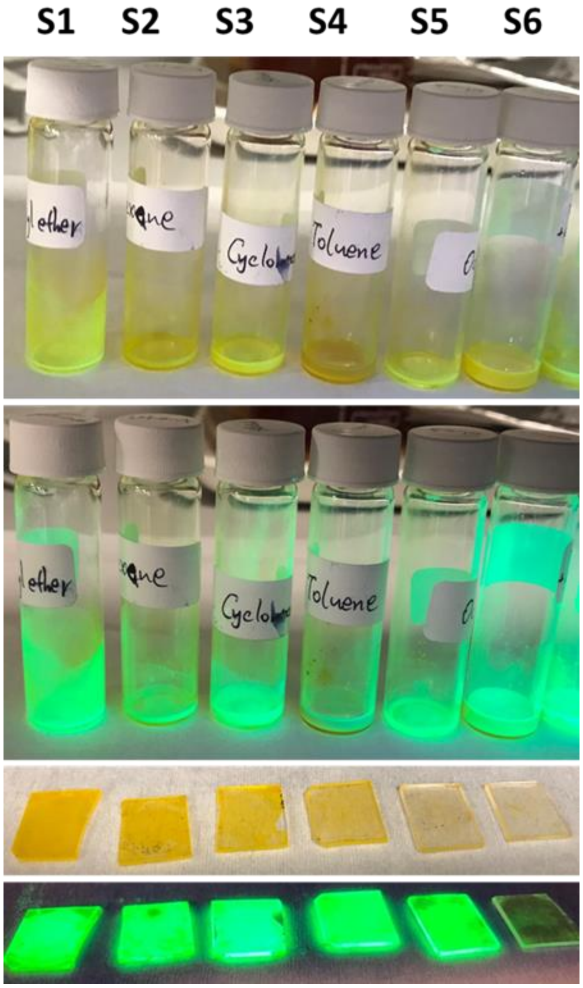

Figure 3.19. Photos of aged NC solutions in various solvents and corresponding spin-coated NC films without and with UV exposure.

Through comparison and combination of different characterization results, it appears that hexane is more favorable solvent to form a compact and smooth NC film with better optical performance on glass substrate than the other solvents in the current case. However, the optimal solvent for dispersing NCs may vary for different NCs and substrates. The difference in the NCs films spin-coated from NCs solutions dissolved in different dispersing solvents, may be attributed to difference in interaction between solvents and substrates [193], interaction between solvents and ligands on LHP NCs [77], and interaction between solvents and LHP NCs [36].

3.6 Alternative way to improve optical performance

Mixture of 2D and 3D LHP or quasi-2D LHP have been widely reported to be beneficial for achieving LHP materials with high PL QY and high efficiency in optoelectronic devices [123, 133, 194]. PEABr is one of the most used additive to synthesize quasi-2D perovskite [124, 132, 134, 183, 195]. In this section, PEA is used to treat the pristine NCs solution together with EA or in combination with BBr and/or SCN solution. The optical properties and crystal structure of the NCs films based on the treated NCs solutions are characterized as shown in Figure 3.20. The images of the NCs solutions under UV light illumination are shown in the inset of the Figure 3.20d (the color of the arrows have the same meaning as the legend in Figure 3.20a).

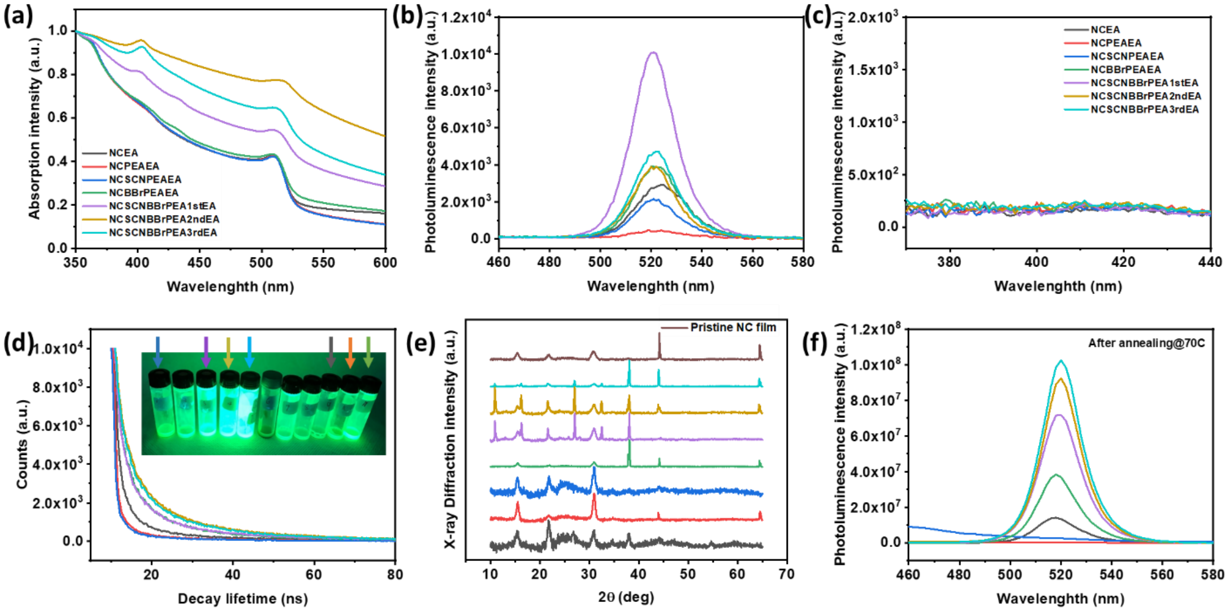

Figure 3.20. Characterization results of films based on PEA-treated NCs. (a) UV-vis absorption spectra; (b) PL spectra; (c) decay lifetime; (e) X-ray diffraction plots of the films based on PEA-treated NCs; and (f) PL spectra of annealed films based on PEA-treated NCs.

From Figure 3.20a, with increase of washing times by EA, the absorption peaks near 500 nm suffer a weak red-shift and new absorption peaks arise ~ 400 nm for films based on NCs solutions treated with SCNBBrPEAEA. These peaks together with new XRD peaks in Figure 3.20e may be attributed to 2D perovskite emerging in the cases of SCNBBrPEAEA. However, the newly introduced 2D phases do not introduce new emissions according to Figure 3.20c. This is tentatively explained by the tunneling effect in quasi-2D perovskite, in which the 2D phases with larger bandgaps transport carriers to 3D phase with relatively smaller bandgap, and light is then emitted from the 3D phase [124, 194].

From Figure 3.20b, we can see that film based on NCs solution treated only with PEAEA has the lowest PL intensity and PL QY (Table 3.6), suggesting that pure PEA caused damage to the NCs. In contrast, the film based on NCs solution treated with SCNBBrPEAEA exhibits the highest PL intensity, suggesting that SCNBBr plays an important role together with PEA. Through comparison, we propose that BBr may react with PEA to form PEABr, which usually facilitates formation of 2D perovskite phase and enhances the PL performance of the NC solution [20, 183], while SCN may play the same role of stabilizing the NCs during treatment as in the case of SCNBBr-treated NCs. The difference in the trend of PL QY (Table 3.6) may be due to different data collection areas on the film and the film being inhomogeneous. From Figure 3.20d and Table 3.6, we can see that films based on NCs solutions treated with EA and SCNPEAEA show relatively shorter average decay lifetime, while NCs solutions treated with SCNBBrPEAEA appear to be favorable thanks to the longer decay lifetime.

The poorer optical performance of the films based on NCs solutions treated with EA, PEAEA and SCNPEAEA (Figure 3.20a-d) are in accord with the XRD profiles (Figure 3.20e), which look noisy, suggesting that the NCs may be damaged during the treatment. Both Figure 3.20b and d show that films based on NCs solutions treated with SCNBBrPEAEA have higher PL QY, suggesting less defects. In addition, films based on so-treated NCs appear to have higher stability than the rest, according to the decay lifetime after ageing (Table 3.6) and the PL intensities after annealing (Figure 3.20f).

Table 3.6. Statistics of the optical performance of films based on PEA-treated NC solutions.

	NCEA	**NCPEA**	**NCSCNPEA**	**NCPEABBr**	**NCSCNPEA BBrEA**	**NCSCNPEA BBr2ndEA**	**NCSCNPEA BBr3rdEA**
τ_{ave}	1.57	3.96	10.34	10.34	10.35	12.60	12.22
PLQY (%)	5.7	1.1	3.3	11.0	17.1	26.9	18.7

In spite of the improved optical performance after addition of PEA, the conductivity of the films is poor when they are applied into LED fabrication, even after the NCs solutions are further washed twice and three-times with EA, as shown in Figure 3.21. Therefore, we did not carry out further work with PEA.

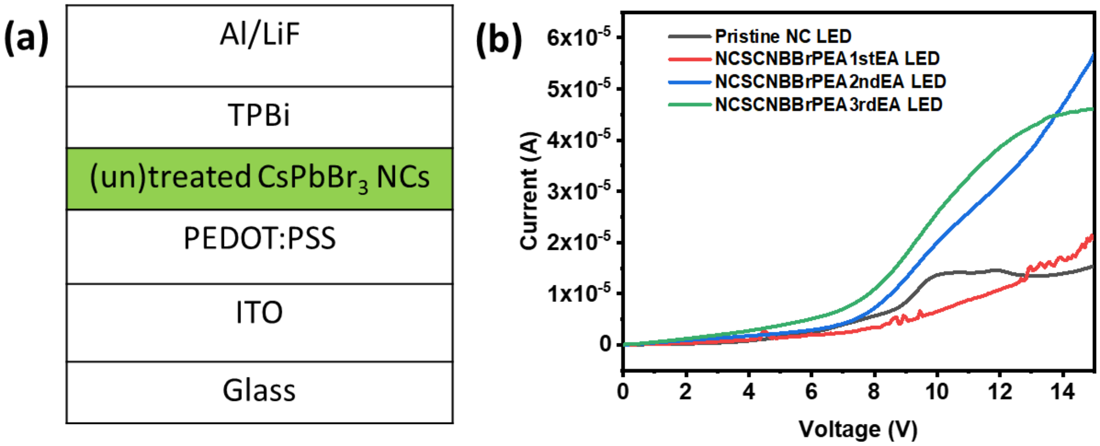

Figure 3.21. (a) LED structure used in the fabrication; (b) Current of LEDs based on SCNBBrPEAEA-treated NCs as a function of voltage.

3.7 Summary

In this chapter, we reported about addressing four issues of LHP NCs for fabrication of optoelectronic devices owing to existence of long-chain and insulating organic ligands. Firstly, various chemicals were tried to treat the LHP NCs in film or in solution. Using a combination of BBr, SCN solution and EA to treat the LHP NCs in solution, the conductivity of the LHP NCs in films was improved. Secondly, the optical properties of the films based on the treated NC solution was improved according to the increased PL QY. Thirdly, various solvents were tried to disperse the treated NCs and morphology of the films based on these NC solutions were characterized. It was found that a compact and smooth LHP NC film could be obtained by spin-coating treated LHP NCs dispersed in hexane. In the meanwhile, we showed that films based on the treated NCs exhibited high stability both in optical performance and film morphology. To be specific, the treated NC films present rather stable optical performance including stable PL emission and PL decay lifetime, and stable NC size between the fresh and the aged films. In contrast, the untreated films used as a control show fast growth in size and degradation of the optical performances during aging. The good stability of the SCNBBr films is attributed to the synergetic effect of SCN and BBr in enhancing the structural stability of NCs during the treatment in solution as well as during the aging of the films. Formation of mixtures of $CsPbBr_3$, Cs_4PbBr_6 and $CsPb_2Br_5$ phases was shown to play a role in stabilizing the SCNBBr films.

Apart from works based on the above treatment, PEA was also tried to improve the optical performance of the NC solution and the corresponding films. A combination of PEA and the SCN solution was proved to be beneficial for higher brightness or PLQY and longer carrier lifetime. In short, the works based on NC films paved roads and expanded the capabilities for realizing applications of pristine LHP NCs in optoelectronic devices.

Chapter 4: Lead bromide perovskite nanocrystal-based green LEDs

In this chapter, green LEDs based on LHP NCs treated with different methods are presented. The methods of NCs treatment include purification with EA containing SCN, SCN accompanied with BBr, potassium compounds, and variation of solvents. In particular, we report for the first time green LED based on $CsPbBr_3$ NCs treated with ammonium thiocyanate solution before purification with polar solvent. The champion device fabricated based on the treated $CsPbBr_3$ NCs showed high efficiency and high stability during operation as well as during storage. A study on morphology and current distribution of NC films under applied voltages was carried out by conductive atomic force microscopy, giving a hint on efficiency roll-off. The current work provides a facile way to treat sensitive perovskite NCs and to fabricate perovskite NC-based LED with high stability. Moreover, the results shed new light on the relation between film morphology and device performance and on the possible mechanism of efficiency roll-off in NC LED.

4.1 Green LED based on perovskite nanocrystals treated with thiocyanate and benzoyl bromide

The results reported in Chapter 3 encouraged us to applied the SCNBBr-treated $CsPbBr_3$ NCs into LED fabrication, and compare the LEDs figures-of-merit with those obtained in devices based on the untreated NCs. Figure 4.1 presents the characterization results of LEDs based on the pristine NCs synthesized by HI and the treated NCs. The layers composing the LED, as shown in Figure 4.1g, follows the common basic LED structure: ITO/PEDOT:PSS/LHP/TPBi/LiF/Al [23, 25, 35, 67, 118, 177, 196].

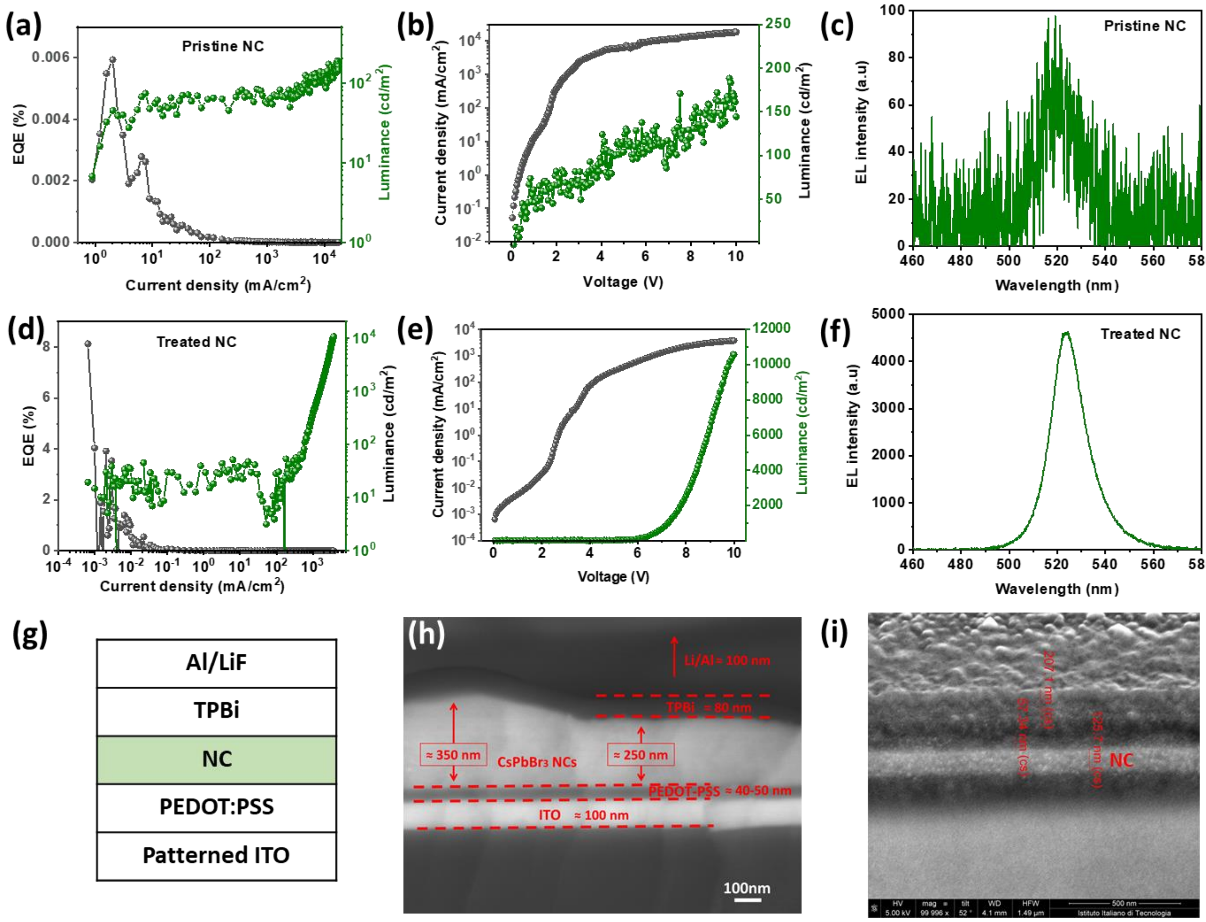

Figure 4.1. (a) EQE and luminance as a function of current density; (b) Current density as a function of driving voltage; (c) EL spectra of LED based on pristine $CsPbBr_3$ NCs; (d) EQE and luminance as a function of current density; (e) Current density as a function of driving voltage; (f) EL spectra of LED based on treated $CsPbBr_3$ NCs; (g) Representative diagram of LED structure; SEM cross sections of (h) LED based on pristine NCs and (i) LED based on treated NCs.

From Figure 4.1a, we can see that the highest EQE based on the pristine NCs is ~ 0.006% with a luminance of 44.9 cd/m^2 at a current density of 2.03 mA/cm^2, which corresponds to 0.5 V (Figure 4.1b). Together with the rapid growth of current density as the voltage increases at the beginning in Figure 4.1b, such a low turn-on voltage suggests serious leakage in the LED. In spite of the thick NC layer ~300 nm (Figure 4.1h), the NC film look rather rough from the side view, suggesting uneven distribution of the NCs, which may cause current leakage and is in line with our previous morphological characterization results on the pristine NC film presented in Chapter 3. The highest luminance of the LED is merely 171.8 cd/m^2 and is achieved at 9.15 V with a high current density of ~ 16 A/cm^2.

Figure 4.1d reports EQE and luminance as a function of the applied bias for the LED based on the treated NCs. Here, the highest EQE reaches 8.135% with a luminance of 19.5 cd/m^2 at a current density of $6 \cdot 10^{-4}$ mA/cm^2, which corresponds to 0.05 V (Figure 4.1e). In spite of the low turn-on voltage, there is less serious current leakage than the LED based on the pristine NCs, as visible in the step occurring at the beginning of the IV plot in Figure 4.1e. However, the EQE drops sharply with increasing current density and applied bias. With further increase of current density higher than 100 mA/cm^2, the luminance starts to surge up and reaches the maximum of 10573 cd/m^2 at 10 V. Given that the $CsPbBr_3$ NC layer is the only emissive material at ~ 520 nm in this case, the luminance could be fully attributed to the NCs.

Furthermore, the EL spectra of the LEDs show a stark contrast in the two cases (Figure 4.1c and f). Obviously the LED based on the treated NCs exhibits smoother EL profile and higher EL intensity. The better performance of the LED based on the treated NCs may be attributed to the synergetic enhancement of the optical property of the NCs, reflected by the rather high luminance at high voltage, and the more compact film based on the treated NCs according to the section 3.5 of this thesis and Figure 4.1i, which shows a smoother and even NC film with a thickness of ~120 nm.

In order to improve the performances of the devices, we aimed to achieve a better band alignment by inserting PVK, whose valence band level is nearer to that of perovskite than PEDOT:PSS [73, 77]. PVK was spin-coated onto the PEDOT:PSS before spin-coating the $CsPbBr_3$ NCs (Figure 4.2d). However, the PVK layer made the LED even less efficient than the one without PVK. The highest EQE achieved is 0.33% with a luminance of 2.44 cd/m^2 at a current density of 0.002 mA/cm^2 (Figure 4.2a), which corresponds to 0.05 V (Figure 4.2b). The highest luminance is 1683.5 cd/m^2 at 10 V, which is lower than that of the LED without PVK layer.

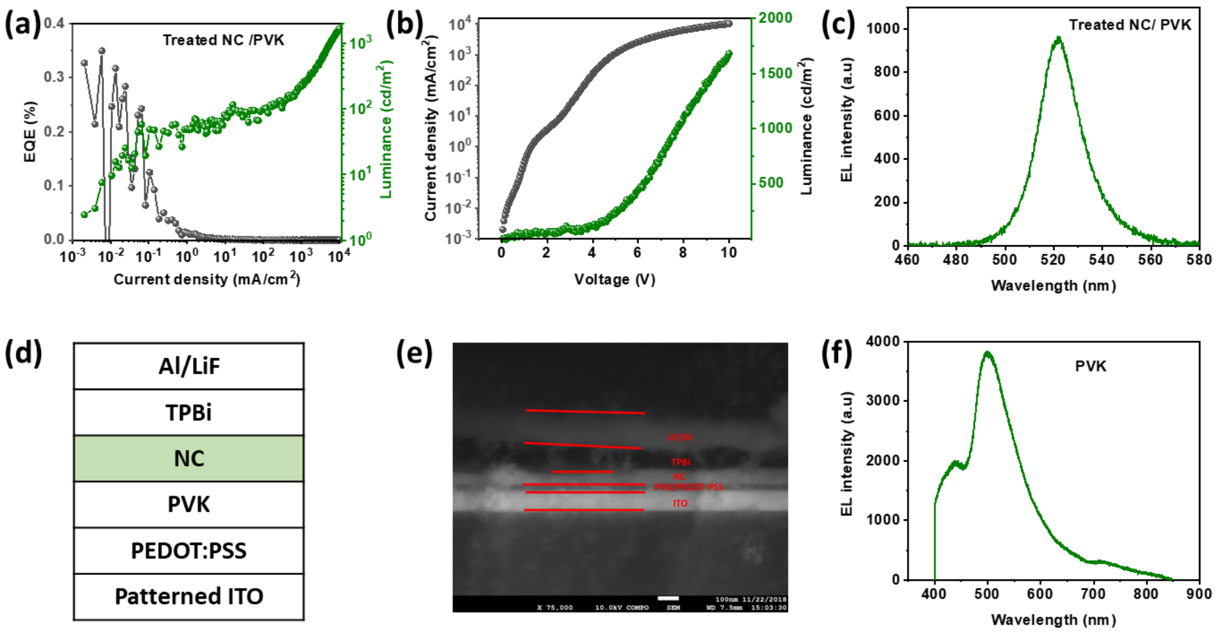

Figure 4.2. (a) EQE and luminance as a function of current density; (b) Current density as a function of driving voltage; (c) EL spectra of LED based on treated $CsPbBr_3$ NCs and with insertion of PVK layer under the NC layer; (g) diagram of the LED structure; (e) SEM cross sections of the LED; and (f) EL spectra of LED with PVK as emissive layer and without a NC layer.

This result cannot find straightforward interpretation. On one side, current leakage seems to be high according to Figure 4.2b. On the other side, there is no emission peak from PVK (Figure 4.2f) in the EL spectra (Figure 4.2c), which suggests negligible leakage. Moreover, the SEM cross section in Figure 4.2e also shows a relatively even film from the side view.

TPBi is deposited onto the NC layer by thermal evaporation, which takes more time than wet-chemical deposition and requires higher purity of TPBi. Therefore, we also fabricated LEDs (Figure 4.3) with TPBi being deposited onto the NCs by spinning coating a 1g/L TPBi:EA solution, which was expected to dissolve TPBi at a minimum cost of damaging the NC layer. However, both the optical property of the NCs and the integrity of the NC film were seriously damaged, such that the highest luminance of the LED was only 170.02 cd/m^2 at a current density of 2208 mA/cm^2 and a bias of 9.9 V (Figure 4.3a-b). The collected EL signal also looked weak (Figure 4.3c). Thus, for all devices fabricated later on, we adopted thermal evaporation to deposit the TPBi layer.

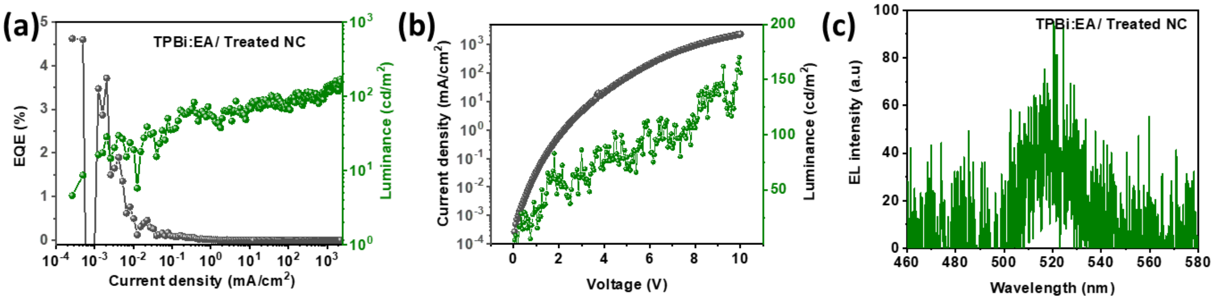

Figure 4.3. (a) EQE and luminance as a function of current density; (b) Current density as a function of driving voltage; (c) EL spectra of LED based on treated CsPbBr$_3$ NCs and with TPBi being deposited by wet-chemical method.

In summary, LEDs based on our treated NCs exhibit higher efficiency and brightness than those based on pristine untreated NCs. This indicates that our treatment method with SCN solution and BBr may be a promising route to apply perovskite NCs into optoelectronic devices. However, optimization of the LED structure with PVK appears still to be unsatisfactory. Wet-chemical deposition of TPBi proves to be unsuitable for achieving high-efficient perovskite NC LED.

4.2 Green LED based on perovskite nanocrystals treated with thiocyanate

Although introduction of BBr in the treatment of CsPbBr$_3$ NC solution is beneficial for the optical performance and stability of CsPbBr$_3$ NCs-based film, as shown in Chapter 3, the formation of other perovskite phases leads to rougher film, which can easily cause current leakage and is unfavorable for LED performance. Thus, we tried to treat the CsPbBr$_3$ NC solution with merely SCN solution and obtained stable green LEDs based on the as-treated NCs.

4.2.1 CsPbBr$_3$ NCs used for the device fabrication

CsPbBr$_3$ NC solution synthesized according to the previous report [21] was treated in such a way that 300 μL as-prepared CsPbBr$_3$ NC solution was firstly added into a vial. Secondly, 10, 30 or 50 μL SCN solution was dropped into the vial. Thirdly, 900 μL EA was gradually added into the solution, and the obtained solution was left under hood for 5 min. Then, the treated CsPbBr$_3$ NC solution was centrifuged at 6000 rpm for 10 min. The supernatant was discarded, and the precipitate was re-dispersed in 300 μL hexane for film and device fabrication. The obtained NC solutions and corresponding LEDs were labeled as 10SCN, 30SCN and 50SCN.

TEM images of respective NC solutions are shown in Figure 4.4a-h together with distribution of NC sizes. Average sizes of the NCs are in the 10-12 nm range. XRD patterns (Figure 4.4i) show that the phases of the treated NCs are well-retained and can be assigned to $CsPbBr_3$. In the case of 10SCN, the XRD diffraction peaks look noisy, which suggests poor crystallinity of the NCs treated with 10SCN. This could be explained by the lack of enough protection on the $CsPbBr_3$ NCs due to insufficient SCN solution when EA are used to purify the NC solution. The sulfur element contained in SCN was, however, not detectable [197] by HAADF-EDS in 30SCN NCs (Figure 4.4j-l). This may be due to either the sulfur content being below detection threshold or to its probable overlap with the signal of lead.

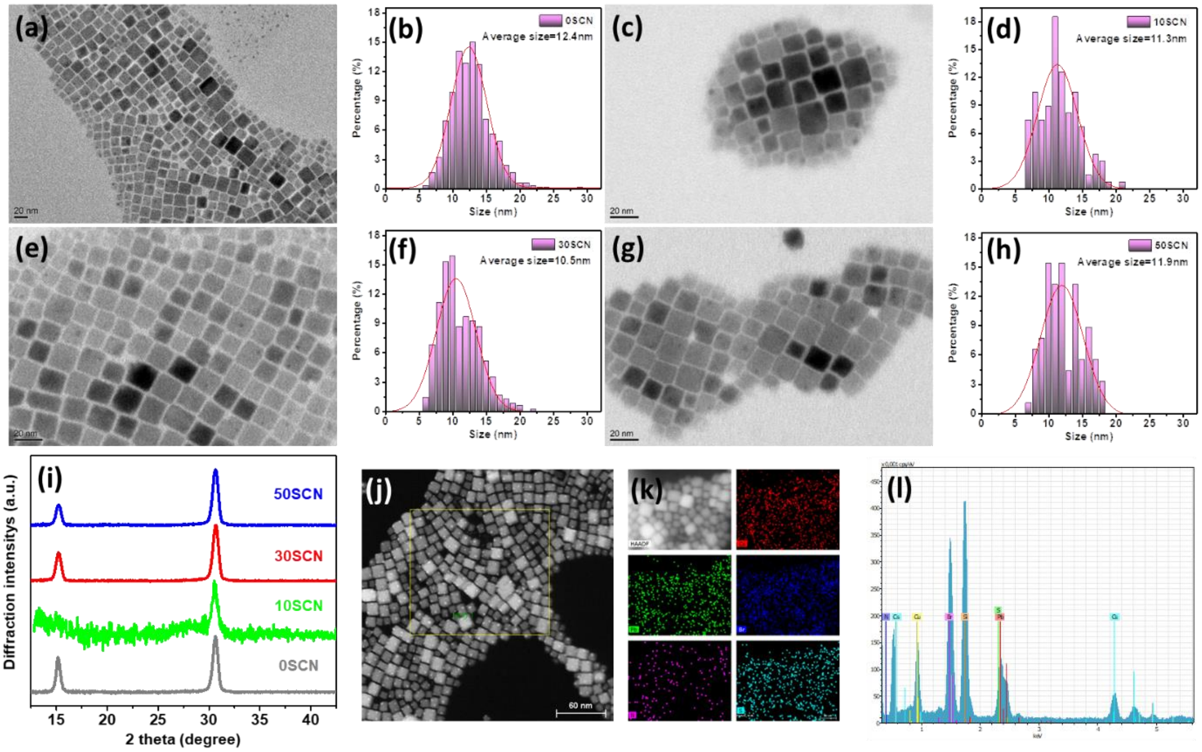

Figure 4.4. Characterization of treated and untreated $CsPbBr_3$ NCs. TEM images and size distributions of NCs in (a-b) 0SCN, (c-d) 10SCN, (e-f) 30SCN, and (g-k) 50SCN NC solutions; (i) XRD patterns of the NCs; (j) HAADF image, (k) Element mapping images, and (l) EDS element analysis spectra of 30SCN NCs.

4.2.2 Performance of fresh LED

With the treated $CsPbBr_3$ NCs used as emissive material, we fabricated and characterized corresponding LEDs. Figure 4.5a presents the LED structure used in this work, ITO/PEDOT:PSS/poly-TPD/$CsPbBr_3$ NC/TPBi/LiF/Al. The SEM cross-section of a 30SCN device is shown in Figure 4.5b. The thickness of the NC layer is ~ 30 nm. Figure 4.5d displays variation of current density with increasing voltage for the three devices. 50SCN presents higher leakage than 10SCN and 30SCN, suggesting higher conductivity of 50SCN NC film due to less organic than in the 10SCN and 30SCN NC films. At voltage higher than 7 V, 30SCN shows higher current density than 10SCN and 50SCN. In the current density plot of 30SCN, there is a turning point ~ 4.3 V, indicating variation of growth rate of the current density with increasing voltage.

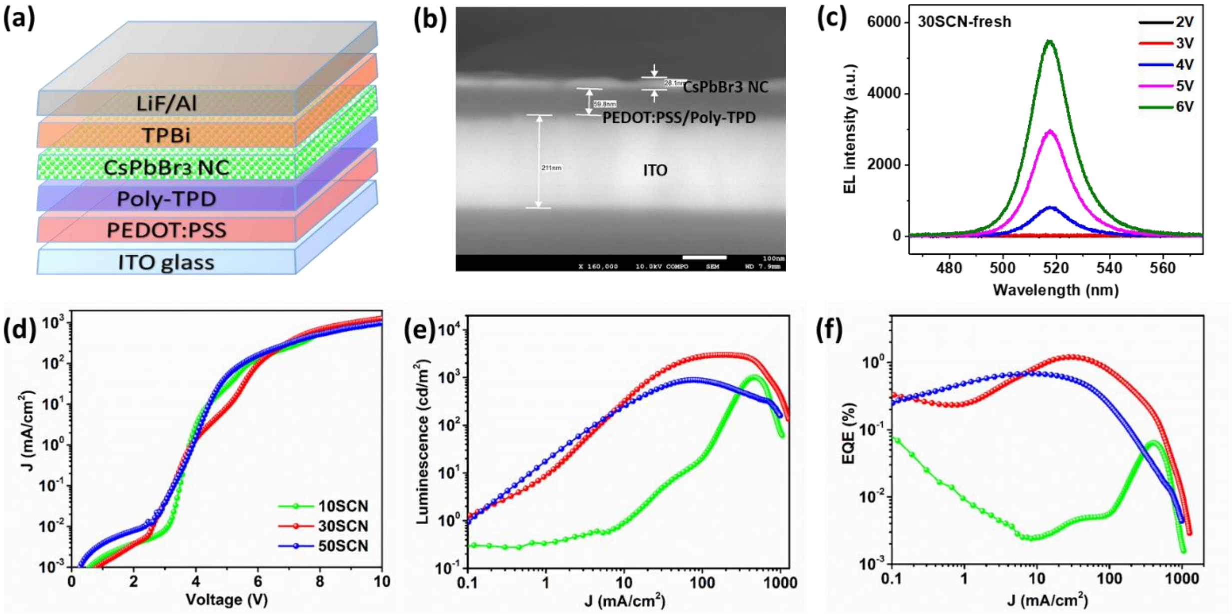

Figure 4.5. Characterization of LED performance. (a) Diagram of the LED structure; (b) SEM cross-section of 30SCN device, from bottom to top, the layers include ITO /PEDOT:PSS + poly-TPD (~ 60 nm) /$CsPbBr_3$ NC (~ 30 nm) /TPBi (~ 45nm); (c) EL spectra of fresh 30SCN LED; (d) Current density as a function of driving voltage; (c) Luminescence and (d) EQE as a function of current density in the NC LEDs [40].

Figure 4.5e displays variation of luminance with increasing current density. It is clear that 30SCN shows higher luminance than 10SCN and 50SCN across the whole range of the current density, and reaches the highest level of 2986 cd/m^2 at 187 mA/cm^2. The EL spectra of a running 30SCN LED is presented in Figure 4.5c. 10SCN reaches its highest luminance of 1018 cd/m^2 at 461 mA/cm^2, and 50SCN reaches its highest luminance of 890 cd/m^2 at 80 mA/cm^2 (Figure 4.5e and Table 4.1). 10SCN has the highest turn-on voltage at 4.4 V with luminance at 1 cd/m^2, while turn-on voltages of 30SCN and 50SCN are at 3.2 V and 3.3 V, respectively, indicating less insulating organic ligands in the $CsPbBr_3$ NC film with increasing SCN additive during treatment. Although 30SCN shows a relatively slower decrease of luminance when the current density is less than 300 mA/cm^2, all the three devices present luminance roll-off after reaching the respective highest luminance.

Table 4.1. Statistics of fresh and 23-day aged LEDs based on NCs treated with different amount of SCN solution.

Sample	Type	EQE	Current efficiency (cd/A)	Luminance (cd/m^2)
10SCN	fresh	0.06%	0.23	1018
	aged	0.52%	1.91	1347
30SCN	fresh	1.20%	4.42	2986
	aged	1.91%	7.04	899
50SCN	fresh	0.68%	2.51	890
	aged	0.95%	3.51	748

Figure 4.5f displays variation of EQE with increasing current density. 30SCN presents the highest EQE of 1.2% at 32 mA/cm^2 or 5.5 V, and the highest current efficiency of 4.42 cd/A among the three devices (Table 4.1). The luminance at the maximum EQE is 1404 cd/m^2, which is relatively high among the LEDs based on $CsPbBr_3$ NCs with organic transporting layers (Table 4.2). In contrast, 10SCN and 50SCN show maximal EQEs of 0.06% at 380 mA/cm^2 and 0.68% at 12 mA/cm^2, respectively. Despite that the profiles of EQE and current density (Figure 4.5f) show similar trend than those of luminance intensity and current (Figure 4.5e), efficiency roll-off is more pronounced, especially in 30SCN and 50SCN. Given that current densities corresponding to the highest luminance or EQE of each device are different, it could be inferred that Auger recombination is not necessarily the reason for the efficiency roll-off in current cases.

Table 4.2. Statistics of performances of green LHP LEDs.

Material	**L50**	**Max EQE(%)**	**Lum @Max EQE (cd/m^2)**	**Current density @Max EQE (mA/cm^2)**	**Voltage @Max EQE (V)**	**Turn-on voltage @ 1cd/m^2**	**Max Current efficiency (cd/A)**	**Max Lum (cd/m^2)**	**EL peak**	**EL FWHM**	**Source**
CsPbBr$_3$ NCs	27min @5V	1.2	1404	31.8	5.50	3.2	4.42	2986	518	19	**This work**
CsPbBr$_3$ QD		0.12	~100	~140	~7	6.5	0.43	946	516	23	[77]
CsPbBr$_3$ QD		0.33	~100	~20	~5	3.8		934	510	25	[32]
CsPbBr$_3$ QD		0.19	~200	~30	~4.3	2.6		2335	523	19	[116]
DDAB-OA-CsPbBr$_3$ QDs		3	~10	~0.05	4.50	3	<10	330	515	19	[73]
CsPbBr$_3$ QD	10min @5V	0.06	~100	~100	>5	3.5	0.19	1377	516	19	[98]
CsPbBr$_3$ -CsPb$_2$Br$_5$ Composites		2.21	~2200	~5	8.6	4.6	8.98	3853	527	24	[118]
DDAB-capped CsPbBr$_3$ QD		8.73	<30	~0.01	~2.8	2.6	~20	1660	512	17	[69]
CsPbBr$_3$ QD		6.27	~3000	<100	~8	3.4	13.3	15185	512	20	[65]
CsPbBr$_3$ QD		1.19	~2000	<100	~6	4.6	3.1	12090	515	18	[20]
CsPbBr$_3$ nanoplate		1.1	~100	~1	<5	3.5		590	520	17	[95]
CsPbBr$_3$ thin film		5.34	~300	~900	~5.2	2.5	19	36600	522	16	[198]
CsPbBr$_3$ QD	>600min	2.39					2.25	3809	522		[199]
DDAB-capped CsPbBr$_3$ QD	27min @3.5V	0.58	~355	~15	4.5	2.5	0.62	355	517		[56]
DDAB-capped CsPbBr$_3$ QD		8.08	1	~0.01	~3	3	25.1	<200	510	20	[70]
Zwitterionic-capped CsPbBr$_3$ NCs		2.5	1641	21.7	3.5	~2.5	7.5	24000	516	16	[36]
4-layered CsPbBr$_3$ NCs		1.3	~6	~0.2	6.50	~4.5	5.2	54	~520	20	[67]
PEABr-capped CsPbBr$_3$ NCs		4.33	~4000	~1000	4.50	2.66	13.43	12650	514		[74]
CsPbBr$_3$ NCs			~25				3.72	106	~518		[66]
CsPbBr$_3$ NCs		3.79	5863.5	~90	9.00	~2.8	7.96	6093.2	519	19	[200]
CsPbBr$_3$ NCs	>60 hrs @8V	4.63	~10000	~350	~10		8.736	10206	518.5		[117]
TOAB/DDAB/OTAc-capped CsxFA1-xPbBr3		11.6	~400	~1	~3.2	2.75	45.4	55800	515	18	[47, 79]
DDAB-capped ZnBr$_2$-treated Cs$_x$FA$_{1-x}$PbBr$_3$ NCs	136min @~2.8V	16.48	~400	~0.6		2.4	66.7	76940	518	18	[47]
OPA-capped CsPbBr$_3$ NCs	30min @~4V	6.5	~400	~2	~3.9	2.8	18.13	7085	516	19	[38]
crown ethers-shelled CsPbBr$_3$ NCs (single-layer)		1.27	~3500	~25	~4.2	2.5	4.29	14454	519		[22]
crown ethers-shelled CsPbBr$_3$ NCs (double-layer)	9.25min @~5V	2.64	~250	~1	~4	2.5	9.22	3880	519		[22]
CsPbBr$_3$ NCs	10.5min @10V	1.7	~1000	<0.1	>10		5.57	1562	522	16	[107]
CsPbBr$_3$ NCs		5.7	~12000	<1000	~6	2.3	19.9	46000	517	<20	[115]
CsPbBr$_3$ – CsPb$_2$Br$_5$ NCs	120min @5.5V	~0.6	~5000	~100	~5.2	2.5		8383	518	19	[168]
CsPbBr$_3$ |Cs$_4$PbBr$_6$ thin film	>420min	2.25		~250		2.9	~7.2	53486	519	23	[177]
CsPbBr$_3$ - Cs$_4$PbBr$_6$ NCs		1.21	~100		8.10			1941.6	515	16.3	[176]
CsPbBr$_3$ thin film	250 hrs @~3.8V	10.5	~10000	~20	~4.5	2.8	32	16436	518	19	[196]

4.2.3 Mechanism of efficiency roll-off in NC LED

Efficiency roll-off is ubiquitous in perovskite NCs-based LEDs [22, 37, 38, 65, 67, 69, 73, 96, 105, 196]. The term “efficiency roll-off” was defined as a description for the decrease of the efficiency of LED at high current density by previous researchers [201]. The origin of efficiency roll-off in perovskite LEDs is still an open question. Auger recombination, which leads to non-radiative process, has been reported to play a main role on this effect in a few reports via in-direct optical characterization methods [194, 202], and some solutions have been proposed correspondingly. For instance, core-shell structure was shown to be beneficial to increase threshold current of efficiency roll-off in QD LED [203]. In another work on 2D perovskite with funnel structure, the roll-off was reduced through increasing content ratio of low-bandgap perovskite [194], which concentrated the injected electrons/holes and played a major role in light emission. For 3D perovskite NCs, material degradation [25] and destruction of film morphology [196] at high current density were predicted to play critical roles in the roll-off. However, there has been no study on efficiency roll-off in NCs LED by direct characterization methods.

Here, we measured evolution of the films under voltage by C-AFM [109], in order to explain the performance difference of the 10SCN and 30SCN LEDs and give some hints on the mechanism of efficiency roll-off. Figure 6.1 shows topographical images and current mapping images of 10SCN and 30SCN under different applied voltages.

In the case of 10SCN, with increasing applied voltages during scanning, the selected scanning area becomes rougher and more aggregations of the $CsPbBr_3$ NCs form. Specifically, when the applied voltage increases from 3 V to 5 V, more areas without coverage of NCs emerge, with the root mean square roughness parameter rising up from 2.9 nm to 3.7 nm (Figure 4.6a, b). When the voltage further increases to 7 V, the uncovered areas become larger in area, in spite of the lesser number of domains (Figure 4.6*c*). The measured roughness apparently stays on the same level (~3.6 nm). Correspondingly, the current distribution follows the morphology evolution. At 3 V, the whole film is at a low current level and the average current is ~18 pA (Figure 4.6d). At 5 V, the overall current of the film increases according to the larger medium current (green yellow) and higher current (red) areas instead of lower current (blue white) areas (Figure 4.6e). The red areas of the current mapping image indicate higher current leakage than the other parts, and may represent absence of $CsPbBr_3$ NCs, in line with the morphology image. When 7 V is applied during scanning, the distribution of red and blue-white domains change (Figure 4.6f). The red domains become more concentrated and larger in size, while the rest of the scanning area mainly lies on the blue-white current levels. This suggests stronger leakage through the uncovered areas and less current flow through the NC areas, supplying evidence for low efficient radiative recombination of injected carriers. This may explain the low luminance and low EQE of 10SCN.

In the case of 30SCN, the overall roughness of the film is less than that of the 10SCN at different voltages (Figure 4.6g-i). With applied voltages increasing from 3 V to 7 V, the roughness of the 30SCN film increases monotonously from 2.2 nm to 3.1 nm (Figure 4.6m). A few large areas without coverage of NCs form (Figure 4.6l), especially at 7 V. The corresponding current images show a rather different appearance from that of 10SCN. At 3 V, the current image is mainly occupied by blue-white and green-yellow areas (Figure 4.6j). At 5 V, small red domains start to increase and green-yellow spots dominate the image (Figure 4.6k), suggesting efficient carrier injection into NCs. This is in accord with the optimal device performance near 5 V. At 7 V, most area of the image is blue-white with a few large red spots (Figure 4.6l), suggesting enhanced leakage at high voltage and lower radiative recombination efficiency at high current density. This is in line with the decreased average current from ~33 pA to ~18 pA (Figure 4.6n), while the maximum current increases from ~0.8 nA to ~1.8 nA when the voltage is increased from 5 V to 7 V (Figure 4.6o). The formation of large uncovered spots together with localized high current density at 7 V may explain the efficiency roll-off at voltage higher than 6 V in 30SCN LED. Thus, morphology deterioration of NC film with increasing applied voltage, which may lead to enhanced leakage, could be a reason for efficiency roll-off in LED at high current density [204], as predicted in a report [196] on $CsPbBr_3$ thin film-based LED. Furthermore, stable morphology of NC film or stable NC distribution in NC film is expected to be able to relieve efficiency roll-off. This could be supported by some reports [116, 201] on embedding perovskite in a matrix, in which the perovskite NCs or particles are fixed in the matrix and morphologies of the films are more stable during operation.

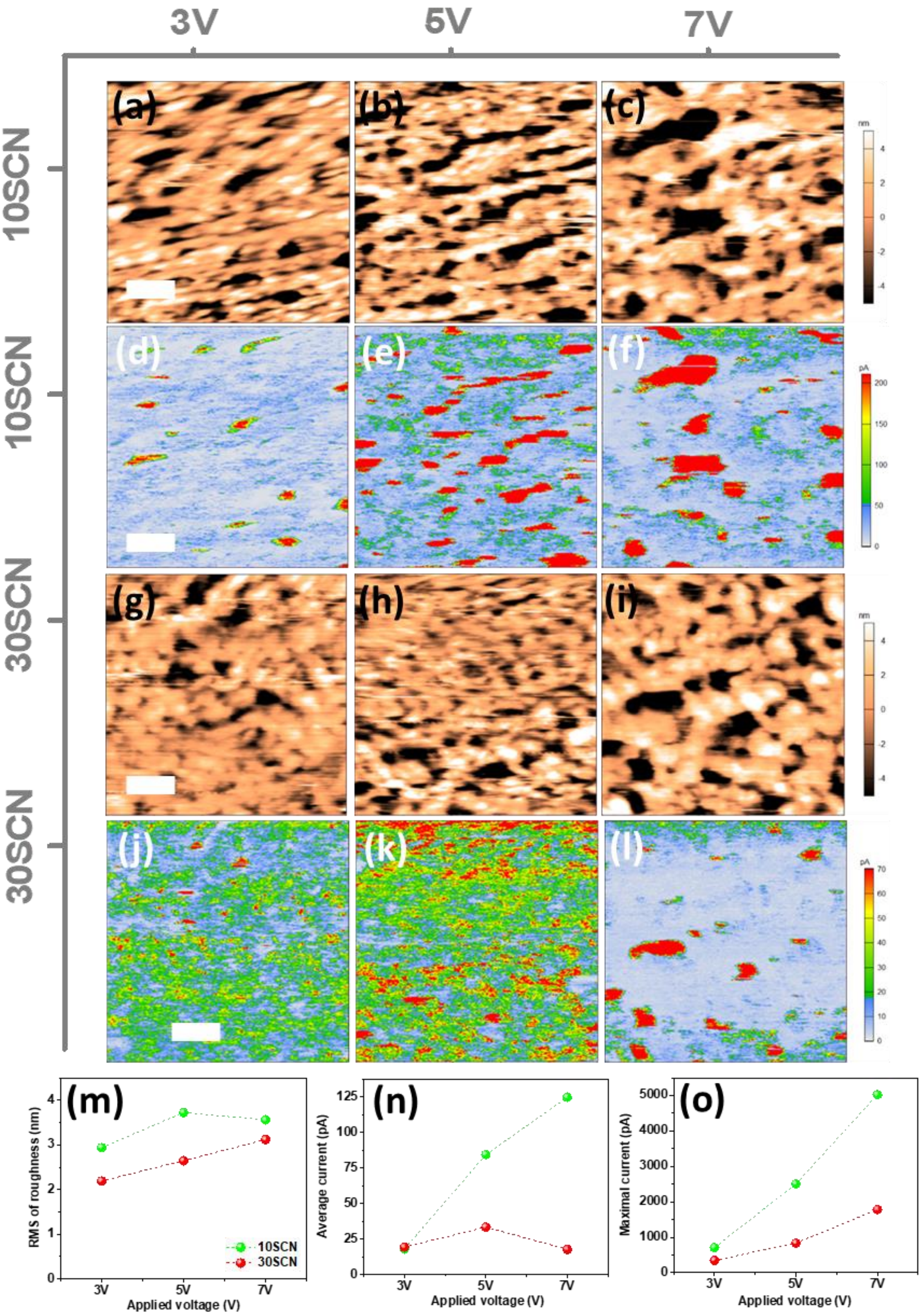

Figure 4.6. (a-c) Topography and (d-f) current mapping images of 10SCN NC film under 3 V, 5 V and 7 V; (g-i) topography and (j-l) current mapping images of 30SCN NC film under 3 V, 5 V and 7 V; comparison of (m) roughness, (n) average current, and (o) maximum current of 10SCN and 30SCN NC films under voltages. The scale bars are 200 nm [40].

Comparing the average current of 10SCN and 30SCN samples at different voltages, it is clear that the initial average current at 3 V are almost the same. However, when the current increases to 5 V, the average current in 10SCN significantly rises from ~18 pA to ~84 pA with a large uncertainty range, while the average current in 30SCN increases only from ~19 pA to ~33 pA (Figure 4.6n). With higher voltage of 7 V, the average current further increases to ~125 pA in 10SCN and decreases to ~18 pA in 30SCN. The maximum current follows a similar trend to the average current (Figure 4.6o). For the 10SCN sample, the maximum current reaches ~2.5 nA and ~5 nA at 5 V and 7 V, respectively. In contrast, the maximum current is merely ~1.8 nA at 7 V for the 30SCN sample. Thus, the higher average current together with the more concentrated uncovered areas in 10SCN may explain the device performance of 10SCN LED being lower than that of the 30SCN LED, in which the current increases more smoothly and few uncovered large areas are formed when the applied voltage is less than 7 V.

According to the C-AFM characterization results and literature study on efficiency roll-off in perovskite LEDs, we attribute the efficiency roll-off in perovskite NC LED to the combination of morphological deterioration of NC film [204], as predicted in a report [196] on $CsPbBr_3$ thin film-based LED, and Auger effect with increasing applied voltage. With increasing bias, the NCs could displace or aggregate and damage the continuity of the NC film, leading to increasing current leakage. Areas with current leakage could lead to direct transport of the carriers through the perovskite layer without forming electron-hole pairs, and thus reducing the luminance efficiency. With increasing bias, the NC film with increased current density could also suffer from Auger effect, which further decreases the luminance. The increased current density together with the decreased luminance accelerates the decrease of EQE of the device, leading to efficiency roll-off.

Furthermore, stable morphology of NC film or stable NC distribution in NC film is expected to be able to relieve efficiency roll-off. This could be supported by some reports showing weakened efficiency roll-off in perovskite NC-based LEDs [116, 201], in which perovskite NCs are embedded or fixed in a matrix and the morphology of the NC films could keep stable during device operation. In addition, thin-film perovskite LEDs, with perovskite settling on the substrate in a stronger way, usually exhibit less pronounced efficiency roll-off with increasing bias [12, 114, 183]. This also suggests the significance of stabilization of the perovskite film morphology on efficiency roll-off in device.

The significance of film morphology on the device performance could also demonstrated by confocal images. Figure 4.7 presents PL mapping images and PL spectra of selected areas on the images. The PL mapping of 30SCN (Figure 4.7b) looks smoother and more homogeneous. Accordingly, quantitative analysis reported in Figure 4.7g shows that the PL intensities of different selected areas with a diameter of 35 μm in 30SCN film sample only exhibits smaller difference in NC distribution for this sample, as compared to those of the other three films. In contrast, there are a few regions brighter than average, which are sparsely distributed in the 10SCN and 50SCN films. These bright areas may be caused by aggregation of NCs. Corresponding PL spectra of the selected areas in 10SCN and 50SCN films show relatively wide distribution in PL intensities. It is said that difference in surface tension and vapor pressure of organic residues and NCs coexisting in the film may affect the morphology of the NC film [38]. A proper ratio between ligands and $CsPbBr_3$ NCs may be beneficial for forming smooth NC film, indicating that the proportion of ligands and $CsPbBr_3$ NCs in 30SCN is at an optimal level. In the PL mapping image of 0SCN (Figure 4.7a), one can clearly see bright dots distributing homogeneously across the film, making the film look rough. This may be due to aggregation of the $CsPbBr_3$ NCs or growth of some $CsPbBr_3$ NCs, as demonstrated in Chapter 3, where we have observed that the untreated $CsPbBr_3$ NCs in film are prone to grow into larger size due to desorption of the labile ligands.

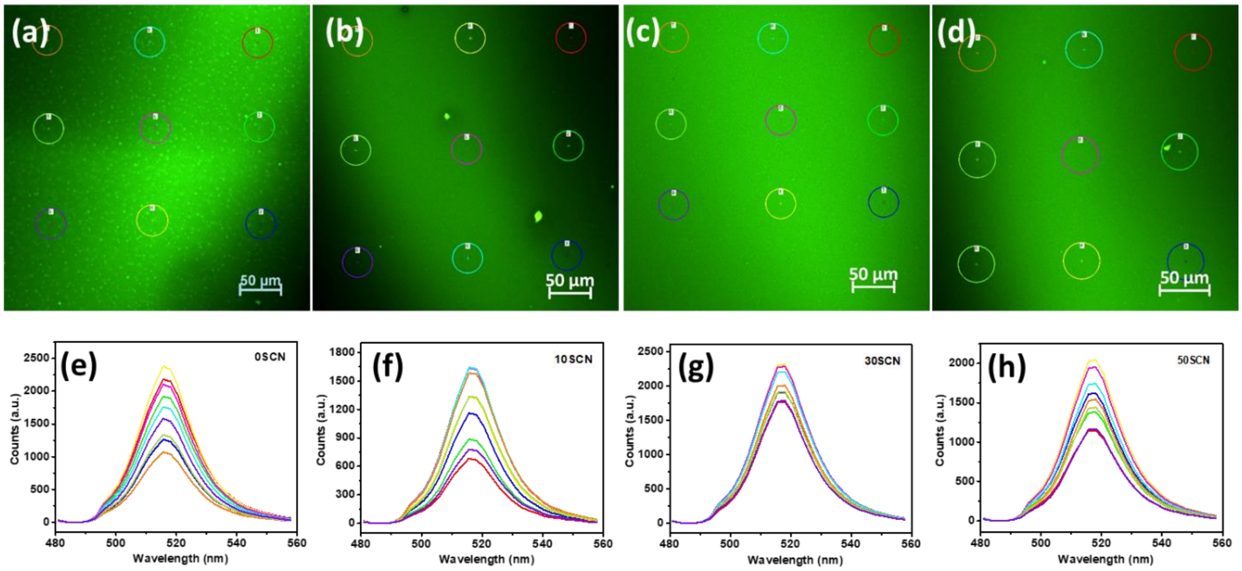

Figure 4.7. PL mapping images of NC films based on (a) 0SCN, (b) 10SCN, (C) 30SCN and (d) 50SCN NC solutions; (e-h) PL spectra of selected areas in each of the corresponding PL mapping images.

The above results on films match well with the LED performance. For example, Figure 4.8 presents the characterization results of 0SCN fresh and aged LEDs. The aging time is 23 days in air and under light at a constant temperature of 20 ℃ and a humidity about 40%, which suits the aged LEDs mentioned in Chapter 4. The rather low current density for the fresh 0SCN LED may be due to excess of ligands, which usually leads to ineffective transport of injected carriers in LED. Obviously there is strong leakage (Figure 4.8a) and emission from HTLs after device aging for some days (Figure 4.8d), which may be related to the bright dots formed in 0SCN film as shown in Figure 4.7a. In contrast, the aged 30SCN LED still shows bright emission (Figure 4.8d). The 30SCN film presents the best film homogeneity and the corresponding LED shows the highest luminance and EQE. The 10SCN film shows inhomogeneous NC distribution and the corresponding device displays the lowest efficiency. The worse 50SCN film quality and LED performance relative to 30SCN, may indicate that excessive SCN is not good for both film formation and consequent LED performance. Thus, we attributed the difference in LED performance between 10SCN and 30SCN to the quality in film morphology.

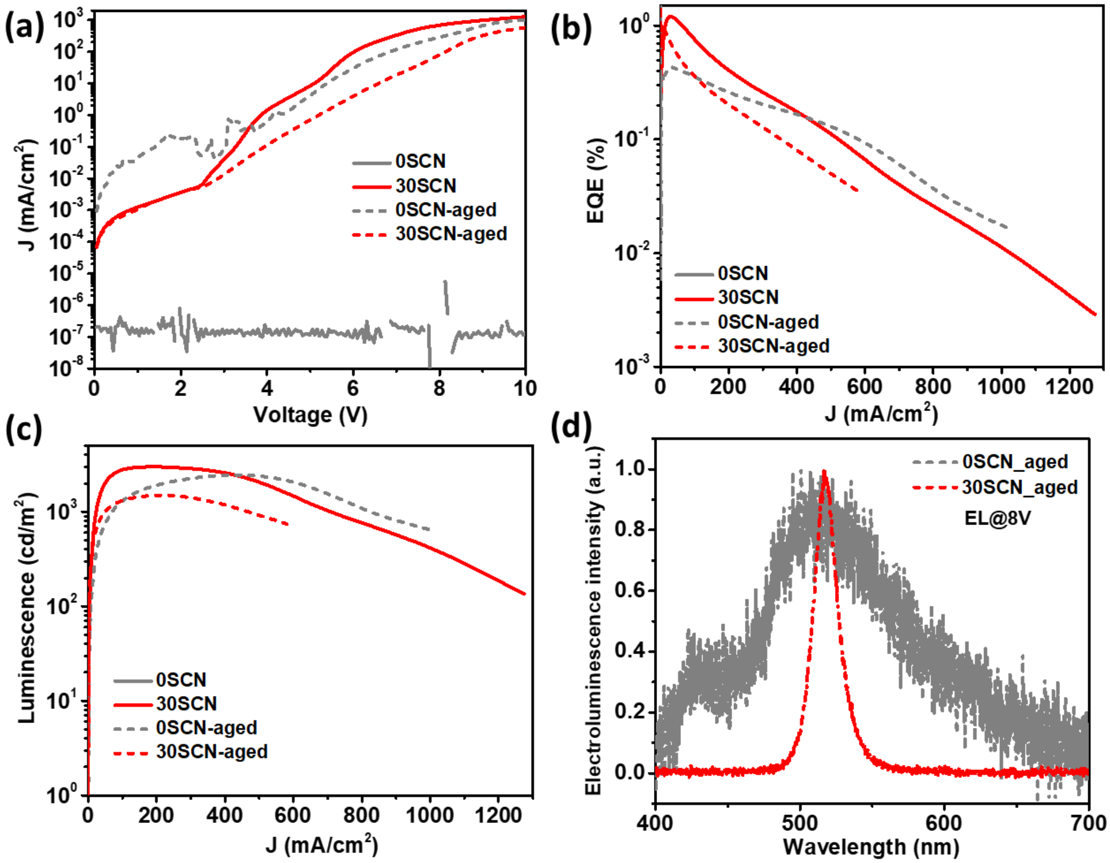

Figure 4.8. Comparison of (a) current density as a function of driving voltage; (b) EQE, (c) luminescence of 0SCN and 30SCN fresh and aged devices as a function of current density. (d) EL spectra of 0SCN and 30SCN aged devices.

4.2.4 Stability of LED

Stability of the devices was also studied. Figure 4.9 presents EL spectra under applied voltage of 6 V for both fresh and aged devices of 10SCN, 30SCN and 50SCN films. With PL spectra of fresh films as reference, it appears that the EL peak of the fresh 30SCN device is the same as corresponding PL peak (Figure 4.9b). The EL peaks of the fresh 10SCN and 50SCN devices are 1.5 nm and 0.8 nm red-shifted with respect to their PL peaks (Figure 4.9a,c), respectively. When comparing the EL peaks of both fresh and aged devices, the devices display a stable EL peak position or exhibit a minor red-shift (Figure 4.9d). For instance, for the 10SCN devices, there is a red-shift from ~519 nm to ~523 nm on aging. On the other hand, the 30SCN devices show only a minor red-shift, if any, from ~518 nm to ~519, and the 50SCN devices exhibit no red-shift at all, suggesting that more SCN within the considered range is favorable for stability of $CsPbBr_3$ NCs in the device. In addition, the FWHMs of the EL peaks of 30SCN and 50SCN show negligible change between the fresh and aged devices (Figure 4.9e). The stable EL spectra of the 30SCN and 50SCN devices at 6 V are also reflected in the CIE coordinate system (Figure 4.9f), indicating that the treated NCs in the 30SCN and 50SCN devices are rather stable even after storage for four months.

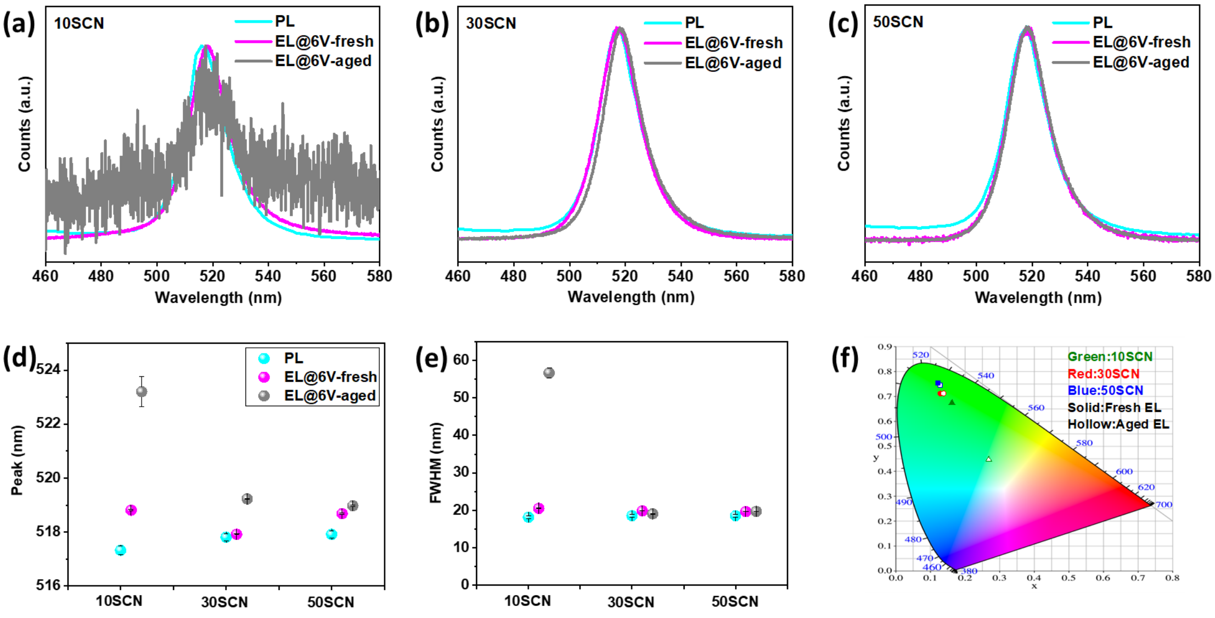

Figure 4.9. Comparison of PL and EL spectra of (a) 10SCN, (b) 30SCN, and (c) 50SCN NC films and fresh as well as aged devices; Comparison of (d) PL and EL peaks; and (e) FWHM of the PL and EL peaks; (f) EL positions of fresh and aged devices in a CIE coordinate system.

Furthermore, EL peaks and corresponding FWHM at different applied voltages were analyzed for both fresh and aged devices (Figure 4.10). In the fresh devices there are a slight blue-shift in the EL peak and a gradual increase in the FWHM with increasing applied voltage, which can be attributed to a field-induced quantum confinement Stark effect and to enhanced longitudinal optical-phonon coupling at high external field [106, 200, 205], respectively. For the aged devices, the FWHM of the EL peak in both 10SCN and 30SCN decrease slightly with increasing voltage, while it increases slightly in 50SCN.

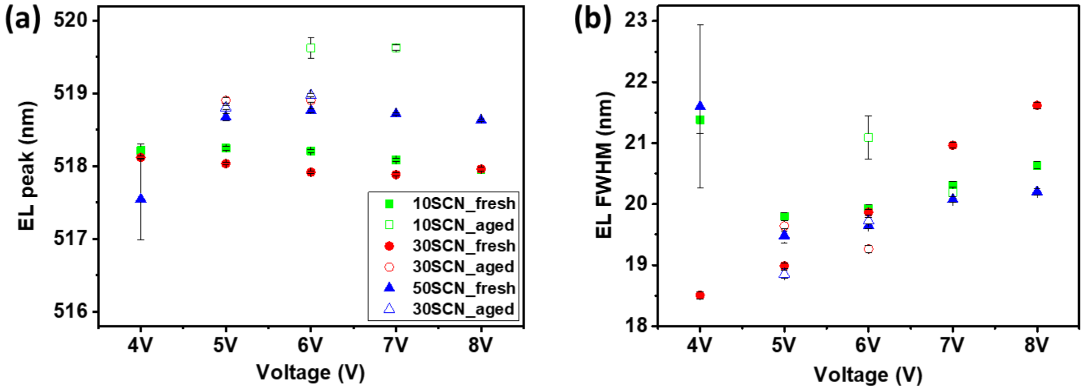

Figure 4.10. Comparison of (a) EL peaks and (b) FWHM of the EL peaks of fresh and aged devices.

The performance of the aged devices was characterized and the statistical results are shown in Figure 4.11. The aged 30SCN devices still show a higher average luminance and EQE than those of 10SCN and 50SCN aged devices. In particular, the champion EQE of the aged 30SCN is 1.9% at 5.6 V, higher than that of the fresh champion device (Figure 4.8 and Table 4.1). The higher EQE of the aged device is due to lower current density. According to our research on conductivity of fresh and aged NC films, the aged NC films show a relatively higher conductivity than the fresh devices, which suggests assignment of the decreased current density in the aged devices to degradation of organic transporting layers and corresponding decreased carrier mobility. Statistical results on performance of 41 aged devices based on 30SCN $CsPbBr_3$ NCs but with variation in spin-coating speed of different layers, are shown in Table 4.3. These results confirm the high stability of the 30SCN devices.

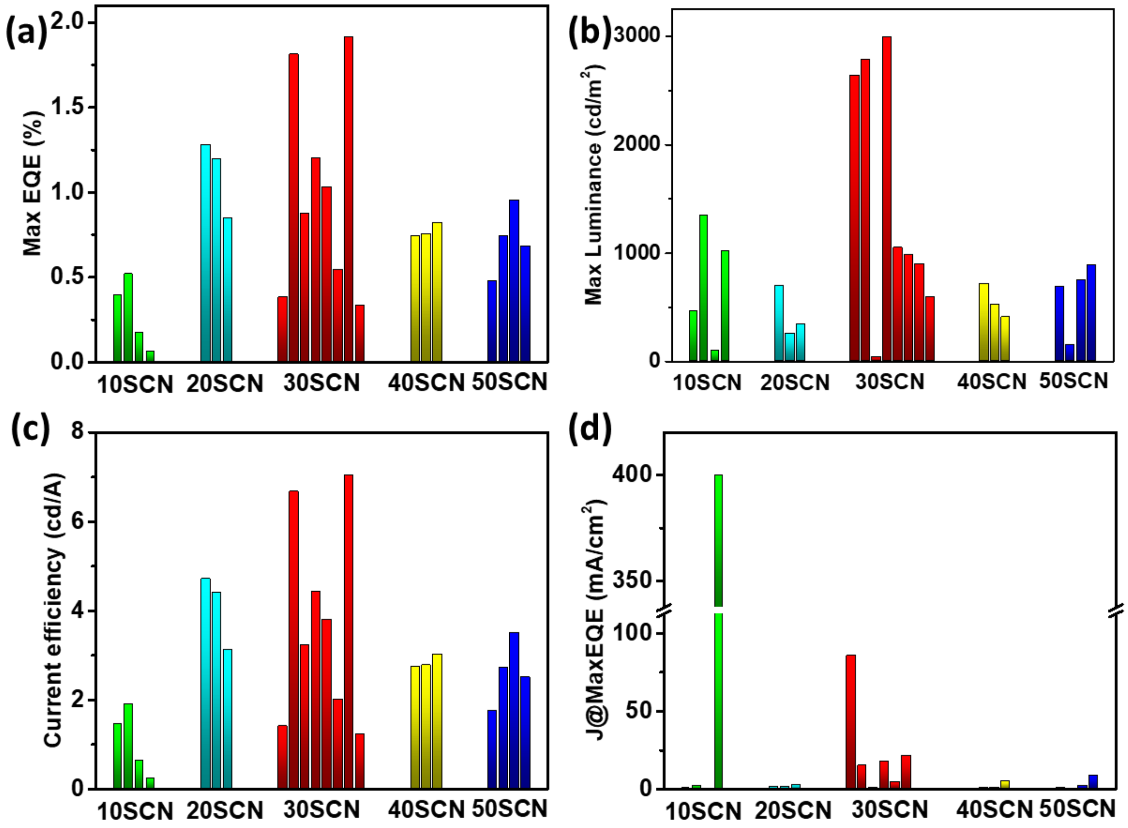

Figure 4.11. Statistics of (a) Maximum EQE, (b) Maximum luminescence, (c) Maximum current efficiency, and (d) current density (J) at the maximum EQE of aged devices.

Table 4.3. Statistics of the average and best properties of LEDs based on 30SCN NCs.

30SCN	**Max EQE (%)**	**Voltage@Max EQE (V)**	**Current efficiency (cd/A)**	**Luminance (cd/m^2)**	**J@Max EQE (mA/cm^2)**
Average	0.7	5.7	2.6	696.5	22.0
Maximum	1.9	5.6	7.0	898.9	4.4

Additionally, operational stability of the 30SCN aged device was measured at 5 V. There is an initial increase in the EL intensity within the first 6 min (Figure 4.12a), then the EL intensity shows an exponential deterioration. The half-lifetime (L50) is ~27 min, showing competitive stability in $CsPbBr_3$ NC-based LED (Table 4.2). EL peaks collected every one minute (Figure 4.12b) are shown to steadily fluctuate ~ 518 nm throughout the measurement, indicating stable emission property of the 30SCN aged device. The inset of Figure 4.12a displays the running device during the measurement.

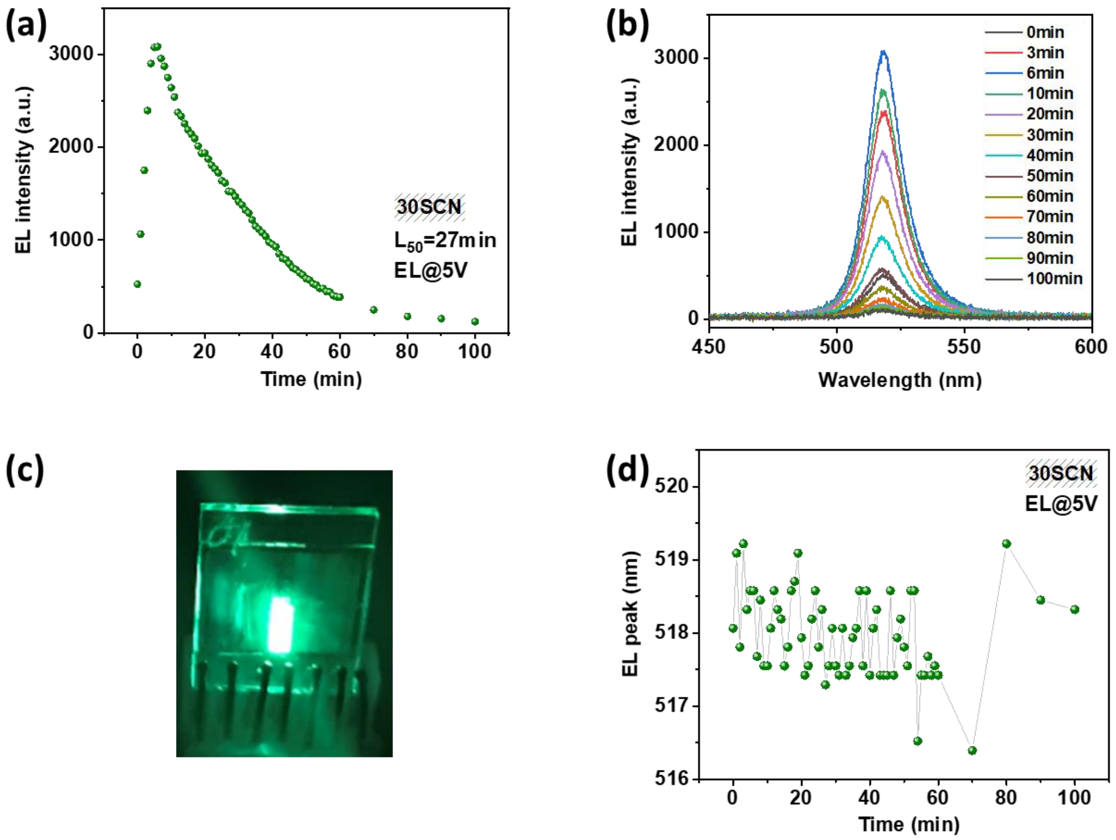

Figure 4.12. Characterization of stability of running LED. (a) Evolution of EL intensity as a function of running time; (b) EL spectra; (c) A capture of the device; and (d) evolution of the EL peaks collected during operation stability test of 30SCN aged device.

In summary, green LEDs were fabricated based on $CsPbBr_3$ NCs synthesized with lead acetate and BBr as source of lead and bromine. SCN solution was used to treat $CsPbBr_3$ NCs before purification with EA. The 30SCN device showed the best performance, and we investigated possible reasons for the score of this champion device. Characterization of fresh and aged devices as well as measurement of running time at 5 V showed relatively high stability of the 30SCN device. The current work proposes a facile route to treat sensitive perovskite NCs and to fabricate perovskite NC-based LED with high stability.

4.3 Green LED based on perovskite nanocrystals treated with potassium salts

Potassium salts[206, 207] and sodium salts[208] have been demonstrated to be able to passivate and stabilize halide perovskite thin films, suppressing ion migration or hysteresis and leading to fabrication of high-efficient perovskite solar cells. The alkali salts in these cases are usually dissolved in polar solvent such as DMSO and DMF during the preparation of the precursors.

However, this cannot apply to halide perovskite NCs, which require a non-polar environment during and after synthesis. Due to the difficulty to dissolve alkali salts into NC solution and the fact of alkali salts being highly hygroscopic, the effect of alkali salts on halide perovskite NCs was seldom explored. Alivisatos and coworkers added solid NaSCN directly into $CsPbBr_3$ NC solution and found that NaSCN improves PLQY and stability of $CsPbBr_3$ NCs [59].

In addition, doping alkali metal ions into halide perovskite NCs by using potassium acetate during the NC synthesis has proved to be a promising route to enhance the optoelectronic performance of halide perovskite NCs and is getting increasing attention this year. For example, Hoang *et al. [209]* improved green LED efficiency from 4.8% to 5.6% by replacing a part of Pb^{2+} with K^+ during the synthesis of $CsPbBr_3$ NC solution. Ma and coworkers [210] obtained hollow $CsPbBr_3$ NCs with efficient blue emission by addition of NaBr during the fabrication of perovskite thin film. Yao and coworkers [211] prepared KBr-passivated $CsPbI_{3-x}Br_x$ NCs with pure red PL emission and PLQY more than 90%. They also fabricated stable red perovskite LEDs with stable EL peaks at 637 nm and a maximum EQE of 3.55% with a maximum brightness of 2671 cd/m^2. More studies are necessary to elucidate the benign effect of alkali metal ions in halide perovskite NCs and LEDs.

4.3.1 Effect of potassium salts on NC solution

We used $CsPbBr_3$ NCs capped with DDAB as pristine NCs [34] and concentrated the NC solution to 30 g/L in toluene. Different kinds of potassium salts, KX (X=F, Cl, Br, I, SCN), were used, and added directly into the NC solution in the form of oversaturated solid powders. KCl showed an obviously higher solubility in the NC solution than the other salts. The other salts, in solid form, were dried and grinded before use; apparently, they showed no visible change on grinding, when judged by naked eyes. Optical performance of the NC solutions was characterized soon after preparation.

Figure 4.13 shows the UV-visible light absorption plot and the PL spectra of the freshly treated NC solutions. The PL intensity of the NC solutions treated with KCl, KBr and KSCN decreased in all cases, while that of the solutions treated with KF and KI almost remained the same. The normalized absorption plots of most of the treated NC solutions remain similar to the pristine DDAB-capped NC solution except the case of KSCN, which presents moderately higher absorption intensity than those of the rest from 350 to 525 nm. Overall, the data suggest almost no effects of KX salts, most likely due to solubility issues.

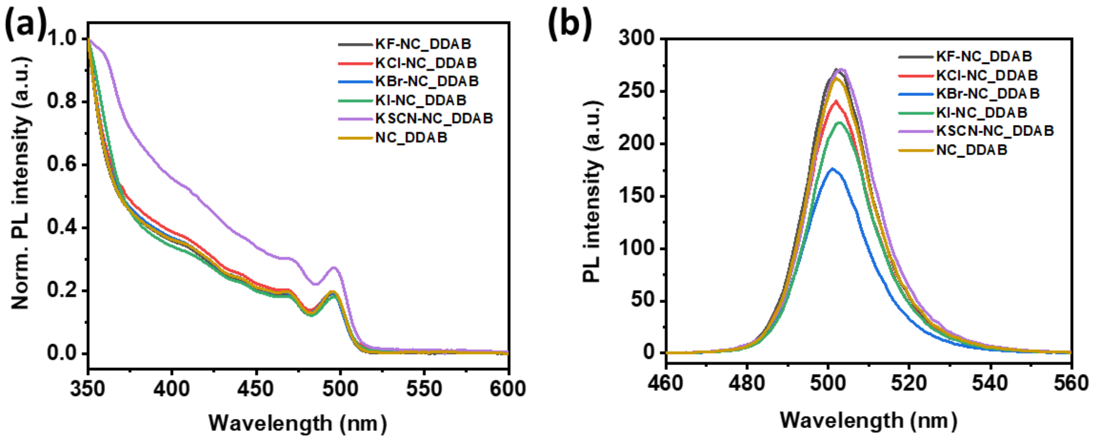

Figure 4.13. (a) PL spectra; and (b) UV-visible light absorption intensity spectra of NC solutions freshly treated with KX (X=F, Cl, Br, I, SCN).

18-Crown-6, an organic compound with a ring structure composed of six ether groups, is reported to be able to increase solubility of potassium salts in solutions, and to passivate perovskite film [183]. It is also reported to act as a shell for perovskite NCs [22]. Here, 18-Crown-6, at a concentration of 3% with respect to the volume of the adopted NC solution, was added to the NC solutions directly to help dissolution of KX. However, the additive seems to accelerate degradation of NCs in most cases. When only 18-Crown-6 is added into the NC solution, the NCs became white powder quickly. In presence of potassium salts, the degradation rate was relatively slower.

Both the NC solutions treated with only KX and those treated with a combination of KX and 18-Crown-6 were stored in air overnight to let them fully react. The so-obtained NC solutions were then investigated. Figure 4.14a-b shows picture of the solution under UV light illumination. NC solutions treated with KCl, KBr and KSCN show similar brightness as the pristine one. NC solutions treated with KF became colorless in both situations (Figure 4.14a), suggesting that F$^-$ could gradually degrade perovskite NCs. KI also seems unfavorable for the emission of the NCs, exhibiting much weaker brightness under UV light (Figure 4.14a). Interestingly, the NC solution treated with a combination of KSCN and 18-Crown-6 remained luminescent (Figure 4.14b), while all the other NC solutions treated with 18-Crown-6 became completely non-luminescent.

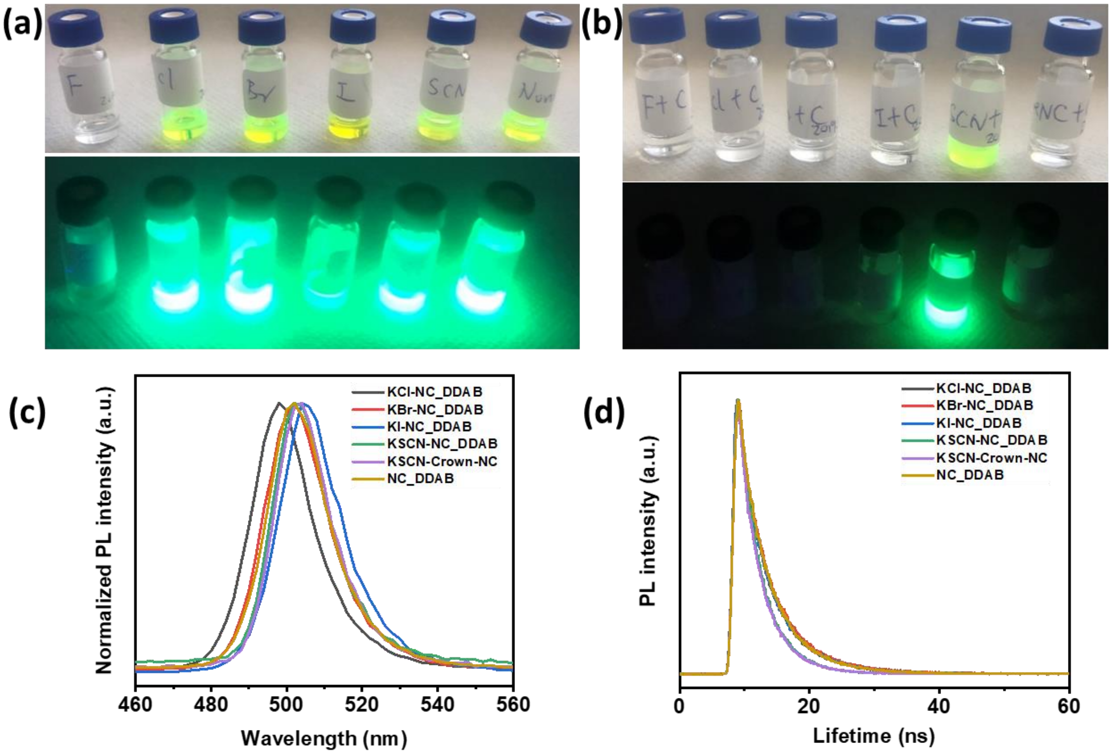

Figure 4.14. (a) Photos of NC solutions stored in air overnight and treated with KX (X=F, Cl, Br, I, SCN); (b) Photos of NC solutions stored in air overnight and treated with a combination of KX (X=F, Cl, Br, I, SCN) and 18-Crown-6 with and without UV exposure; (c) UV-visible light absorption intensity spectra; and (d) PL spectra of the NC solutions stored in air overnight and treated with KCl, KBr, KI, KSCN and KSCN:18-Crown-6 with DDAB-capped NC as a reference.

PL spectra and PL decay lifetime of the NC solutions that remained bright were collected. As shown in Figure 4.14c and Table 4.4, the PL peak of KCl-treated NC solution showed blue-shift and the PL peak of KI-treated NC solution showed red-shift with respect to that of the DDAB-capped NC solution. This most likely indicates anion exchange between Br^- and Cl^- or I^-. In addition, the FWHM of PL peaks of KSCN-treated NC solutions decreased. According to the plots in Figure 4.14d, we can see that the decay lifetime of the NC solutions suffers negligible influence from treatment with KCl, KBr and KI. When the NCs are treated with SCN, the decay lifetime decreases, suggesting that SCN^- may damage the DDAB-capped $CsPbBr_3$ NCs.

Table 4.4. Statistics of optical properties of NC solutions treated with KCl, KBr, KI, KSCN and KSCN:18-Crown-6 with pristine DDAB-capped NC solution as a reference.

	KCl	**KBr**	**KI**	**KSCN**	**KSCN : Crown**	**NC-DDAB**
τ_{ave} (ns)	5.03	5.25	5.05	3.64	3.55	5.01
PL peak (nm)	499	503	506	504	504	503
PL FWHM (nm)	20	21	21	18	18	20

In order to see whether the treatment has effect on the morphology of the NCs, TEM images were collected, as shown in Figure 4.15.

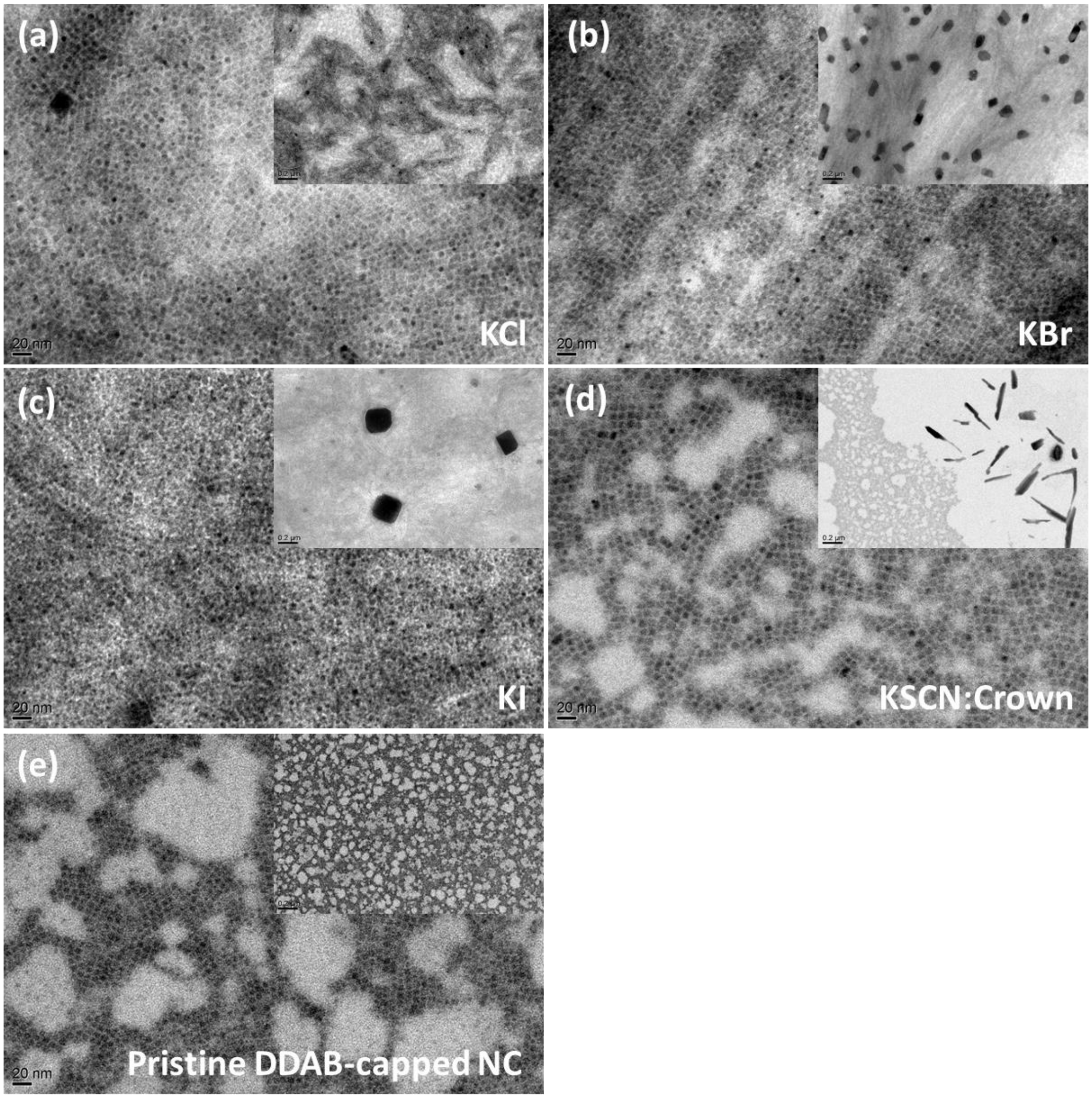

Figure 4.15. TEM images of NC solutions treated with (a) KCl; (b) KBr; (c) KI; (d) KSCN:18-Crown-6; and TEM images of (e) pristine DDAB-capped NCs.

We can see that the size and shape of most of the NCs were well-retained in all cases, similar to the pristine DDAB-capped NCs (Figure 4.15e). However, there are new particles or aggregates with different morphologies formed on treatment. According to Figure 4.15a, the KCl-treated NCs apparently aggregate into spindle shapes. , The treatment with KBr induced the presence of it is clear that polyhedral particles with size ranging from 100 to 200 nm, as shown in Figure 4.15b. Based on our study carried out in Chapter 3, on the effect of excess Br^- in $CsPbBr_3$ NC solution, the particles could be attributed to Cs_4PbBr_6. In Figure 4.15c, we can see a few big squares with size ~ 200 nm, which may be due to growth of some NCs. The inset of Figure 4.15d presents some needle-like particles. In conclusion, treatment with different potassium salts has different effects on the morphology and distribution of the NCs.

We then collected the XRD patterns of the set of NC solutions as shown in Figure 4.16. Most treated NC solutions show widened diffraction peaks similar to that of the DDAB-capped NC solution, suggesting negligible influence of the treatment on NC phase. However, in the case of KSCN-treated NCs, the XRD pattern presents sharp peaks, which may indicate enlarged size and enhanced crystallinity of the NCs. This could be corroborated by the fact that the KSCN-treated NC solution without 18-Crown-6 had already become colorless by the time that we took XRD measurement. In addition, in the XRD pattern of KBr-treated NCs there is a sharp peak at 26.3°. The newly emerged diffraction peak could be attributed to formation of new perovskite phases, as discussed in Chapter 3.

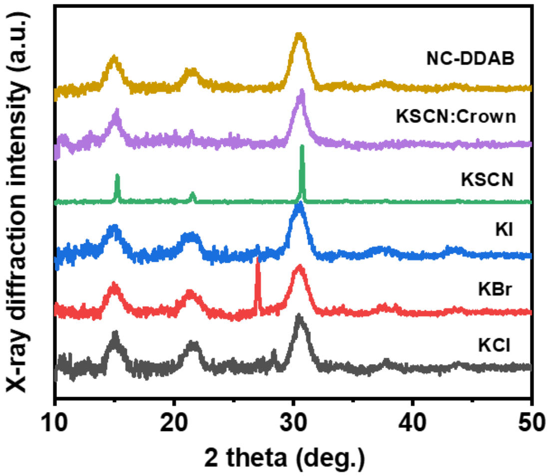

Figure 4.16. XRD patterns of NCs treated with KCl, KBr, KI, KSCN and KSCN:18-Crown-6, with DDAB-capped NC as a reference.

4.3.2 LEDs based on NCs treated with KX

In order to see the effect of the treatment with KX on the optoelectronic properties of the NCs, we applied the treated NC solutions in LEDs fabrication. The LED structure was ITO/PEDOT:PSS/poly-TPD/$CsPbBr_3$ NCs/LiF/TPBi/LiF/Al. Here, the LiF layer between the $CsPbBr_3$ NC layer and the TPBi layer is used for balancing carrier injection. However, the performance of LEDs based on KX-treated NCs showed lower luminescence intensities and EQEs (Figure 4.17c-e) than that of the LED based on the pristine DDAB-capped NCs. Since the luminance of LED based on KI-treated NCs is lower than 1 cd/m^2 during the whole operation process, the related data is not shown here.

From Figure 4.17a, we can see that the current density trend of LED based on pristine DDAB-capped NCs and KBr-treated NCs are similar, and both show relatively low current leakage. However, the luminance and EQE of the LED based on KBr-treated NCs are rather low. This may be due to the optical properties of the pristine DDAB-capped NCs being damaged after treatment with KBr. This is strange and opposite than the results in the recent literature report according to which KBr could enhance the PL QY of halide perovskite NCs [211]. LED based on KCl-treated NCs appear to be more efficient than those treated with the other method, in spite of higher current leakage. LEDs based on KSCN:Crown-treated NCs require a current density higher than 200 mA/cm^2 to have luminance higher than 5 cd/m^2. Combining the current density as a function of applied voltage, the poor performance of LEDs based on KSCN:Crown-treated NCs could be attributed to high leakage of NC film and weakened optical property of the treated NCs.

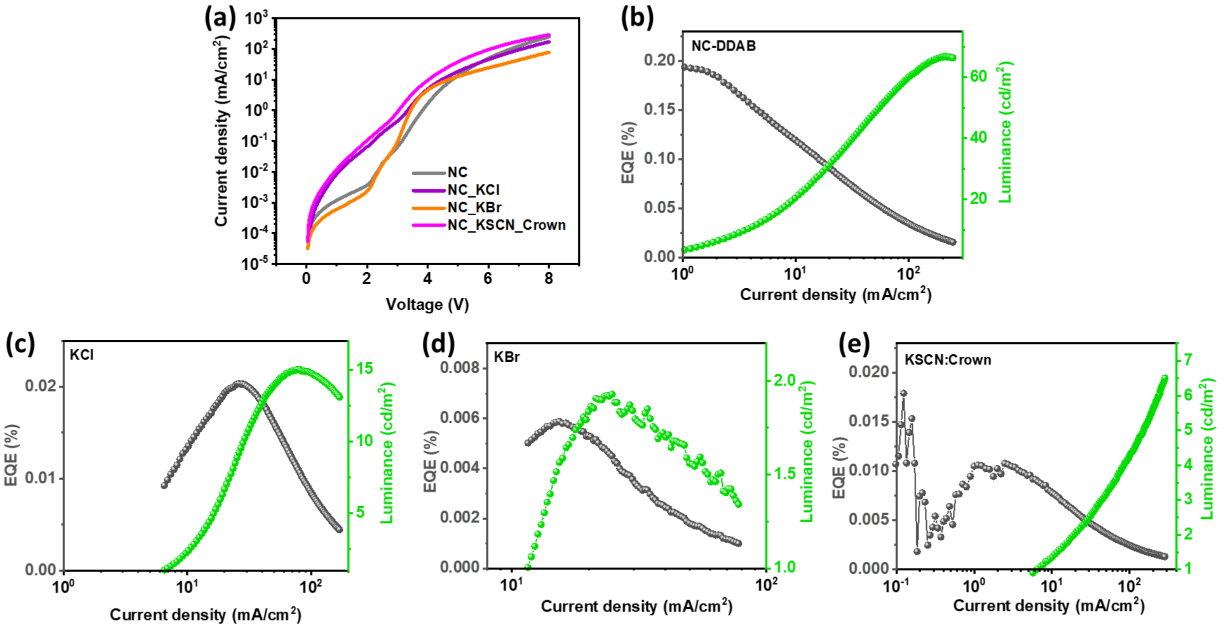

Figure 4.17. LED performance. (a) Current densities of LEDs based on pristine DDAB-capped NCs and based on NCs treated with KCl, KBr, KI, KSCN and KSCN:18-Crown-6 as a function of voltages; EQE and luminance of (b) LEDs based on pristine DDAB-capped NCs; and LEDs based on NCs treated with (c) KCl; (d) KBr; and (e) KSCN:18-Crown-6 as a function of current density.

In summary, post treatment of the DDAB-capped $CsPbBr_3$ NCs with solid alkali salts show poorer optical properties and device performance than the untreated one. However, it does not mean that alkali salts are unfavorable for halide perovskite NCs. According to the previous introduction, potassium salts are favorable for optical performance of LHP NCs when the potassium additives are used during NC synthesis [209].

4.4 Green LED with ZnO NCs as electron transporting layer

Organic electron transporting materials like TPBi are usually used as ETL in perovskite-based LEDs. However, TPBi is expensive and easily degradable in air. It is therefore highly desirable to use an inorganic ETL like ZnO, which is much cheaper, more stable, and with a higher electron mobility, to replace the organic one. ZnO could be deposited on the ITO substrate to fabricate LED with inverted structure. It could also be deposited on top the perovskite layer in a normal LED structure. In this section, the tests performed in both configurations are reported, with commercial ZnO NCs (Sigma-Aldrich) used as the ETL.

4.4.1 LED with ZnO NCs beneath LHP NCs layer

ZnO NCs have been used as ETL as reported by Yang *et al.* [212]. In order to fabricate LEDs with inverted structure, that is, with ZnO NCs layer beneath the LHP NCs layer, a smooth and compact ZnO NC film is highly desired. Here, we explored the effect of the ZnO NCs dispersing solvent on the quality of the ZnO NC film. ZnO NCs originally dissolved in ethanol with an average size of 130 nm and a concentration of 40% were diluted in three different solvents, namely 1-butanol, CB and MeOH, to obtain ZnO NC solutions with a concentration of 2 wt%. Then, the ZnO solutions were spin-coated onto ITO substrates at 1500 rpm and annealed at 150 °C for 30 min. The roughness (Figure 4.18a-c) and thickness (Figure 4.19a-c) of the ZnO NC films were measured by AFM, and the statistic results are shown in Table 4.5. According to the roughness values and Figure 4.18a-c, it seems that the smoothest NC film occurred when ZnO was dissolved in CB. The film based on ZnO NCs dispersed in butanol present aggregates (Figure 4.18a).

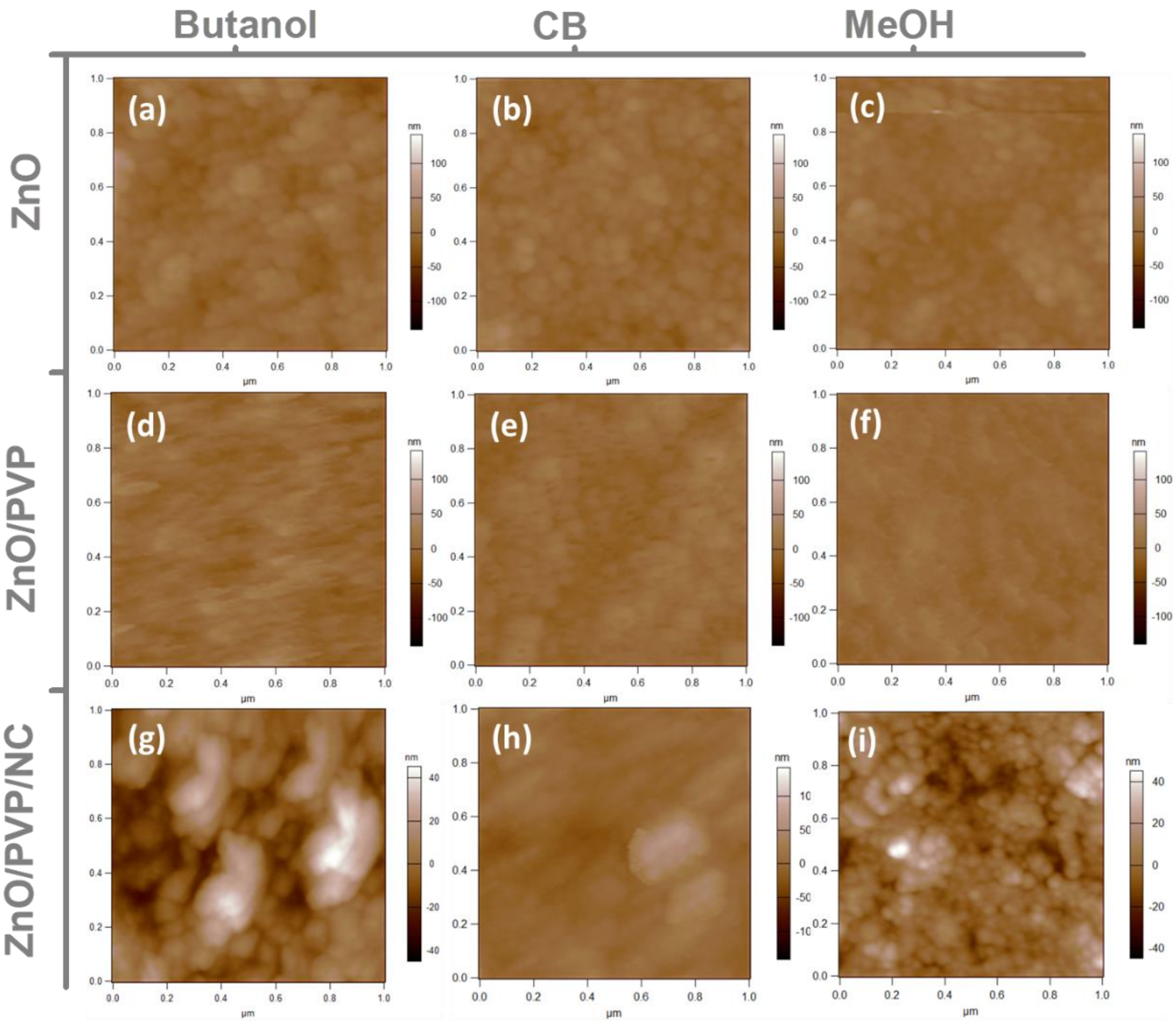

Figure 4.18. AFM images of: (a)-(c) ZnO films spin-coated from ZnO NCs dissolved in (a) 1-Butanol, (b) CB, and (c) MeOH; ZnO/PVP films spin-coated atop ZnO NCs layers dissolved in (d) 1-Butanol, (e) CB, and (f) MeOH; ZnO/PVP/NC films spin-coated atop PVP layers corresponding to ZnO NCs dissolved in (g) 1-Butanol, (h) CB, and (i) MeOH. Note: In (d), the sample was significantly drifting horizontally in time, but drift would anyway not affect significantly the measured roughness. And panel g was affected by large tip size due to showing its own footprint.

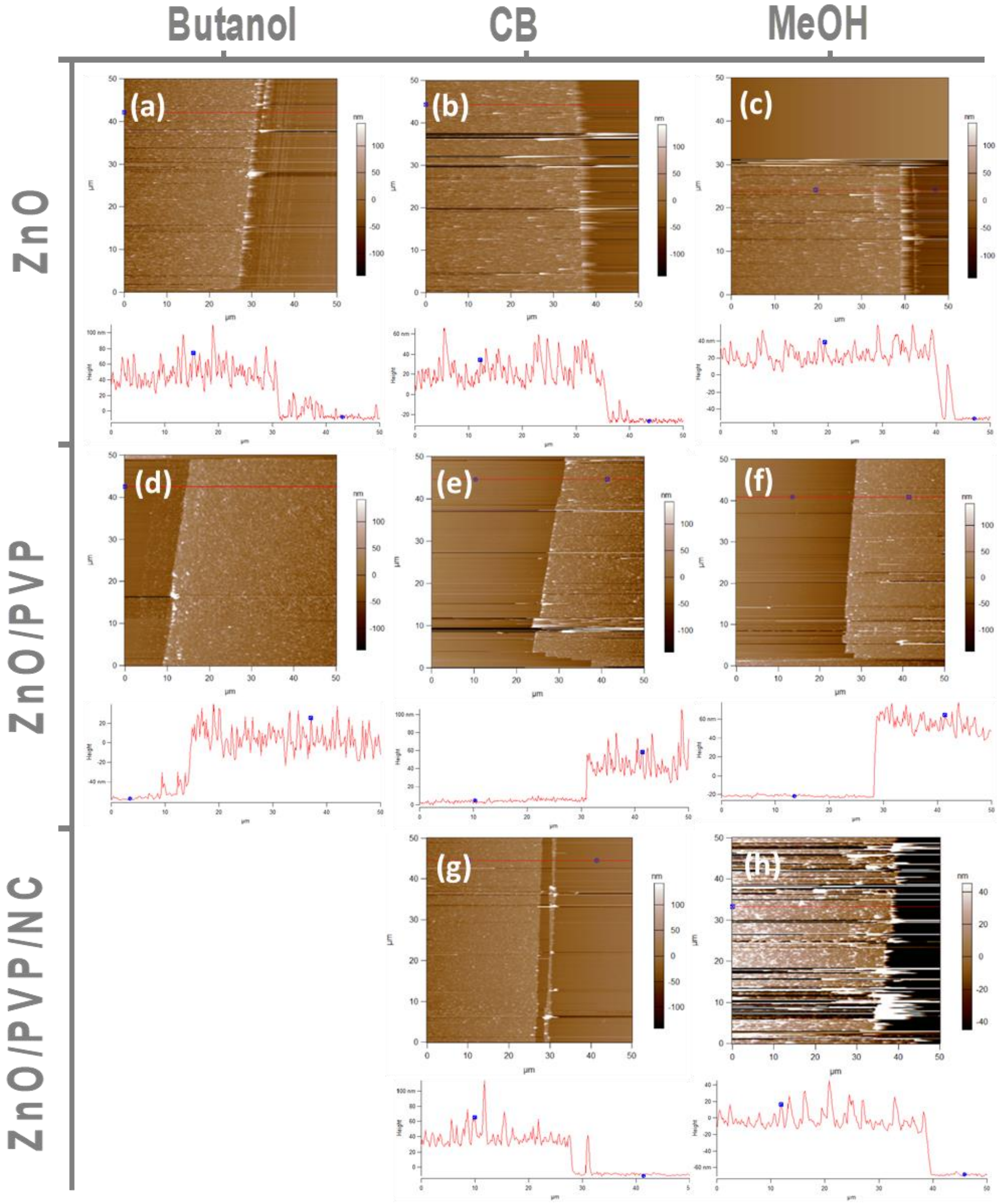

Figure 4.19. Representative AFM images and cross section images of: (a)-(c) ZnO films spin-coated from ZnO NCs dissolved in (a) 1-Butanol, (b) CB, and (c) MeOH; ZnO/PVP films spin-coated atop ZnO NCs layers dissolved in (d) 1-Butanol, (e) CB, and (f) MeOH; ZnO/PVP/NC films spin-coated atop PVP layers corresponding to ZnO NCs dissolved in (g) CB, and (h) MeOH.

In order to avoid leakage and reduce interface defects between the ZnO NCs layer and the LHP NCs one, a layer of polymer is further spin-coated onto the ZnO NCs layer at 5000 rpm with 5 wt% PVP dissolved in DMSO. Later, perovskite NC layer was spin-coated onto the PVP layer at 2000 rpm. According to the AFM images on the roughness (Figure 4.18d-f) and thickness (Figure 4.19d-f) for each layer and the statistic results in Table 4.5, we can see that when MeOH is used to disperse the ZnO NCs, the finally deposited LHP NCs film has the lowest roughness and the most homogeneous NC distribution (Figure 4.18i). Thus, it is clear that a proper choice of solvent for ZnO NCs matters for the quality of the ZnO film [213] and has a great influence on the quality of multilayers.

Table 4.5. Statistics of thickness and roughness of films based on ZnO NCs dispersed in different solvents.

Roughness (nm)	**ZnO**	**ZnO/PVP**	**ZnO/PVP/NC**
1-Butanol	11.5	10.7	13.7
CB	9.2	9.3	15.1
MeOH	9.5	6.5	9.6
Thickness (nm)	**ZnO**	**ZnO/PVP**	**ZnO/PVP/NC**
1-Butanol	87	73	-
CB	73	54	59
MeOH	92	88	82

Based on the above results, MeOH was chosen to disperse the ZnO NCs, and an inverted LED with a structure as shown in Figure 4.20a was fabricated. However, there was serious leakage in the corresponding LEDs and the current is beyond the measuring range when the bias is near 12V. A representative current-voltage (I-V) plot is shown in Figure 4.20b. According to the thicknesses of the multilayers listed in Table 4.5, it is clear that there is a wash-away effect on previous layers, when spin-coating the subsequent upper layer. This may explain the poor quality of the LEDs.

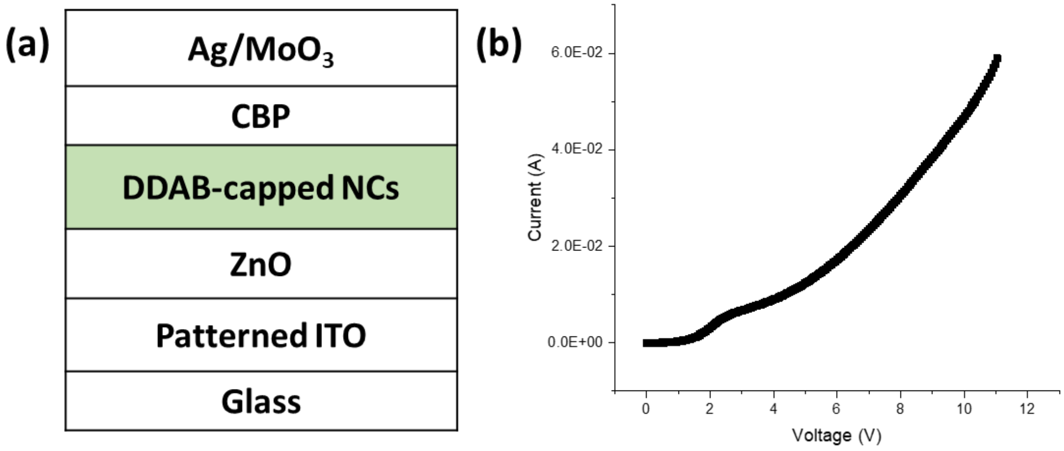

Figure 4.20. (a) A schematic diagram of LED with inverted structure; and (b) a representative I-V plot of the LED with ZnO as ETL in the inverted structure.

4.4.2 LED with ZnO NCs atop LHP NCs layer

We further tried to replace the organic ETL with the ZnO NCs in a normal LED structure. The main problem here is to harmonize perovskite NCs and ZnO NCs during spin-coating, since the perovskite NCs layer may be washed off or damaged in optical performance after this device fabrication step. Therefore, we looked for a feasible way to make the perovskite NC layer more robust, before depositing the ZnO NC layer.

Considering that the ZnO NCs film based on ZnO NCs dispersed in CB has the lowest roughness (Table 4.5) and no more polymer layer is necessary in current case, CB was chosen as the solvent of ZnO NCs. We found that NCs capped with different ligands show different resistance to the washing effect of the upper layer. . When the NCs have DDAB as ligands, it is clear even by the naked eye that the NC layers were mostly destroyed and washed off after depositing ZnO NCs. When the NCs have OA and OLAM as ligands and purified with SCN solution, the LHP NC film looks still good in quality after spin-coating the ZnO NC layer.

According to our previous study about the effect of dispersing solvent on perovskite NCs films as reported in Chapter 3, we decided to disperse the perovskite NCs in a mixed solvent of hexane and DE. To be specific, $CsPbBr_3$ NCs, which are capped with OA and OLAM and purified with EA under protection of SCN solution, were dispersed in 300 mL of mixture solvents, obtained with different volume ratios of hexane and DE (namely300:0, 270:30, 240:60, 210:90, 180:120, and 150:150 mL of hexane:DE).

Figure 4.21 presents the results of the LEDs with ZnO as ETL atop of perovskite NCs layer. When the solvent for NCs contained only hexane, there was a serious leakage in the LED (Figure 4.21a), and a relatively high voltage was required to obtain luminance higher than 1 cd/m^2. Although LEDs from NCs dispersed in a 1:1 mixture of hexane and DE also show a high leakage, the turn-on voltage (with 1 cd/m^2 as reference) was 3.9 V (Figure 4.21c), much lower than that of the case without DE, and the corresponding LED showed the highest EQE in the current set (Figure 4.21d). Not all LEDs based on $CsPbBr_3$ NCs dispersed in a mixed hexane:DE solution exhibit high luminance and EQE, but the LEDs showed lower turn-on voltages and higher EQEs in general with respect to the LED based on NCs dispersed purely in hexane (Figure 4.21c,d). Thus, a mixed solvent with a proper ratio between hexane and DE may be a plausible way to fix perovskite NCs layer before depositing ZnO NCs layer.

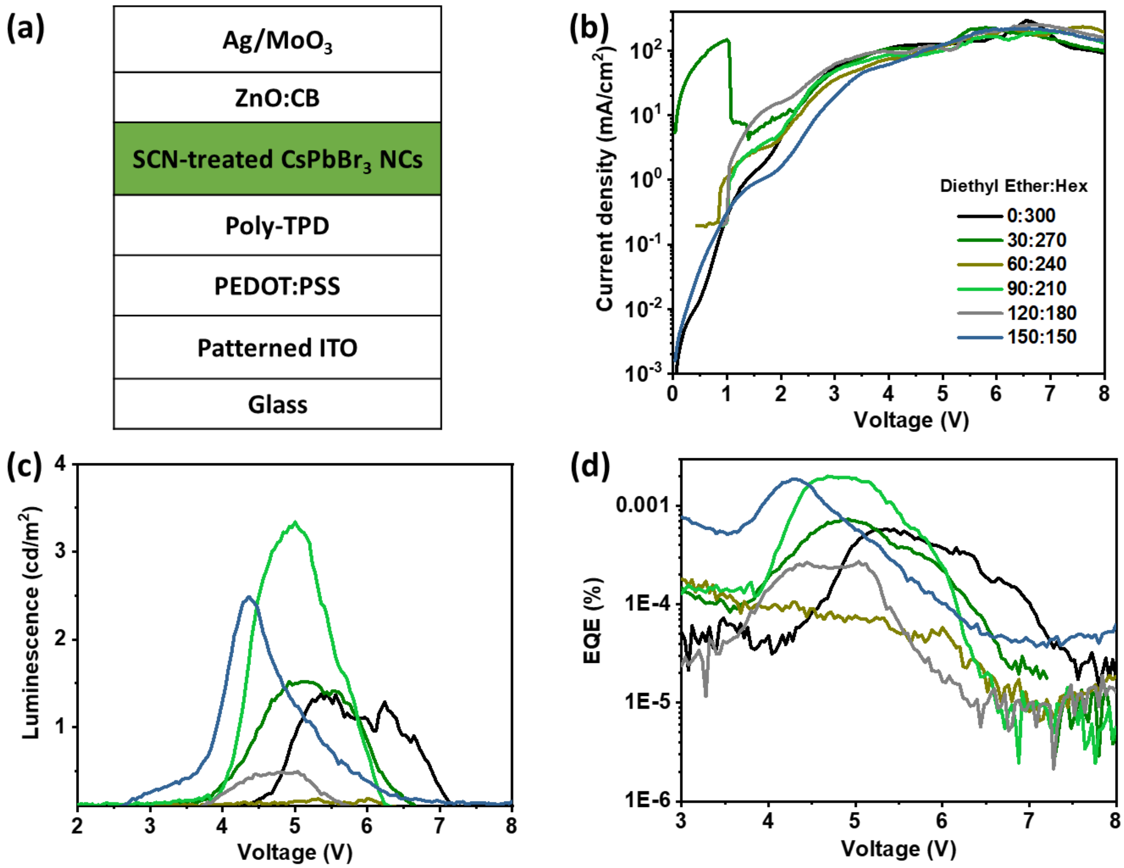

Figure 4.21. (a) A diagram of the LED structure, (b) current density, (c) luminescence; and (d) EQE as a function of driving voltage in the perovskite NC LEDs with ZnO NC as ETL atop of perovskite NC layer.

In addition, the low absolute EQEs may be attributed to two reasons. On one hand, the pristine NC solution capped with OA and OLAM has been stored for a long time in air and is not as bright as the fresh one. On the other hand, the CB solvent used to disperse ZnO NCs may cause a damage to the optical performance of the perovskite NCs. This would be supported by the better performance of LEDs with thermally-evaporated TPBi as ETL as shown in Figure 4.22.

Moreover, the higher EQE and lower efficiency roll-off of the LED based on NCs in mixed solvent (Figure 4.22d) proves the significance of fixation of NCs in the film for better LED performance.

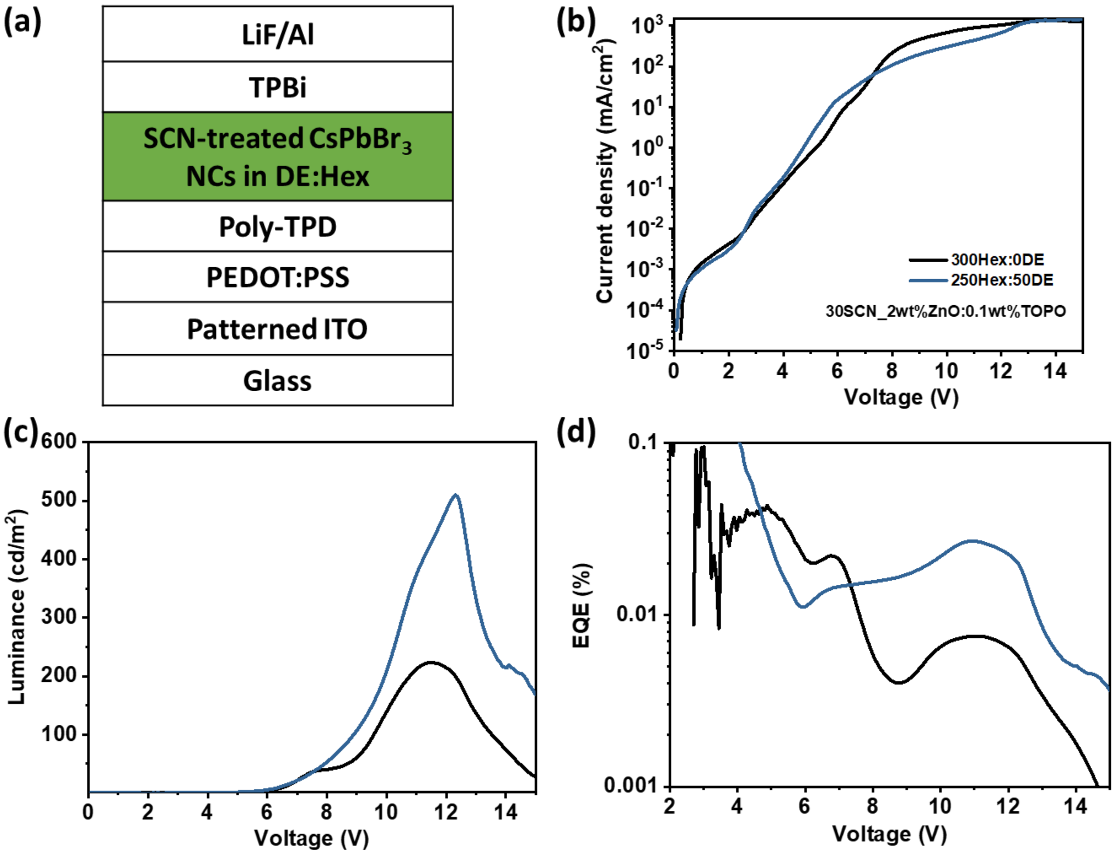

Figure 4.22. (a) Diagram of the LED structure, (b) current density, (c) luminescence, and (d) EQE as a function of driving voltage in the LEDs based on SCN-treated NCs dispersed in a mixture of DE and hexane (Hex).

Since ZnO has a much higher electron mobility than organic transporting materials, it is easy to cause unbalanced carrier injection in LED, leading to poor performance and fast degradation of the device [188]. In order to reduce electron mobility of ZnO NCs or balance the carrier injection into the perovskite NCs layer, polymers[11, 42] or macromolecules[195] are usually used to act as a blocking layer between ZnO layer and emissive layer. Here, we tried mixing 2 wt% ZnO NCs with 0.1 wt% TOPO in CB. The performances of corresponding LEDs are shown in Figure 4.23. It is clear that the LED with ZnO:TOPO as ETL has lower leakage and current density, and higher luminance as well as higher EQE than the LED with only ZnO as ETL. This indicates that TOPO helps in balancing carrier injection into the perovskite NCs layer and in improving the LED performance.

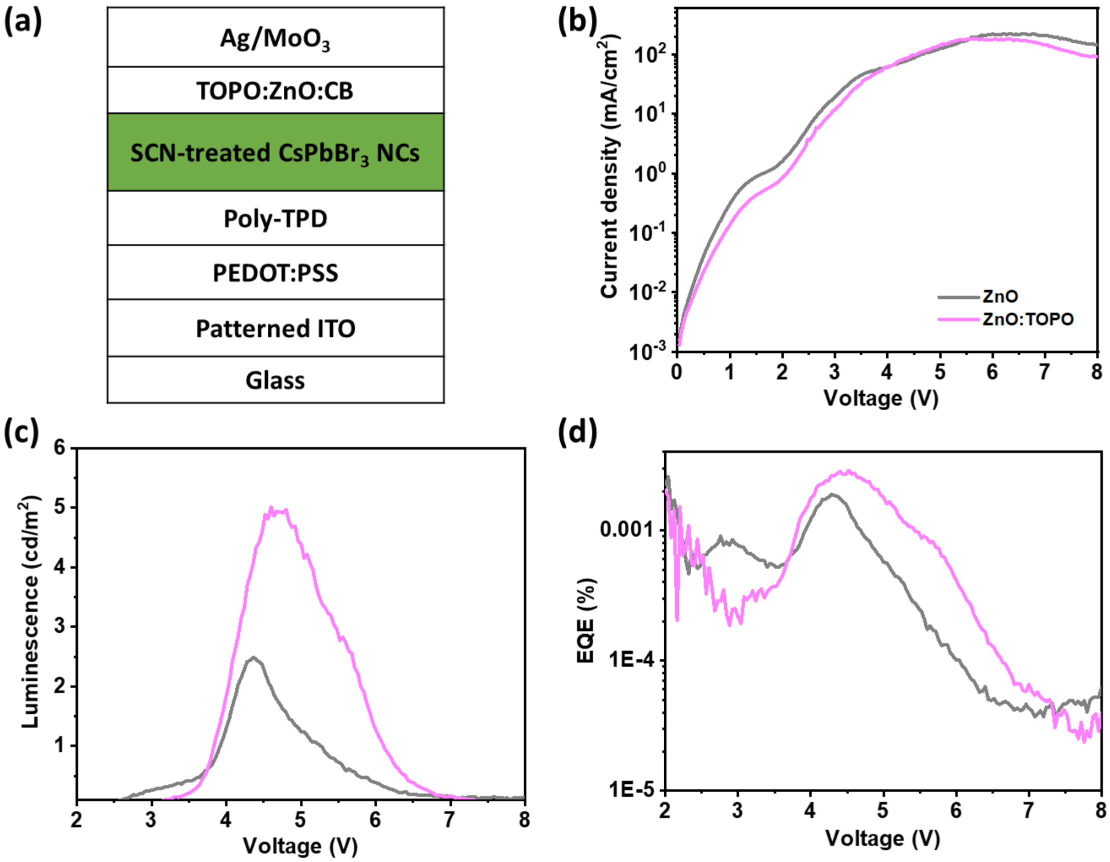

Figure 4.23. (a) Diagram of the LED structure, (b) current density, (c) luminescence; and (d) EQE as a function of driving voltage in the perovskite NC LEDs with a mixture of TOPO and ZnO NCs as ETL atop of perovskite NC layer.

In summary, a ZnO NC solution was explored to act as ETL in perovskite NCs-based LEDs. The effect of the dispersion solvent for ZnO NCs on the roughness of the ZnO NCs films and the LED performance was studied. LEDs with inverted structure suffer serious leakage with ZnO NCs layer beneath the perovskite NCs layer. A mixed solvent of hexane and DE at a proper ratio was found to be more resistant to being washed away by ZnO NC solution in LEDs with a normal structure. TOPO improved the performance of LEDs with ZnO NCs as ETL atop perovskite NCs layer. The work gives guidance to fabrication of all-inorganic perovskite LEDs.

4.5 Summary

In conclusion, green LEDs were fabricated based on $CsPbBr_3$ NC solutions treated in different ways. Highly stable and efficient green LEDs, with L_{50} of 27 min at 5 V, were obtained, based on $CsPbBr_3$ NC solutions treated with proper amount of SCN solution. Possible reasons for the performance of the champion device were investigated by C-AFM in terms of morphology and current distribution of NC film under applied voltages. The results show that performance of NC-based LEDs strongly depends on the distribution of NCs in the emissive layer, and that the efficiency roll-off in the NC-based LEDs at high current density can be attributed to displacement and deterioration of NC film with increasing applied voltages. The work proposes a facile route to treat sensitive perovskite NCs and to fabricate perovskite NC-based LED with high stability. Moreover, a new evidence was supplied for the efficiency roll-off in NC LED.

The effect of potassium on $CsPbBr_3$ NC solutions and LEDs was also studied. It was found that treating $CsPbBr_3$ NC solutions with potassium salts during post-synthesis is unfavorable, although it is usually beneficial when used directly during synthesis of halide perovskite according to literature.

In addition, LEDs with inorganic ETL, ZnO NCs, was explored. The effect of the dispersion solvent for ZnO NCs on the roughness of the ZnO NCs films and the LED performance was studied. A mixed solvent of hexane and DE at a proper ratio was found to be resistant to being washed away by ZnO NC solution in LEDs with a normal structure. TOPO was found to be able to further improve the performance of green LEDs. The work gives guidance to fabrication of all-inorganic perovskite LEDs.

Chapter 5: Lead bromide perovskite nanocrystal-based blue LEDs

In this chapter, halide perovskite NC solutions treated with copper chloride and LEDs based on the NC solutions are presented. Various parameters, such as types of metal chloride, treatment method, reaction time, the concentration of copper chloride, types of ligands, purification cycles and dispersion solvent for preparation of the LHP NCs were studied. The optimized NC solutions were used to fabricate LEDs. The results of device characterization indicate a significant impact of the solvent used in the NC dispersion on the efficiency and spectral stability of the LEDs. The champion device, based on NCs with optimized ligands, results in an EQE of 5.02% and a luminance of 130 cd m^{-2} at the maximum EQE. This work provides a novel and promising way for the fabrication of highly efficient LHP NC-based blue LEDs.

5.1 Towards LHP NCs with blue emission

5.1.1 Pristine NC solution

The pristine NC solution (labeled as Cu0) was synthesized according to the procedure reported by Song *et al* [79]. TEM images of the obtained Cu0 NCs are shown in Figure 5.1a-b. The NCs show a wide size distribution, as particles ranging from 8 to 25 nm in size are present. Figure 5.1c presents the PL spectrum of the Cu0 NCs. The PL peak is at 512 nm, corresponding to a green emission. The FWHM of the PL is 23 nm, which may be due to the wide size distribution. Figure 5.1d presents the UV-Vis absorption spectrum of the Cu0 NC solution.

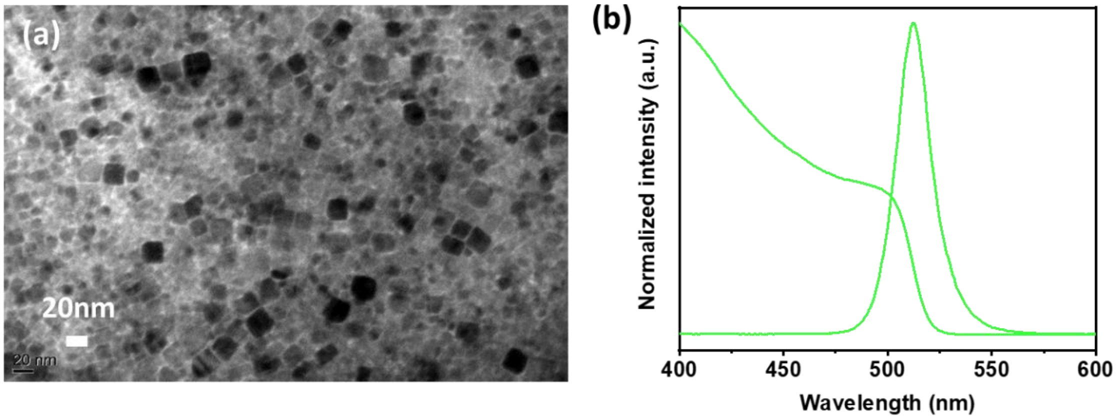

Figure 5. 1. Characterization of Cu0 NC solution: (a) representative TEM image, and (b) UV-Vis absorption plot and PL spectra.

5.1.2 Effect of metal chloride treatment

We treated the Cu0 NC solution with different metal chlorides solutions during the ligand exchange process with DDAB. To be specific, $ZnCl_2$, $MgCl_2$, $MnCl_2$, $CuCl_2$ and $NiCl_2$, with a fixed molar ratio of 30% vs. $PbBr_2$, was dissolved together with DDAB in toluene by sonication for one hour. The obtained NC solutions were individually labeled as Zn30, Mg30, Mn30, Cu30, and Ni30. Figure 5.2 shows the absorption spectra and PL plots of the resulting NC solutions.

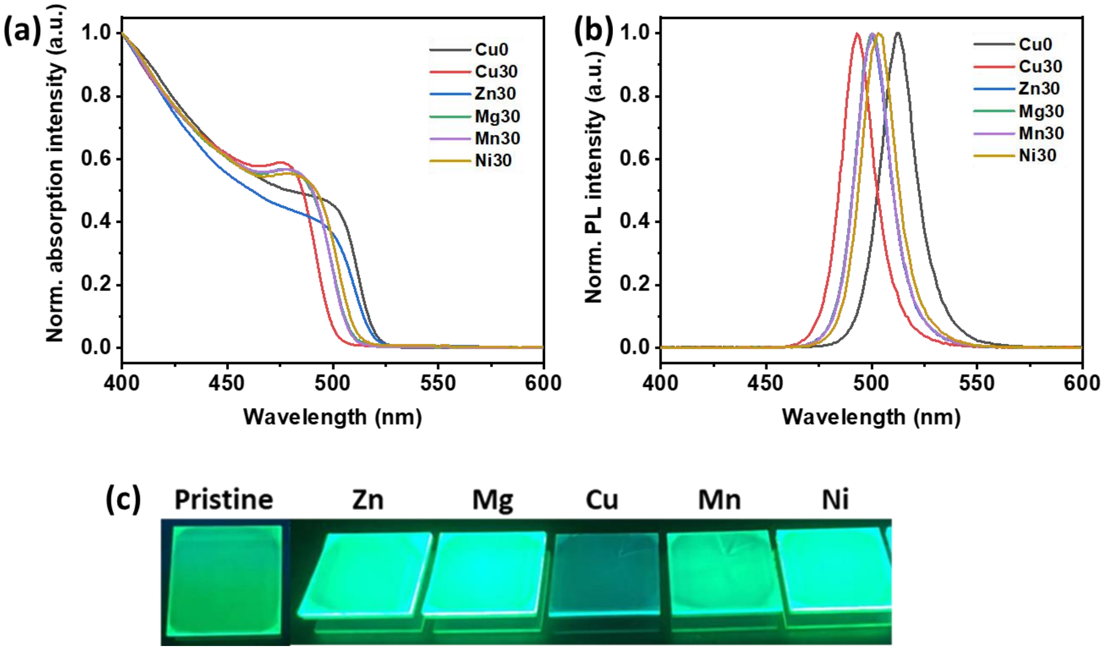

Figure 5.2. Characterization of NC solutions treated with metal chlorides. Normalized (a) UV-Vis absorption and (b) PL spectra; (c) photos of the films based on the treated NC solutions under UV illumination.

All treated NC solutions show blue-shifted absorption edges and PL peaks (Figure 5.2a, b). In particular, relative to the Cu0 NCs, Zn30, Mg30 and Mn30 NCs present a blue-shift of ~12 nm, Ni30 of ~10 nm and Cu30 NCs of ~20 (Table 5.1). Figure 5.2c shows the photos of the treated

NCs-based films under UV illumination. Obviously, all films exhibit brighter and greener color than the Cu0 NC film, except the CuCl2-treated one. In addition, all NC solutions present PL plots with slightly narrower FWHM than that of the Cu0 NC solution (Table 5.1).

Table 5. 1. Statistics of the PL peaks and FWHM of the NC solutions treated with different types of metal chlorides.

NC solutions ID	**PL peak position (nm)**	**PL peak FWHM (nm)**
Cu0	512.7	21.6
$ZnCl_2$	500.5	20.7
$MgCl_2$	500.6	20.6
$CuCl_2$	493.6	20.1
$MnCl_2$	500.7	20.5
$NiCl_2$	503.4	20.7

Overall, the treatment with $CuCl_2$ could lead to obvious blue-shift of the emission of the NC solution, while treatment with $ZnCl_2$, $MgCl_2$ or $MnCl_2$ or $NiCl_2$ have relatively less influence on the emission wavelength.

A representative synthesis diagram for the Cu30 NC solution is shown in Figure 5.3a. Pristine green NCs were transformed to NCs with sky-blue emission under UV light, simply by introducing $CuCl_2$ during the DDAB ligand exchange in the post-synthesis. The Cu30 NCs are characterized by particles of size in the range of 5-25 nm, with an average value of 10 nm (Figure 5.3c), similar to that of Cu0 NCs (Figure 5.3b). Photos of the NC solutions with and without UV illumination are displayed beside the TEM images in Figure 5.3b, c, with the Cu0 NC solution showing green emission and the Cu30 NC solution showing sky-blue emission.

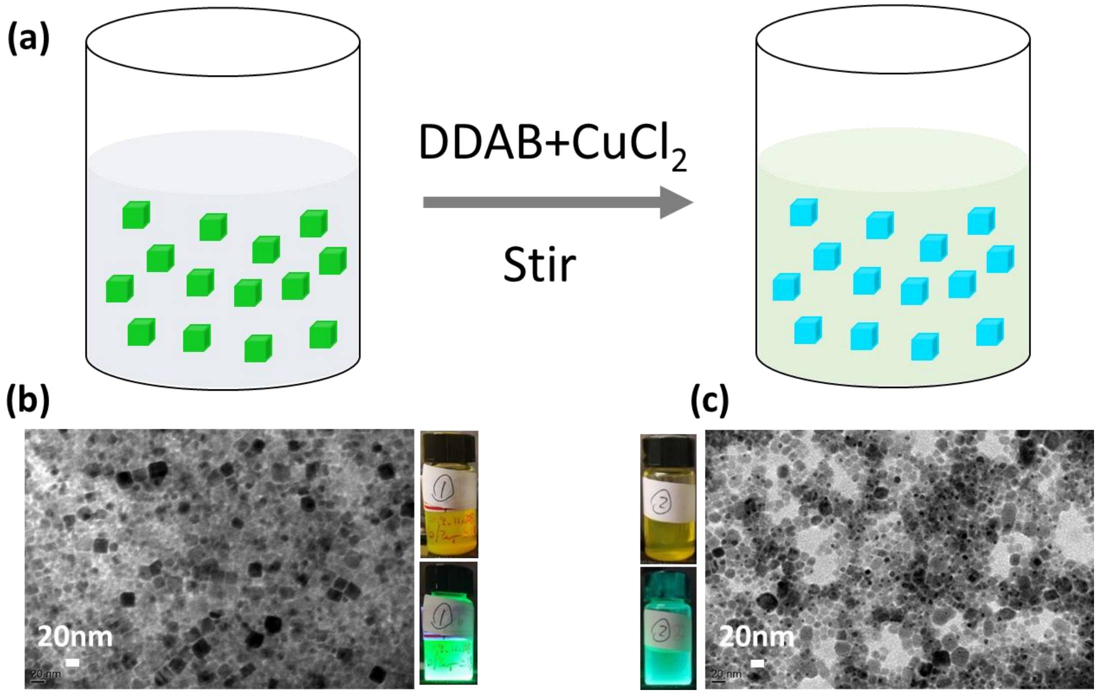

Figure 5.3. Synthesis and characterization of Cu0 and Cu30 NCs. (a) Schematic diagram of the synthesis of Cu30 NC solution; and representative TEM images of (b) the Cu0 NC solution and (d) Cu30 NC solution, together with photos of the NC solutions under sunlight and UV light, beside each TEM image [108].

5.1.3 Treatment methods of $CuCl_2$

Since $CuCl_2$ leads to emission of the NC solution most shifted to the blue range, three methods were developed to make the treatment with $CuCl_2$. Firstly, $CuCl_2$ was mixed with $PbBr_2$ precursor during the synthesis stage. Secondly, $CuCl_2$ was mixed with DDAB precursor during the ligand exchange stage. Thirdly, $CuCl_2$ was mixed with EA during the purification stage. The optical performance of the obtained NC solutions were characterized and the results are shown in Figure 5.4.

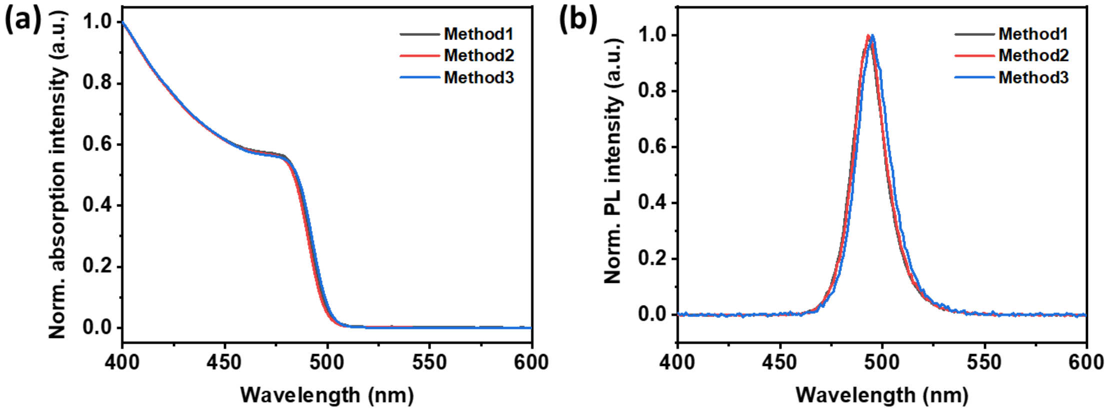

Figure 5.4. Characterization of NC solutions obtained by different synthesis routes. Normalized (a) UV-Vis absorption spectra; and (b) PL spectra.

Table 5.2. Statistics of the PL peaks and FWHM of the NC solutions obtained by the three different $CuCl_2$ treatments tested.

	PL peak position (nm)	**PL peak FWHM (nm)**
Method1	493.5	20.4
Method2	493.9	20.3
Method3	495.6	20.7

The absorption edges and PL spectra of the three NC solutions look similar (Figure 5.4a, b), in spite that the solutions obtained with the third method exhibits slightly longer emission wavelength (Table 5.2).

However, the NC solutions obtained by the three methods show different stability in air. The first and third NC solutions started to become blurred and presented precipitation after storing for a few days in air. In contrast, the second NC solution remained clear and bright for more than half a year. Thus, we adopted the second method to treat the NC solutions in the subsequent experiments.

5.1.4 Effect of reaction time

The DDAB ligand exchange process together with $CuCl_2$ was investigated, in order to determine the most suitable reaction time. The characterization results of the obtained NC solutions are shown in Figure 5.5.

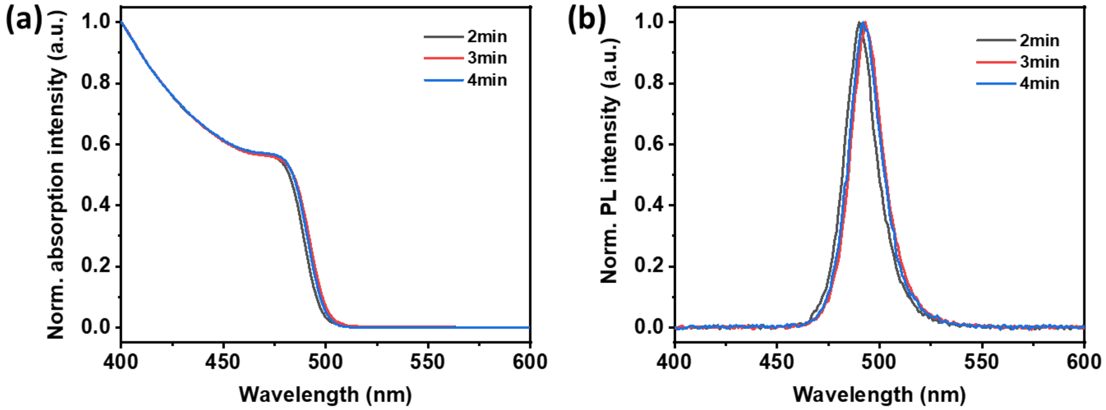

Figure 5.5. Characterization of NC solutions obtained after different reaction time. Normalized (a) UV-Vis absorption and (b) PL spectra.

Table 5.3. Statistics of the PL peaks and FWHM of the NC solutions obtained after reacting for different time during treatment with $CuCl_2$

Reaction time (min)	PL peak position (nm)	PL peak FWHM (nm)
2	491.0	20.3
3	494.0	20.4
4	493.1	20.3

The UV-vis absorption spectra and the PL intensities look similar (Figure 5.5a, b). When the reaction time is 2 min, a PL peak at 491 nm was obtained. With increasing reaction time, the PL peak wavelength increased. Thus, 2 min is determined as the optimal reaction time.

5.1.5 Effect of $CuCl_2$ concentration

Given that $CuCl_2$ could shift the emission wavelength from green to sky-blue, we investigated the role of the $CuCl_2$ concentration on the extent of the blue-shift. Therefore, the pristine green NC solutions were treated with different amount of $CuCl_2$ in the presence of DDAB. The characterization results of the obtained NC solutions are shown in Figure 5.6.

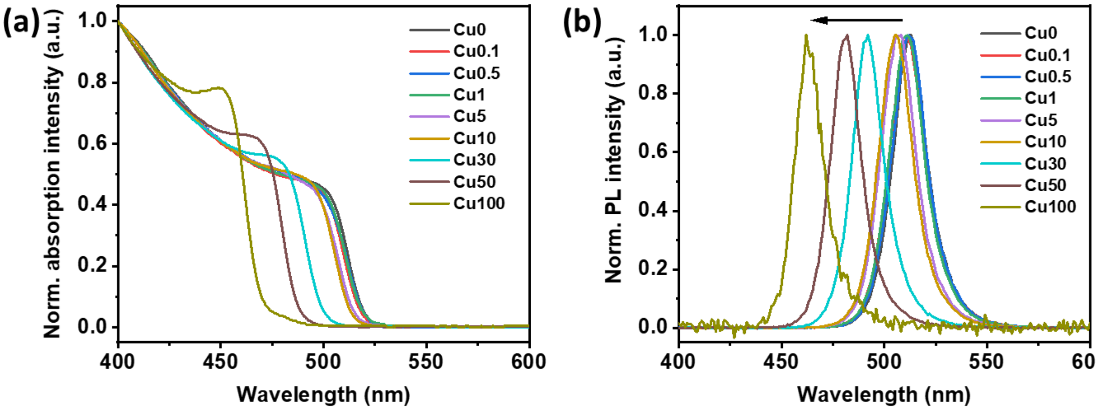

Figure 5.6. Characterization of NC solutions obtained with different amount of $CuCl_2$. Normalized (a) UV-Vis absorption and (b) PL spectra.

Table 5.4. Statistics of the PL peaks and FWHM of the NC solutions treated with different amount of $CuCl_2$

NC solution ID	PL peak position (nm)	PL peak FWHM (nm)
Cu0	512.7	21.6
Cu0.1	511.4	22.4
Cu0.5	512.3	22.0
Cu1	511.2	21.9
Cu5	507.0	21.5
Cu10	505.7	21.1
Cu30	492.2	20.0
Cu50	481.4	19.0
Cu100	463.6	17.9

Different amounts of $CuCl_2$ were added in a series into the reaction system, labeled sequentially as Cu0, Cu0.1, Cu0.5, Cu1, Cu5, Cu10, Cu50 and Cu100, where the number indicates the molar percentage of Cu added to the Pb used in the synthesis, and the optical performance of the obtained NCs was characterized. When the amount of $CuCl_2$ was lower than 1% of the mole amount of $PbBr_2$, the absorption spectra and the PL peaks kept almost the same (Figure 5.6a, b). In contrast, when the amount of $CuCl_2$ was more than 5% of that of $PbBr_2$ used in the reaction system, the PL peaks displayed gradually enlarged blue-shift, moving from 513 nm for the Cu0 NCs, up to 507 nm, 506 nm, 481 nm, and 464 nm for the Cu5, Cu10, Cu50, and Cu100 NCs, respectively (Table 5.4). The obtained results are consistent with the effect of anion exchange as reported in the literature, where it appears to have a non-linear relation to the concentration [75].

Considering that the Cu30 NC solution remained stable in air for a long time while Cu50 and Cu70 precipitated after a week, further investigations were carried out on Cu30 NC solutions.

5.1.6 Effect of ligands

Treatment with high concentration of $CuCl_2$ could lead to blue-shifted emission, but the emission intensities were reduced. The brightness of NCs could be enhanced by choosing the proper ligands to reduce the density of non-radiative defects on the NCs [37, 38, 56, 149]. Here, DDAB, DDAC, and a mixture of DDAB and dimethyl didodecylammonium chloride (DDAC) in equal amounts were used, to perform post-synthesis ligand exchange on the NCs. The obtained NCs were labeled as Cu30DDAB, Cu30DDABDDAC and Cu30DDAC, respectively.

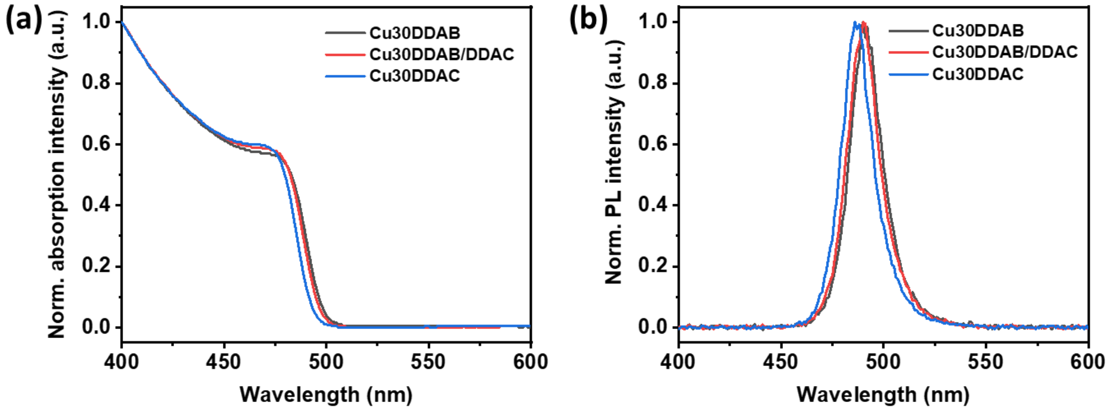

Figure 5.7. Characterization of NC solutions obtained with different ligands. (a) UV-Vis absorption, (b) PL, and (c) normalized PL spectra; (d) statistics of the PL peaks and FWHM of the PL peaks of the Cu30DDAB, Cu30DDABDDAC and Cu30DDAC NC solutions.

Table 5.5. Statistics of the PL peaks and FWHM of the NC solutions treated with different ligands

Ligand	**PL peak position (nm)**	**PL peak FWHM (nm)**
DDAB	491.5	20.2
DDABDDAC	490.2	20.3
DDAC	487.3	20.0

The UV-Vis absorption edge and the emission wavelength shift stronger to the blue with increasing amount of DDAC (Figure 5.7 and Table 5.5). With the PL peak of the Cu30DDAB NC solution as a reference, the blue-shifts are ~2 nm and 5 nm for the PL peaks of the Cu30DDABDDAC and Cu30DDAC NC solutions (Figure 5.7b and Table 5.5), respectively. The PLQY of the Cu30-DDAB and Cu30DDABDDAC is 58% and 67%, respectively.

5.1.7 Effect of washing times

The as-synthesized perovskite NCs usually have poor conductivity, due to the presence of many organic ligands [67]. Purification or ligand exchange of the as-synthesized NCs are usually performed, to improve the conductivity of the NCs [40, 70]. However, NCs are usually easy to be damaged with increasing washing or purification cycles [65]. Hereafter, we compared the optical performance of the treated and untreated NC solutions after once and twice purification by EA (Figure 5.8). The detailed experimental procedure was the same as what was described in Chapter 2.

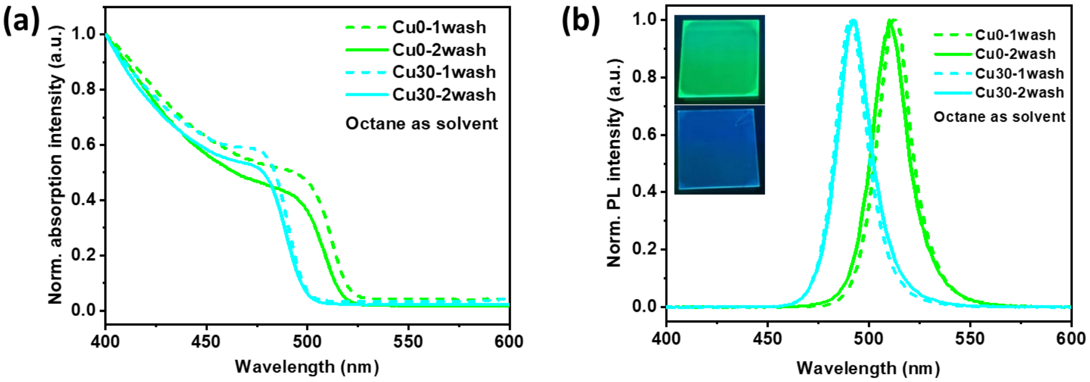

Figure 5.8. Comparison of Cu0 and Cu30 NC solutions after purifying for different times. Normalized (a) UV-Vis absorption and (b) PL spectra.

Table 5.6. Statistics of the PL peaks and FWHM of the Cu0 and Cu30 NCs dissolved in octane after being washed once and twice

Octane as solvent	PL peak position (nm)	PL peak FWHM (nm)
Cu0-1wash	512.7	21.8
Cu0-2wash	510.6	22.8
Cu30-1wash	491.5	20.4
Cu30-2wash	492.8	21.5

The pristine NC solution showed a 2-nm blue-shift in absorption edge and PL peak after the second purification (Figure 5.8a, b). In contrast, after the second wash, the Cu30 NC solution showed merely a 1-nm red-shift in PL peak (Figure 5.8b and Table 5.6), which is within the error range. Particularly, the Cu30 NC solution presented a steeper absorption edge (Figure 5.8a) than that of the Cu0 NC solutions in both cases. The inset of Figure 5.7b displays the photos of the films based on twice-washed Cu0 and Cu30 NC solutions under UV light. The films look smooth and bright. Thus, the Cu30 NC solution presented high resistance to purification with EA and the twice-washed Cu30 NC solution showed not only well-retained PL performance but also good conductivity in LEDs, which will be shown in next section.

5.1.8 Effect of ageing

The stability of NCs in solution could impact on the stability of corresponding devices. To fabricate stable LEDs, highly stable NC solutions are therefore desired. To check for the stability, we recorded the optical performance of the fresh and aged Cu30 NC solutions over time, as shown in Figure 5.9.

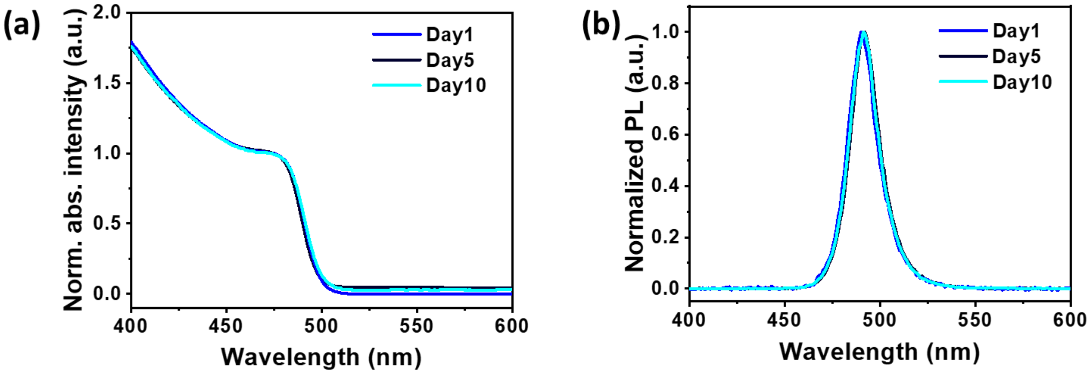

Figure 5.9. Characterization of fresh and aged Cu30 NC solutions. (a) UV-Vis absorption, (b) PL, and (c) normalized PL spectra; (d) statistics of the PL peaks and FWHM of the PL peaks of the fresh and aged Cu30 NC solutions.

Table 5.7. Statistics of the PL peaks and FWHM of the fresh and aged Cu30 NC solutions

	PL peak (nm)	**FWHM (nm)**
Day1	491.0	20.3
Day5	492.2	20.0
Day10	491.7	20.0

The absorption edges of the fresh and aged Cu30 NC solutions remained similar (Figure 5.9a). The PL peaks remained almost unchanged after ageing (Figure 5.9c). In particular, the PL intensities did not decrease after ageing for more than ten days (Figure 5.9b). These results indicate that the Cu30 NC solution has high stability in air.

5.1.9 Effect of solvent

The solvent used for dispersing the NCs has been reported to have a significant effect on the film formability [214]. We therefore compared the effect of using hexane and octane as dispersing solvent for the Cu30 NC solution. There is some difference in the absorption profile (Figure 5.10a), while the PL spectra are almost the same (Figure 5.10b).

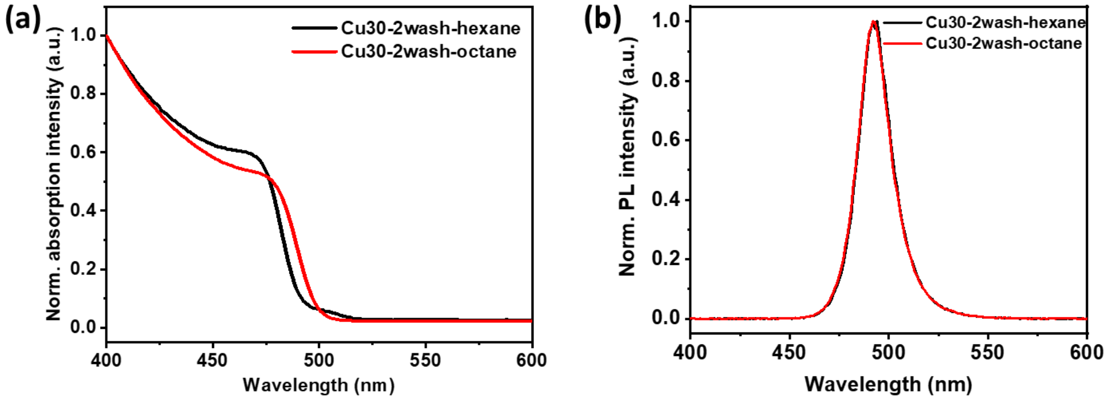

Figure 5.10. Characterization of Cu30 NC solutions dissolved in different solvents. Normalized (a) UV-Vis absorption, and (b) PL spectra.

Table 5.8. Statistics of the PL peaks and FWHM of the Cu30-hexane and Cu30-octane NC solutions.

Sample ID	PL peak position (nm)	PL peak FWHM (nm)
Cu30-2wash-hexane	493.2	21.3
Cu30-2wash-octane	492.8	21.5

The films based on the Cu30-octane and Cu30-hexane NC solutions were imaged by AFM, with a scan size of 5 μm. In Figure 5.11, representative images are shown. Sa in the Figure 5.11 is defined as the amplitude parameter of average deviation from the mean of the height distribution.

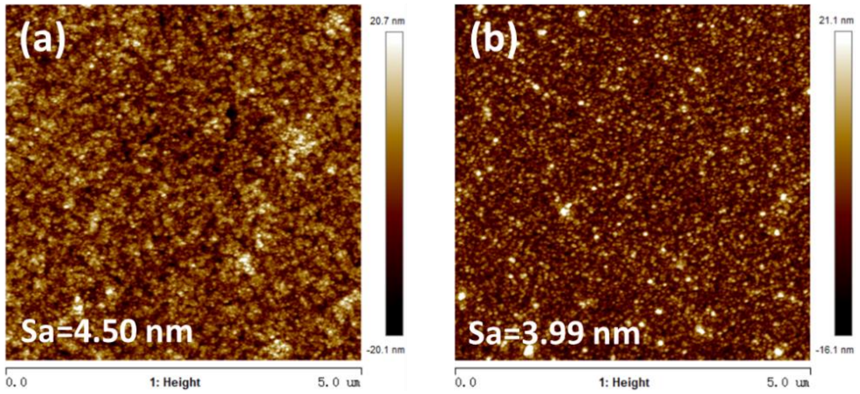

Figure 5. 11. Surface topography of the NC films. AFM images of (a) Cu30-hexane, and (b) Cu30-octane NCs-based films.

In the specific case shown, the film from the Cu30-octane solution (Figure 5.11b) appears slightly smoother than that obtained from the Cu30-hexane solution (Figure 5.11a). Actually, the film roughness should correlate positively with the higher evaporation rate of the respective solvent during spin-coating [136, 214]. According to Sun and coworkers, the higher evaporation rate of hexane could lead to striation defects on the film [214], and generally result in perturbation of the NCs self-assembly into a smooth film.. In addition to the evaporation rate, the different viscosity of the solvents, also associated with the evaporation time, may also play a role in influencing the drying process and uniformity of the films [215]. Independent on the equivalent roughness observed in Figure 5.11, octane seemed to be overall a better solvent for the Cu30 NC solution, in terms of film quality as compactness and general long-range uniformity.

5.1.10 Discussion on the role of $CuCl_2$

According to the above studies, the transformation observed from Cu0 to Cu30 may be anion exchange between bromide and chloride, which has been reported to be thermodynamically favorable [216], after introduction of metal chlorides during the ligand exchange process. Indeed, all NC solutions treated with metal chlorides presented blue-shift relative to the Cu0 NC solution (Figure 5.12a, b). Moreover, treatment of Cu0 NC solution with $CuBr_2$ or $ZnBr_2$ [47] showed almost no shift in PL peak position, as shown in Figure 5.12c, d. This is most likely due to the absence of anion exchange between the NCs and the added salts, which is reported to be necessary for metal doping inside HP NCs [217, 218].

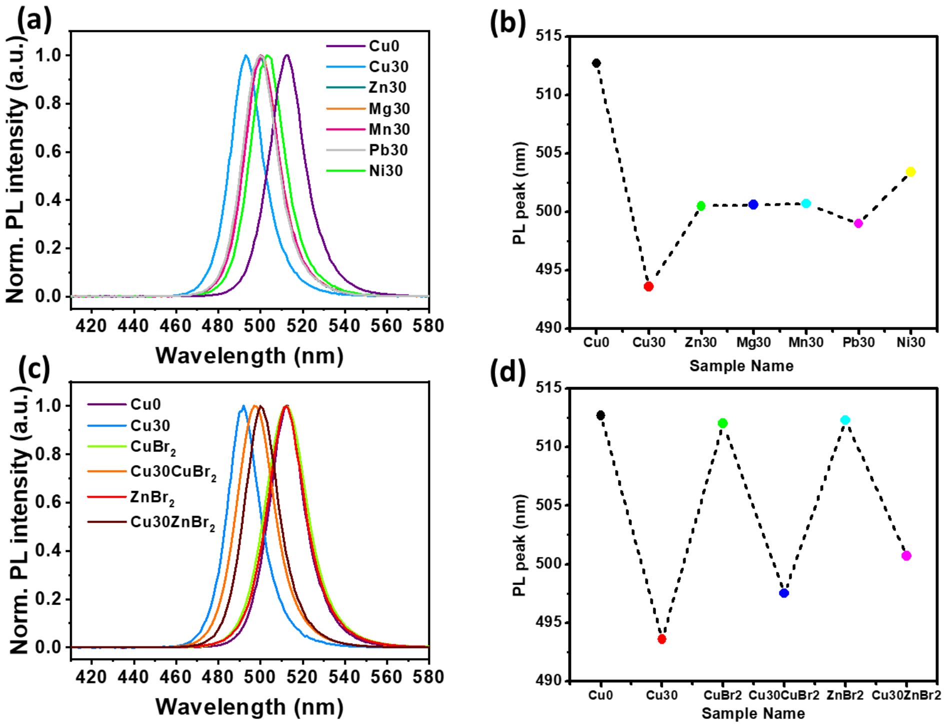

Figure 5.12. (a) PL spectra and (b) PL peak position of NC solutions treated with different types of metal chlorides; and (c) PL spectra and (d) PL peak position of NC solutions treated with $CuBr_2$ or $ZnBr_2$ in the presence or absence of $CuCl_2$.

Secondly, the experiments performed by us suggest that the presence of copper ions may facilitate the anion exchange [219], when $CuCl_2$ concentration in the reaction system is beyond a certain threshold. Indeed, the Cu30 NC solution presents a blue-shift in PL peak position which is 10 nm larger than those of the rest treated NC solutions (Figure 5.12a, b). Co-doping experiments with $ZnCl_2$, $MgCl_2$, or $MnCl_2$ added together with $CuCl_2$ to the Cu0 NCs solution, also support a role of Cu in the transformation. As shown in Figure 5.13 and Table 5.9, the PL peak of the Cu50 NCs is at 481 nm, which is lower wavelength than that of the PL peak of the Cu30Zn30 sample. The Cu30Zn30 was obtained by adding $CuCl_2$ and $ZnCl_2$ at a ratio of 30% of $PbBr_2$, respectively, to the Cu0 sample. This means that there is more chloride in the reaction system for the Cu30Zn30 NCs than that for the Cu50 NCs.

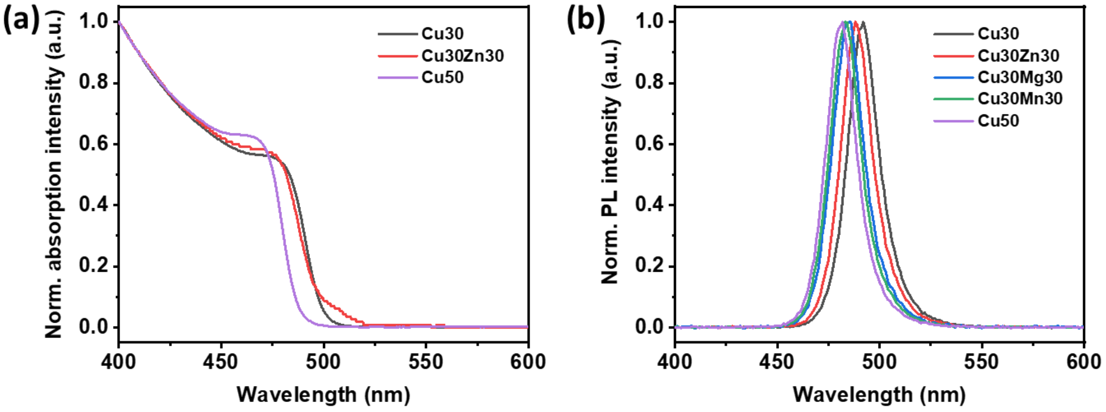

Figure 5.13. Characterization of NC solutions treated with a mixture of $CuCl_2$ and other metal chlorides. Normalized (a) UV-Vis absorption and (b) PL spectra.

Table 5.9. Statistics of the PL peaks and FWHM of NC solutions treated with a mixture of $CuCl_2$ and other metal chlorides

Sample ID	PL peak position (nm)	PL peak FWHM (nm)
Cu30	492.2	20.0
Zn30Cu30	489.0	20.0
Mg30Cu30	484.8	19.9
Mn30Cu30	483.4	19.6
Cu50	481.4	19.0

Thirdly, we tried to understand if copper ions may be doped inside the NCs, which is reported to be able to cause lattice contraction and further enlarged bandgap [220]. In order to figure out whether the effect of PL shift could be ascribed also to copper ions doped into the NCs, on one hand, we treated the as-synthesized NCs with either $CuBr_2$ or $ZnBr_2$, or with a mixture of $CuBr_2$ and $CuCl_2$ or $ZnBr_2$ and $CuCl_2$. The PL peak of the obtained Cu30-$CuBr_2$ NC solution is more blue-shifted than that of the Cu30-$ZnBr_2$ NC solution (Figure 5.12c, d). Considering that the same amount of bromide should be present in both reaction systems, this observation suggests that copper ions may be playing an active role, e.g., by doping the NCs.

On the other hand, $CuCl_2$ was used to treat not only $Cs_xFA_{1-x}PbBr_3$ NCs, but also similarly-synthesized $Cs_xFA_{1-x}PbCl_{1.5}Br_{1.5}$ NCs and $Cs_xFA_{1-x}PbCl_3$ NCs during post-synthesis, with the Cu/Pb molar ratios set at 0.3:1. The addition of $CuCl_2$ leads to a blue-shift of the absorption spectra and PL peak in all the three systems (Figure 5.14). In particular, we observed a blue-shift of ~6 nm in the PL of $Cs_xFA_{1-x}PbCl_3$ NCs after treatment with $CuCl_2$ and DDAB (Figure 5.14a and Table 5.10). The Br^- in DDAB could have induced anion exchange, but this is expected to cause a red-shift of the PL peak. The observed blue-shift could be due to doping of Cu ions into the NCs, which may have happened owing to the anion exchange [217]. Chen *et al.* observed a 2-nm PL blue-shift of $CsPbCl_3$ NCs during treatment with $CuCl_2$, and attributed it to the change of dielectric constant due to existence of copper ions in solution and on NC surface [219]. In our case, considering that the blue-shift is much larger, even in the presence of Br^- from DDAB, we attribute it to doping of copper ions into the NCs rather than merely absorbing on NC surface.

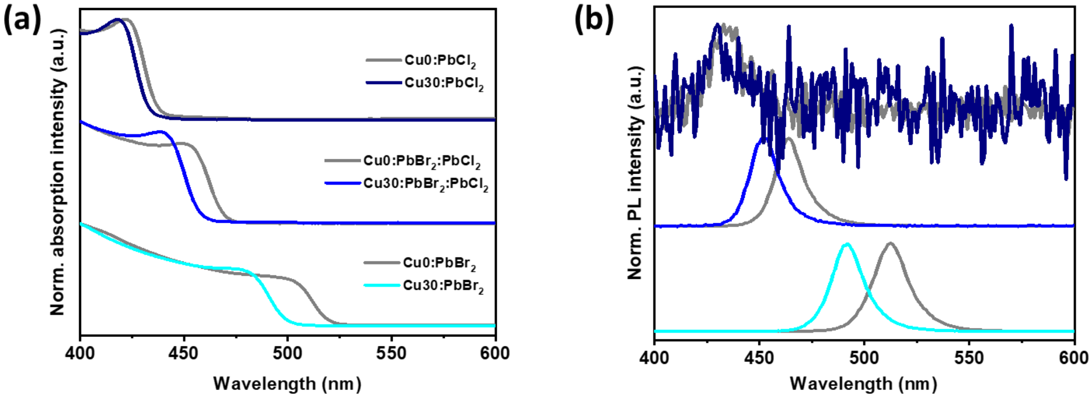

Figure 5.14. Comparison of (a) UV-Vis absorption and (b) normalized PL spectra of $Cs_xFA_{1-x}PbBr_3$, $Cs_xFA_{1-x}Pb(BrCl)_3$ and $Cs_xFA_{1-x}PbCl_3$ NC solutions treated with and without $CuCl_2$.

Table 5.10. Statistics of the PL peaks and FWHM of NC solutions treated with $CuCl_2$ in different NC systems.

Sample ID	PL peak position (nm)	PL peak FWHM (nm)
CsPbBr1.5Cl1.5-Cu0	464.4	17.6
CsPbBr1.5Cl1.5-Cu30	452.5	17.3
CsPbCl3-Cu0	435.5	21.4
CsPbCl3-Cu30	429.7	/

In addition, with element analysis by ICP-OES, we estimated a Cu/Pb molar ratio of approx. 3% in the NCs. This value has also been confirmed *via* XPS investigation, suggesting that Cu is homogeneously distributed in the NCs volume. Also, XPS analysis of the Cu 2p peaks (Figure 5.15) suggests that Cu is likely to be present as Cu(I) in the system, differently from what was reported by Rogach and coworkers [220], and it might occupy crystallographic sites different from those of Pb(II). We speculate that $CuCl_2$ may have made a difference in the crystal structure of the NCs. This may help improve the stability of the Cu-treated NCs compared with the pristine ones in air, in addition to the effect of ligand exchange with DDAB, which was reported to be able to lead to improved colloidal, structural, and morphological stability of perovskite NCs [34]. Further investigations are needed to elucidate this point.

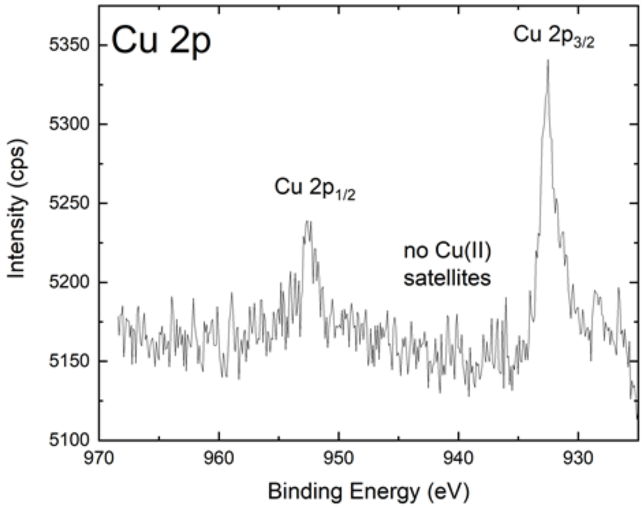

Figure 5.15. Cu 2p XPS peaks measured on the Cu30 sample. The main peak is centered at (932.6±0.3) eV. Together with the absence of the typical Cu(II) satellites in the 940 - 950 eV range [221], the data support the presence of Cu(I) in the system.

In summary, the blue-shift of the PL peak of the Cu30 NCs in comparison with the Cu0 NCs may be attributed to a combination of anion exchange enhanced by copper ions and doping of Cu ions into the NCs.

Combining the results of our analysis of the effect of $CuCl_2$ on the Cu0 NCs and our observations during the experiments, in Figure 5.16 we propose a possible reaction mechanism for the synthesis of the Cu30 NC solution.

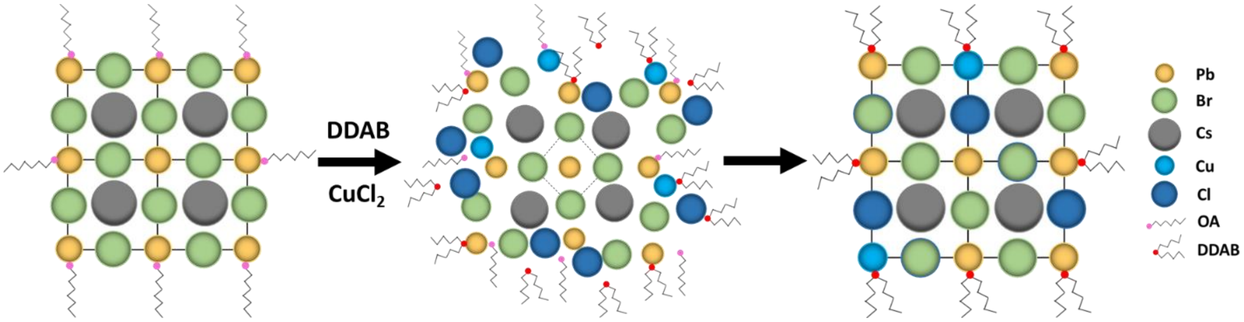

Figure 5.16. A proposed scheme of the reaction mechanism after the addition of $CuCl_2$ and DDAB into Cu0 NC solution.

Here, the observations represent that the turbid yellow-green $Cs_xFA_{1-x}PbBr_3$ NC solution turns transparent instantaneously and completely once DDAB:Toluene solution is poured into the crude NC solution to do ligand exchange, suggesting re-dissolution of the NCs. After a short time, the transparent solution gradually becomes turbid again, indicating formation of the final Cu0 NCs. This also applies to the Cu30 NCs. After addition of $CuCl_2$:DDAB:Toluene solution, the initial NCs may disintegrate and re-dissolve into the solvent. With increasing reaction time, lead bromide and/or chloride octahedral re-connect to each other and re-crystalize, together with some lead sites and OA ligands replaced by copper and DDAB, respectively, obtaining the final Cu30 NCs.

5.2 Towards blue LEDs

The structure that we adopted for all LED devices in this section is: ITO/PEDOT:PSS/PTAA/LHP NCs/TOPO/TPBi/LiF/Al (Figure 5.17a), which resembles the one previously reported by Song *et al.* [47]. Please refer to the Chapter2 for the detailed device fabrication procedure.

5.2.1 Effect of dispersing solvent for NCs on LED performance

Given that the solvent could influence the NC solutions and the subsequent quality of LEDs [214], we compared the performances of LEDs based on the Cu30-hexane NC solution and on the Cu30-octane NC solution.

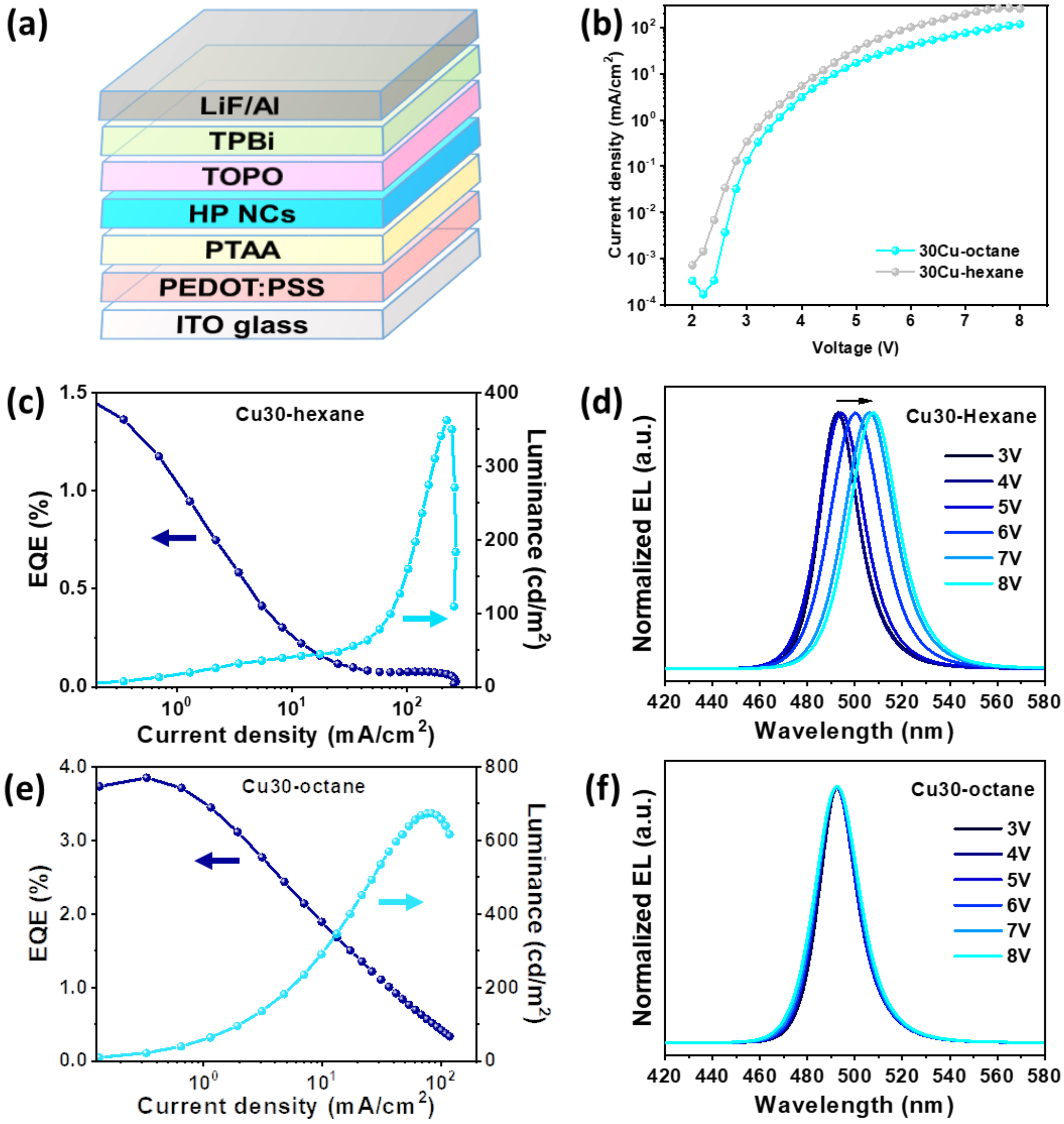

Figure 5.17. Performance of LEDs based on Cu30 NCs in different solvents. (a) Representative diagram of the LED structure; (b) comparison of the current density of Cu30-hexane and Cu30-octane LEDs as a function of applied bias; EQEs and luminance of (c) Cu30-hexane and (e) Cu30-octane LEDs as a function of current density; and normalized EL spectra of (d) Cu30-hexane and (f) Cu30-octane LEDs under increasing bias [108].

EQEs and luminance of LEDs with Cu30-hexane and Cu30-octane NCs as emissive layers are displayed as a function of current densities in Figure 5.17c, e, respectively. In both cases, the LEDs show a low turn-on voltage of 2.8 V at a luminance of 1 cd/m^2 (Figure 5.17b, c, e). For the LEDs based on the Cu30-octane NCs, the maximum EQE and CE reach 3.85% and 6.07 cd/A (Figure 5.17e and Table 5.11), respectively, which are higher than those of LHP NC-based sky-blue LEDs reported so far (Table 5.12) [102, 122, 124-134, 143, 144, 148, 149, 222]. The maximum luminance is 672 cd/m^2 and the luminance corresponding to the maximum EQE is 20 cd/m^2 (Table 5.11) [77, 136, 145, 146].

In contrast, the maximum EQE and CE of the LEDs based on the Cu30-hexane NCs only reach 1.51% and 2.45 cd/A (Figure 5.17c), respectively. The maximum luminance is 714 cd/m^2, while the luminance at the maximum EQE of the device is merely 3 cd/m^2. Besides, in the Cu30-hexane LED case there is a severe luminance roll-off, whereas this effect is less pronounced in the Cu30-octane LED one. Given that the current density of the Cu30-hexane LED is higher than that of the Cu30-octane LED throughout all the operation (Figure 5.17b), the roll-off could be attributed to degradation and displacement of the Cu30-hexane NCs, in agreement with our study on the mechanism of efficiency and luminance roll-off in NC-based LED by conductive AFM [40].

Table 5.11. Device performance of the LEDs based on Cu30 NCs in hexane or octane (Max: maximum; Lum: luminance).

Material	**Turn-on voltage (V)**	**Max Lum (cd/m^2)**	**Max EQE (%)**	**CE (cd/A)**	**Max PE (lm/W)**	**Lum@MaxEQE (cd/m^2)**	**J@Max EQE (mA/cm^2)**	**EL peak (nm)**	**FWHM (nm)**	**Ave. MaxEQEs (%)**	**Ave. MaxLum (cd/m^2)**
30-hexane	2.8	714	1.51	2.45	2.75	3	0.13	493	19	1.5	389.1
30Cu-octane	2.8	672	3.85	6.07	5.96	20	0.33	493	19	3.7	756.5
30Cu-Day10	2.8	692	4.02	6.54	6.85	8	0.12	494	18	3.7	670.3

Additionally, we could see a stark contrast between the EL spectra of the two devices made by using different solvents (Figure 5.17d, f). For the Cu30-octane LED, there is no shift in the EL peak with increasing bias, although the FWHM increases 1-2 nm at high voltage. Instead, for the Cu30-hexane LED, there is a severe red-shift of the EL peak during operation, together with an increased FWHM. Here, the different EL behaviors may be related to the quality of films, as previously discussed, and may further affect the current density and the current leakage of the devices under bias [136, 214]. Poor film quality for the Cu30-hexane case as demonstrated in Figure 5.11a is probable to cause current leakage and is unfavorable for devices. In addition, the higher current density of the Cu30-hexane LED may boost halide ion migration or degradation of the LHP NC layer, resulting in a red-shift of the EL spectra [223]. The significant differences in performance of the Cu30-octane and Cu30-hexane LEDs indicate that the solvent of NCs used for device fabrication matters, even if there is not much difference between the pure NC solutions.

Table 5.12. Statistics of performance of LHP sky-blue LEDs from literatures and the current work (TF: thin film).

Type	Material	Turn-on voltage (V)@cd/m2	Max Lum (cd/m2)	Max EQE (%)	CE (cd/A)	Max PE (lm/W)	Lum@MaxEQE (cd/m2)	J@MaxEQE (mA/cm2)	EL peak (nm)	FWHM (nm)	Ref.
3D TF	$MAPbBr_{1.08}Cl_{1.92}$	~3.3	~1.75	~0.0003	~0.00035	/	~1.65	~650	482	~20	[126]
	$Rb_xCs_{1-x}PbBr_{3-y}Cl_y$	~3.3	244	0.17	0.32	/	~7	~2	492	~20	[127]
	$PEA_{0.2}Cs_{0.4}MA_{0.6}Pb_{0.85}Mn_{0.15}(BrCl)_3$	~4.5	11800	0.58	/	/	~70	~90	~495	/	[128]
2D TF	$(EA)_2(MA)_{n-1}Pb_nBr_{3n+1}$	2.7	70	2.6	/	~3.8	~0.02	0.5	473, 485	~50	[129]
	$IPA/PEA_2MA/Cs_{n-1}PbnBr_{3n-1}$(80nm)	~7.1	~400	1.5	2.8	0.92	~280	8	490	28	[122]
	$IPA/PEA_2MA/Cs_{n-1}PbnBr_{3n-1}$(40nm)	~5.4	2480	~1	~1.9	~0.8	~500	30	490	28	
	$BA_2Cs_{n-1}Pb_n(BrCl)_{3n+1}$	4.5	~3000	6.2	~7	~2.5	3340	~45	487	/	[130]
Quasi-2D TF	$(4\text{-}PBA)_2PbBr_4:CsPbBr_3$	2.9	186	0.015	/	/	186	600	491	/	[131]
	$KBr:PA_2(CsPbBr_3)_{n-1}PbBr_4$	3.31	4359	1.45	2.25	/	4359	40	492	26	[102]
	$KBr:PA_2(CsPbBr_3)_{n-1}PbBr_4$	/	5737	1.07	/	/	5737	/	492	26	
	$100\%PEABr/CsPbCl_{0.9}Br_{2.1}$	3.2	3780	5.7	6.1	/	700	10	480	21	[132]
	$RbBr:PEA_2(Rb_{0.4}Cs_{0.6})_2Pb_3Br_{10}$	~3.5	854	1.48	/	/	~200	~4	490	~30	[124]
	$PBABr_{1.1}(Cs_{0.7}FA_{0.3}PbBr_3)$	3.3	800	9.5	12	/	54	~0.3	483	26	[133]
	$2\%YCl_3:PEACl:CsPbBr_3$	~3.3	9040	11	/	/	~600	~5	485	/	[134]
	$PEABr:(Cs_xGA_{1-x}PbBr_yCl_{1-y})$	~3.8	1003	8.2	13.1	10.5	2	~0.02	492	18	[125]
NP	$MAPbBr_3$	~3.5	<10	0.23	/	/	8.5	4.7	492	24	[222]
	$Cs[PbBr_6]^{4-}$	~4	48	0.55	1.1	0.19	/	<1	487	21	[143]
NC	$MAPbBr_xCl_{3-x}$	>7.8	2252	1.01	/	/	/	/	495	<30	[144]
	$CsPbBr_xCl_{3-x}$	~4.2	830	1.41	/	/	10.5	/	488	<25	[148]
	$Rb_xCs_{1-x}PbBr_3$	~4.2	186	0.87	/	/	93	~7	490	22	[149]
	$CsPbBr_{2.71}Cl_{0.19}$	~3	2063	3.5	/	/	~7	~0.06	490	~20	[75]
	Cu30-octane	~2.8	672	3.85	6.1	6	20	0.3	493	~19	Our work
	Cu30DDABDDAC	~2.6	1946	5.02	7.3	7.2	130	1.8	491	~20	Our work

Similar phenomena were also observed in LEDs based on Cu0 NCs dispersed in hexane or octane. EQEs and luminance of LEDs with Cu0-hexane and Cu0-octane NCs as emissive layers are displayed as a function of current densities in Figure 5.18a, c, respectively. For the LEDs based on the Cu0-octane NCs, the maximum EQE and CE reach 10% and 30 cd/A (Figure 5.18c), respectively. The maximum luminance is 6319 cd/m^2 and the luminance corresponding to the maximum EQE is 26 cd/m^2. In contrast, the maximum EQE and CE of the LEDs based on the Cu0-hexane NCs only reach 2.5% and 7.5 cd/A, respectively. The maximum luminance is 620 cd/m^2. This relatively low maximum luminance may be attributed to the relatively low current density of the device (Figure 5.18e). Moreover, there is a little red-shift of the EL spectra for the Cu0-hexane LED during operation (Figure 5.18b), while there is almost no shift in the EL peak under increasing bias for the Cu0-octane LED (Figure 5.18d).

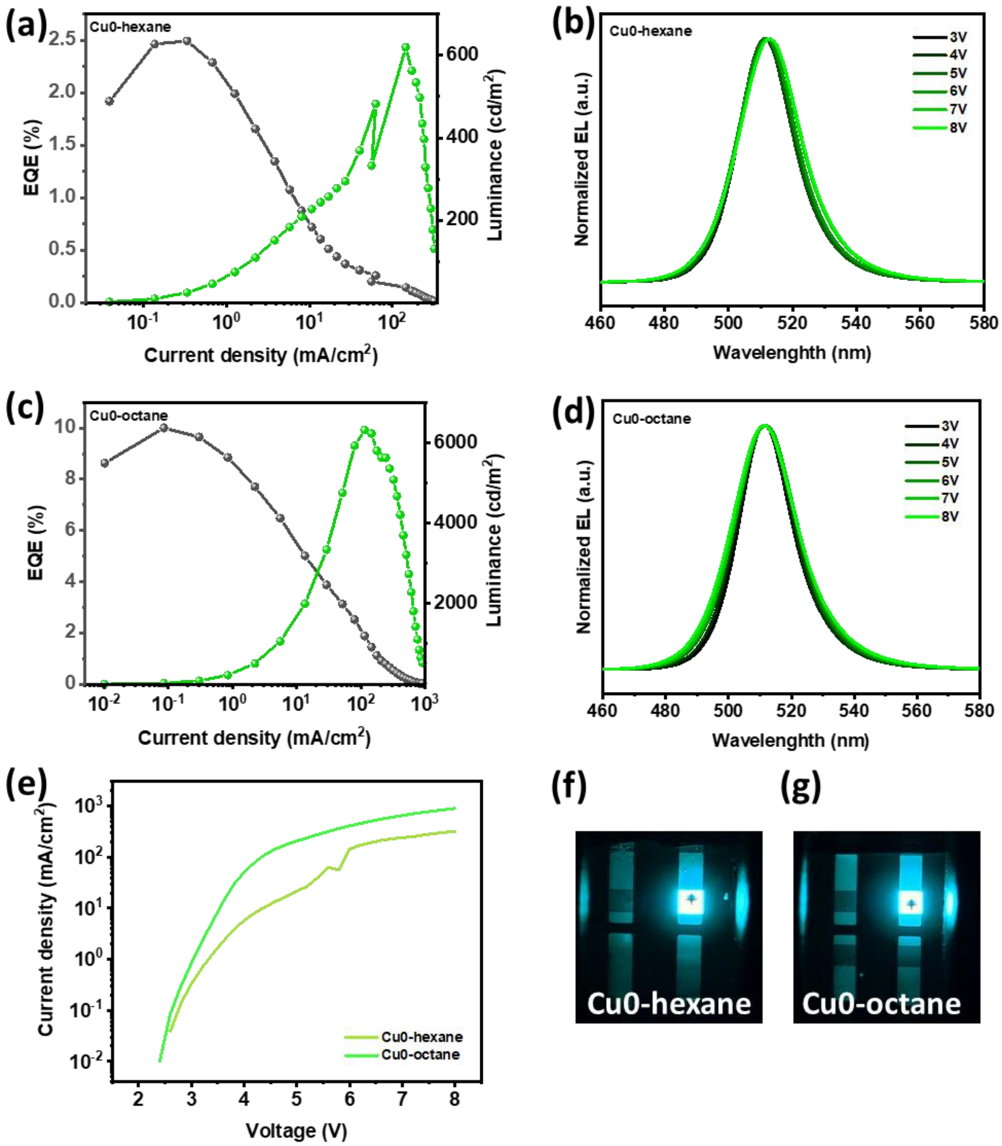

Figure 5.18. Performance of LEDs based on Cu0 NCs in different solvents. EQEs and luminance of (a) Cu0-hexane and (c) Cu0-octane LEDs as a function of current density; normalized EL spectra of (b) Cu0-hexane and (d) Cu30-octane LEDs under increasing bias; (e) a comparison of the current density of Cu30-hexane and Cu30-octane LEDs as a function of applied bias; and photos of the running (f) Cu0 and (g) Cu30 NCs-based LEDs.

Furthermore, we checked the operation lifetime of the Cu30-octane LED under a constant current density of 100 mA/cm^2, which corresponds to a bias ~ 5 V and a high luminance. The fitted L50 is ~ 14 s as shown in Figure 5.19.

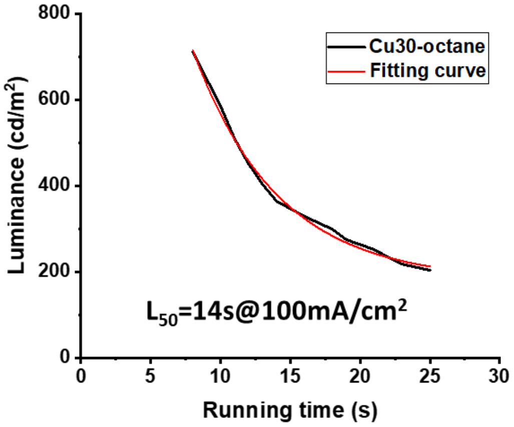

Figure 5.19. Exponential fitting curves of L50 of Cu30-octane LED operated at a constant current density of 100 mA/cm^2.

5.2.2 Effect of ageing of NCs on LED performance

Given that the optical performance of the Cu30 NCs remains stable even after storage in air for some days (Figure 5.9), we checked whether the aged NCs could also be used for LED fabrication. The 10-days-aged Cu30-octane NC solution was then used to fabricate LEDs. The maximum EQE and luminance are even higher than those of the LEDs based on fresh Cu30-octane NC solutions (Figure 5.20 and Table 5.11). The average EQE, 3.7%, is the same as that of the fresh Cu30-octane NCs-based LED. The EL peak is also stable without visible peak shift as the applied voltage increases, and the FWHM of the EL spectra remains stable during operation.

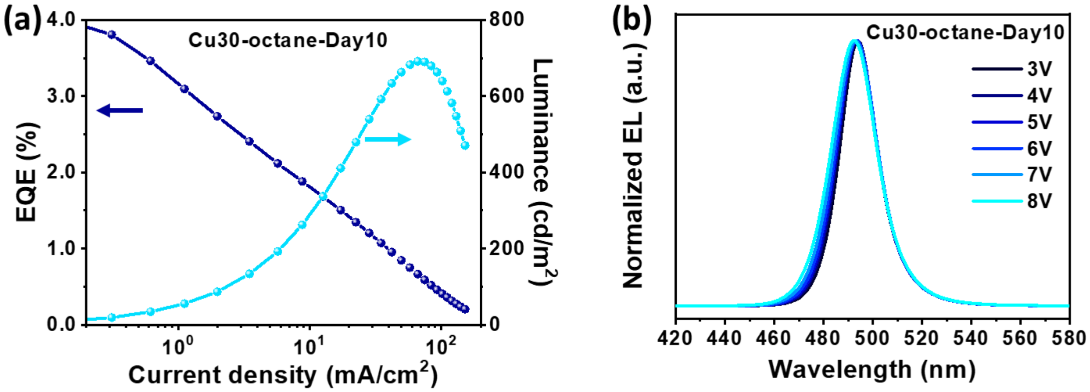

Figure 5.20. Stability of Cu30-octane NCs. (a) EQE and luminance as a function of current density; and (d) normalized EL spectra of the Cu30-octane-Day10 LED under increasing bias.

The similar device performance of the LEDs based on fresh and aged Cu30-octane NC solutions indicate high stability of the Cu30-octane NC solution in air and high reliability of the NC solutions to be applied in fabrication of devices.

5.2.3 Effect of $CuCl_2$ concentration on LED performance

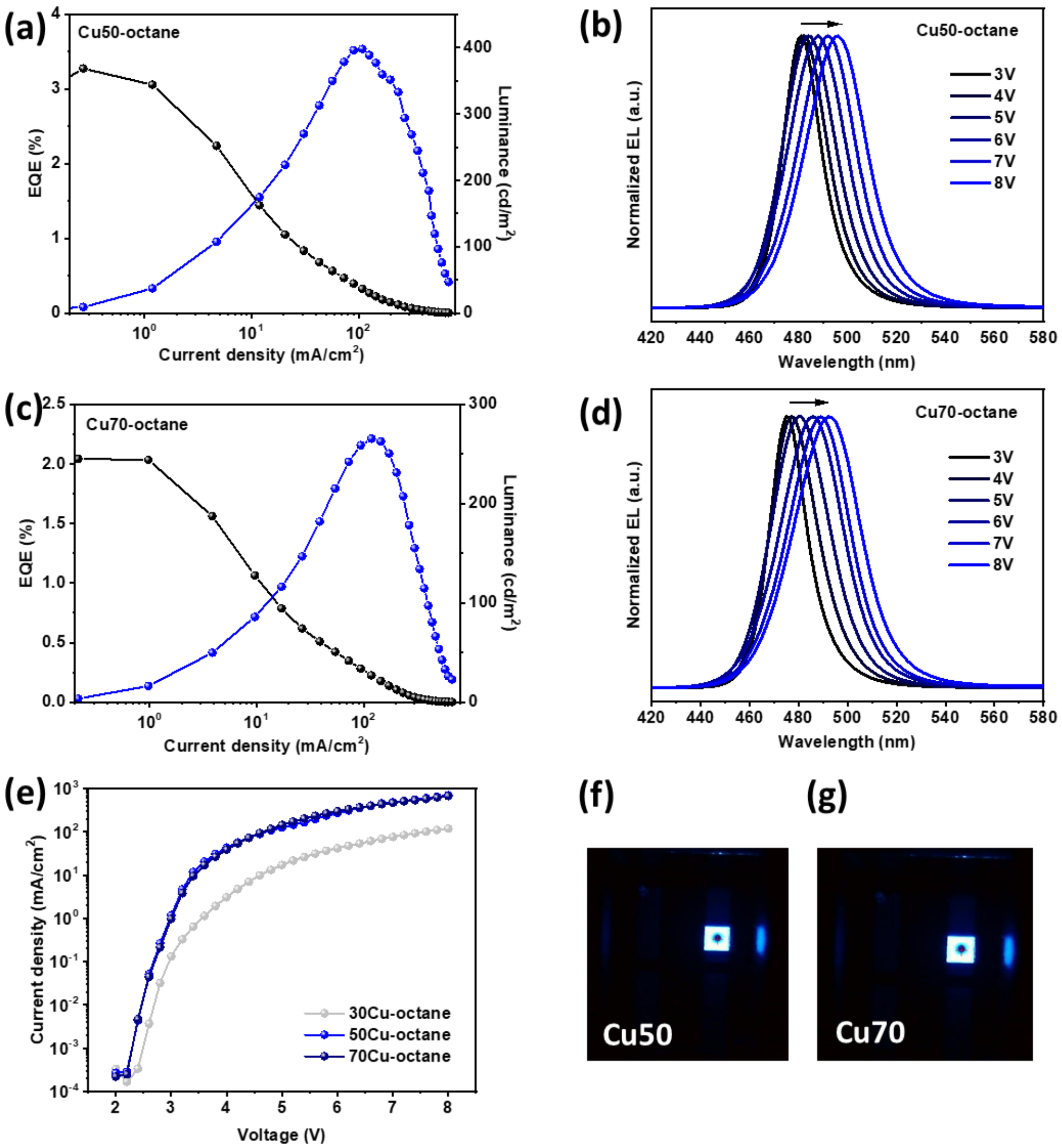

Figure 5.21. Performance of Cu50-octane and Cu70-octane LEDs. (a) EQE and luminance as a function of current density; and (b) normalized EL spectra under increasing bias of the Cu50-octane LED; (c) EQE and luminance as a function of current density; and (d) normalized EL spectra under increasing bias of the Cu70-octane LED; (e) comparison of current densities of the Cu30-octane LED, Cu50-octane LED and Cu70-octane LED as a function of applied voltage; and photos of the running (f) Cu50-octane and (g) Cu70-octane LEDs.

The excellent LED performance based on Cu30-octane NCs motivated us to apply the Cu50-octane and Cu70-octane NC solutions into blue LED fabrication. The Cu50-octane and Cu70-

octane LEDs achieve the maximum EQEs of 3.27% and 2.03%, respectively, at 481 nm and 475 nm with relatively high luminance (Figure 5.21a, c and Table 5.13). However, both EL spectra suffer from serious red-shift at bias higher than 3.8 V (Figure 5.21b, d). This may be caused by either phase segregation, due to the coexistence of Br^- and Cl^-, or to the high current densities observed in both cases with increasing operation voltage (Figure 5.21e) [132]. Figure 5.21f, g display the photos of the running LEDs with high brightness.

Table 5.13. Device performance of the 50Cu-octane and 70Cu-octane LEDs.

Material	**Turn-on voltage (V)**	**Max Lum (cd/m^2)**	**Max EQE (%)**	**CE (cd/A)**	**Max PE (lm/W)**	**Lum@ MaxEQE (cd/m^2)**	**J@Max EQE (mA/cm^2)**	**EL peak (nm)**	**FWHM (nm)**	**Ave. MaxEQEs (%)**	**Ave. MaxLum (cd/m^2)**
50Cu-octane	2.6	398	3.27	3.4	3.82	9	0.27	481	18	3.1	418.8
70Cu-octane	2.8	266	2.03	1.71	1.92	4	0.21	475	18	2	269.9

5.2.4 Effect of ligands for NCs on LED performance

LED efficiency depends on luminance and current density [182]. Introduction of a mixture of DDAB and DDAC during ligand exchange process has been demonstrated to be favorable for achieving NC solution with higher PL QY. Thus, the Cu30DDABDDAC NC solution was selected as the emissive layer to fabricate LEDs.

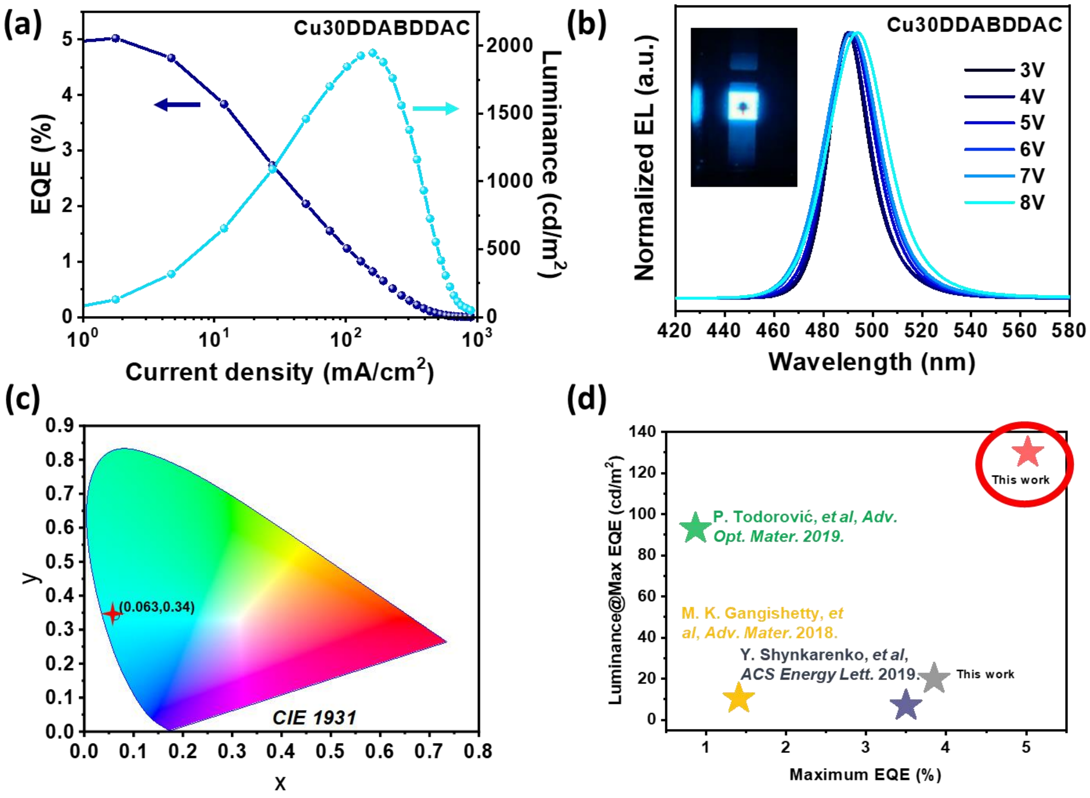

Figure 5.22. Performance of Cu30DDABDDAC LED and comparison with current literature. (a) EQEs and luminance of a Cu30DDABDDAC LED as a function of current density; (b) normalized EL spectra of the Cu30DDABDDAC LED under increasing bias, together with a photo of the running device in the inset; (c) CIE coordinates of the Cu30DDABDDAC LED; (d) comparison of maximum EQEs and luminance at the maximum EQEs of LHP NC-based sky-blue LEDs of our work with others available from the literature [108].

The maximum EQE and CE reach 5.02% and 7.31 cd/A (Figure 5.22), respectively, which were the highest values among the LHP NC-based sky-blue LEDs at that time (Figure 5.22a and Table 5.14). The maximum luminance is 1946 cd/m^2, which is a bit lower than what was reported by Deng *et al.*[143] with $MAPb(Br/Cl)_3$ NC-based LED and by Shynkarenko *et al.*[149] with $CsPbBr_{2.71}Cl_{0.19}$ NC-based LED. The EL peak at 490 nm wavelength falls within the sky-blue area, with CIE coordinates of (0.063, 0.341) (Figure 4c); see a photo of the running device in the inset of Figure 5.22b. Despite a small red-shift of the EL peak from 490 nm to 493 nm with the bias rising to 8 V (Figure 4b), the Cu30DDABDDAC LED still reflects good spectral stability, when considering the high associated current density (Figure 5.22a). The L50 of the device at a constant current density of 100 mA/cm^2 was ~ 17 s. A comparison between our device and others found in the literature for the maximum EQEs and corresponding luminance of the Cs-containing LHP NC-based LEDs, which emit at 490±5 nm wavelength, is presented in Figure 5.22d. Clearly, the Cu30

LED and Cu30DDABDDAC LED exhibit remarkably high scores, and the latter also achieves the highest luminance of 130 cd/m^2 at the maximum EQE.

Table 5.14. Device performance of LHP NC-based blue LEDs from literature and the current work.

Reference	Turn-on voltage [V]	Max Lum [cd m^{-2}]	Max EQE [%]	Lum@MaxEQE [cd m^{-2}]	EL peak [nm]	FWHM [nm]
[77]	5.1	742	0.07	/	455	20
[145]	~4.2	245	2.12	~0.2	466	18
[136]	~3.7	350	0.07	/	470	20
[224]	~2.8	~500	12.3	<20	<480	20
[146]	~5	30	0.86	~0.06	479	19
[144]	~4.2	830	1.41	10.5	488	<25
[148]	~4.2	186	0.87	93	490	22
[149]	~3	2063	3.5	~7	490	~20
[143]	>7.8	2252	1.01	/	495	<30
This work	**~2.6**	**1946**	**5.02**	**130**	**491**	**~20**

5.2.5 Effect of $CuBr_2$ on LED performance

As an alternative way of ligand engineering, different kinds of metal bromide have been used to enhance the PLQY of LHP NCs. We firstly treated the Cu0 NCs with $CuBr_2$ together with $CuCl_2$ and without $CuCl_2$. As shown in Figure 5.12c-d, co-treatment of the Cu0 NCs with $CuBr_2$ and $CuCl_2$ could lead to an emission with shorter wavelength than that of the Cu30 NC solution. Then, we changed the ligand from DDAB to DDAC or a mixture of DDAB and DDAC. The obtained NC solutions, labeled as CuClCuBr-DDAB, CuClCuBr-DDABDDAC and CuClCuBr-DDAC, were then used to fabricate LEDs.

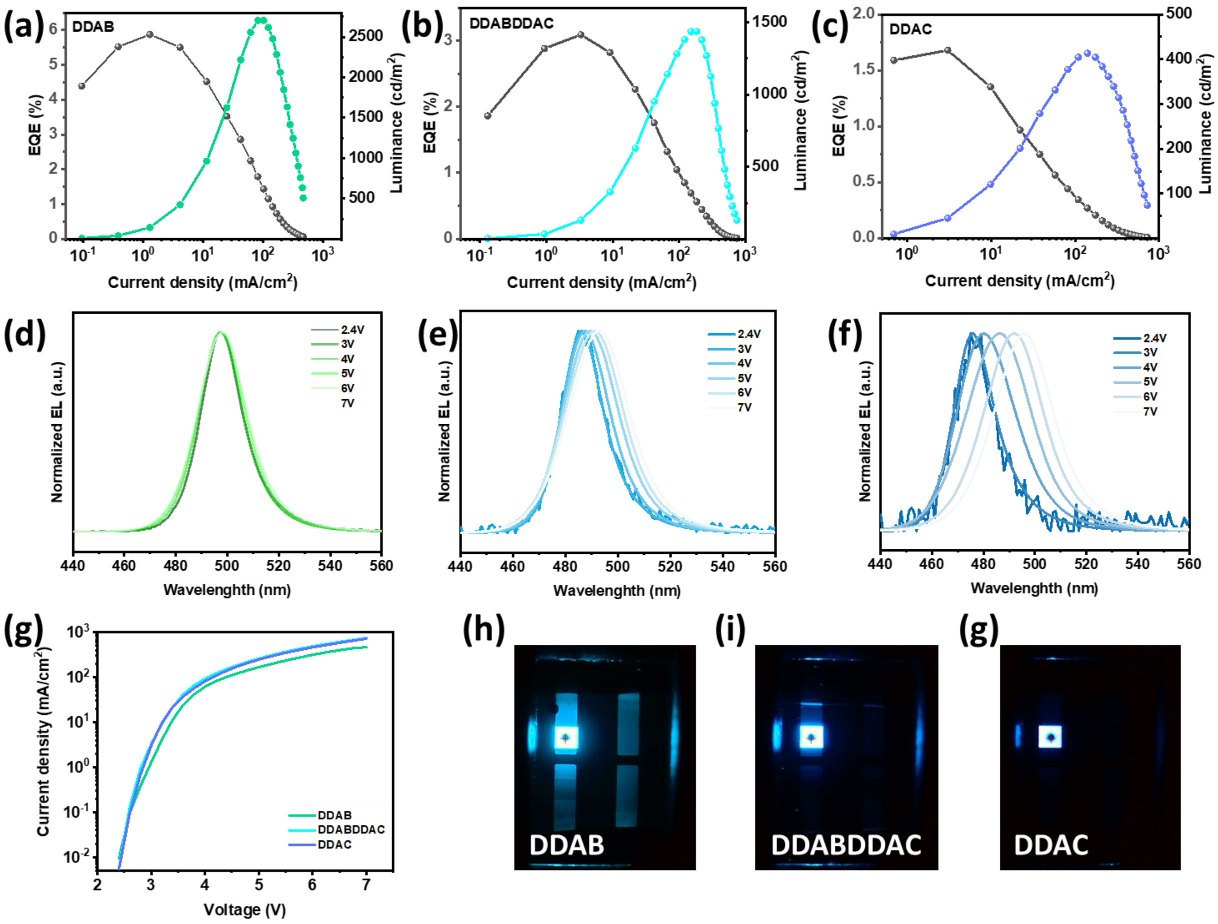

Figure 5.23. Performance of CuClCuBr-DDAB, CuClCuBr-DDABDDAC and CuClCuBr-DDAC LEDs. (a) EQE and luminance as a function of current density; (d) normalized EL spectra under increasing bias of the CuClCuBr-DDAB LED; (b) EQE and luminance as a function of current density; (e) normalized EL spectra under increasing bias of the CuClCuBr-DDABDDAC LED; (c) EQE and luminance as a function of current density; (f) normalized EL spectra under increasing bias of the CuClCuBr-DDAC LED; (g) comparison of current densities of the CuClCuBr-DDAB, CuClCuBr-DDABDDAC and CuClCuBr-DDAC LEDs as a function of applied voltage; and photos of the running (h) CuClCuBr-DDAB, (i) CuClCuBr-DDABDDAC, and (g) CuClCuBr-DDAC LEDs.

For the CuClCuBr-DDAB NCs-based LED, green EL emission peaked at 498 nm was obtained and remained stable with increasing bias (Figure 5.23d). The maximum EQE and luminance of the LED were 5.9% and 2704 cd/m^2 (Figure 5.23a). For the CuClCuBr-DDABDDAC NCs-based LED, sky-blue EL emission was obtained, with the maximum EQE and luminance of 3.1% and 1436 cd/m^2 (Figure 5.23b). However, the EL spectra red-shifted from 485 nm to 493 nm with the bias increasing from 2.4 V to 7 V (Figure 5.23e).

For the CuClCuBr-DDAC NCs-based LED, blue EL emission was obtained (Figure 5.23f), with the maximum EQE and luminance of 1.7% and 413 cd/m^2 (Figure 5.23c). However, the EL spectra suffered from serious red-shift from 475 nm to 496 nm, when the bias increased from 2.4 V to 7 V. The red-shift presents similar phenomena as we observed in Figure 5.21b, d; that is, the more chloride content in the NCs, the more serious the red-shift of the EL spectra under increasing voltages. This may be attributed to ion migration due to co-existence of chloride and bromide ions. This also suggests that there is an optimal ratio between chloride and bromide in order to obtain NCs which are stable under bias.

Figures 5.23h-g display the photos of the three running devices. Although the current density of the CuClCuBr-DDAB during the operation, which is usually proportional to device brightness, is lower than the other two (Figure 5.23g), the brightness of the CuClCuBr-DDABDDAC LED and the CuClCuBr-DDAC LED were lower. This may be due to misalignment of the band energies between the emissive layer and the transporting layers, considering that the same LED structure was adopted for all the devices.

5.3 Summary

In summary, we prepared LHP NCs with sky-blue emission at RT by addition $CuCl_2$ during ligand exchange process in the post-synthesis. The NCs showed high stability in air and excellent performance in optoelectronic devices. Solvent proved to have a significant effect on device performance and EL spectra stability. LEDs based on Cu30-octane NCs exhibited much higher device efficiency than Cu30-hexane NCs-based LED, and presented highly stable EL spectra during operation. Optimization of the ligand of the Cu30-octane NCs by a mixture of DDAB and DDAC allowed it possible to fabricate LEDs with the highest EQE, 5.02%, and luminance at the maximum EQE, 130 cd/m^2, among the reported sky-blue LHP NC LEDs at the time.

Through a series control experiments together with experimental observations, a probable post-synthesis mechanism during the treatment with $CuCl_2$ was proposed. The work introduced for the first time Cu-treated LHP NCs into the preparation of high-efficient sky-blue NC LEDs, and provided a promising way towards the fabrication of highly performing blue LEDs.

Chapter 6: Conclusions and prospects

6.1 Conclusions

In this thesis (as shown in Chapter 3), we worked at addressing four issues of LHP NCs for the fabrication of optoelectronic devices, owing to existence of long-chain and insulating organic ligands. Firstly, various chemicals were tried to treat the LHP NCs in film or in solution. Using a combination of BBr, SCN solution and EA to treat the LHP NCs in solution, the conductivity of the LHP NCs in films was improved. The optical properties of films based on the treated NC solution were also improved, as testified by the increased PL QY. Moreover, various solvents were tried to disperse the treated NCs and the morphology of the films based on these NC solutions was characterized. We found that a compact and smooth LHP NC film could be obtained by spin-coating treated LHP NCs dispersed in hexane. In the meanwhile, we showed that films based on the treated NCs exhibited high long-term stability both in optical performance and film morphology. To be specific, the treated NC films present rather stable optical performance including stable PL emission and PL decay lifetime, and stable NC size between the fresh and the aged films. In contrast, the untreated films used as a control show fast growth in NCs size and degradation of the optical performances during aging. The good stability of the SCNBBr films is attributed to the synergetic effect of SCN and BBr in enhancing the structural stability of NCs during the treatment in solution as well as during the aging of the films. The formation of mixtures of $CsPbBr_3$, Cs_4PbBr_6 and $CsPb_2Br_5$ phases was suggested to play a role in stabilizing the SCNBBr films.

Apart from works based on the above treatment, PEA was also tried to improve the optical performance of the NC solution and the corresponding films. A combination of PEA and the SCN solution was proved to be beneficial for higher brightness or PLQY and longer carrier lifetime. The works based on NC films expanded the capabilities for applying pristine LHP NCs in optoelectronic devices.

In Chapter 4, we reported our results on green LEDs based on $CsPbBr_3$ NC solutions treated in different ways. Highly stable and efficient green LEDs, with L_{50} of 27 min at 5 V, were obtained, based on $CsPbBr_3$ NC solutions treated with proper amount of SCN solution. Possible reasons for the champion device was investigated by C-AFM in terms of morphology and current distribution of NC film under applied voltages. The results show that performance of NC-based LEDs strongly depends on the distribution of NCs in the emissive layer, and that the efficiency roll-off in the NC-based LEDs at high current density can be attributed to displacement and deterioration of NC film with increasing applied voltages. The work proposes a facile route to treat sensitive perovskite NCs and to fabricate perovskite NC-based LED with high stability. Moreover, a new evidence was supplied for the efficiency roll-off in NC LED.

The effect of potassium on $CsPbBr_3$ NC solutions and LEDs was also studied. It was found that treating $CsPbBr_3$ NC solutions with potassium salts during post-synthesis is unfavorable, although it is usually beneficial when used directly during synthesis of halide perovskite according to literature.

In addition, LEDs realized using an inorganic ETL, ZnO NCs, were explored. The effect of the dispersion solvent for ZnO NCs on the roughness of the ZnO NCs films and the LED performance was studied. A mixed solvent of hexane and DE at a proper ratio was found to be resistant to being washed away by ZnO NC solution in LEDs with a normal structure. TOPO was found to be able to further improve the performance of green LEDs. The work gives guidance to fabrication of all-inorganic perovskite LEDs.

In Chapter 5, LHP NCs with sky-blue emission were synthesized at RT by addition of $CuCl_2$ during the post-synthesis ligand exchange process. Through optimization of various synthesis parameter, $CuCl_2$-treated NCs with high stability in air and excellent performance in optoelectronic devices were achieved. When the NC solutions were applied into LEDs, a few interesting results were obtained. Solvent proved to have a significant effect on device performance and EL spectra stability. LEDs based on Cu30-octane NCs exhibited much higher device efficiency than Cu30-hexane NCs-based LED, and presented highly stable EL spectra during operation. Optimization of the ligand of the Cu30-octane NCs by a mixture of DDAB and DDAC allowed it possible to fabricate LEDs with the highest EQE, 5.02%, and luminance at the maximum EQE, 130 cd/m^2, among the reported sky-blue LHP NC LEDs at the time. Moreover, based on a series of control experiments in combination with experimental observations, a probable post-synthesis mechanism during the treatment with $CuCl_2$ was proposed. The work introduced for the first time Cu-treated LHP NCs into the preparation of high-efficient sky-blue NC LEDs, and provided a promising way towards the fabrication of highly performing blue LEDs.

6.2 Prospects

There is still large room to optimize LHP NCs-based LEDs before these could be actually commercialized. In terms of the synthesis of LHP NCs, it is highly desired to get NCs which could be directly used to fabricate LEDs, thus avoiding post-synthesis treatments of the LHP NC solutions. According to current reports on one-pot synthesis of LHP NCs with proper conductivity, new ligands are required to be designed and produced in large amount. At the same time, the effect of doping to tune the emission wavelength and stability of the LHP NCs deserves further investigations.

In terms of LED efficiency, the device structure needs to be further optimized by selecting ETL and HTL with better band alignment with the LHP NCs. Moreover, passivation of the interface between the transporting layers and the LHP NC layer should be emphasized in order to increase the radiative recombination and improve the EQE of the LEDs.

In terms of commercialization of LHP NCs-based LEDs, attention should be paid to improve both the stability of the LHP NCs and the development of inorganic transporting layers. In addition, it is necessary and important to delve deeper into the mechanism of both highly performing and poorly performing devices in order to provide effective guidance for fabrication of highly efficient and stable LHP NCs-based LED.

List of papers

1. **Fang Chen**, Muhammad Imran, Lea Pasquale, Marco Salerno and Mirko Prato. "Long-term optical and morphological stability of $CsPbBr_3$ nanocrystal-based films." Materials Research Bulletin (2021) 134, 111107. DOI: 10.1016/j.materresbull.2020.111107.
2. **Fang Chen**, Leimeng Xu, Yan Li, Tao Fang, Tiantian Wang, Marco Salerno, Mirko Prato and Jizhong Song. "Highly efficient sky-blue light-emitting diodes based on Cu-treated halide perovskite nanocrystals." Journal of Materials Chemistry C (2020) 8, 13445-13452. DOI: 10.1039/D0TC03042B.
3. **Fang Chen**, Karunakara Moorthy Boopathi, Muhammad Imran, Simone Lauciello and Marco Salerno. "Thiocyanate-Treated Perovskite-Nanocrystal-Based Light-Emitting Diodes with Insight in Efficiency Roll-Off." Materials (2020)13, 2, 367. DOI: 10.3390/ma13020367.
4. **Fang Chen**, Marco Salerno and Mirko Prato. "Effect of dispersing solvent on lead halide perovskite nanocrystal film." (in preparation)
5. Palazon Francisco, **Fang Chen**, Quinten A. Akkerman, Muhammad Imran, Roman Krahne and Liberato Manna. "Effects of Oxygen Plasma on the Chemical, Light-emitting, and Electrical Transport Properties of Inorganic and Hybrid Lead Bromide Perovskite Nanocrystal Films." ACS Applied Nano Materials (2018) 1, 10, 5396–5400. DOI: 10.1021/acsanm.8b01424.

Acknowledgements

It was a precious experience for me to do this PhD. There was happy time and hard time. I am glad that I come to the end. I am happy for myself. I am also grateful for the great help provided by others.

First of all, I would like to give my sincere appreciation and big thanks to my supervisor Dr. Mirko Prato and to my advisor Dr. Marco Salerno. Without their kind guidance and great support, it would have been impossible for me to finish the PhD successfully. I am happy to have been in a team with them. They accepted me and gave me trust as well as confidence in the second half of my PhD period. Dr. Mirko Prato was always serious in editing my drafts and improved considerably the accuracy of the logic and the content of the articles. Dr. Marco Salerno gave me a lot of help in scientific writing. I am thankful for their guiding me towards achieving better works. I would also like to appreciate Dr. Roman Krahne for his providing me this opportunity to work in iit. I am thankful for his kind guidance in experiments and in work skills at the beginning of the PhD period.

Also, I would like to extend my appreciation to Prof. Liberato Manna, Dr. Davide Spirito, Dr. Muhammad Imran and Dr. Quinten A. Akkerman for their kind advice during discussion and great assistance in experiments. I would like to thank Dr. Karunakara Moorthy Boopathi, Dr. Vincenzo Caligiuri, Dr. Dmitry Baranov, Dr. Ahmed Abdelhady, Dr. Milan Palei, Dr. Francesco Di Stasio, Dr. Beatriz Martin Garcia, Dr. Zhiya Dang and Dr. Irene Rosina for their kind support and help in experiments. I am also grateful for Simone Lauciello, Gabriele La Rosa, Lea Pasquale, Filippo Drago, Marco Leoncini, Fabio Moia, Francesco De Donato, Simone Nitti, and Claudio Biagini for their kind training and help in the labs.

I am thankful to Iulia Manolache Orlatan, Noemi Pretelli (UniGe) and Prof. Renata Riva (UniGe). With their kind help in dealing with many administration work, research and study in Genova and in other countries have become smooth.

Special thanks are given to Dr. Marco Salerno, Dr. Giuseppe Vicidomini, Dr. Yanlong Huang, Dr. Jianyao Zheng (AMOLF), Dr. Aymeric Marcel Louis Le Gratiet, Dr. Yingqi Zhao, Prof. Davide Comoretto (UniGe), Dr. Fei Chen and Dr. Peng Chen for their kind advice and psychological support during my most difficult time.

I also would like to give my great thanks to my dear Chinese friends (Haiyan Sun, Xinyuan Zhao, Jiatao Ding, Yuqiang Wu, Gaofeng Li, Jianan Huang, Qi Qin, Xiangping Zhu, Lvye Lin, Anqing Duan, Kun Li, Xue Bai, Tao Li, Zhuoqi Cheng, Wei Fu, Lin Chen, etc.) and dear foreign friends (Lia Vasquez Sanchez, Aniruddha Ray, Ngoc Mai An, Balaji Dhanabalan, Roman Kaiukov, Giulia Biffi, etc.) in Genova. We spent a lot of happy time together and they made my life more colorful.

Moreover, I am extremely grateful to Prof. Dr. Jizhong Song (NUST) and Dr. Sai Bai (Linköping University) for their providing me exchange opportunity and giving me guidance in research. Great thanks are also extended to Dr. Leimeng Xu, Ye Wu, Yan Li, Tiantian Wang, Song Bai, Jiawei Chen and Le Ma from Nanjing University of science and technology for their kind help during my exchange period.

Finally, I would like to thank my parents and my little brother for their agreeing on my choice of doing PhD, their forgiving my not giving them enough time and their constant love.

With the kind help from all the people mentioned above, my PhD period has become meaningful and colorful. All the best to all of them.

References

1. Quan, L.N., et al., *Perovskites for Next-Generation Optical Sources.* Chemical Reviews, 2019.
2. Bai, S., et al., *Planar perovskite solar cells with long-term stability using ionic liquid additives.* Nature, 2019. **571**(7764): p. 245-250.
3. Yang, S., et al., *Stabilizing halide perovskite surfaces for solar cell operation with wide-bandgap lead oxysalts.* Science, 2019. **365**(6452): p. 473-478.
4. Tong, J., et al., *Carrier lifetimes of >1 μs in Sn-Pb perovskites enable efficient all-perovskite tandem solar cells.* Science, 2019. **364**(6439): p. 475-479.
5. Jeong, M., et al., *Stable perovskite solar cells with efficiency exceeding 24.8% and 0.3-V voltage loss.* Science, 2020. **369**(6511): p. 1615-1620.
6. Wang, Z., et al., *27%-Efficiency Four-Terminal Perovskite/Silicon Tandem Solar Cells by Sandwiched Gold Nanomesh.* Advanced Functional Materials, 2020. **30**(4): p. 1908298.
7. Li, Y., et al., *High-performance perovskite photodetectors based on solution-processed all-inorganic CsPbBr3 thin films.* Journal of Materials Chemistry C, 2017. **5**(33): p. 8355-8360.
8. Liu, X., et al., *Metal Halide Perovskites: Synthesis, Ion Migration, and Application in Field-Effect Transistors.* Small, 2018. **14**(36): p. 1801460.
9. Service, R.F., *Perovskite LEDs begin to shine.* Science, 2019. **364**(6444): p. 918-918.
10. Sutherland, B.R. and E.H. Sargent, *Perovskite photonic sources.* Nature Photonics, 2016. **10**: p. 295.
11. Lin, K., et al., *Perovskite light-emitting diodes with external quantum efficiency exceeding 20 per cent.* Nature, 2018. **562**(7726): p. 245-248.
12. Xu, W., et al., *Rational molecular passivation for high-performance perovskite light-emitting diodes.* Nature Photonics, 2019. **13**: p. 418–424.
13. Shamsi, J., et al., *Metal Halide Perovskite Nanocrystals: Synthesis, Post-Synthesis Modifications, and Their Optical Properties.* Chemical reviews, 2019. **119**(5): p. 3296-3348.
14. Zou, Y., et al., *Recent progress toward perovskite light-emitting diodes with enhanced spectral and operational stability.* Materials Today Nano, 2019. **5**: p. 100028.
15. Akkerman, Q.A. and L. Manna, *What Defines a Halide Perovskite?* ACS Energy Letters, 2020. **5**(2): p. 604-610.
16. Manser, J.S., J.A. Christians, and P.V. Kamat, *Intriguing Optoelectronic Properties of Metal Halide Perovskites.* Chemical Reviews, 2016. **116**(21): p. 12956-13008.
17. Song, Z., J. Zhao, and Q. Liu, *Luminescent perovskites: recent advances in theory and experiments.* Inorganic Chemistry Frontiers, 2019. **6**(11): p. 2969-3011.
18. Akkerman, Q.A., et al., *Genesis, challenges and opportunities for colloidal lead halide perovskite nanocrystals.* Nature Materials, 2018. **17**(5): p. 394-405.
19. Protesescu, L., et al., *Nanocrystals of Cesium Lead Halide Perovskites (CsPbX3, X = Cl, Br, and I): Novel Optoelectronic Materials Showing Bright Emission with Wide Color Gamut.* Nano Letters, 2015. **15**(6): p. 3692-3696.
20. Liu, P., et al., *Halide-Rich Synthesized Cesium Lead Bromide Perovskite Nanocrystals for Light-Emitting Diodes with Improved Performance.* Chemistry of Materials, 2017. **29**(12): p. 5168-5173.

21. Imran, M., et al., *Benzoyl Halides as Alternative Precursors for the Colloidal Synthesis of Lead-Based Halide Perovskite Nanocrystals.* Journal of the American Chemical Society, 2018. **140**(7): p. 2656-2664.
22. Veldhuis, S.A., et al., *Crown Ethers Enable Room-Temperature Synthesis of CsPbBr3 Quantum Dots for Light-Emitting Diodes.* ACS Energy Letters, 2018. **3**(3): p. 526-531.
23. Yan, F., et al., *Highly Efficient Visible Colloidal Lead-Halide Perovskite Nanocrystal Light-Emitting Diodes.* Nano Letters, 2018. **18**(5): p. 3157-3164.
24. Yao, Y., et al., *Efficient Quantum Dot Light-Emitting Diodes Based on Trioctylphosphine Oxide-Passivated Organometallic Halide Perovskites.* ACS Omega, 2019. **4**(5): p. 9150-9159.
25. Perumal, A., et al., *High brightness formamidinium lead bromide perovskite nanocrystal light emitting devices.* Scientific Reports, 2016. **6**: p. 36733.
26. Hassan, Y., et al., *Facile Synthesis of Stable and Highly Luminescent Methylammonium Lead Halide Nanocrystals for Efficient Light Emitting Devices.* Journal of the American Chemical Society, 2019.
27. Nim, G.K., P. Bansal, and P. Kar, *Nitrate Ion-Incorporated Stable Perovskite Nanocrystals by a Solvent-Free Mechanochemical Reaction.* ACS Omega, 2019. **4**(13): p. 15678-15683.
28. Karmakar, A., et al., *Mechanochemical synthesis of 0D and 3D cesium lead mixed halide perovskites.* Chemical Communications, 2019. **55**(35): p. 5079-5082.
29. Protesescu, L., et al., *Low-Cost Synthesis of Highly Luminescent Colloidal Lead Halide Perovskite Nanocrystals by Wet Ball Milling.* ACS Applied Nano Materials, 2018. **1**(3): p. 1300-1308.
30. Heuer-Jungemann, A., et al., *The Role of Ligands in the Chemical Synthesis and Applications of Inorganic Nanoparticles.* Chemical Reviews, 2019. **119**(8): p. 4819-4880.
31. Nenon, D.P., et al., *Design Principles for Trap-Free CsPbX3 Nanocrystals: Enumerating and Eliminating Surface Halide Vacancies with Softer Lewis Bases.* Journal of the American Chemical Society, 2018. **140**(50): p. 17760-17772.
32. Emre, Y., et al., *Amine-Free Synthesis of Cesium Lead Halide Perovskite Quantum Dots for Efficient Light-Emitting Diodes.* Advanced Functional Materials, 2016. **26**(47): p. 8757-8763.
33. Imran, M., et al., *Shape-Pure, Nearly Monodispersed CsPbBr3 Nanocubes Prepared Using Secondary Aliphatic Amines.* Nano Letters, 2018. **18**(12): p. 7822-7831.
34. Imran, M., et al., *Simultaneous Cationic and Anionic Ligand Exchange For Colloidally Stable CsPbBr3 Nanocrystals.* ACS Energy Letters, 2019. **4**(4): p. 819-824.
35. Dai, J., et al., *Charge Transport between Coupling Colloidal Perovskite Quantum Dots Assisted by Functional Conjugated Ligands.* Angewandte Chemie International Edition, 2018. **57**(20): p. 5754-5758.
36. Krieg, F., et al., *Colloidal CsPbX3 (X = Cl, Br, I) Nanocrystals 2.0: Zwitterionic Capping Ligands for Improved Durability and Stability.* ACS Energy Letters, 2018. **3**(3): p. 641-646.
37. Pan, J., et al., *Bidentate Ligand-Passivated CsPbI3 Perovskite Nanocrystals for Stable Near-Unity Photoluminescence Quantum Yield and Efficient Red Light-Emitting Diodes.* Journal of the American Chemical Society, 2018. **140**(2): p. 562-565.
38. Tan, Y., et al., *Highly Luminescent and Stable Perovskite Nanocrystals with Octylphosphonic Acid as a Ligand for Efficient Light-Emitting Diodes.* ACS Applied Materials & Interfaces, 2018. **10**(4): p. 3784-3792.
39. Lu, M., et al., *Ammonium Thiocyanate-Passivated CsPbI3 Perovskite Nanocrystals for Efficient Red Light-Emitting Diodes.* The Journal of Physical Chemistry C, 2019. **123**(37): p. 22787−22792.
40. Chen, F., et al., *Thiocyanate-Treated Perovskite-Nanocrystal-Based Light-Emitting Diodes with Insight in Efficiency Roll-Off.* Materials, 2020. **13**(2): p. 367.
41. Han, T.-H., et al., *Perovskite-polymer composite cross-linker approach for highly-stable and efficient perovskite solar cells.* Nature Communications, 2019. **10**(1): p. 520.

42. Zhao, B., et al., *High-efficiency perovskite–polymer bulk heterostructure light-emitting diodes.* Nature Photonics, 2018. **12**(12): p. 783-789.
43. Di Stasio, F., et al., *Near-Unity Photoluminescence Quantum Yield in CsPbBr3 Nanocrystal Solid-State Films via Postsynthesis Treatment with Lead Bromide.* Chemistry of Materials, 2017. **29**(18): p. 7663-7667.
44. Ghosh, S. and L. Manna, *The Many "Facets" of Halide Ions in the Chemistry of Colloidal Inorganic Nanocrystals.* Chemical Reviews, 2018. **118**(16): p. 7804-7864.
45. Leng, M., et al., *Surface Passivation of Bismuth-Based Perovskite Variant Quantum Dots To Achieve Efficient Blue Emission.* Nano Letters, 2018. **18**(9): p. 6076-6083.
46. Li, H., et al., *Enhancing Luminescence and Photostability of CsPbBr3 Nanocrystals via Surface Passivation with Silver Complex.* The Journal of Physical Chemistry C, 2018. **122**(24): p. 12994-13000.
47. Song, J., et al., *Organic-Inorganic Hybrid Passivation Enables Perovskite QLEDs with an EQE of 16.48.* Adv Mater, 2018. **30**(50): p. 1805409.
48. Safdari, M., et al., *Layered 2D alkyldiammonium lead iodide perovskites: synthesis, characterization, and use in solar cells.* Journal of Materials Chemistry A, 2016. **4**(40): p. 15638-15646.
49. Zhang, T., et al., *In Situ Fabrication of Highly Luminescent Bifunctional Amino Acid Crosslinked 2D/3D NH3C4H9COO(CH3NH3PbBr3)n Perovskite Films.* Advanced Functional Materials, 2017. **27**(1): p. 1603568.
50. Kovalenko, M.V., L. Protesescu, and M.I. Bodnarchuk, *Properties and potential optoelectronic applications of lead halide perovskite nanocrystals.* Science, 2017. **358**(6364): p. 745-750.
51. Zabet-Khosousi, A. and A.-A. Dhirani, *Charge Transport in Nanoparticle Assemblies.* Chemical Reviews, 2008. **108**(10): p. 4072-4124.
52. Kovalenko, M.V. and M.I. Bodnarchuk, *Lead Halide Perovskite Nanocrystals: From Discovery to Self-assembly and Applications.* CHIMIA International Journal for Chemistry, 2017. **71**(7-8): p. 461-470.
53. Almeida, G., I. Infante, and L. Manna, *Resurfacing halide perovskite nanocrystals.* Science, 2019. **364**(6443): p. 833-834.
54. Chen, B., et al., *Imperfections and their passivation in halide perovskite solar cells.* Chemical Society Reviews, 2019. **48**(14): p. 3842-3867.
55. Zheng, X., et al., *Reducing Defects in Halide Perovskite Nanocrystals for Light-Emitting Applications.* The Journal of Physical Chemistry Letters, 2019. **10**(10): p. 2629-2640.
56. Chen, W., et al., *Surface ‐ Passivated Cesium Lead Halide Perovskite Quantum Dots: Toward Efficient Light ‐ Emitting Diodes with an Inverted Sandwich Structure.* Advanced Optical Materials, 2018.
57. Woo, J.Y., et al., *Highly Stable Cesium Lead Halide Perovskite Nanocrystals through in Situ Lead Halide Inorganic Passivation.* Chemistry of Materials, 2017. **29**(17): p. 7088-7092.
58. Yue, W. and S. Handong, *All ‐ Inorganic Metal Halide Perovskite Nanostructures: From Photophysics to Light ‐ Emitting Applications.* Small Methods, 2018. **2**(1): p. 1700252.
59. Koscher, B.A., et al., *Essentially Trap-Free CsPbBr3 Colloidal Nanocrystals by Postsynthetic Thiocyanate Surface Treatment.* Journal of the American Chemical Society, 2017. **139**(19): p. 6566-6569.
60. van der Stam, W., et al., *Highly Emissive Divalent-Ion-Doped Colloidal CsPb(1-x)M(x)Br(3) Perovskite Nanocrystals through Cation Exchange.* Journal of the American Chemical Society, 2017. **139**(11): p. 4087-4097.
61. Rastogi, P., et al., *Enhancing the Performance of CdSe/CdS Dot-in-Rod Light-Emitting Diodes via Surface Ligand Modification.* ACS Applied Materials & Interfaces, 2018. **10**(6): p. 5665-5672.

62. Bian, H., et al., *Graded Bandgap CsPbI2+xBr1-x Perovskite Solar Cells with a Stabilized Efficiency of 14.4%.* Joule, 2018. **2**(8): p. 1500-1510.
63. Palazon, F., et al., *Effects of Oxygen Plasma on the Chemical, Light-emitting, and Electrical Transport Properties of Inorganic and Hybrid Lead Bromide Perovskite Nanocrystal Films.* ACS Applied Nano Materials, 2018. **1**(10): p. 5396–5400.
64. Guyot-Sionnest, P., *Electrical Transport in Colloidal Quantum Dot Films.* The Journal of Physical Chemistry Letters, 2012. **3**(9): p. 1169-1175.
65. Li, J., et al., *50-Fold EQE Improvement up to 6.27% of Solution-Processed All-Inorganic Perovskite CsPbBr3 QLEDs via Surface Ligand Density Control.* Advanced Materials, 2017. **29**(5): p. 1603885.
66. Moyen, E., et al., *Ligand removal and photo-activation of CsPbBr3 quantum dots for enhanced optoelectronic devices.* Nanoscale, 2018. **10**(18): p. 8591-8599.
67. Kumawat, N.K., et al., *Ligand Engineering to Improve the Luminance Efficiency of CsPbBr3 Nanocrystal Based Light-Emitting Diodes.* The Journal of Physical Chemistry C, 2018. **122**(25): p. 13767-13773.
68. Kim, Y., et al., *Efficient Luminescence from Perovskite Quantum Dot Solids.* ACS Applied Materials & Interfaces, 2015. **7**(45): p. 25007-25013.
69. Chiba, T., et al., *High-Efficiency Perovskite Quantum-Dot Light-Emitting Devices by Effective Washing Process and Interfacial Energy Level Alignment.* ACS Applied Materials & Interfaces, 2017. **9**(21): p. 18054-18060.
70. Hoshi, K., et al., *Purification of Perovskite Quantum Dots Using Low-Dielectric-Constant Washing Solvent "Diglyme" for Highly Efficient Light-Emitting Devices.* ACS Applied Materials & Interfaces, 2018. **10**(29): p. 24607–24612.
71. Jo, J.W., et al., *Acid-Assisted Ligand Exchange Enhances Coupling in Colloidal Quantum Dot Solids.* Nano Letters, 2018. **18**(7): p. 4417-4423.
72. Wheeler, L.M., et al., *Targeted Ligand-Exchange Chemistry on Cesium Lead Halide Perovskite Quantum Dots for High-Efficiency Photovoltaics.* Journal of the American Chemical Society, 2018. **140**(33): p. 10504-10513.
73. Pan, J., et al., *Highly Efficient Perovskite-Quantum-Dot Light-Emitting Diodes by Surface Engineering.* Advanced Materials, 2016. **28**(39): p. 8718-8725.
74. Li, G., et al., *Highly bright and low turn-on voltage CsPbBr3 quantum dot LEDs via conjugation molecular ligand exchange.* Nano Research, 2018. **12**: p. 109–114.
75. Akkerman, Q.A., et al., *Tuning the Optical Properties of Cesium Lead Halide Perovskite Nanocrystals by Anion Exchange Reactions.* Journal of the American Chemical Society, 2015. **137**(32): p. 10276-10281.
76. Chiba, T., et al., *Anion-exchange red perovskite quantum dots with ammonium iodine salts for highly efficient light-emitting devices.* Nature Photonics, 2018. **12**(11): p. 681-687.
77. Song, J., et al., *Quantum Dot Light-Emitting Diodes Based on Inorganic Perovskite Cesium Lead Halides (CsPbX3).* Advanced Materials, 2015. **27**(44): p. 7162-7167.
78. Di Stasio, F., et al., *High-Efficiency Light-Emitting Diodes Based on Formamidinium Lead Bromide Nanocrystals and Solution Processed Transport Layers.* Chemistry of Materials, 2018. **30**(18): p. 6231-6235.
79. Song, J., et al., *Room-Temperature Triple-Ligand Surface Engineering Synergistically Boosts Ink Stability, Recombination Dynamics, and Charge Injection toward EQE-11.6% Perovskite QLEDs.* Advanced Materials, 2018. **30**(30): p. 1800764.
80. Creutz, S.E., et al., *Anion Exchange in Cesium Lead Halide Perovskite Nanocrystals and Thin Films Using Trimethylsilyl Halide Reagents.* Chemistry of Materials, 2018. **30**(15): p. 4887-4891.
81. Qing‐Dong, O., et al., *Recent Advances in Energetics of Metal Halide Perovskite Interfaces.* Advanced Materials Interfaces, 2017. **4**(2): p. 1600694.

82. Rudd, P.N. and J. Huang, *Metal Ions in Halide Perovskite Materials and Devices.* Trends in Chemistry, 2019. **1**(4): p. 394-409.
83. Walsh, A., *Principles of Chemical Bonding and Band Gap Engineering in Hybrid Organic–Inorganic Halide Perovskites.* The Journal of Physical Chemistry C, 2015. **119**(11): p. 5755-5760.
84. Xiao, G., et al., *Pressure Effects on Structure and Optical Properties in Cesium Lead Bromide Perovskite Nanocrystals.* Journal of the American Chemical Society, 2017. **139**(29): p. 10087-10094.
85. Akkerman, Q.A., et al., *Strongly emissive perovskite nanocrystal inks for high-voltage solar cells.* Nature Energy, 2016. **2**: p. 16194.
86. Shan, X., et al., *Junction Propagation in Organometal Halide Perovskite–Polymer Composite Thin Films.* The Journal of Physical Chemistry Letters, 2017. **8**(11): p. 2412-2419.
87. Wei, Z. and J. Xing, *The Rise of Perovskite Light-Emitting Diodes.* The Journal of Physical Chemistry Letters, 2019. **10**(11): p. 3035-3042.
88. Quan, L.N., et al., *Perovskites for Light Emission.* Advanced Materials. **0**(0): p. 1801996.
89. Yan, F. and H.V. Demir, *LEDs using halide perovskite nanocrystal emitters.* Nanoscale, 2019. **11**(24): p. 11402-11412.
90. A., V.S., et al., *Perovskite Materials for Light ‑ Emitting Diodes and Lasers.* Advanced Materials, 2016. **28**(32): p. 6804-6834.
91. Kim, H.P., et al., *High-Efficiency, Blue, Green, and Near-Infrared Light-Emitting Diodes Based on Triple Cation Perovskite.* Advanced Optical Materials, 2017. **5**(7): p. 1600920.
92. Birkhold, S.T., et al., *Direct Observation and Quantitative Analysis of Mobile Frenkel Defects in Metal Halide Perovskites Using Scanning Kelvin Probe Microscopy.* The Journal of Physical Chemistry C, 2018. **122**(24): p. 12633-12639.
93. Shan, Q., et al., *High Performance Metal Halide Perovskite Light-Emitting Diode: From Material Design to Device Optimization.* Small, 2017. **13**(45): p. 1701770.
94. Pimputkar, S., et al., *Prospects for LED lighting.* Nature Photonics, 2009. **3**(4): p. 180-182.
95. Shamsi, J., et al., *Bright-Emitting Perovskite Films by Large-Scale Synthesis and Photoinduced Solid-State Transformation of CsPbBr3 Nanoplatelets.* ACS Nano, 2017. **11**(10): p. 10206-10213.
96. Xu, L., et al., *A bilateral interfacial passivation strategy promoting efficiency and stability of perovskite quantum dot light-emitting diodes.* Nature Communications, 2020. **11**(1): p. 3902.
97. Xiao, Z., et al., *Efficient perovskite light-emitting diodes featuring nanometre-sized crystallites.* Nature Photonics, 2017. **11**: p. 108.
98. Zhang, X., et al., *Enhancing the Brightness of Cesium Lead Halide Perovskite Nanocrystal Based Green Light-Emitting Devices through the Interface Engineering with Perfluorinated Ionomer.* Nano Letters, 2016. **16**(2): p. 1415-1420.
99. Li, X., et al., *Bright colloidal quantum dot light-emitting diodes enabled by efficient chlorination.* Nature Photonics, 2018. **12**(3): p. 159-164.
100. Fang, T., et al., *Perovskite QLED with an external quantum efficiency of over 21% by modulating electronic transport.* Science Bulletin, 2020.
101. Kumawat, N.K., et al., *Blue perovskite light-emitting diodes: progress, challenges and future directions.* Nanoscale, 2019. **11**(5): p. 2109-2120.
102. Ren, Z., et al., *Hole Transport Bilayer Structure for Quasi-2D Perovskite Based Blue Light-Emitting Diodes with High Brightness and Good Spectral Stability.* Advanced Functional Materials, 2019. **29**(43): p. 1905339.
103. Williamson, S., H.Z. Cummins, and J.N. Kidder. *Light and Color in Nature and Art*. 1983.
104. Smith, T. and J. Guild, *The C.I.E. colorimetric standards and their use.* Transactions of the Optical Society, 1931. **33**(3): p. 73-134.

105. Kumar, S., et al., *Mixing Entropy-Induced Layering Polydispersity Enabling Efficient and Stable Perovskite Nanocrystal Light-Emitting Diodes.* ACS Energy Letters, 2019. **4**(1): p. 118-125.
106. Lee, K.-H., et al., *Over 40 cd/A Efficient Green Quantum Dot Electroluminescent Device Comprising Uniquely Large-Sized Quantum Dots.* ACS Nano, 2014. **8**(5): p. 4893-4901.
107. Wang, L., et al., *Solvent-Assisted Surface Engineering for High-Performance All-Inorganic Perovskite Nanocrystal Light-Emitting Diodes.* ACS Applied Materials & Interfaces, 2018. **10**(23): p. 19828-19835.
108. Chen, F., et al., *Highly efficient sky-blue light-emitting diodes based on Cu-treated halide perovskite nanocrystals.* Journal of Materials Chemistry C, 2020.
109. Shi, Y., et al., *A Strategy for Architecture Design of Crystalline Perovskite Light-Emitting Diodes with High Performance.* Advanced Materials, 2018. **30**(25): p. 1800251.
110. Chiba, T. and J. Kido, *Lead halide perovskite quantum dots for light-emitting devices.* Journal of Materials Chemistry C, 2018. **6**(44): p. 11868-11877.
111. Shirasaki, Y., et al., *Emergence of colloidal quantum-dot light-emitting technologies.* Nature Photonics, 2012. **7**: p. 13.
112. Wang, H.-C., et al., *Perovskite Quantum Dots and Their Application in Light-Emitting Diodes.* Small, 2018. **14**(1): p. 1702433.
113. Zhou, Q., et al., *In Situ Fabrication of Halide Perovskite Nanocrystal-Embedded Polymer Composite Films with Enhanced Photoluminescence for Display Backlights.* Advanced Materials, 2016. **28**(41): p. 9163-9168.
114. Yuan, Z., et al., *Unveiling the synergistic effect of precursor stoichiometry and interfacial reactions for perovskite light-emitting diodes.* Nature Communications, 2019. **10**(1): p. 2818.
115. Yu, H., et al., *Green Light-Emitting Devices Based on Perovskite CsPbBr3 Quantum Dots.* Frontiers in Chemistry, 2018. **6**(381).
116. Li, G., et al., *Highly Efficient Perovskite Nanocrystal Light-Emitting Diodes Enabled by a Universal Crosslinking Method.* Advanced Materials, 2016. **28**(18): p. 3528-3534.
117. Shi, Z., et al., *Localized Surface Plasmon Enhanced All-Inorganic Perovskite Quantum Dot Light-Emitting Diodes Based on Coaxial Core/Shell Heterojunction Architecture.* Advanced Functional Materials, 2018. **28**(20): p. 1707031.
118. Zhang, X., et al., *All-Inorganic Perovskite Nanocrystals for High-Efficiency Light Emitting Diodes: Dual-Phase CsPbBr3-CsPb2Br5 Composites.* Advanced Functional Materials, 2016. **26**(25): p. 4595-4600.
119. Barbagiovanni, E.G., et al., *Quantum confinement in Si and Ge nanostructures: Theory and experiment.* Applied Physics Reviews, 2014. **1**(1): p. 011302.
120. Neikov, O.D. and N.A. Yefimov, *Chapter 9 - Nanopowders*, in *Handbook of Non-Ferrous Metal Powders (Second Edition)*, O.D. Neikov, S.S. Naboychenko, and N.A. Yefimov, Editors. 2019, Elsevier: Oxford. p. 271-311.
121. Verma, J., et al., *12 - Nitride LEDs based on quantum wells and quantum dots*, in *Nitride Semiconductor Light-Emitting Diodes (LEDs)*, J. Huang, H.-C. Kuo, and S.-C. Shen, Editors. 2014, Woodhead Publishing. p. 368-408.
122. Xing, J., et al., *Color-stable highly luminescent sky-blue perovskite light-emitting diodes.* Nature Communications, 2018. **9**(1): p. 3541.
123. Yuan, S., et al., *Optimization of Low-Dimensional Components of Quasi-2D Perovskite Films for Deep-Blue Light-Emitting Diodes.* Advanced Materials, 2019. **31**(44): p. 1904319.
124. Jiang, Y., et al., *Spectra stable blue perovskite light-emitting diodes.* Nature Communications, 2019. **10**(1): p. 1868.
125. Kumar, S., et al., *Efficient Blue Electroluminescence Using Quantum-Confined Two-Dimensional Perovskites.* ACS Nano, 2016. **10**(10): p. 9720-9729.

126. Kumawat, N.K., et al., *Band Gap Tuning of CH3NH3Pb(Br1–xClx)3 Hybrid Perovskite for Blue Electroluminescence.* ACS Applied Materials & Interfaces, 2015. **7**(24): p. 13119-13124.
127. Wang, H., et al., *Blue perovskite light-emitting diodes based on RbX-doped polycrystalline CsPbBr3 perovskite films.* Journal of Materials Chemistry C, 2019. **7**(19): p. 5596-5603.
128. Gangishetty, M.K., S.N. Sanders, and D.N. Congreve, *Mn2+ Doping Enhances the Brightness, Efficiency, and Stability of Bulk Perovskite Light-Emitting Diodes.* ACS Photonics, 2019. **6**(5): p. 1111-1117.
129. Wang, Q., et al., *Efficient Sky-Blue Perovskite Light-Emitting Devices Based on Ethylammonium Bromide Induced Layered Perovskites.* ACS Applied Materials & Interfaces, 2017. **9**(35): p. 29901-29906.
130. Vashishtha, P., et al., *High Efficiency Blue and Green Light-Emitting Diodes Using Ruddlesden–Popper Inorganic Mixed Halide Perovskites with Butylammonium Interlayers.* Chemistry of Materials, 2019. **31**(1): p. 83-89.
131. Cheng, L., et al., *Sky-blue perovskite light-emitting diodes based on quasi-two-dimensional layered perovskites.* Chinese Chemical Letters, 2017. **28**(1): p. 29-31.
132. Li, Z., et al., *Modulation of recombination zone position for quasi-two-dimensional blue perovskite light-emitting diodes with efficiency exceeding 5%.* Nature Communications, 2019. **10**(1): p. 1027.
133. Liu, Y., et al., *Efficient blue light-emitting diodes based on quantum-confined bromide perovskite nanostructures.* Nature Photonics, 2019. **13**(11): p. 760-764.
134. Wang, Q., et al., *Efficient sky-blue perovskite light-emitting diodes via photoluminescence enhancement.* Nature Communications, 2019. **10**(1): p. 5633.
135. Zhang, F., et al., *Efficient Blue Perovskite Light-Emitting Diodes Boosted by 2D/3D Energy Cascade Channels.* Advanced Functional Materials, 2020. **n/a**(n/a): p. 2001732.
136. Yao, E.-P., et al., *High-Brightness Blue and White LEDs based on Inorganic Perovskite Nanocrystals and their Composites.* Advanced Materials, 2017. **29**(23): p. 1606859.
137. van der Stam, W., et al., *Highly Emissive Divalent-Ion-Doped Colloidal CsPb1–xMxBr3 Perovskite Nanocrystals through Cation Exchange.* Journal of the American Chemical Society, 2017. **139**(11): p. 4087-4097.
138. Wu, Y., X. Li, and H. Zeng, *Highly Luminescent and Stable Halide Perovskite Nanocrystals.* ACS Energy Letters, 2019. **4**(3): p. 673-681.
139. Yong, Z.-J., et al., *Doping-Enhanced Short-Range Order of Perovskite Nanocrystals for Near-Unity Violet Luminescence Quantum Yield.* Journal of the American Chemical Society, 2018. **140**(31): p. 9942-9951.
140. Xu, L., et al., *A comprehensive review of doping in perovskite nanocrystals/quantum dots: evolution of structure, electronics, optics, and light-emitting diodes.* Materials Today Nano, 2019. **6**: p. 100036.
141. Zhang, X., et al., *Rational chemical doping of metal halide perovskites.* Chemical Society Reviews, 2019. **48**(2): p. 517-539.
142. Zhou, Y., et al., *Metal-Doped Lead Halide Perovskites: Synthesis, Properties, and Optoelectronic Applications.* Chemistry of Materials, 2018. **30**(19): p. 6589-6613.
143. Deng, W., et al., *Organometal Halide Perovskite Quantum Dot Light-Emitting Diodes.* Advanced Functional Materials, 2016. **26**(26): p. 4797-4802.
144. Gangishetty, M.K., et al., *Reducing Architecture Limitations for Efficient Blue Perovskite Light-Emitting Diodes.* Advanced Materials, 2018. **30**(20): p. 1706226.
145. Hou, S., et al., *Efficient Blue and White Perovskite Light-Emitting Diodes via Manganese Doping.* Joule, 2018. **2**(11): p. 2421-2433.

146. Shin, Y.S., et al., *Vivid and Fully Saturated Blue Light-Emitting Diodes Based on Ligand-Modified Halide Perovskite Nanocrystals.* ACS Applied Materials & Interfaces, 2019. **11**(26): p. 23401-23409.
147. Ochsenbein, S.T., et al., *Engineering Color-Stable Blue Light-Emitting Diodes with Lead Halide Perovskite Nanocrystals.* ACS Applied Materials & Interfaces, 2019. **11**(24): p. 21655-21660.
148. Todorović, P., et al., *Spectrally Tunable and Stable Electroluminescence Enabled by Rubidium Doping of CsPbBr3 Nanocrystals.* Advanced Optical Materials, 2019. **7**(24): p. 1901440.
149. Shynkarenko, Y., et al., *Direct Synthesis of Quaternary Alkylammonium-Capped Perovskite Nanocrystals for Efficient Blue and Green Light-Emitting Diodes.* ACS Energy Letters, 2019. **4**(11): p. 2703-2711.
150. De Roo, J., et al., *Highly Dynamic Ligand Binding and Light Absorption Coefficient of Cesium Lead Bromide Perovskite Nanocrystals.* ACS Nano, 2016. **10**(2): p. 2071-2081.
151. de Mello, J.C., H.F. Wittmann, and R.H. Friend, *An improved experimental determination of external photoluminescence quantum efficiency.* Advanced Materials, 1997. **9**(3): p. 230-232.
152. Numata, Y., et al., *Thiocyanate Containing Two-Dimensional Cesium Lead Iodide Perovskite, Cs2PbI2(SCN)2: Characterization, Photovoltaic Application, and Degradation Mechanism.* ACS Applied Materials & Interfaces, 2018. **10**(49): p. 42363-42371.
153. Jiang, Q., et al., *Pseudohalide-Induced Moisture Tolerance in Perovskite CH3NH3Pb(SCN)2I Thin Films.* Angewandte Chemie International Edition, 2015. **54**(26): p. 7617-7620.
154. Zhang, B., et al., *Alkyl Phosphonic Acids Deliver CsPbBr3 Nanocrystals with High Photoluminescence Quantum Yield and Truncated Octahedron Shape.* Chemistry of Materials, 2019. **31**(21): p. 9140-9147.
155. Na Quan, L., et al., *Edge stabilization in reduced-dimensional perovskites.* Nature Communications, 2020. **11**(1): p. 170.
156. Dastidar, S., et al., *High chloride doping levels stabilize the perovskite phase of cesium lead iodide.* Nano letters, 2016. **16**(6): p. 3563-3570.
157. Li, C., et al., *Origins and mechanisms of hysteresis in organometal halide perovskites.* Journal of Physics: Condensed Matter, 2017. **29**(19): p. 193001.
158. Zhou, Y. and Y. Zhao, *Chemical stability and instability of inorganic halide perovskites.* Energy & Environmental Science, 2019. **12**(5): p. 1495-1511.
159. Guo, X., et al., *Investigation of moisture stability and PL characteristics of terpineol-passivated organic–inorganic hybrid perovskite.* Materials for Renewable and Sustainable Energy, 2016. **5**(4): p. 17.
160. Li, J., B. Bo, and X. Gao, *The degradation of structure and luminescence in CsPbBr3 perovskite nanocrystals under UV light illumination.* AIP Conference Proceedings, 2018. **2036**(1): p. 030018.
161. Scheidt, R.A., C. Atwell, and P.V. Kamat, *Tracking Transformative Transitions: From CsPbBr3 Nanocrystals to Bulk Perovskite Films.* ACS Materials Letters, 2019. **1**(1): p. 8-13.
162. Chen, F., et al., *Long-term optical and morphological stability of CsPbBr3 nanocrystal-based films.* Materials Research Bulletin, 2021. **134**: p. 111107.
163. Zhao, Q., et al., *Size-Dependent Lattice Structure and Confinement Properties in CsPbI3 Perovskite Nanocrystals: Negative Surface Energy for Stabilization.* ACS Energy Letters, 2019. **5**(1): p. 238-247.
164. Zhang, R., et al., *A potassium thiocyanate additive for hysteresis elimination in highly efficient perovskite solar cells.* Inorganic Chemistry Frontiers, 2019. **6**(2): p. 434-442.
165. de Quilettes, D.W., et al., *Impact of microstructure on local carrier lifetime in perovskite solar cells.* Science, 2015. **348**(6235): p. 683-686.

166. González-Carrero, S., R.E. Galian, and J. Pérez-Prieto, *Organometal Halide Perovskites: Bulk Low-Dimension Materials and Nanoparticles.* Particle & Particle Systems Characterization, 2015. **32**(7): p. 709-720.
167. Yin, H., et al., *Excitonic and Confinement Effects of 2D Layered (C10H21NH3)2PbBr4 Single Crystals.* ACS Applied Energy Materials, 2018. **1**(4): p. 1476-1482.
168. Zhu, B.-S., et al., *Room temperature precipitated dual phase CsPbBr3–CsPb2Br5 nanocrystals for stable perovskite light emitting diodes.* Nanoscale, 2018. **10**(41): p. 19262-19271.
169. Acharyya, P., et al., *Single pot synthesis of indirect band gap 2D CsPb2Br5 nanosheets from direct band gap 3D CsPbBr3 nanocrystals and the origin of their luminescence properties.* Nanoscale, 2019. **11**(9): p. 4001-4007.
170. Wang, K.-H., et al., *Large-Scale Synthesis of Highly Luminescent Perovskite-Related CsPb2Br5 Nanoplatelets and Their Fast Anion Exchange.* Angewandte Chemie International Edition, 2016. **55**(29): p. 8328-8332.
171. Wang, W., et al., *CsPbBr3/Cs4PbBr6 Nanocomposites: Formation Mechanism, Large-scale and Green Synthesis, and Application in White Light-Emitting Diodes.* Crystal Growth & Design, 2018. **18**(10): p. 6133-6141.
172. Chen, X., et al., *Centimeter-Sized Cs4PbBr6 Crystals with Embedded CsPbBr3 Nanocrystals Showing Superior Photoluminescence: Nonstoichiometry Induced Transformation and Light-Emitting Applications.* Advanced Functional Materials, 2018. **28**(16): p. 1706567.
173. Xu, L., et al., *Synthesis of stable and phase-adjustable CsPbBr3@Cs4PbBr6 nanocrystals via novel anion–cation reactions.* Nanoscale Advances, 2019. **1**(3): p. 980-988.
174. de Weerd, C., et al., *Hybridization of Single Nanocrystals of Cs4PbBr6 and CsPbBr3.* The Journal of Physical Chemistry C, 2017. **121**(35): p. 19490-19496.
175. Sun, C., et al., *One Stone, Two Birds: High-Efficiency Blue-Emitting Perovskite Nanocrystals for LED and Security Ink Applications.* Chemistry of Materials, 2019. **31**(14): p. 5116-5123.
176. Su, Y., et al., *Highly efficient CsPbBr3 perovskite nanocrystals induced by structure transformation between CsPbBr3 and Cs4PbBr6 phases.* Journal of Materials Chemistry C, 2019. **7**(25): p. 7548-7553.
177. Lian, X., et al., *Light Emitting Diodes Based on Inorganic Composite Halide Perovskites.* Advanced Functional Materials, 2019. **29**(5): p. 1807345.
178. Qiao, B., et al., *Water-resistant, monodispersed and stably luminescent CsPbBr3/CsPb2Br5 core–shell-like structure lead halide perovskite nanocrystals.* Nanotechnology, 2017. **28**(44): p. 445602.
179. Lou, Y., et al., *Rod-shaped thiocyanate-induced abnormal band gap broadening in SCN− doped CsPbBr3 perovskite nanocrystals.* Nano Research, 2018. **11**(5): p. 2715-2723.
180. Akkerman, Q.A., A.L. Abdelhady, and L. Manna, *Zero-Dimensional Cesium Lead Halides: History, Properties, and Challenges.* The Journal of Physical Chemistry Letters, 2018. **9**(9): p. 2326-2337.
181. Zhang, X., et al., *Bright Perovskite Nanocrystal Films for Efficient Light-Emitting Devices.* The Journal of Physical Chemistry Letters, 2016. **7**(22): p. 4602-4610.
182. Zhang, L., et al., *Ultra-bright and highly efficient inorganic based perovskite light-emitting diodes.* Nature Communications, 2017. **8**: p. 15640.
183. Ban, M., et al., *Solution-processed perovskite light emitting diodes with efficiency exceeding 15% through additive-controlled nanostructure tailoring.* Nature Communications, 2018. **9**(1): p. 3892.
184. Tyona, M.D., 2013. **2**.
185. Roy, S., et al., *Influence of Substrate Wettability on the Morphology of Thin Polymer Films Spin-Coated on Topographically Patterned Substrates.* ACS Applied Materials & Interfaces, 2012. **4**(4): p. 1887-1896.

186. Mohd Arif, N.A.A., C.C. Jiun, and S. Shaari, *Effect of Annealing Temperature and Spin Coating Speed on Mn-Doped ZnS Nanocrystals Thin Film by Spin Coating.* Journal of Nanomaterials, 2017. **2017**: p. 6.
187. Yu, J.C., et al., *Effect of the solvent used for fabrication of perovskite films by solvent dropping on performance of perovskite light-emitting diodes.* Nanoscale, 2017. **9**(5): p. 2088-2094.
188. Lou, S., T. Xuan, and J. Wang, *Stability: A desiderated problem for the lead halide perovskites.* Optical Materials: X, 2019. **1**: p. 100023.
189. Chu, Y., et al., *Efficient and Stable Perovskite Photodetectors Based on Thiocyanate-Assisted Film Formation.* ACS Applied Materials & Interfaces, 2019. **11**(16): p. 14510-14514.
190. Wang, W.-T., S.K. Das, and Y. Tai, *Fully Ambient-Processed Perovskite Film for Perovskite Solar Cells: Effect of Solvent Polarity on Lead Iodide.* ACS Applied Materials & Interfaces, 2017. **9**(12): p. 10743-10751.
191. De Wolf, S., et al., *Organometallic Halide Perovskites: Sharp Optical Absorption Edge and Its Relation to Photovoltaic Performance.* The Journal of Physical Chemistry Letters, 2014. **5**(6): p. 1035-1039.
192. Zhang, W., et al., *Red shift in the photoluminescence of colloidal carbon quantum dots induced by photon reabsorption.* Applied Physics Letters, 2014. **104**(9): p. 091902.
193. Tavana, H., et al., *Contact Angles and Coating Film Thickness.* The Journal of Adhesion, 2005. **81**(1): p. 29-39.
194. Zou, W., et al., *Minimising efficiency roll-off in high-brightness perovskite light-emitting diodes.* Nature Communications, 2018. **9**(1): p. 608.
195. Yang, X., et al., *Efficient green light-emitting diodes based on quasi-two-dimensional composition and phase engineered perovskite with surface passivation.* Nature Communications, 2018. **9**(1): p. 570.
196. Wang, H., et al., *Trifluoroacetate induced small-grained CsPbBr3 perovskite films result in efficient and stable light-emitting devices.* Nature Communications, 2019. **10**(1): p. 665.
197. Gao, F., et al., *Enhanced performance of tin halide perovskite solar cell by addition of lead thiocyanate.* RSC Advances, 2018. **8**(25): p. 14025-14030.
198. Song, L., et al., *Efficient Inorganic Perovskite Light-Emitting Diodes with Polyethylene Glycol Passivated Ultrathin CsPbBr3 Films.* The Journal of Physical Chemistry Letters, 2017. **8**(17): p. 4148-4154.
199. Shan, Q., et al., *All-inorganic quantum-dot light-emitting diodes based on perovskite emitters with low turn-on voltage and high humidity stability.* Journal of Materials Chemistry C, 2017. **5**(18): p. 4565-4570.
200. Shi, Z., et al., *Strategy of Solution-Processed All-Inorganic Heterostructure for Humidity/Temperature-Stable Perovskite Quantum Dot Light-Emitting Diodes.* ACS Nano, 2018. **12**(2): p. 1462-1472.
201. Giuri, A., et al., *Ultra-Bright Near-Infrared Perovskite Light-Emitting Diodes with Reduced Efficiency Roll-off.* Scientific Reports, 2018. **8**(1): p. 15496.
202. Shen, J.-X., et al., *Unexpectedly Strong Auger Recombination in Halide Perovskites.* Advanced Energy Materials, 2018. **8**(30): p. 1801027.
203. Bae, W.K., et al., *Controlling the influence of Auger recombination on the performance of quantum-dot light-emitting diodes.* Nature Communications, 2013. **4**: p. 2661.
204. Sun, G., K. Lu, and F. Kun, *Percolation-induced conductor-insulator transition in a system of metal spheres in a dielectric fluid.* Physical Review E, 2011. **83**(4): p. 041405.
205. Wood, V., et al., *Air-Stable Operation of Transparent, Colloidal Quantum Dot Based LEDs with a Unipolar Device Architecture.* Nano Letters, 2010. **10**(1): p. 24-29.

206. Abdi-Jalebi, M., et al., *Maximizing and stabilizing luminescence from halide perovskites with potassium passivation.* Nature, 2018. **555**: p. 497.
207. Kuai, L., et al., *Passivating Crystal Boundaries with Potassium-Rich Phase in Organic Halide Perovskite.* Solar RRL, 2019. **3**(5): p. 1900053.
208. Bi, C., et al., *Spontaneous Passivation of Hybrid Perovskite by Sodium Ions from Glass Substrates: Mysterious Enhancement of Device Efficiency Revealed.* ACS Energy Letters, 2017. **2**(6): p. 1400-1406.
209. Hoang, M.T., et al., *Potassium Doping to Enhance Green Photoemission of Light-Emitting Diodes Based on CsPbBr3 Perovskite Nanocrystals.* Advanced Optical Materials. **n/a**(n/a): p. 2000742.
210. Worku, M., et al., *Hollow metal halide perovskite nanocrystals with efficient blue emissions.* Science Advances, 2020. **6**(17): p. eaaz5961.
211. Yang, J.-N., et al., *Potassium Bromide Surface Passivation on CsPbI3-xBrx Nanocrystals for Efficient and Stable Pure Red Perovskite Light-Emitting Diodes.* Journal of the American Chemical Society, 2020. **142**(6): p. 2956-2967.
212. Liang, X., et al., *Colloidal metal oxide nanocrystals as charge transporting layers for solution-processed light-emitting diodes and solar cells.* Chemical Society Reviews, 2017. **46**(6): p. 1730-1759.
213. Zhang, C., et al., *Hydrofluoroethers as orthogonal solvents for all-solution processed perovskite quantum-dot light-emitting diodes.* Nano Energy, 2018. **51**: p. 358-365.
214. Zou, Y., et al., *A General Solvent Selection Strategy for Solution Processed Quantum Dots Targeting High Performance Light-Emitting Diode.* Advanced Functional Materials, 2017. **27**(1): p. 1603325.
215. Yang, P., et al., *High-Resolution Inkjet Printing of Quantum Dot Light-Emitting Microdiode Arrays.* Advanced Optical Materials, 2020. **8**(1): p. 1901429.
216. Lv, W., et al., *Assessment for Anion-Exchange Reaction in CsPbX3 (X = Cl, Br, I) Nanocrystals from Bond Strength of Inorganic Salt.* The Journal of Physical Chemistry C, 2019. **123**(39): p. 24313-24320.
217. Shapiro, A., et al., *Significance of Ni Doping in CsPbX3 Nanocrystals via Postsynthesis Cation–Anion Coexchange.* The Journal of Physical Chemistry C, 2019. **123**(40): p. 24979-24987.
218. Das Adhikari, S., et al., *Chemically Tailoring the Dopant Emission in Manganese‐Doped CsPbCl3 Perovskite Nanocrystals.* Angewandte Chemie International Edition, 2017. **56**(30): p. 8746-8750.
219. Chen, Y.-C., et al., *Enhanced Luminescence and Stability of Cesium Lead Halide Perovskite CsPbX3 Nanocrystals by Cu2+-Assisted Anion Exchange Reactions.* The Journal of Physical Chemistry C, 2019. **123**(4): p. 2353-2360.
220. Bi, C., et al., *Thermally Stable Copper(II)-Doped Cesium Lead Halide Perovskite Quantum Dots with Strong Blue Emission.* The Journal of Physical Chemistry Letters, 2019. **10**(5): p. 943-952.
221. Biesinger, M.C., *Advanced analysis of copper X-ray photoelectron spectra.* Surface and Interface Analysis, 2017. **49**(13): p. 1325-1334.
222. Hoye, R.L.Z., et al., *Identifying and Reducing Interfacial Losses to Enhance Color-Pure Electroluminescence in Blue-Emitting Perovskite Nanoplatelet Light-Emitting Diodes.* ACS Energy Letters, 2019. **4**(5): p. 1181-1188.
223. Lee, H., D. Ko, and C. Lee, *Direct Evidence of Ion-Migration-Induced Degradation of Ultrabright Perovskite Light-Emitting Diodes.* ACS Applied Materials & Interfaces, 2019. **11**(12): p. 11667-11673.
224. Dong, Y., et al., *Bipolar-shell resurfacing for blue LEDs based on strongly confined perovskite quantum dots.* Nature Nanotechnology, 2020. **15**: p. 668–674.